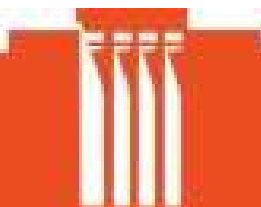# The influence of cavity photons on the transient transport of correlated electrons through a quantum ring with magnetic field and spin-orbit interaction

Thorsten Ludwig Arnold

THE INFLUENCE OF CAVITY PHOTONS ON THE TRANSIENT TRANSPORT OF CORRELATED ELECTRONS THROUGH A QUANTUM RING WITH MAGNETIC FIELD AND SPIN-ORBIT INTERACTION

Thorsten Ludwig Arnold

Advisor
Viðar Guðmundsson

Ph.D. committee
Andrei Manolescu
Hannes Jónsson

Opponents
Catalin Pascu Moca
Department of Theoretical Physics, Budapest University of Technology
and Economics, Budapest, Hungary
Kristján Leósson
University of Iceland

Faculty of Physical Sciences
School of Engineering and Natural Sciences
University of Iceland
Reykjavik, August 2014

The influence of cavity photons on the transient transport of correlated electrons through a quantum ring with magnetic field and spin-orbit interaction
Dissertation submitted in partial fulfillment of a Ph.D. degree in Physics

Abstract

We investigate time-dependent transport of Coulomb and spin-orbit interacting electrons through a finite-width quantum ring of realistic geometry under non-equilibrium conditions using a time-convolutionless non-Markovian master equation formalism. The ring is embedded in an electromagnetic cavity with a single mode of linearly or circularly polarized photon field. The electron-photon and Coulomb interactions are taken into full account using "exact" numerical diagonalization. A bias voltage is applied to external, semi-infinite leads along the x-axis, which are coupled to the quantum ring. The ring and leads are in a perpendicular magnetic field. The strength of the spin-orbit interaction and of the magnetic field penetrating the ring and leads are tunable.

We find that the lead-system-lead current is strongly suppressed by the y-polarized photon field at magnetic field with two flux quanta due to a degeneracy of the many-body energy spectrum of the mostly occupied states. Furthermore, the current can be significantly enhanced by the y-polarized field at magnetic field with half integer flux quanta. The y-polarized photon field perturbs the periodicity of the persistent current with the magnetic field and suppresses also its magnitude. Charge current vortices at the contact areas to the leads influence the charge circulation in the ring.

Moreover, a pronounced charge current dip associated with many-electron level crossings at the Aharonov-Casher (AC) phase $\Delta\Phi = \pi$ is found, which can be disguised by linearly polarized light. Comparing our numerical two-dimensional (2D) model to the analytical results of a toy model of a one-dimensional (1D) ring of non-interacting electrons with spin-orbit coupling, qualitative agreement can be found for the spin polarization currents. Quantitatively, however, the spin polarization currents are weaker in the more realistic 2D ring, especially for weak spin-orbit interaction, but can be considerably enhanced with the aid of a linearly polarized electromagnetic field. Specific spin polarization current symmetries relating the Dresselhaus spin-orbit interaction case to the Rashba one are found to hold for the 2D ring, which is embedded in the photon cavity.

The spin polarization and spin photocurrents of the quantum ring are largest for circularly polarized photon field and destructive AC phase interference. The charge current suppression dip due to the destructive AC phase becomes threefold under the circularly polarized photon field as the interaction of the electrons' angular momentum and spin angular momentum of light causes many-body level splitting leading to three level crossing locations instead of one. The circular charge current inside the ring, which is induced by the circularly polarized photon field, is found to be suppressed in a much wider range around the destructive AC phase than the lead-device-lead charge current. The charge current can be directed through one

of the two ring arms with the help of the circularly polarized photon field, but is superimposed by vortices of a smaller scale. Unlike the charge photocurrent, the flow direction of the spin photocurrent is found to be independent of the handedness of the circularly polarized photon field.

Útdráttur

Við könnum tímaháðan flutning rafeinda sem víxlverka innbyrðis með Coulomb-krafti og með víxlverkun spuna og brautar í gegnum skammtahring með raunsæju mætti og endanlegri breidd í ójafnvægisástandi með því að nota aðferðafræði sem byggist á ómarkóvsku stýrijöfnunni án tímaföldunar. Hringurinn er staðsettur í raf-segulsholi með stökum ljóseindahætti með hring- eða línulegri skautun. Fullt tillit er tekið til víxlverkana ljóseinda og rafeinda og Coulomb-víxlverkana rafeindanna með því að nota "nákvæma" tölulega reikninga í afstífðu fjöleindarúmi. Skammta-hringurinn er tengdur tveimur ytri forspenntum, hálfóendalegum leiðslum samsíða x-ásnum. Hringurinn og leiðslurnar eru staðsett í hornréttu segulsviði. Styrkur spuna og brautar víxlverkunarinnar og segulsviðsins sem smýgur gegnum hringinn og leiðslurnar er breytanlegur.

Við finnum töluverða veikingu straums um kerfið vegna y-skautaðs ljóseindasviðs ef segulflæðið um hringinn jafngildir tveimur flæðiskömmtum vegna þess að þau tvö fjöleindaástönd sem eru langmest setin skerast í orkurófinu. Ennfremur getur straumurinn verið töluvert meiri vegna y-skautaðs ljóseindasviðs þegar segulsvið-ið jafngildir hálftölu flæðiskömmtum. y-skautað ljóseindasvið raskar einnig lotu-eiginleikum stöðuga hringstraumsins sem fall af segulsviðinu og dregur úr honum. Hleðslustraumiður á snertisvæðum við leiðslurnar hafa áhrif á hleðsluhringrásina í hringnum.

Við finnum áberandi hleðslustraumlægð sem tengist skörun fjöleindastiga í orkuróf-inu þegar Aharonov-Casher (AC) fasinn $\Delta\Phi = \pi$. Þessi lægð hverfur að mestu leyti með víxlverkun við línulega skautað ljóseindasvið. Við bárum niðurstöður úr tölu-lega tvívíða líkani okkar saman við niðurstöður einfaldara líkans einvíðs hrings með óvíxlverkjandi rafeindum, en með spuna og brautar víxlverkun. Eigindleg samsvörun fannst fyrir spunaskautuðu straumana. Hins vegar skilar magnbundinn samanburð-ur þeirri niðurstöðu að spunaskautuðu straumarnir séu minni í raunsærri tvívíða hringnum, sérstaklega þegar víxlverkun spuna og brautar er lítil. Spunaskautuðu straumana er aftur á móti hægt að auka með línulega skautuðu rafsegulsviði. Sér-stakar samhverfur fundust fyrir spunaskautuðu straumana sem tengja saman tilfellin með Dresselhaus- og Rashba-víxlverkanir spuna og brautar. Þessar samhverfur rofna ekki í tvívíða hringnum í ljóseindaholinu.

Spunaskautunin og spunaljósstraumar skammtahringsins eru mestir fyrir hringskaut-að ljóseindasvið og eyðandi AC fasavíxl. Hleðslustraumlægðin sem orsakast af eyð-andi AC fasa verður þreföld undir áhrifum hringskautaðs ljóseindasviðs vegna þess að víxlverkunin milli hverfiþunga rafeindanna og spunahverfiþunga ljóssins veldur klofnun fjöleindaástanda í orkurófinu og birtist á þremur stöðum í stað eins þar sem skörun er í orkurófinu. Hringhleðslustraumurinn í hringnum sem orsakast af

hringskautaða ljóseindasviðinu er minni á miklu breiðara svæði kringum eyðandi AC fasann en hleðslustraumurinn í gegnum kerfið. Hægt er að stýra hleðslustraumnum þannig með hringskautaða ljóseindasviðinu að hann fari aðeins í gegnum annan hvorn arm hringsins. Samt þarf að geta þess að í hleðslustraumnum myndast iður á minni skala. Stefnan spunaljósstraumsins er ólíkt hleðsluljósstraumnum óháð því hvort hringskautaða ljóseindasviðið snúist rétt- eða andsælis.

List of publications

1. **Magnetic-field-influenced nonequilibrium transport through a quantum ring with correlated electrons in a photon cavity.**
   T. Arnold, C.-S. Tang, A. Manolescu, and V. Gudmundsson.
   Phys. Rev. B **87**, 035314 (2013).

2. **Stepwise introduction of model complexity in a generalized master equation approach to time- dependent transport.**
   V. Gudmundsson, O. Jonasson, T. Arnold, C.-S. Tang, H.-S. Goan, and A. Manolescu.
   Fortschritte der Physik **61**, no 2-3, 305 (2013).

3. **Impact of a circularly polarized cavity photon field on the charge and spin flow through an Aharonov-Casher ring.**
   T. Arnold, C.-S. Tang, A. Manolescu, and V. Gudmundsson.
   Physica E **60**, 170 (2014).

4. **Effects of geometry and linearly polarized cavity photons on charge and spin currents in a quantum ring with spin-orbit interactions.**
   T. Arnold, C.-S. Tang, A. Manolescu, and V. Gudmundsson.
   The European Physical Journal B **87**, 113 (2014).

Acknowledgements

I would like to thank Viðar Guðmundsson for his supervision. He was always willing to hear technical or physical problems that I encountered in the project and was very honestly trying to give a good answer. Furthermore, he aroused my interest in quantum optics, exact calculations and master equations and advised me very honestly and transparently by giving me freedom and responsibility to follow my interests.

I would like to thank Chi-Shung Tang for his interest in my research and his practical help in paper writing. I am grateful for fruitful discussions with Andrei Manolescu, Tómas Örn Rosdahl and Ólafur Jónasson.

Contents

List of Figures

1. Introduction

Quantum interference phenomena are essential when developing quantum devices. Quantum confined geometries conceived for such studies may consist of which-path interferometers [2, 3], coupled quantum wires [4, 5] or side-coupled quantum dots [6, 7]. These coupled quantum systems have captured interest due to their potential applications in electronic spectroscopy tools [8] and quantum information processing [9]. In this work, we focus on the charge and spin transport through a particular quantum device, the quantum ring [10, 11]. Quantum rings are interferometers with unique properties owing to their geometry. The magnetic flux through the ring system can drive persistent currents [12] and leads to the topological quantum interference phenomenon known as the Aharonov-Bohm (AB) effect [13–17]. Both, the persistent current and the ring conductance show characteristic oscillations with the period of one flux quantum, $\Phi_0 = hc/e$. The latter were first measured in 1985 [15]. The free spectrum of the one-dimensional (1D) quantum ring exhibits level crossings at half integer and integer multiples of Φ_0 [18, 19]. The persistent current dependence on the magnetic field [20] and electron-electron interaction strength [21] has been investigated adopting a two-dimensional quantum ring model with analytically known non-interacting properties [22]. Varying either the magnetic field or the electrostatic confining potentials allows the quantum interference to be tuned [23].

The non-trivially connected topology of quantum rings leads to further geometrical phases than the AB phase, which are important in the field of quantum transport. This is caused by the interaction of the electrons' spin with a magnetic field via the Zeeman interaction and an electric field via a so-called effective magnetic field stemming from special relativity [24]. The interaction between the spin and the electronic motion in, for example, the electric field, is called the Rashba SOI [25], which leads to the Aharonov-Casher (AC) effect. While the AB phase is acquired by a charged particle moving around a magnetic flux, an AC phase [26] is acquired by a particle with magnetic moment encircling, for example, a charged line. Hence, the AB phase can be tuned via the magnetic flux through the ring, while the AC phase can be tuned by the strength of the spin-orbit interaction (SOI). The Aharonov-Anandan (AA) phase [27] is the remaining phase of the AC phase when subtracting the so-called dynamical phase. When the system is propagated adiabatically, the dynamical phase describes the whole time-dependence while the remaining AA phase is static. This can be seen by introducing time-dependent parameters in the Hamilto-

nian under consideration [28]. In the non-adiabatic case, if the AA phase is defined similarly to the AA phase of the adiabatic system (for an alternative definition see Ref. [29]), a dependence of the AA phase on time-dependent fields can in general not totally be avoided. The dynamical phase captures then only a part of the dynamics of the global phase. Filipp [30] showed that the splitting of the global phase into the AA phase and the remaining dynamical phase can be achieved also in the non-adiabatic case. The Berry phase [31] is the adiabatic approximation of the AA phase.

The AC effect can be observed in the case of a more general electric field than the one produced by a charged line, i.e. including the radial component and a component in the z-direction [32]. Experimentally, it is relatively simple to realize an electric field in the z-direction, i.e. which is directed perpendicular to the two-dimensional (2D) plane containing the quantum ring structure. By changing the strength of the electric field, the SOI strength of the Rashba effect can be tuned. The AC effect appears also for a Dresselhaus SOI [33], which is typically stronger in GaAs than the Rashba SOI. Persistent equilibrium spin currents due to geometrical phases were addressed for the Zeeman interaction with an inhomogeneous, static magnetic field [34]. Later, Balatsky and Altshuler studied persistent spin currents related to the AC phase [35]. Several authors addressed the persistent spin current oscillations as the strength of the SOI [32, 36, 37] (or magnetic flux through the ring [38]) is increased. Opposite to the AB oscillations with the magnetic flux, the AC oscillations are not periodic with the SOI strength. The persistent spin current violates in general conservation laws [39]. Suggestions to measure persistent spin currents by the induced mechanical torque [40] or the induced electric field [39] have been proposed. An analytical state-dependent expression for a specific spin polarization of the spin current has been stated in Ref. [41].

The electronic transport through a quantum ring connected to leads, which is embedded in a magnetic field, has been addressed in several studies for only Rashba SOI [42–44], only Dresselhaus SOI [45] or both [46]. There has been considerable interest in the study of electronic transport through a quantum system in a strong system-lead coupling regime driven by periodic time-dependent potentials [47–50], longitudinally polarized fields [51–53], or transversely polarized fields [54, 55]. On the other hand, quantum transport driven by a transient time-dependent potential enables the development of switchable quantum devices, in which the interplay of the electronic system with external perturbation plays an important role [56–59]. These systems are usually operated in the weak system-lead coupling regime and described within the wide-band or the Markovian approximation [60–62]. Within this approximation, the energy dependence of the electron tunneling rate or the memory effect in the system are neglected by assuming that the correlation time of the electrons in the leads is much shorter than the typical response time of the central system. However, the transient transport is intrinsically linked to the coherence and relaxation dynamics and cannot generally be described in the Markovian ap-

2

proximation. The energy-dependent spectral density in the leads has to be included for accurate numerical calculation.

Quantum systems embedded in an electromagnetic cavity have become one of the most promising devices for quantum information processing applications [63–65]. Charge persistent currents in quantum rings can be produced by two time-delayed light pulses with perpendicularly oriented, linear polarization [66] and phase-locked laser pulses based on the circular photon polarization influencing the many-electron (ME) angular momentum [67]. Moreover, energy splitting of degenerate states in interaction with a monochromatic circularly polarized electromagnetic mode and its vacuum fluctuations can lead to charge persistent currents [68, 69]. Optical control of the spin current can be achieved by a nonadiabatic, two-component laser pulse [70]. Dynamical spin currents can be obtained by two asymmetric electromagnetic pulses [71]. Furthermore, the nonequilibrium dynamical response of the dipole moment and spin polarization of a quantum ring with SOI and magnetic field under two linearly polarized electromagnetic pulses has been studied [72]. The rotational symmetry of the ring resembles the characteristics of a circularly polarized photon field suggesting a strong light-matter interaction between single photons and the ring electrons. Circularly polarized light emission [73] and absorption [74] have been studied for quantum rings. Moreover, circularly polarized light has been used to generate persistent charge currents in quantum wells [75] and quantum rings [67–69, 76]. The basic principle behind this is a change of the orbital angular momentum of the electrons in the quantum ring by the absorption or emission of a photon leading to the circular charge transport. Improvements over circularly polarized light to optimize optical control for a finite-width quantum ring have been achieved [77]. We are considering here the influence of the cavity photons on the transient charge and spin transport inside and into and out of the ring. We treat the electron-photon interaction by using exact numerical diagonalization including many levels [78], i.e. beyond a two-level Jaynes-Cummings model or the rotating wave approximation and higher order corrections of it [79–81].

When the light-matter interaction is combined with the strong coupling of the quantum ring to the leads, further interesting phenomena arise (especially when the leads have a bias, which breaks additional transport symmetries). The electronic transport through a quantum system in a strong system-lead coupling regime was studied for longitudinally polarized fields [51–53], or transversely polarized fields [54, 55]. For a weak coupling between the system and the leads, the Markovian approximation, which neglects memory effects in the system, can be used [60–62, 82]. How to appropriately describe the carrier dynamics under non-equilibrium conditions with realistic device geometries is a challenging problem [83, 84]. Utilizing the giant dipole moments of inter-subband transitions in quantum wells [85, 86] enables researchers to reach the ultrastrong electron-photon coupling regime [87–89]. In this regime, the dynamical electron-photon coupling mechanism has to be explored beyond the wide-band and rotating-wave approximations [81, 90, 91]. To describe a stronger

transient system-lead coupling, we use a non-Markovian generalized master equation [92–94] involving energy-dependent coupling elements. The dynamics of our open system under non-equilibrium conditions and with a realistic device geometry is described with the time-convolutionless generalized master equation (TCL-GME) [95, 96], which is suitable for higher system-lead coupling and allows for a controlled perturbative expansion in the system-lead coupling strength.

In this work, we explore the transient effects of the spin and charge transport of electrons through a broad quantum ring in a linearly or circularly polarized electromagnetic cavity coupled to electrically biased leads. The electrons are interacting via the Coulomb interaction, Rashba SOI and Dresselhaus SOI and are influenced by a magnetic field. The electron-photon coupled system under investigation is mainly tuned by the applied magnetic field, the strength of the Rashba an Dresselhaus SOI and the polarization of the photon field. This thesis is organized as follows. In Chapter 2 we present the non-Markovian generalized master equation approach that we use. The Hamiltonian of the central system and the Hamiltonian of the leads is described in Chapter 3. Chapter 4 discusses the derivation and implementation of several time-dependent densities. Chapter 5 gives some numerical results and summarizes the main results of the attached papers.

2. Time-convolutionless non-Markovian generalized quantum master equation

2.1. Open quantum system

The dynamics of a general quantum system is given by the Liouville-von Neumann equation

$$i\hbar \frac{\partial \hat{\rho}(t)}{\partial t} = [\hat{H}(t), \hat{\rho}(t)] =: \mathcal{L}\hat{\rho}(t) \tag{2.1}$$

with $\hat{\rho}(t)$ being the density operator, which satisfies the properties

$$\hat{\rho}^\dagger(t) = \hat{\rho}(t) \ , \ \hat{\rho}(t) \geq 0 \ , \ \mathrm{Tr}[\hat{\rho}(t)] = 1. \tag{2.2}$$

If $\mathrm{Tr}[\hat{\rho}^2(t)] = 1$, then the density operator describes a pure state, if $\mathrm{Tr}[\hat{\rho}^2(t)] \leq 1$, then it describes a mixed state. The solution of Eq. (2.1) is

$$\hat{\rho}(t) = \hat{U}(t)\hat{\rho}(0)\hat{U}^\dagger(t) \tag{2.3}$$

with

$$\hat{U}(t) = \exp\left(-\frac{i}{\hbar}\hat{H}t\right). \tag{2.4}$$

When the quantum system is open, Eq. (2.1) is in principle a problem of infinite size in the matrices when the space is discretized meaning that the spectrum of $\hat{H}(t)$ is dense. Therefore, Eq. (2.1) can not be treated numerically and is commonly separated in a system of finite size and the remaining part of the quantum size called environment, which is of infinite size. The Hamiltonian is then split into three parts

$$\hat{H}(t) = \hat{H}_S + \hat{H}_E + \hat{H}_T(t), \tag{2.5}$$

where $\hat{H}_S$ describes the Hamiltonian of the finite system, $\hat{H}_E$ the Hamiltonian of the environment and $\hat{H}_T(t)$ the coupling between the system and the environment. Accordingly, the Liouville super-operator

$$\mathcal{L} = \mathcal{L}_S + \mathcal{L}_E + \mathcal{L}_T(t) \tag{2.6}$$

is decomposed into a system, environment and coupling part. As a consequence, the Liouville-von Neumann equation, Eq. (2.1) is

$$i\hbar\frac{\partial\hat{\rho}(t)}{\partial t} = [\mathcal{L}_S + \mathcal{L}_E + \mathcal{L}_T(t)]\,\hat{\rho}(t). \tag{2.7}$$

The density operator can be reduced to the finite system called the reduced density operator (RDO)

$$\hat{\rho}_S(t) := \text{Tr}_E[\hat{\rho}(t)]. \tag{2.8}$$

The equation of motion for the finite system is then of a similar form as the Liouville-von Neumann equation, Eq. (2.1), with the density operator, $\hat{\rho}(t)$, replaced by the RDO, $\hat{\rho}_S(t)$, but with an additional complicated term containing an integral kernel. The latter describes the coupling to the environment and would vanish if the system would be closed.

In principal, quantum master equations can be grouped into two groups, Markovian master equations, where the time evolution of the RDO does not depend on the evolution of the RDO in the past and non-Markovian master equations (where the Markovian approximation is not applied), where memory effects are important (especially when the correlation time of the environment is long). In this work, only non-Markovian quantum master equations are used.

2.2. Nakajima-Zwanzig projection operator technique [1]

We define the super-operators, $\mathcal{P}$ and $\mathcal{Q}$, which project the density operator on the central system and environment, respectively,

$$\mathcal{P}\hat{\rho}(t) = \text{Tr}_E[\hat{\rho}(t)] \otimes \hat{\rho}_E, \tag{2.9}$$

and

$$\mathcal{Q}\hat{\rho}(t) = \hat{\rho}(t) - \mathcal{P}\hat{\rho}(t), \tag{2.10}$$

with $\hat{\rho}_E$ being some fixed, normalized state of the environment to derive an exact equation of motion for the RDO. We apply the super-operators, $\mathcal{P}$ and $\mathcal{Q}$, on the Von Neumann equation, Eq. (2.1), which gives the following equations, if we use $\mathcal{P} + \mathcal{Q} = 1$,

$$i\hbar\frac{\partial}{\partial t}\mathcal{P}\hat{\rho}(t) = \mathcal{P}\mathcal{L}(t)\mathcal{P}\hat{\rho}(t) + \mathcal{P}\mathcal{L}(t)\mathcal{Q}\hat{\rho}(t) \tag{2.11}$$

and

$$i\hbar\frac{\partial}{\partial t}\mathcal{Q}\hat{\rho}(t) = \mathcal{Q}\mathcal{L}(t)\mathcal{P}\hat{\rho}(t) + \mathcal{Q}\mathcal{L}(t)\mathcal{Q}\hat{\rho}(t). \tag{2.12}$$

We can simplify the terms [97]

$$\mathcal{P}\mathcal{L}(t)\mathcal{P} = \mathcal{P}\mathcal{L}_S\mathcal{P} + \mathcal{P}\mathcal{L}_E\mathcal{P} + \mathcal{P}\mathcal{L}_T(t)\mathcal{P} = \mathcal{L}_S\mathcal{P}, \tag{2.13}$$

$$\mathcal{P}\mathcal{L}(t)\mathcal{Q} = \mathcal{P}\mathcal{L}_S\mathcal{Q} + \mathcal{P}\mathcal{L}_E\mathcal{Q} + \mathcal{P}\mathcal{L}_T(t)\mathcal{Q} = \mathcal{P}\mathcal{L}_T(t)\mathcal{Q}, \tag{2.14}$$

$$\mathcal{Q}\mathcal{L}(t)\mathcal{P} = \mathcal{Q}\mathcal{L}_S\mathcal{P} + \mathcal{Q}\mathcal{L}_E\mathcal{P} + \mathcal{Q}\mathcal{L}_T(t)\mathcal{P} = \mathcal{L}_T(t)\mathcal{P}, \tag{2.15}$$

and

$$\mathcal{Q}\mathcal{L}(t)\mathcal{Q} = \mathcal{Q}\mathcal{L}_S\mathcal{Q} + \mathcal{Q}\mathcal{L}_E\mathcal{Q} + \mathcal{Q}\mathcal{L}_T(t)\mathcal{Q} = \mathcal{L}_S\mathcal{Q} + \mathcal{L}_E\mathcal{Q} + \mathcal{Q}\mathcal{L}_T(t)\mathcal{Q} \tag{2.16}$$

in Eqs. (2.11) and (2.12) using

$$\mathcal{P}\mathcal{L}_S = \mathcal{L}_S\mathcal{P}, \tag{2.17}$$

$$\mathcal{P}\mathcal{L}_E\mathcal{P} = 0, \tag{2.18}$$

$$\mathcal{P}\mathcal{L}_E\mathcal{Q} = 0, \tag{2.19}$$

$$\mathcal{P}^2 = \mathcal{P}, \tag{2.20}$$

$$\mathcal{L}_E\mathcal{P} = 0 \tag{2.21}$$

and

$$\mathcal{P}\mathcal{L}_T(t)\mathcal{P} = 0. \tag{2.22}$$

Equation (2.17) is proven by

$$\hat{\rho}_E \otimes \text{Tr}_E[\mathcal{L}_S\hat{\rho}(t)] = \hat{\rho}_E \otimes \mathcal{L}_S\text{Tr}_E[\hat{\rho}(t)] = \mathcal{L}_S\hat{\rho}_E \otimes \text{Tr}_E[\hat{\rho}(t)]. \tag{2.23}$$

Equation (2.18) is satisfied when we assume that the environment is in equilibrium

$$[\hat{H}_E, \hat{\rho}_E] = 0 \tag{2.24}$$

since

$$\text{Tr}_E[\mathcal{L}_E\mathcal{P}\hat{\rho}(t)] = \text{Tr}_E[\hat{H}_E\hat{\rho}_E \otimes \text{Tr}_E[\hat{\rho}(t)] - \hat{\rho}_E \otimes \text{Tr}_E[\hat{\rho}(t)]\hat{H}_E] = 0. \tag{2.25}$$

Equation (2.19) can be proven with Eq. (2.10), Eq. (2.18) and

$$\text{Tr}_E[\mathcal{L}_E\hat{\rho}(t)] = \text{Tr}_E[\hat{H}_E\hat{\rho}(t) - \hat{\rho}(t)\hat{H}_E] = 0, \tag{2.26}$$

which is correct as the trace over the environment can be proven to be cyclic invariant as only $\hat{\rho}(t)$ extends also over the space of the central system. Equation (2.21) is satisfied with Eq. (2.24)

$$\mathcal{L}_E \mathcal{P} \hat{\rho}(t) = \mathcal{L}_E \hat{\rho}_E \otimes \mathrm{Tr}_E[\hat{\rho}(t)] = 0. \tag{2.27}$$

Equation (2.22) is satisfied since

$$\mathrm{Tr}_E[\hat{H}_T(t), \hat{\rho}_S(t) \otimes \hat{\rho}_E] = \sum_{ij} \langle i|\hat{H}_T(t)|j\rangle \, \hat{\rho}_S(t) \otimes \langle j|\hat{\rho}_E|i\rangle$$
$$- \sum_{ij} \hat{\rho}_S(t) \otimes \langle i|\hat{\rho}_E|j\rangle \, \langle j|\hat{H}_T(t)|i\rangle = 0, \tag{2.28}$$

where we have used the assumption, Eq. (2.24), to choose $\{|i\rangle\}$ and $\{|j\rangle\}$ to be the basis of the environment in which $\hat{H}_E$ and $\hat{\rho}_E$ are simultaneously diagonal. Furthermore, we assume that $\hat{H}_T(t)$ is linear in the creation or annihilation operators of the environment and system (which is an assumption, which is in practice often made, when the lead-environment coupling is described by sequential tunneling). Then, for $i \neq j$, $\langle j|\hat{\rho}_E|i\rangle = 0$, but for $i = j$, $\langle i|\hat{H}_T(t)|j\rangle = 0$ due to the linearity in the operators.

2.3. Time-convolutionless projection operator method

In order to have scaling parameter of the coupling strength between the environment and the system, we redefine

$$\hat{H}_T(t) \to \alpha \hat{H}_T(t) , \quad \mathcal{L}_T(t) \to \alpha \mathcal{L}_T(t) \tag{2.29}$$

and let $\alpha = 1$ at the end. Equation (2.12) can be rewritten to be

$$\frac{\partial}{\partial t} \mathcal{Q}\hat{\rho}(t) = -\frac{i}{\hbar} \alpha \mathcal{L}_T(t)\mathcal{P}\hat{\rho}(t) - \frac{i}{\hbar}[\mathcal{L}_S + \mathcal{L}_E + \alpha \mathcal{Q}\mathcal{L}_T(t)]\mathcal{Q}\hat{\rho}(t). \tag{2.30}$$

The solution of Eq. (2.30) is

$$Q\hat{\rho}(t) = -\frac{i}{\hbar} \alpha \int_0^t dt' \, \mathfrak{G}(t,t')\mathcal{L}_T(t')\mathcal{P}\hat{\rho}(t') + \mathfrak{G}(t,0)\mathcal{Q}\hat{\rho}(0) \tag{2.31}$$

with the propagator

$$\mathfrak{G}(t,t') = T_\leftarrow \exp\left(-\frac{i}{\hbar} \int_{t'}^t ds \, [\mathcal{L}_S + \mathcal{L}_E + \alpha \mathcal{Q}\mathcal{L}_T(s)]\right). \tag{2.32}$$

where $T_{\leftarrow}$ describes the chronological time ordering such that the time arguments of the super-operators increase from right to left. To confirm that Eq. (2.31) is the solution, we note that

$$\frac{\partial}{\partial t}\mathfrak{G}(t,t') = -\frac{i}{\hbar}[\mathcal{L}_S + \mathcal{L}_E + \alpha\mathcal{Q}\mathcal{L}_T(t)]\mathfrak{G}(t,t') \tag{2.33}$$

and

$$\frac{\partial}{\partial t}\mathcal{Q}\hat{\rho}(t) = -\frac{i}{\hbar}\alpha\mathfrak{G}(t,t)\mathcal{L}_T(t)\mathcal{P}\hat{\rho}(t)$$
$$-\frac{\alpha}{\hbar^2}[\mathcal{L}_S + \mathcal{L}_E + \alpha\mathcal{Q}\mathcal{L}_T(t)]\int_0^t dt'\,\mathfrak{G}(t,t')\mathcal{L}_T(t')\mathcal{P}\hat{\rho}(t')$$
$$-\frac{i}{\hbar}[\mathcal{L}_S + \mathcal{L}_E + \alpha\mathcal{Q}\mathcal{L}_T(t)]\mathfrak{G}(t,0)\mathcal{Q}\hat{\rho}(0). \tag{2.34}$$

We assume that the initial state of the system $\hat{\rho}(0)$ is an uncoupled tensor-product state of an environment and system state, which means that $\mathcal{Q}\hat{\rho}(0) = 0$, thus yielding for the solution of Eq. (2.30)

$$Q\hat{\rho}(t) = -\frac{i}{\hbar}\alpha\int_0^t dt'\,\mathfrak{G}(t,t')\mathcal{L}_T(t')\mathcal{P}\hat{\rho}(t'). \tag{2.35}$$

For $t > 0$, the lead-system coupling is switched on smoothly in our system meaning that $\mathcal{Q}\hat{\rho}(t) \neq 0$. The condition $\mathcal{Q}\hat{\rho}(0) = 0$ can be satisfied in realistic electronic systems when the tunneling barrier is high and when the system and environment have reached equilibrium states [98].

Now, the basic step in deriving the time-convolutionless (TCL) generalized master equation is the introduction of the backward time propagator of the total system

$$G(t,t') = T_{\rightarrow}\exp\left(\frac{i}{\hbar}\int_{t'}^t ds\,(\mathcal{L}_S + \mathcal{L}_E + \alpha\mathcal{L}_T(s))\right) \tag{2.36}$$

with the time ordering operator $T_{\rightarrow}$ ordering the time arguments of the super-operators such that they increase from the left to the right. Therefore, Eq. (2.35) can be written to be

$$\mathcal{Q}\hat{\rho}(t) = -\frac{i}{\hbar}\alpha\int_0^t dt'\,\mathfrak{G}(t,t')\mathcal{L}_T(t')\mathcal{P}G(t,t')(\mathcal{P}+\mathcal{Q})\hat{\rho}(t) \tag{2.37}$$

Next, we define the super-operator

$$\Sigma(t) := -\frac{i}{\hbar}\alpha\int_0^t dt'\,\mathfrak{G}(t,t')\mathcal{L}_T(t')\mathcal{P}G(t,t') \tag{2.38}$$

to simplify Eq. (2.37)

$$\mathcal{Q}\hat{\rho}(t) = \frac{1}{1-\Sigma(t)}\Sigma(t)\mathcal{P}\hat{\rho}(t). \tag{2.39}$$

2. Time-convolutionless non-Markovian generalized master equation

Then, we can turn to the equation of motion for the system, Eq. (2.11),

$$\frac{\partial}{\partial t}P\hat{\rho}(t) = -\frac{i}{\hbar}\mathcal{L}_S P\hat{\rho}(t) - \frac{i}{\hbar}\alpha\mathcal{P}\mathcal{L}_T(t)\mathcal{Q}\hat{\rho}(t) \tag{2.40}$$

and insert Eq. (2.39) into it

$$\frac{\partial}{\partial t}\mathcal{P}\hat{\rho}(t) = \left[-\frac{i}{\hbar}\mathcal{L}_S - \frac{i}{\hbar}\alpha\mathcal{P}\mathcal{L}_T(t)\frac{1}{1-\Sigma(t)}\Sigma(t)\right]\mathcal{P}\hat{\rho}(t)$$

$$= -\frac{i}{\hbar}\mathcal{L}_S\mathcal{P}\hat{\rho}(t) + \mathcal{K}(t)\mathcal{P}\hat{\rho}(t) \tag{2.41}$$

with the kernel of the TCL generalized master equation using Eq. (2.20)

$$\mathcal{K}(t) = -\frac{i}{\hbar}\alpha\mathcal{P}\mathcal{L}_T(t)\frac{1}{1-\Sigma(t)}\Sigma(t)\mathcal{P}. \tag{2.42}$$

For small coupling strength or not to large time argument t, one can assume that the inverse of $1 - \Sigma(t)$ exists

$$\frac{1}{1-\Sigma(t)} = \sum_{n=0}^{\infty}[\Sigma(t)]^n. \tag{2.43}$$

Then, the kernel, Eq. (2.42), becomes

$$\mathcal{K}(t) = -\frac{i}{\hbar}\alpha\mathcal{P}\mathcal{L}_T(t)\sum_{n=1}^{\infty}[\Sigma(t)]^n\mathcal{P}. \tag{2.44}$$

We will now show a systematic approximation of the kernel, Eq. (2.44), by expanding it perturbatively in terms of the coupling strength α. This can be achieved by expanding

$$\Sigma(t) = \sum_{n=1}^{\infty}\alpha^n\Sigma_n(t). \tag{2.45}$$

Note that the zeroth order term vanishes as can be seen from the definition of $\Sigma(t)$, Eq. (2.38). Inserting this into Eq. (2.44), we find

$$\mathcal{K}(t) = \sum_{n=2}^{\infty}\alpha^n\mathcal{K}_n(t) = -\frac{i}{\hbar}\alpha\mathcal{P}\mathcal{L}_T(t)\sum_{n=1}^{\infty}\left[\sum_{m=1}^{\infty}\alpha^m\Sigma_m(t)\right]^n\mathcal{P} \tag{2.46}$$

with the lowest order contribution to the kernel being

$$\mathcal{K}_2(t) = -\frac{i}{\hbar}\mathcal{P}\mathcal{L}_T(t)\Sigma_1(t)\mathcal{P}. \tag{2.47}$$

The lowest order in α of $\mathfrak{G}(t,t')$ is

$$\mathfrak{G}(t,t') = \exp\left(-\frac{i}{\hbar}(t-t')\mathcal{L}_0\right) \tag{2.48}$$

10

with $\mathcal{L}_0 = \mathcal{L}_E + \mathcal{L}_S$, which can be seen from a series expansion of the exponential. The lowest order of $G(t, t')$ is

$$G(t, t') = \exp\left(\frac{i}{\hbar}(t - t')\mathcal{L}_0\right).$$ (2.49)

As a consequence, the lowest order of the super-operator $\Sigma(t)$ is

$$\Sigma_1(t) = -\frac{i}{\hbar}\int_0^t dt'\ \exp\left(-\frac{i}{\hbar}(t - t')\mathcal{L}_0\right)\mathcal{L}_T(t')\mathcal{P}\exp\left(\frac{i}{\hbar}(t - t')\mathcal{L}_0\right).$$ (2.50)

The lowest (second) order contribution to the kernel, Eq. (2.47), then turns out to be

$$\mathfrak{K}_2(t) = -\frac{1}{\hbar^2}\mathcal{P}\mathcal{L}_T(t)\int_0^t dt'\ \exp\left(-\frac{i}{\hbar}(t - t')\mathcal{L}_0\right)\mathcal{L}_T(t')\mathcal{P}\exp\left(\frac{i}{\hbar}(t - t')\mathcal{L}_0\right)\mathcal{P}.$$ (2.51)

Now, that we have found the lowest order in α, we let $\alpha = 1$ and find for Eq. (2.41)

$$\frac{\partial}{\partial t}\mathcal{P}\hat{\rho}(t) = \left[-\frac{i}{\hbar}\mathcal{L}_S - \frac{1}{\hbar^2}\mathcal{P}\mathcal{L}_T(t)\right.$$
$$\left.\times\int_0^t dt'\ \exp\left(-\frac{i}{\hbar}(t - t')\mathcal{L}_0\right)\mathcal{L}_T(t')\mathcal{P}\exp\left(\frac{i}{\hbar}(t - t')\mathcal{L}_0\right)\right]\mathcal{P}\hat{\rho}(t).$$ (2.52)

Tracing over the environment yields a dynamical equation

$$\frac{\partial}{\partial t}\hat{\rho}_S(t) = -\frac{i}{\hbar}[\hat{H}_S, \hat{\rho}_S(t)]$$
$$-\frac{1}{\hbar^2}\mathrm{Tr}_E\left\{\left[\hat{H}_T(t), \int_0^t dt'\ \exp\left(-\frac{i}{\hbar}(t - t')\mathcal{L}_0\right)\left[\hat{H}_T(t'),\right.\right.\right.$$
$$\left.\left.\left.\mathcal{P}\exp\left(\frac{i}{\hbar}(t - t')\mathcal{L}_0\right)(\rho_E \otimes \rho_S(t))\right]\right]\right\}$$ (2.53)

for the RDO, Eq. (2.8).

Before we continue with a reformulation of Eq. (2.53), we proof a theorem about the action of the Liouville operator in the exponential, which we want to apply

$$\exp\left(-\frac{i}{\hbar}\mathcal{L}_0 t\right)\hat{X} = \exp\left(-\frac{i}{\hbar}\hat{H}_0 t\right)\hat{X}\exp\left(\frac{i}{\hbar}\hat{H}_0 t\right).$$ (2.54)

2. Time-convolutionless non-Markovian generalized master equation

The proof can be seen from the series expansion

$$
\exp\left(-\frac{i}{\hbar}\mathcal{L}_0 t\right)\hat{X} = \sum_{n=0}^{\infty}\frac{(-\frac{i}{\hbar}\mathcal{L}_0 t)^n}{n!}\hat{X}
$$

$$
= \sum_{n=0}^{\infty}\frac{(-it)^n}{\hbar^n n!}\sum_{m=0}^{n}(-1)^{n-m}\binom{n}{m}(\hat{H}_0)^m\hat{X}(\hat{H}_0)^{n-m}
$$

$$
\overset{p=n-m}{=}\sum_{m=0}^{\infty}\sum_{p=0}^{\infty}\frac{(-\frac{i}{\hbar}t)^m}{m!}\frac{(\frac{i}{\hbar}t)^p}{p!}\hat{H}_0^m\hat{X}\hat{H}_0^p
$$

$$
\overset{n=p}{=}\sum_{m=0}^{\infty}\frac{(-\frac{i}{\hbar}\hat{H}_0 t)^m}{m!}\hat{X}\sum_{n=0}^{\infty}\frac{(\frac{i}{\hbar}\hat{H}_0 t)^n}{n!}
$$

$$
= \exp\left(-\frac{i}{\hbar}\hat{H}_0 t\right)\hat{X}\exp\left(\frac{i}{\hbar}\hat{H}_0 t\right). \tag{2.55}
$$

Applying Eq. (2.54) to Eq. (2.53) yields

$$
\frac{\partial}{\partial t}\hat{\rho}_S(t) = -\frac{i}{\hbar}[\hat{H}_S, \hat{\rho}_S(t)]
$$

$$
-\frac{1}{\hbar^2}\mathrm{Tr}_E\left(\left[\hat{H}_T(t), \int_0^t dt'\ \exp\left(-\frac{i}{\hbar}(t-t')\hat{H}_0\right)\left[\hat{H}_T(t'), \mathcal{P}\exp\left(\frac{i}{\hbar}(t-t')\hat{H}_0\right)\right.\right.\right.
$$

$$
(\hat{\rho}_E\otimes\hat{\rho}_S(t))\exp\left(-\frac{i}{\hbar}(t-t')\hat{H}_0\right)\bigg]\exp\left(\frac{i}{\hbar}(t-t')\hat{H}_0\right)\bigg]\bigg). \tag{2.56}
$$

Using $[\hat{H}_S, \hat{H}_E] = 0$, the cyclic invariance of the trace in the environmental subspace and the fact that $\exp\left(\frac{i}{\hbar}(t-t')\hat{H}_E\right)$ is unitary we can reformulate an inner structure in Eq. (2.56)

$$
\mathcal{P}\exp\left(\frac{i}{\hbar}(t-t')\hat{\mathcal{H}}_0\right)(\hat{\rho}_E\otimes\hat{\rho}_S(t))\exp\left(-\frac{i}{\hbar}(t-t')\hat{H}_0\right)
$$

$$
= \hat{\rho}_E\otimes\mathrm{Tr}_E\left[\exp\left(\frac{i}{\hbar}(t-t')\hat{H}_E\right)\hat{\rho}_E\exp\left(-\frac{i}{\hbar}(t-t')\hat{H}_E\right)\right.
$$

$$
\otimes\exp\left(\frac{i}{\hbar}(t-t')\hat{H}_S\right)\hat{\rho}_S(t)\exp\left(-\frac{i}{\hbar}(t-t')\hat{H}_S\right)\bigg]
$$

$$
= \hat{\rho}_E\otimes\exp\left(\frac{i}{\hbar}(t-t')\hat{H}_S\right)\hat{\rho}_S(t)\exp\left(-\frac{i}{\hbar}(t-t')\hat{H}_S\right)
$$

$$
= \hat{\rho}_E\otimes\exp\left(\frac{i}{\hbar}(t-t')\hat{H}_0\right)\hat{\rho}_S(t)\exp\left(-\frac{i}{\hbar}(t-t')\hat{H}_0\right). \tag{2.57}
$$

Applying Eq. (2.57) to Eq. (2.56) yields

$$
\begin{aligned}
\frac{\partial}{\partial t}\hat{\rho}_S(t) = & -\frac{i}{\hbar}[\hat{H}_S, \hat{\rho}_S(t)] \\
& -\frac{1}{\hbar^2}\mathrm{Tr}_E\left(\left[\hat{H}_T(t), \int_0^t dt' \, \exp\left(-\frac{i}{\hbar}(t-t')\hat{H}_0\right)\right.\right. \\
& \times \left[\hat{H}_T(t'), \hat{\rho}_E \otimes \exp\left(\frac{i}{\hbar}(t-t')\hat{H}_0\right)\hat{\rho}_S(t)\exp\left(-\frac{i}{\hbar}(t-t')\hat{H}_0\right)\right] \\
& \left.\left. \times \exp\left(\frac{i}{\hbar}(t-t')\hat{H}_0\right)\right]\right),
\end{aligned}
\tag{2.58}
$$

which can be rewritten by restructuring the commutators as

$$
\begin{aligned}
\frac{\partial}{\partial t}\hat{\rho}_S(t) = & -\frac{i}{\hbar}[\hat{H}_S, \hat{\rho}_S(t)] \\
& -\frac{1}{\hbar^2}\mathrm{Tr}_E\left(\left[\hat{H}_T(t), \int_0^t dt' \left[\exp\left(-\frac{i}{\hbar}(t-t')\hat{H}_0\right)\hat{H}_T(t')\exp\left(\frac{i}{\hbar}(t-t')\hat{H}_0\right),\right.\right.\right. \\
& \left.\left.\left. \exp\left(-\frac{i}{\hbar}(t-t')\hat{H}_0\right)\hat{\rho}_E\exp\left(\frac{i}{\hbar}(t-t')\hat{H}_0\right)\otimes\hat{\rho}_S(t)\right]\right]\right)
\end{aligned}
\tag{2.59}
$$

or by using the fact that $\exp\left(\frac{i}{\hbar}(t-t')\hat{H}_S\right)$ is unitary

$$
\begin{aligned}
\frac{\partial}{\partial t}\hat{\rho}_S(t) = & -\frac{i}{\hbar}[\hat{H}_S, \hat{\rho}_S(t)] \\
& -\frac{1}{\hbar^2}\mathrm{Tr}_E\left(\left[\hat{H}_T(t), \int_0^t dt' \left[\exp\left(-\frac{i}{\hbar}(t-t')\hat{H}_0\right)\hat{H}_T(t')\exp\left(\frac{i}{\hbar}(t-t')\hat{H}_0\right),\right.\right.\right. \\
& \left.\left.\left. \exp\left(-\frac{i}{\hbar}(t-t')\hat{H}_E\right)\hat{\rho}_E\exp\left(\frac{i}{\hbar}(t-t')\hat{H}_E\right)\otimes\hat{\rho}_S(t)\right]\right]\right).
\end{aligned}
\tag{2.60}
$$

Using Eq. (2.24) meaning that ρ_E is an equilibrium environmental state, we find

$$
\begin{aligned}
\frac{\partial}{\partial t}\hat{\rho}_S(t) = & -\frac{i}{\hbar}[\hat{H}_S, \hat{\rho}_S(t)] -\frac{1}{\hbar^2}\mathrm{Tr}_E\left(\left[\hat{H}_T(t),\right.\right. \\
& \left[\int_0^t dt' \left\{\exp\left(-\frac{i}{\hbar}(t-t')\hat{H}_0\right)\hat{H}_T(t')\exp\left(\frac{i}{\hbar}(t-t')\hat{H}_0\right)\right\},\right. \\
& \left.\left. \times \ \hat{\rho}_E\otimes\hat{\rho}_S(t)]\right]\right).
\end{aligned}
\tag{2.61}
$$

This is the second order TCL generalized master equation in the Schrödinger picture in a general form, where we have not yet assumed a specific form of the coupling Hamiltonian, $\hat{H}_T$, and the Hamiltonian describing the environment, $\hat{H}_E$. The term "TCL" becomes clear from the time variable of the RDO, $\hat{\rho}_S(t)$, in the second term with the kernel on the right-hand side of Eq. (2.61). Equation (2.61) is local in time meaning that is does not possess a time-convolution under the kernel structure with

respect to the RDO. When we would replace $\hat{\rho}_S(t)$ in the kernel (the second term on the right-hand side) of Eq. (2.61) by

$$\hat{\rho}_S(t) = \exp\left(-\frac{i}{\hbar}(t-t')\hat{H}_S\right)\hat{\rho}_S^{\text{NZ}}(t')\exp\left(\frac{i}{\hbar}(t-t')\hat{H}_S\right), \qquad (2.62)$$

we would get the Nakajima-Zwanzig equation [1, 99, 100]. The unitary time-evolution operators appear due to our derivation of the TCL master equation in the Schrödinger picture. In the interaction picture, they would not have appeared [1]. There, the only difference would be the time argument. Equation (2.62) can be interpreted as follows: in the Schrödinger picture, the NZ kernel takes the central system time propagated RDO (which lets it become convoluted), while the TCL kernel takes just the unpropagated RDO. The deviation between the two approaches is therefore only of relevance when the central system is far from a steady state and when the coupling to the leads is strong.

2.4. Time-convolutionless generalized master equation for a concrete system

We will now derive a specific generalized master equation for a concrete Hamiltonian describing the coupling between the system and its environment as well as a concrete Hamiltonian for the environment. For the environment, we assume two semi-infinite leads $l = L, R$ (left or right lead), which are connected to the finite central system.

For the coupling Hamiltonian,

$$\hat{H}_T(t) = \sum_a \sum_{l=L,R} \int dq\, \chi^l(t)\left[T_{qa}^l\hat{C}_a^\dagger\hat{C}_{ql} + T_{qa}^{l*}\hat{C}_{ql}^\dagger\hat{C}_a\right], \qquad (2.63)$$

we allow tunneling of single electrons between the system and the leads. In Eq. (2.63), $\hat{C}_a^\dagger$ is the creation operator of an electron in the state a in the central system and $\hat{C}_{ql}^\dagger$ is the creation operator of an electron in the state q in the lead l. Furthermore, $\chi^l(t)$ is the switching function of the system-lead coupling for $t \geq 0$,

$$\chi^l(t) = 1 - \frac{2}{e^{\alpha^l t} + 1} \qquad (2.64)$$

with the switching parameter α^l. For $t < 0$, the system-lead coupling is assumed to be zero. The coupling in Eq. (2.63) is modeled geometry dependent through the coupling tensor [101]

$$T_{qa}^l = \sum_\sigma \sum_{\sigma'} \int_{\Omega^l} d^2r \int_{\Omega_S^l} d^2r'\, \psi_{ql}^*(\mathbf{r}, \sigma)g_{aq}^l(\mathbf{r}, \mathbf{r}', \sigma, \sigma')\psi_a^S(\mathbf{r}', \sigma'), \qquad (2.65)$$

which couples the lead single electron states (SES) $\{\psi_{ql}(\mathbf{r}, \sigma)\}$ with energy spectrum $\{\epsilon^l(q)\}$ to the system SES $\{\psi_a^S(\mathbf{r}, \sigma)\}$ with energy spectrum $\{E_a\}$ that reach into the contact regions [102], Ω_S^l and Ω_l, of the system and the lead l, respectively. The coupling kernel in Eq. (2.65) is

$$g_{aq}^l(\mathbf{r}, \mathbf{r}', \sigma, \sigma') = g_0^l \delta_{\sigma, \sigma'} \exp\left[-\delta_x^l (x - x')^2\right]$$
$$\times \exp\left[-\delta_y^l (y - y')^2\right] \exp\left(-\frac{|E_a - \epsilon^l(q)|}{\Delta_E^l}\right). \tag{2.66}$$

Note that the meaning of x in Eq. (2.66) is $\mathbf{r} = (x, y)$ and not $x = (\mathbf{r}, \sigma)$. In Eq. (2.66), g_0^l is the lead coupling strength and δ_x^l and δ_y^l are the contact region parameters for lead l in the x- and y-direction, respectively. Moreover, Δ_E^l denotes the affinity constant between the central system SES energy levels $\{E_a\}$ and the lead energy levels $\{\epsilon^l(q)\}$. The $\delta_{\sigma, \sigma'}$ expresses the assumption of same-spin coupling. Without spin, this factor and the sum over the spins in Eq. (2.65) drops out.

In our system, we include Coulomb interaction and couple the interacting electronic system with a single photon mode. The resulting many-body (MB) system Hamiltonian can then be identified with $\hat{H}_S$. Accordingly, the coupling Hamiltonian, Eq. (2.63), has to be expressed in terms of the MB eigenbasis $\{|\alpha\rangle\}$. For this reason, we define

$$\hat{\mathfrak{T}}^l(q) = \sum_{\alpha\beta} |\alpha\rangle\langle\beta| \sum_a T_{qa}^l \langle\alpha|\hat{C}_a^\dagger|\beta\rangle \tag{2.67}$$

to rewrite Eq. (2.63)

$$\hat{H}_T(t) = \sum_{l=L,R} \int dq\, \chi^l(t) \left[\hat{\mathfrak{T}}^l(q)\hat{C}_{ql} + \hat{C}_{ql}^\dagger \hat{\mathfrak{T}}^{l\dagger}(q)\right]. \tag{2.68}$$

It is assumed that the lead Hamiltonian can be expressed as

$$\hat{H}_E = \sum_{l=L,R} \int dq\, \epsilon^l(q)\hat{C}_{ql}^\dagger \hat{C}_{ql}. \tag{2.69}$$

The detailed assumptions about the lead Hamiltonian will be given later.

According to Eq. (2.54), we have

$$\tilde{\hat{C}}_{ql}(t) := \exp\left(\frac{i}{\hbar}t\hat{H}_E\right)\hat{C}_{ql}\exp\left(-\frac{i}{\hbar}t\hat{H}_E\right)$$
$$= \exp\left(\frac{i}{\hbar}\mathcal{L}_E t\right)\hat{C}_{ql} = \exp\left(-\frac{i}{\hbar}\epsilon^l(q)t\right)\hat{C}_{ql}, \tag{2.70}$$

where the reason for the last equality can be explained by a series expansion of the exponential function when the action of $\mathcal{L}_E$ on $\hat{C}_{ql}$ is known

$$
\begin{aligned}
\mathcal{L}_E \hat{C}_{ql} &= [\hat{H}_E, \hat{C}_{ql}] = \sum_{l'=L,R} \int dq' \; \epsilon^{l'}(q') [\hat{C}_{q'l'}^\dagger \hat{C}_{q'l'}, \hat{C}_{ql}] \\
&= \sum_{l'=L,R} \int dq' \; \epsilon^{l'}(q') [-\delta(q-q')\delta_{l,l'} \hat{C}_{q'l'}] = -\epsilon^l(q)\hat{C}_{ql}.
\end{aligned}
\tag{2.71}
$$

Using Eq. (2.70), we find

$$
\mathrm{Tr}_E \left[\hat{C}_{ql} \tilde{\hat{C}}_{q'l'}^\dagger (t'-t) \hat{\rho}_E \right] = \exp\left(\frac{i}{\hbar}(t'-t)\epsilon^l(q) \right) \delta(q-q')\delta_{ll'}(1-f(\epsilon^l(q))),
\tag{2.72}
$$

$$
\mathrm{Tr}_E \left[\hat{C}_{ql}^\dagger \tilde{\hat{C}}_{q'l'} (t'-t) \hat{\rho}_E \right] = \exp\left(\frac{i}{\hbar}(t-t')\epsilon^l(q) \right) \delta(q-q')\delta_{ll'} f(\epsilon^l(q)),
\tag{2.73}
$$

$$
\mathrm{Tr}_E \left[\tilde{\hat{C}}_{q'l'} (t'-t) \hat{C}_{ql}^\dagger \hat{\rho}_E \right] = \exp\left(\frac{i}{\hbar}(t-t')\epsilon^l(q) \right) \delta(q-q')\delta_{ll'}(1-f(\epsilon^l(q))),
\tag{2.74}
$$

and

$$
\mathrm{Tr}_E \left[\tilde{\hat{C}}_{q'l'}^\dagger (t'-t) \hat{C}_{ql} \hat{\rho}_E \right] = \exp\left(\frac{i}{\hbar}(t'-t)\epsilon^l(q) \right) \delta(q-q')\delta_{ll'} f(\epsilon^l(q)).
\tag{2.75}
$$

with $f(E)$ being the Fermi function by noticing that $\hat{\rho}_E$ is a mixed environmental state composed of the SES of the leads. We note that cyclic permutations of the operators under the trace over the environment on the left hand side in Eqs. (2.72) to (2.75) keep the results unchanged.

Turning back to the TCL generalized master equation, Eq. (2.61), we are now prepared to reformulate it for our concrete coupling and lead Hamiltonian. The main steps are to insert Eq. (2.68), employ the relations, Eq. (2.72) to Eq. (2.75), identify the Hermitian conjugate and reorganize the commutator structure. This gives

$$
\begin{aligned}
\frac{\partial}{\partial t} \hat{\rho}_S(t) = &-\frac{i}{\hbar}[\hat{H}_S, \hat{\rho}_S(t)] - \frac{1}{\hbar^2} \sum_{l=L,R} \int dq \; \chi^l(t) \left[\left[\hat{\mathfrak{T}}^l(q), \right. \right. \\
&\exp\left(-\frac{i}{\hbar} t \epsilon^l(q) \right) \left[\int_0^t dt' \; \exp\left(\frac{i}{\hbar} t' \epsilon^l(q) \right) \chi^l(t') \hat{U}_S^\dagger(t-t') \hat{\mathfrak{T}}^{l\dagger}(q) \hat{U}_S(t-t') \hat{\rho}_S(t) \right. \\
&\left. -f(\epsilon^l(q)) \left\{ \hat{\rho}_S(t), \int_0^t dt' \; \exp\left(\frac{i}{\hbar} t' \epsilon^l(q) \right) \chi^l(t') \hat{U}_S^\dagger(t-t') \hat{\mathfrak{T}}^{l\dagger}(q) \hat{U}_S(t-t') \right\} \right] \right] \\
&+\text{H.c.} \Big],
\end{aligned}
\tag{2.76}
$$

where H.c. denotes the Hermitian conjugate, $\{\cdot, \cdot\}$ the anticommutator and $\hat{U}_S(t)$ is the inverse time evolution operator of the system

$$
\hat{U}_S(t) := \exp\left(\frac{i}{\hbar} \hat{H}_S t \right).
\tag{2.77}
$$

16

Equation (2.76) can be simplified by defining

$$\hat{\Omega}^l(q,t) := \frac{1}{\hbar^2} \chi^l(t) \exp\left(-\frac{i}{\hbar} t \epsilon^l(q)\right) \hat{U}_S(t) \hat{\Pi}^l(q,t) \hat{U}_S^\dagger(t) \tag{2.78}$$

and

$$\hat{\Pi}^l(q,t) := \int_0^t dt' \left[\exp\left(\frac{i}{\hbar} t' \epsilon^l(q)\right) \chi^l(t') \hat{U}_S^\dagger(t') \hat{\mathfrak{T}}^{l\dagger}(q) \hat{U}_S(t')\right]. \tag{2.79}$$

to become

$$\begin{aligned}
\dot{\hat{\rho}}_S(t) = &-\frac{i}{\hbar}[\hat{H}_S, \hat{\rho}_S(t)] \\
&- \left(\sum_{l=L,R} \int dq \left[\hat{\mathfrak{T}}^l(q), \hat{\Omega}^l(q,t)\hat{\rho}_S(t)\right.\right. \\
&- \left.\left. f(\epsilon^l(q))\left\{\hat{\rho}_S(t), \hat{\Omega}^l(q,t)\right\}\right] + \text{H.c.}\right).
\end{aligned} \tag{2.80}$$

Equations (2.78) to (2.80) are the equations of motion, which were implemented in the program to describe the time evolution of the RDO.

We conclude with some numerical notes and a comparison of the TCL with the Nakajima-Zwanzig equations. First, the structure of Eqs. (2.78) to (2.80) is numerically very convenient, because we can save $\hat{\Pi}^l(q,t_n)$ at each time step t_n of a numerical discretization scheme meaning that we can calculate $\hat{\Pi}^l(q,t_{n+1})$ at the next time step t_{n+1} by a single addition without having to integrate over the whole range in t'. This is because in the TCL-approach, $\hat{\Pi}^l(q,t)$ depends not on the RDO $\hat{\rho}_S(t)$. However, the most costly operations in computational time remain the matrix multiplications in Eq. (2.80) and therefore, the numerical effort of the TCL and Nakajima-Zwanzig (where similar equations to Eqs. (2.78) to (2.80) have to be solved iteratively instead of only solving Eq. (2.80) iteratively) is similar. Equation (2.80) is a transcendental differential equation for the RDO, while the Nakajima-Zwanzig equation would be a transcendental integro-differential equation. This means that $\hat{\Pi}^l(q,t_{n+1})$ and $\hat{\Omega}^l(q,t_{n+1})$ can be directly calculated for each time step. To solve Eq. (2.80), we use a Crank-Nicolson algorithm until sufficient convergence for the RDO is achieved, which is assumed when

$$\sqrt{\left|\sum_{i,j} \left[\hat{\rho}_S^{m+1}\right]_{i,j}(t_n) - \left[\hat{\rho}_S^m\right]_{i,j}(t_n)\right|} < 1.0 \times 10^{-6}, \tag{2.81}$$

where the upper index denotes the Crank-Nicolson step and i and j specify the

2. Time-convolutionless non-Markovian generalized master equation

matrix elements. The initial step of the Crank-Nicolson algorithm is

$$
\begin{aligned}
\hat{\rho}_S(t_{n+1}) =& \hat{\rho}_S(t_n) - \frac{i\Delta t}{\hbar}[\hat{H}_S, \hat{\rho}_S(t_n)] \\
& - \Bigg[\sum_{l=L,R} \int dq \, \Big[\hat{\mathfrak{T}}^l(q), \Delta t\hat{\Omega}^l(q,t_n)\hat{\rho}_S(t_n) - f(\epsilon^l(q)) \left\{ \hat{\rho}_S(t_n), \Delta t\hat{\Omega}^l(q,t_n) \right\} \Big] \\
& + \text{H.c.} \Bigg]
\end{aligned}
\tag{2.82}
$$

with the time increment Δt. The Crank-Nicolson iteration step is

$$
\begin{aligned}
\hat{\rho}_S(t_{n+1}) =& \hat{\rho}_S(t_n) - \frac{i\Delta t}{2\hbar}[\hat{H}_S, \hat{\rho}_S(t_n)] - \frac{i\Delta t}{2\hbar}[\hat{H}_S, \hat{\rho}_S(t_{n+1})] \\
& - \Bigg(\sum_{l=L,R} \int dq \, \Big[\hat{\mathfrak{T}}^l(q), \frac{\Delta t}{2}\hat{\Omega}^l(q,t_n)\hat{\rho}_S(t_n) \\
& \quad - f(\epsilon^l(q)) \left\{ \hat{\rho}_S(t_n), \frac{\Delta t}{2}\hat{\Omega}^l(q,t_n) \right\} \Big] + \text{H.c.} \Bigg) \\
& - \Bigg(\sum_{l=L,R} \int dq \, \Big[\hat{\mathfrak{T}}^l(q), \frac{\Delta t}{2}\hat{\Omega}^l(q,t_{n+1})\hat{\rho}_S(t_{n+1}) \\
& \quad - f(\epsilon^l(q)) \left\{ \hat{\rho}_S(t_{n+1}), \frac{\Delta t}{2}\hat{\Omega}^l(q,t_{n+1}) \right\} \Big] + \text{H.c.} \Bigg).
\end{aligned}
\tag{2.83}
$$

The time increment is attached to $\hat{\Omega}^l(q,t)$ for numerical convenience. Compared to the Nakajima-Zwanzig approach, it is our experience that the positivity conditions for the state occupation probabilities in the RDO are satisfied to a higher system-lead coupling strength for the TCL equations.

3. Hamiltonian of the central system and the leads

In this Chapter we present the Hamiltonian describing the central system and the Hamiltonian describing the leads. We also note how we implement them in our numerical calculations. We start with the single-particle Hamiltonian and describe how we add stepwise the Coulomb interaction between the electrons and the interaction between the electrons and the photons in an electromagnetic cavity.

3.1. Single particle central system Hamiltonian

The Hamiltonian of the central system that we use includes the Coulomb interaction between the electrons and the photon-electron interaction. However, here we concentrate first on the description and numerical treatment of the single-electron (SE) Hamiltonian that we use

$$\hat{H}_{\mathrm{SE}}\left(\hat{\mathbf{p}}(\mathbf{r}),\mathbf{r}\right)=\frac{\hat{\mathbf{p}}^2(\mathbf{r})}{2m^*}+V_S(\mathbf{r})+H_Z+\hat{H}_R(\hat{\mathbf{p}}(\mathbf{r}))+\hat{H}_D(\hat{\mathbf{p}}(\mathbf{r})). \qquad (3.1)$$

The Hamiltonian is describing a two-dimensional system of electrons at an interface of semiconductors. It contains the kinetic energy and a confinement potential $V_S(\mathbf{r})=\frac{1}{2}m^*\Omega_0^2 y^2+V_g(\mathbf{r})$, where the latter part $V_g(\mathbf{r})$ is assumed to be of the form of a superposition of Gaussian functions for numerical convenience

$$V_g(\mathbf{r})=\sum_{i=1}^{6}V_i\exp\left[-\left(\beta_{xi}(x-x_{0i})\right)^2-\left(\beta_{yi}(y-y_{0i})\right)^2\right]. \qquad (3.2)$$

Furthermore, Eq. (3.1) contains the interaction between the spin and a magnetic field $\mathbf{B}=B\mathbf{e}_z$ (Zeeman interaction)

$$H_Z=-\boldsymbol{\mu}\cdot\mathbf{B}=\frac{\mu_B g_S B}{2}\sigma_z, \qquad (3.3)$$

where $\boldsymbol{\mu}$ is the spin magnetic moment, g_S is the electron spin g-factor and $\mu_B=e\hbar/(2m_e c)$ is the Bohr magneton with the electron rest mass m_e. Moreover, Eq. (3.1)

contains the interaction between the spin and the orbital motion [103] described by the Rashba part

$$\hat{H}_R(\hat{\mathbf{p}}(\mathbf{r})) = \frac{\alpha}{\hbar} \left(\sigma_x \hat{p}_y(\mathbf{r}) - \sigma_y \hat{p}_x(\mathbf{r}) \right) \tag{3.4}$$

with the Rashba coefficient α and the Dresselhaus part

$$\hat{H}_D(\hat{\mathbf{p}}(\mathbf{r})) = \frac{\beta}{\hbar} \left(\sigma_x \hat{p}_x(\mathbf{r}) - \sigma_y \hat{p}_y(\mathbf{r}) \right) \tag{3.5}$$

with the Dresselhaus coefficient β. In Eqs. (3.3) to (3.5), σ_x, σ_y and σ_z represent the spin Pauli matrices. The momentum operator for the system, which is not coupled to photons, is

$$\hat{\mathbf{p}}(\mathbf{r}) = \begin{pmatrix} \hat{p}_x(\mathbf{r}) \\ \hat{p}_y(\mathbf{r}) \end{pmatrix} = \frac{\hbar}{i}\nabla + \frac{e}{c}\mathbf{A}(\mathbf{r}), \tag{3.6}$$

which includes the static external magnetic field $\mathbf{B} = B\mathbf{e}_z$, in Landau gauge being represented by the vector potential $\mathbf{A}(\mathbf{r}) = -By\mathbf{e}_x$.

The first part of Eq. (3.1) can be written

$$\hat{H}_{\text{SE},1} = \frac{\hat{\mathbf{p}}^2}{2m^*} + \frac{1}{2}m^*\Omega_0^2 y^2 = -\frac{\hbar^2}{2m^*}\left(\nabla^2 - \frac{2i}{l^2}y\frac{\partial}{\partial x} - \frac{y^2}{l^4} \right) + \frac{1}{2}m^*\Omega_0^2 y^2 \tag{3.7}$$

with the magnetic length

$$l = \sqrt{\frac{c\hbar}{eB}}. \tag{3.8}$$

Equation (3.7) has some similarity to a harmonic oscillator in the y-direction and free particles in the x-direction

$$\hat{H}_{\text{SE},1} = -\frac{\hbar^2}{2m^*}\nabla^2 + \frac{1}{2}m^*\Omega_W^2 y^2 + \frac{i\hbar^2}{m^*l^2}y\frac{\partial}{\partial x}. \tag{3.9}$$

with

$$\Omega_W = \sqrt{\Omega_0^2 + \omega_c^2} \tag{3.10}$$

and

$$\omega_c = \frac{eB}{m^*c}. \tag{3.11}$$

The eigenfunctions of the two first terms in Eq. (3.9) are pure harmonic oscillator eigenfunctions in the y-direction and free eigenfunctions in the x-direction, however the last term in Eq. (3.9) couples the harmonic oscillator eigenfunctions in the y-direction and the free eigenfunctions in the x-direction. The boundary conditions are

$$\psi\left(-\frac{L_x}{2}, y\right) = \psi\left(\frac{L_x}{2}, y\right) = 0 \tag{3.12}$$

and

$$\psi(x, y \to \pm\infty) \to 0, \tag{3.13}$$

where the latter boundary condition is a consequence of the confinement $V_S(\mathbf{r})$ and L_x is the length of the central system in the x-direction. The eigenfunctions of the two first terms on the right hand side of Eq. (3.9) are

$$\psi_{m,n}(x,y) = \frac{\exp\left(-\frac{y^2}{2a_W^2}\right)}{\sqrt{2^m \sqrt{\pi} m! a_W}} H_m\left(\frac{y}{a_W}\right) \begin{cases} \sqrt{\frac{2}{L_x}} \cos\left(\frac{n\pi x}{L_x}\right) & \text{if } n = 1, 3, 5, \ldots \\ \sqrt{\frac{2}{L_x}} \sin\left(\frac{n\pi x}{L_x}\right) & \text{if } n = 2, 4, 6, \ldots \end{cases}$$
$$(3.14)$$

with the Hermite polynomials $H_m(x)$ and the magnetic length (modified due to the confinement in the y-direction)

$$a_W := \sqrt{\frac{\hbar}{m^* \Omega_W}}, \tag{3.15}$$

which is related to the magnetic length by $a_W = \sqrt{\frac{\omega_c}{\Omega_W}} l$. For the third term on the right hand side of Eq. (3.9), we consider the matrix elements

$$I_{\mu,\mu'} = \int dx\, \rho_\mu^*(x) \frac{\partial}{\partial x} \rho_{\mu'}(x) \tag{3.16}$$

with $\mu = \tilde{n}$ if $\mu = 1, 3, 5, \ldots$, $\mu' = \tilde{n}'$ if $\mu' = 1, 3, 5, \ldots$, $\mu = n$ if $\mu = 2, 4, 6, \ldots$, $\mu' = n'$ if $\mu' = 2, 4, 6, \ldots$,

$$\rho_{\tilde{n}}(x) = \sqrt{\frac{2}{L_x}} \cos\left(\frac{\tilde{n}\pi x}{L_x}\right) \tag{3.17}$$

and

$$\rho_n(x) = \sqrt{\frac{2}{L_x}} \sin\left(\frac{n\pi x}{L_x}\right). \tag{3.18}$$

The result of Eq. (3.16) is found in the Appendix A,

$$\int dx\, \rho_n^*(x) \frac{\partial}{\partial x} \rho_{n'}(x) = \begin{cases} \frac{4n'n(-1)^{\frac{n+n'-1}{2}}}{L_x(n^2 - n'^2)} & \text{if } n + n' = 3, 5, 7, \ldots \\ 0 & \text{if } n + n' = 2, 4, 6, \ldots \end{cases}. \tag{3.19}$$

We also consider the following matrix elements for the third term on the right hand side of Eq. (3.9)

$$\langle m| \frac{y}{a_W} |m'\rangle = \langle m| \frac{1}{\sqrt{2}}(\hat{a} + \hat{a}^\dagger) |m'\rangle = \sqrt{\frac{m'}{2}} \delta_{m,m'-1} + \sqrt{\frac{m'+1}{2}} \delta_{m,m'+1} \tag{3.20}$$

with $\hat{a}^\dagger$ being the ladder operator for the harmonic oscillator of frequency Ω_W in the y-direction and where it can be understood that the integral indicated by the bra-ket notation is over $u := y/a_W$ when

$$\langle u|m\rangle = \frac{\exp\left(-\frac{u^2}{2}\right)}{\sqrt{2^m \sqrt{\pi} m!}} H_m(u). \tag{3.21}$$

3. Hamiltonian of the central system and the leads

Now, we can write the Hamiltonian, Eq. (3.9), in the basis of the eigenfunctions of the two first terms of Eq. (3.9) given in Eq. (3.14). In the case that $n + n'$ is odd, we get

$$
\langle m, n | \hat{H}_{\mathrm{SE},1} | m', n' \rangle = i\hbar\omega_c a_W \left[\sqrt{\frac{m'}{2}} \delta_{m,m'-1} + \sqrt{\frac{m'+1}{2}} \delta_{m,m'+1} \right] \frac{4n'n(-1)^{\frac{n+n'-1}{2}}}{L_x(n^2 - n'^2)}
$$
$$
+ \hbar\Omega_W \left[m + \frac{1}{2} + \frac{1}{2}\left(\frac{n\pi a_W}{L_x} \right)^2 \right] \delta_{m,m'} \delta_{n,n'} \tag{3.22}
$$

and in the case that $n + n'$ is even, we get

$$
\langle m, n | \hat{H}_{\mathrm{SE},1} | m', n' \rangle = \hbar\Omega_W \left[m + \frac{1}{2} + \frac{1}{2}\left(\frac{n\pi a_W}{L_x} \right)^2 \right] \delta_{m,m'} \delta_{n,n'}. \tag{3.23}
$$

We can now proceed one step further and include the terms describing the interactions of the spin, Eq. (3.3), Eq. (3.4) and Eq. (3.5). In order to do this, we expand the basis functions Eq. (3.14) by the spin function

$$
\langle x, y, \sigma | m, n, \sigma' \rangle = \tilde{\psi}_{m,n,\sigma'}(x, y, \sigma)
$$
$$
= \delta_{\sigma,\sigma'} \frac{\exp\left(-\frac{y^2}{2a_W^2} \right)}{\sqrt{2^m \sqrt{\pi} m! a_W}} H_m\left(\frac{y}{a_W} \right) \begin{cases} \sqrt{\frac{2}{L_x}} \cos\left(\frac{n\pi x}{L_x} \right) & \text{if } n = 1, 3, 5, \ldots \\ \sqrt{\frac{2}{L_x}} \sin\left(\frac{n\pi x}{L_x} \right) & \text{if } n = 2, 4, 6, \ldots \end{cases} \tag{3.24}
$$

We are then writing the Hamiltonian of Eq. (3.1) without the Gaussian potential functions,

$$
\hat{H}_{\mathrm{SE},2} := \hat{H}_{\mathrm{SE}} - V_g(\mathbf{r}), \tag{3.25}
$$

as a matrix expanded in the spin functions

$$
\langle \sigma | \otimes \langle m, n | \hat{H}_{\mathrm{SE},2} | m', n' \rangle \otimes | \sigma' \rangle
$$
$$
= \begin{pmatrix} \langle \uparrow | \otimes \langle m, n | \hat{H}_{\mathrm{SE},2} | m', n' \rangle \otimes | \uparrow \rangle & \langle \uparrow | \otimes \langle m, n | \hat{H}_{\mathrm{SE},2} | m', n' \rangle \otimes | \downarrow \rangle \\ \langle \downarrow | \otimes \langle m, n | \hat{H}_{\mathrm{SE},2} | m', n' \rangle \otimes | \uparrow \rangle & \langle \downarrow | \otimes \langle m, n | \hat{H}_{\mathrm{SE},2} | m', n' \rangle \otimes | \downarrow \rangle \end{pmatrix} \tag{3.26}
$$

to get the following structure

$$
\langle m, n, \sigma | \hat{H}_{\mathrm{SE},2} | m', n', \sigma' \rangle
$$
$$
= \begin{pmatrix} H^{\mathrm{SE},1}_{m,n,m',n'} + \frac{\hbar\omega_c m^* g_S}{4m_e} \delta_{m,m'} \delta_{n,n'} & A_{m,n,m',n'} \\ A^*_{m',n',m,n} & H^{\mathrm{SE},1}_{m,n,m',n'} - \frac{\hbar\omega_c m^* g_S}{4m_e} \delta_{m,m'} \delta_{n,n'} \end{pmatrix} \tag{3.27}
$$

with

$$
A_{m,n,m',n'} = (\beta - i\alpha) \langle m, n | \partial_y | m', n' \rangle
$$
$$
+ (\alpha - i\beta) \langle m, n | \partial_x | m', n' \rangle - (i\alpha + \beta)\frac{eB}{c\hbar} \langle m, n | y | m', n' \rangle \tag{3.28}
$$

22

and

$$H^{\text{SE},1}_{m,n,m',n'} = \langle m,n | \, \hat{H}_{\text{SE},1} \, | m',n' \rangle . \tag{3.29}$$

The matrix element

$$\langle m,n | \, \partial_y \, | m',n' \rangle = -\delta_{n,n'} \sqrt{\frac{m^* \Omega_W}{2\hbar}} \, \langle m | \, \hat{a}^\dagger - \hat{a} \, | m' \rangle$$
$$= -\delta_{n,n'} \frac{1}{a_W \sqrt{2}} \left(\sqrt{m'+1}\delta_{m,m'+1} - \sqrt{m'}\delta_{m,m'-1} \right) . \tag{3.30}$$

Equation (3.28) then becomes if $n + n'$ is odd

$$A_{m,n,m',n'} = -\left(\beta - i\alpha \right) \delta_{n,n'} \frac{1}{a_W \sqrt{2}} \left(\sqrt{m'+1}\delta_{m,m'+1} - \sqrt{m'}\delta_{m,m'-1} \right)$$
$$+ \left(\alpha - i\beta \right) \delta_{m,m'} \frac{4n'n(-1)^{\frac{n+n'-1}{2}}}{L_x(n^2 - n'^2)}$$
$$- \left(i\alpha + \beta \right) \frac{\hbar \omega_c}{\hbar \Omega_W a_W \sqrt{2}} \delta_{n,n'} \left(\sqrt{m'}\delta_{m,m'-1} + \sqrt{m'+1}\delta_{m,m'+1} \right) ; \tag{3.31}$$

else, if $n + n'$ is even, it becomes

$$A_{m,n,m',n'} = -\left(\beta - i\alpha \right) \delta_{n,n'} \frac{1}{a_W \sqrt{2}} \left(\sqrt{m'+1}\delta_{m,m'+1} - \sqrt{m'}\delta_{m,m'-1} \right)$$
$$- \left(i\alpha + \beta \right) \frac{\hbar \omega_c}{\hbar \Omega_W a_W \sqrt{2}} \delta_{n,n'} \left(\sqrt{m'}\delta_{m,m'-1} + \sqrt{m'+1}\delta_{m,m'+1} \right) . \tag{3.32}$$

Finally, in order to represent the complete SE Hamiltonian, Eq. (3.1), in the basis, Eq. (3.24), and diagonalize it, we have to calculate the matrix elements $\langle m,n | \, \hat{V}_{gi} \, | m',n' \rangle$ with

$$\langle \mathbf{r} | \, \hat{V}_{gi} \, | \mathbf{r}' \rangle = \delta(\mathbf{r} - \mathbf{r}') \exp \left[-\left(\beta_{xi}(x - x_{0i}) \right)^2 - \left(\beta_{yi}(y - y_{0i}) \right)^2 \right] . \tag{3.33}$$

These matrix elements have to be added to the diagonal elements in the spin space of the Hamiltonian Eq. (3.27). In other words, in Eq. (3.27), we have to replace $\langle m,n | \, \hat{H}_{\text{SE},1} \, | m',n' \rangle$ by $\langle m,n | \, \hat{H}_{\text{SE},1} \, | m',n' \rangle + \langle m,n | \, \hat{V}_{gi} \, | m',n' \rangle$. The matrix elements are

$$\langle m,n | \, \hat{V}_{gi} \, | m',n' \rangle = \int_{-\frac{L_x}{2}}^{\frac{L_x}{2}} dx \, \rho_n^*(x) \exp \left[-\left(\beta_{xi}(x - x_{0i}) \right)^2 \right] \rho_{n'}(x)$$
$$\times \int_{-\infty}^{\infty} dy \, \phi_m^*(y) \exp \left[-\left(\beta_{yi}(y - y_{0i}) \right)^2 \right] \phi_{m'}(y) \tag{3.34}$$

with

$$\phi_m(y) = \frac{\exp \left(-\frac{y^2}{2a_W^2} \right)}{\sqrt{2^m \sqrt{\pi} m! a_W}} H_m \left(\frac{y}{a_W} \right) . \tag{3.35}$$

We calculate the first integral in Eq. (3.34) numerically in our approach, but treat the latter integral analytically

$$\int_{-\infty}^{\infty} dy\, \phi_m^*(y) \exp\left[-\left(\beta_{yi}(y-y_{0i})\right)^2\right] \phi_{m'}(y)$$

$$= \int_{-\infty}^{\infty} dy\, \phi_m^*(y) \exp\left[-\gamma_{yi}(u-u_{0i})^2\right] \phi_{m'}(y) = \frac{\exp\left(-\frac{\gamma_{yi}u_{0i}^2}{1+\gamma_{yi}}\right)}{\left(2^{m+m'}m!m'!(1+\gamma_{yi})\right)^{\frac{1}{2}}}$$

$$\times \sum_{k=0}^{\min(m,m')} 2^k k! \binom{m}{k}\binom{m'}{k}\left(\frac{\gamma_{yi}}{1+\gamma_{yi}}\right)^{\frac{m+m'}{2}-k} H_{m+m'-2k}\left(\frac{\gamma_{yi}^{\frac{1}{2}}u_{0i}}{(1+\gamma_{yi})^{\frac{1}{2}}}\right) \quad (3.36)$$

with $\gamma_{yi} = (\beta_{yi}a_W)^2$, $u = y/a_W$ and $u_{0i} = y_{0i}/a_W$. The derivation for Eq. (3.36) can be found in the Appendix B. After the diagonalization of the SE Hamiltonian, Eq. (3.1), the SES $\{\psi_a^S(x)\}$ in the central system are truncated to about $N_{\text{SES}} \approx 40$.

3.2. Coulomb interaction

The single particle Hamiltonian of the central system Eq. (3.1) does not include interactions between the electrons themselves. This is corrected here by adding the Coulomb interaction. For a small system, the electron–electron interaction can be treated asymptotically numerically exactly. For larger electronic systems, mean field theories are commonly applied. Here, we are treating systems with about 40 SES, which is at the boundary of the capability of state of the art machines. Nevertheless, cutting down to the relevant many-electron states (MES) in the Fock states before and after diagonalization of the many-electron (ME) Hamiltonian allows us to handle the Coulomb interaction exactly.

The additional Hamiltonian to be added to Eq. (3.1) is

$$\hat{H}_{ee} = \frac{e^2}{2\kappa} \int dx' \int dx\, \frac{\hat{\Psi}^\dagger(x)\hat{\Psi}^\dagger(x')\hat{\Psi}(x')\hat{\Psi}(x)}{\sqrt{|\mathbf{r}-\mathbf{r}'|^2+\eta^2}} \quad (3.37)$$

with $e > 0$ being the magnitude of the electron charge and $\kappa = 12.4$ the background relative dielectric constant and the field operator

$$\hat{\Psi}(x) = \sum_{a=1}^{N_{\text{SES}}} \psi_a^S(x)\hat{C}_a \quad (3.38)$$

with $x \equiv (\mathbf{r},\sigma)$, $\sigma \in \{\uparrow,\downarrow\}$ and the annihilation operator, $\hat{C}_a$, for the SES $\psi_a^S(x)$ in the central system, which is an eigenstate of the SE Hamiltonian, Eq. (3.1) with eigenenergy E_a. The total ME Hamiltonian (from Eq. (3.1) and Eq. (3.37))

$$\hat{H}_{\text{ME}} = \hat{H}_{\text{SE}}\left(\hat{\mathbf{p}}(\mathbf{r}),\mathbf{r}\right) + \hat{H}_{ee} \quad (3.39)$$

can be represented in the Fock basis $\{|\mu\rangle\}$. Each Fock state $|\mu\rangle$ corresponds to a specific array of occupation number of the SESs. The occupation number for the SES a in the Fock state $|\mu\rangle$ is given by $N_a^\mu = 0, 1$. We restrict ourselves to represent the ME Hamiltonian in the Fock states for which $\sum_a N_a^\mu < 4$. Furthermore, we restrict ourselves to the three-electron states ($\sum_a N_a^\mu = 3$), which are composed of the 16 lowest SESs (for calculations without spin, we restrict ourselves to the 8 lowest SESs). The total size of the Fock space is denoted by N_{Fock}. The matrix element representation of the ME Hamiltonian Eq. (3.39) is

$$\langle \mu | \hat{H}_{\mathrm{ME}} | \mu' \rangle = \sum_{a=1}^{N_{\mathrm{SES}}} N_a^\mu E_a \delta_{\mu,\mu'} + \langle \mu | \hat{H}_{ee} | \mu' \rangle \tag{3.40}$$

in the Fock basis in which it can be diagonalized. We truncate the ME eigenfunctions from N_{Fock} to $N_{\mathrm{MES}} \approx 200$ eigenfunctions after the diagonalization.

Only for numerical reasons, we include a small regularization parameter $\eta = 0.2387$ nm in Eq. (3.37). Without SOI, this parameter can be further reduced to, for example, a value of $\eta = 1.0 \times 10^{-15}$ nm. The method has been developed by Jonasson [104], but shall be repeated here for matters of clearness of the presentation. We write Eq. (3.37) differently,

$$\hat{H}_{ee} = \frac{e^2}{2\kappa} \sum_{a,b,c,d} \left[\int dx' \int dx \, \frac{\psi_a^{S*}(x)\psi_b^{S*}(x')\psi_c^S(x)\psi_d^S(x')}{\sqrt{|\mathbf{r} - \mathbf{r}'|^2 + \eta^2}} \right] \hat{C}_a^\dagger \hat{C}_b^\dagger \hat{C}_d \hat{C}_c, \tag{3.41}$$

and define

$$I_{bd}(\mathbf{r}) := \int d^2 r' \, \frac{\psi_b^{S*}(\mathbf{r}')\psi_d^S(\mathbf{r}')}{\sqrt{|\mathbf{r} - \mathbf{r}'|^2 + \eta^2}}, \tag{3.42}$$

in the case of a spinless system with two dimensions in the space such that

$$I_{bd}(\mathbf{r}) = \int d^2 r' \, \left[\psi_b^{S*}(\mathbf{r}') - \psi_b^{S*}(\mathbf{r}) \right] \frac{1}{\sqrt{|\mathbf{r} - \mathbf{r}'|^2 + \eta^2}} \left[\psi_d^S(\mathbf{r}') - \psi_d^S(\mathbf{r}) \right]$$
$$+ I'_{bd}(\mathbf{r}) + I''_{bd}(\mathbf{r}) \tag{3.43}$$

with

$$I'_{bd}(\mathbf{r}) = \int d^2 r' \, \frac{\psi_b^{S*}(\mathbf{r}')\psi_d^S(\mathbf{r}) + \psi_b^{S*}(\mathbf{r})\psi_d^S(\mathbf{r}')}{\sqrt{|\mathbf{r} - \mathbf{r}'|^2 + \eta^2}} \tag{3.44}$$

and

$$I''_{bd}(\mathbf{r}) = -\psi_b^{S*}(\mathbf{r})\psi_d^S(\mathbf{r}) \int d^2 r' \, \frac{1}{\sqrt{|\mathbf{r} - \mathbf{r}'|^2 + \eta^2}}. \tag{3.45}$$

In the following, we will show that the contributions of $I'_{bd}(\mathbf{r})$ and $I''_{bd}(\mathbf{r})$ are vanishing

3. Hamiltonian of the central system and the leads

when substituted in the Coulomb interaction

$$
\begin{aligned}
\hat{H}_{ee} &= \frac{e^2}{2\kappa} \sum_{a,b,c,d} \left[\int d^2r \; \psi_a^{S*}(\mathbf{r}) I_{bd}(\mathbf{r}) \psi_c^S(\mathbf{r}) \right] \hat{C}_a^\dagger \hat{C}_b^\dagger \hat{C}_d \hat{C}_c \\
&= \frac{e^2}{2\kappa} \sum_{a,b,c,d} \langle a | \, \hat{I}_{bd} \, | c \rangle \, \hat{C}_a^\dagger \hat{C}_b^\dagger \hat{C}_d \hat{C}_c,
\end{aligned}
\tag{3.46}
$$

instead of $I_{bd}(\mathbf{r})$. Provided this can be assumed, we could replace the expression for $I_{bd}(\mathbf{r})$, Eq. (3.42), by

$$
I_{bd}(\mathbf{r}) = \int d^2r' \; \left[\psi_b^{S*}(\mathbf{r}') - \psi_b^{S*}(\mathbf{r}) \right] \frac{1}{\sqrt{|\mathbf{r} - \mathbf{r}'|^2 + \eta^2}} \left[\psi_d^S(\mathbf{r}') - \psi_d^S(\mathbf{r}) \right]
\tag{3.47}
$$

before we insert $I_{bd}(\mathbf{r})$ in Eq. (3.46). The $I_{bd}(\mathbf{r})$ in Eq. (3.46) has the property that the singularity in the denominator for $\mathbf{r} \to \mathbf{r}'$ and $\eta = 0$ is canceled out for sufficiently smooth wavefunctions $\psi_b^S(\mathbf{r})$ and $\psi_d^S(\mathbf{r})$. Therefore, the regularization parameter η can be reduced. The proof that the contribution of $I_{bd}'(\mathbf{r})$ in Eq. (3.44) is vanishing is (using the commutation relations for the operators $\hat{C}_i^\dagger$ and $\hat{C}_i$)

$$
\begin{aligned}
\hat{H}_{ee}' &= \frac{e^2}{8\kappa} \sum_{a,b,c,d} \int d^2r \; \left[\psi_a^{S*}(\mathbf{r}) \psi_c^S(\mathbf{r}) \left(\psi_b^{S*}(\mathbf{r}) F_d(\mathbf{r}) + \psi_d^S(\mathbf{r}) F_b^*(\mathbf{r}) \right) \right. \\
&\quad - \psi_a^{S*}(\mathbf{r}) \psi_d^S(\mathbf{r}) \left(\psi_b^{S*}(\mathbf{r}) F_c(\mathbf{r}) + \psi_c^S(\mathbf{r}) F_b^*(\mathbf{r}) \right) \\
&\quad - \psi_b^{S*}(\mathbf{r}) \psi_c^S(\mathbf{r}) \left(\psi_a^{S*}(\mathbf{r}) F_d(\mathbf{r}) + \psi_d^S(\mathbf{r}) F_a^*(\mathbf{r}) \right) \\
&\quad \left. + \psi_b^{S*}(\mathbf{r}) \psi_d^S(\mathbf{r}) \left(\psi_a^{S*}(\mathbf{r}) F_c(\mathbf{r}) + \psi_c^S(\mathbf{r}) F_a^*(\mathbf{r}) \right) \right] \hat{C}_a^\dagger \hat{C}_b^\dagger \hat{C}_d \hat{C}_c = 0
\end{aligned}
\tag{3.48}
$$

with

$$
F_i(\mathbf{r}) := \int d^2r' \; \frac{\psi_i^S(\mathbf{r}')}{\sqrt{|\mathbf{r} - \mathbf{r}'|^2 + \eta^2}}.
\tag{3.49}
$$

The proof that the contribution of $I_{bd}''(\mathbf{r})$ in Eq. (3.45) is vanishing is (renaming the dummy indexes, using the anticommutation relations for the operators $\hat{C}_i$ and using $\langle a | \, \hat{I}_{bc}'' \, | d \rangle = \langle a | \, \hat{I}_{bd}'' \, | c \rangle$) due to the same space argument in $\psi_c^S(\mathbf{r})$ and $\psi_d^S(\mathbf{r})$)

$$
\begin{aligned}
\hat{H}_{ee}'' &= \frac{e^2}{2\kappa} \sum_{a,b,c,d} \langle a | \, \hat{I}_{bd}'' \, | c \rangle \, \hat{C}_a^\dagger \hat{C}_b^\dagger \hat{C}_d \hat{C}_c \\
&= \frac{e^2}{4\kappa} \sum_{a,b,c,d} \left[\langle a | \, \hat{I}_{bd}'' \, | c \rangle \, \hat{C}_a^\dagger \hat{C}_b^\dagger \hat{C}_d \hat{C}_c + \langle a | \, \hat{I}_{bc}'' \, | d \rangle \, \hat{C}_a^\dagger \hat{C}_b^\dagger \hat{C}_c \hat{C}_d \right] \\
&= \frac{e^2}{4\kappa} \sum_{a,b,c,d} \left[\langle a | \, \hat{I}_{bd}'' \, | c \rangle \, \hat{C}_a^\dagger \hat{C}_b^\dagger \hat{C}_d \hat{C}_c - \langle a | \, \hat{I}_{bc}'' \, | d \rangle \, \hat{C}_a^\dagger \hat{C}_b^\dagger \hat{C}_d \hat{C}_c \right] \\
&= \frac{e^2}{4\kappa} \sum_{a,b,c,d} \left[\langle a | \, \hat{I}_{bd}'' \, | c \rangle \, \hat{C}_a^\dagger \hat{C}_b^\dagger \hat{C}_d \hat{C}_c - \langle a | \, \hat{I}_{bd}'' \, | c \rangle \, \hat{C}_a^\dagger \hat{C}_b^\dagger \hat{C}_d \hat{C}_c \right] = 0.
\end{aligned}
\tag{3.50}
$$

26

The smaller η together with Eq. (3.47) instead of Eq. (3.42) could also be used when only the Zeeman interaction, Eq. (3.3), is present. This is because the SESs in the system $\{\psi_a^S(x)\}$ are with the same space dependence for different spin indexes with the spin coordinate chosen to be the same as the spin index (the eigenvalues $\{E_a\}$ depend though on the spin due to the Zeeman shift). When SOI is present (either Rashba, Eq. (3.4), or Dresselhaus, Eq. (3.5)) then the SES in the system become dependent on the spin coordinate meaning that $\psi_a^S(\mathbf{r}, \sigma) \neq \psi_a^S(\mathbf{r}, \sigma')$. In this case, Eq. (3.42) would have to be replaced by

$$I_{bd}(\mathbf{r}, \sigma) = \sum_{\sigma'} \int d^2r' \left[\psi_b^{S*}(\mathbf{r}', \sigma') - \psi_b^{S*}(\mathbf{r}, \sigma)\right] \frac{1}{\sqrt{|\mathbf{r} - \mathbf{r}'|^2 + \eta^2}} \left[\psi_d^S(\mathbf{r}', \sigma') - \psi_d^S(\mathbf{r}, \sigma)\right],$$
(3.51)

but since $\psi_a^S(\mathbf{r}', \sigma') \neq \psi_a^S(\mathbf{r}, \sigma)$ for $\mathbf{r}' = \mathbf{r}$ a very small η cannot be used in this case. On the other hand, if we would define

$$I_{bd}(\mathbf{r}) = \sum_{\sigma'} \int d^2r' \left[\psi_b^{S*}(\mathbf{r}', \sigma') - \psi_b^{S*}(\mathbf{r}, \sigma')\right] \frac{1}{\sqrt{|\mathbf{r} - \mathbf{r}'|^2 + \eta^2}} \left[\psi_d^S(\mathbf{r}', \sigma') - \psi_d^S(\mathbf{r}, \sigma')\right]$$
(3.52)

such that $\psi_a^S(\mathbf{r}', \sigma') \to \psi_a^S(\mathbf{r}, \sigma')$ for $\mathbf{r}' \to \mathbf{r}$, then the contributions of the corresponding $I'_{bd}(\mathbf{r})$, Eq. (3.44), and $I''_{bd}(\mathbf{r})$, Eq. (3.45), would not vanish. This is why we have to use a larger $\eta = 0.2387$ nm when SOI is included.

3.3. Electron-photon coupling

We are interested in studying the effect of a single quantized cavity photon mode on the electrons. We include a photon bath

$$\hat{H}_{\mathrm{ph}} = \hbar\omega\hat{a}^\dagger\hat{a} \tag{3.53}$$

to the ME Hamiltonian Eq. (3.39), where $\hat{a}^\dagger$ is the photon creation operator and $\hbar\omega$ is the photon excitation energy. Furthermore, we include the interaction between the electrons and photons by replacing Eq. (3.6) by

$$\hat{\mathbf{p}}^{\mathrm{ph}}(\mathbf{r}) = \begin{pmatrix} \hat{p}_x(\mathbf{r}) \\ \hat{p}_y(\mathbf{r}) \end{pmatrix} = \frac{\hbar}{i}\nabla + \frac{e}{c}\left[\mathbf{A}(\mathbf{r}) + \hat{\mathbf{A}}^{\mathrm{ph}}(\mathbf{r})\right] \tag{3.54}$$

in Eq. (3.1). This changes the kinetic ($\hat{\mathbf{p}}^2/2m^*$), Rashba (Eq. (3.4)) and Dresselhaus (Eq. (3.5)) Hamiltonian and thus the photon field couples directly to the spin. In Eq. (3.54), the vector potential due to the photon field is given by

$$\hat{\mathbf{A}}^{\mathrm{ph}} = A(\mathbf{e}\hat{a} + \mathbf{e}^*\hat{a}^\dagger) \tag{3.55}$$

3. Hamiltonian of the central system and the leads

with

$$
\mathbf{e} = \begin{cases} \mathbf{e}_x, & \text{TE}_{011} \\ \mathbf{e}_y, & \text{TE}_{101} \\ \frac{1}{\sqrt{2}} \left[\mathbf{e}_x + i\mathbf{e}_y \right], & \text{RH circular} \\ \frac{1}{\sqrt{2}} \left[\mathbf{e}_x - i\mathbf{e}_y \right], & \text{LH circular} \end{cases} \tag{3.56}
$$

for a longitudinally-polarized (x-polarized) photon field (TE$_{011}$), transversely-polarized (y-polarized) photon field (TE$_{101}$), right-hand (RH) or left-hand (LH) circularly polarized photon field. The electron-photon coupling constant $g^{EM} = eAa_w\Omega_w/c$ scales with the amplitude A of the electromagnetic field. The space dependence (standing waves) of the vector potential due to the photon field was neglected in Eq. (3.55) as we assume that the photon cavity is much larger than the central system. The total MB electron-photon Hamiltonian of the central system is given by

$$
\hat{H}_{\text{MB}} = \hat{H}_{\text{SE}} \left(\hat{\mathbf{p}}^{\text{ph}}(\mathbf{r}), \mathbf{r} \right) + \hat{H}_{ee} + \hat{H}_{\text{ph}}. \tag{3.57}
$$

For reasons of comparison and to determine the photocurrents (additional currents invoked by the photo cavity), we also consider results without photons in the system. In this case, we replace the MB Hamiltonian Eq. (3.57) by the ME Hamiltonian Eq. (3.39). We diagonalize Hamiltonian Eq. (3.57) in the product space (MB space) of the MESs and photon states. This basis is constructed by combining the N_{MES} MESs with $N_{\text{ph}} \approx 30$ photon states and is therefore of size $N_{\text{prod}} = N_{\text{MES}} \times N_{\text{ph}}$. To calculate the matrix elements of the Hamiltonian in Eq. (3.57) in the product MB basis, several operators have first to be transformed (for example the action of the Pauli matrices is only defined in the spin coordinate space, but how they operate in the ME space is not defined directly). Therefore, they have to be transformed in several steps to the basis functions Eq. (3.24), SE eigenfunction basis $\{\psi_a^S(x)\}$, Fock basis and ME eigenfunction basis. The transformation to the SE basis and ME basis are unitary transformations defined by the corresponding eigenfunctions and a truncation to the matrix sizes N_{SES} or N_{MES}. The transformation to the Fock basis for a one-particle operator matrix element is given by

$$
\hat{O}_{\text{Fock}} = \sum_{a,b} \int dx \, \psi_a^{*S}(x) \hat{O}_{\text{SES}}(x) \psi_b^S(x) \hat{C}_a^\dagger \hat{C}_b, \tag{3.58}
$$

and the representation of the operator in the Fock basis by calculating the action of the electron creation or annihilation operators $\hat{C}_a^\dagger$ or $\hat{C}_a$ on the Fock states. In Eq. (3.58), the action of $\hat{O}_{\text{SES}}(x)$ on $\psi_a^S(x)$ has to be evaluated indirectly as the wave functions are defined in terms of the basis functions given in Eq. (3.24). When it is known how the operators operate in the ME space, they can be straightforwardly expanded to the MB space by considering their action in the photon space. If they contain no photon creation or annihilation operators they can assumed to be diagonal in the photon space. After the diagonalization of the MB Hamiltonian Eq. (3.57), we truncate the MB eigenfunctions to $N_{\text{MBS}} \approx 200$.

The additional Hamiltonian due to the electron-photon interaction in the Fock-photon space is

$$
\begin{aligned}
\hat{H}_{e-ph} =& \hat{H}_{\text{SE}}\left(\hat{\mathbf{p}}^{\text{ph}}(\mathbf{r}),\mathbf{r}\right) - \hat{H}_{\text{SE}}\left(\hat{\mathbf{p}}(\mathbf{r}),\mathbf{r}\right) \\
=& \sum_{a,b}(g_{a,b}^{\text{SE}}\hat{a} + \tilde{g}_{a,b}^{\text{SE}}\hat{a}^{\dagger})\hat{C}_a^{\dagger}\hat{C}_b + \frac{e^2 A^2}{2mc^2}(\mathbf{e}^{\dagger}\mathbf{e}^*\hat{a}^{\dagger 2} + \mathbf{e}^T\mathbf{e}\hat{a}^2 + \hat{a}^{\dagger}\hat{a} + \hat{a}\hat{a}^{\dagger})\sum_a \hat{C}_a^{\dagger}\hat{C}_a \\
&+ \frac{eA\hat{a}}{c\hbar}\sum_{a,b}\sum_{\sigma}\sum_{\sigma'}\int d^2r\ \left[\psi_a^{S*}(\mathbf{r},\sigma)[\alpha\sigma_x(\sigma,\sigma')e_y - \alpha\sigma_y(\sigma,\sigma')e_x\right. \\
&+ \beta\sigma_x(\sigma,\sigma')e_x - \beta\sigma_y(\sigma,\sigma')e_y]\psi_b^{S}(\mathbf{r},\sigma')\Big]\,\hat{C}_a^{\dagger}\hat{C}_b \\
&+ \frac{eA\hat{a}^{\dagger}}{c\hbar}\sum_{a,b}\sum_{\sigma}\sum_{\sigma'}\int d^2r\ \left[\psi_a^{S*}(\mathbf{r},\sigma)[\alpha\sigma_x(\sigma,\sigma')e_y^* - \alpha\sigma_y(\sigma,\sigma')e_x^*\right. \\
&+ \beta\sigma_x(\sigma,\sigma')e_x^* - \beta\sigma_y(\sigma,\sigma')e_y^*]\psi_b^{S}(\mathbf{r},\sigma')\Big]\,\hat{C}_a^{\dagger}\hat{C}_b
\end{aligned}
\tag{3.59}
$$

with $g_{a,b}^{\text{SE}} = \langle a|\,\hat{g}\,|b\rangle$ and $\tilde{g}_{a,b}^{\text{SE}} = \langle a|\,\hat{\tilde{g}}\,|b\rangle$ being the representation of the operators

$$
\hat{g} := \frac{eA}{m^*c}\mathbf{e}^T\hat{\mathbf{p}}(\mathbf{r})
\tag{3.60}
$$

and

$$
\hat{\tilde{g}} := \frac{eA}{m^*c}\mathbf{e}^{\dagger}\hat{\mathbf{p}}(\mathbf{r})
\tag{3.61}
$$

in the SESs $\psi_a^S(x)$ and $\psi_b^S(x)$ and with

$$
\sigma_{x,y} = \begin{pmatrix} \sigma_{x,y}(\uparrow,\uparrow) & \sigma_{x,y}(\uparrow,\downarrow) \\ \sigma_{x,y}(\downarrow,\uparrow) & \sigma_{x,y}(\downarrow,\downarrow) \end{pmatrix}.
\tag{3.62}
$$

In Eq. (3.59), the action of the Pauli matrices and $\mathbf{e}\hat{\mathbf{p}}$ in Eqs. (3.60) and (3.61) on $\psi_a^S(x)$ must be evaluated indirectly over the basis functions given in Eq. (3.24) and in case of the Pauli matrices also over the coordinates. In the basis functions, Eq. (3.60) is given by

$$
\begin{aligned}
\langle m,n,\sigma|\,\hat{g}\,|m',n',\sigma'\rangle =& \delta_{\sigma,\sigma'}\frac{eA\hbar}{m^*ca_W}\left(-e_x\frac{\omega_c}{\Omega_W}\left[\sqrt{\frac{m'+1}{2}}\delta_{m,m'+1} + \sqrt{\frac{m'}{2}}\delta_{m,m'-1}\right]\delta_{n,n'}\right. \\
&- ie_y\left[-\sqrt{\frac{m'+1}{2}}\delta_{m,m'+1} + \sqrt{\frac{m'}{2}}\delta_{m,m'-1}\right]\delta_{n,n'} \\
&\left.- ie_x a_W \frac{4n'n(-1)^{\frac{n+n'-1}{2}}}{L_x(n^2 - n'^2)}\delta_{m,m'}\right)
\end{aligned}
\tag{3.63}
$$

if $n + n'$ is odd and by

$$
\begin{aligned}
\langle m,n,\sigma|\,\hat{g}\,|m',n',\sigma'\rangle =& \delta_{\sigma,\sigma'}\frac{eA\hbar}{m^*ca_W}\left(-e_x\frac{\omega_c}{\Omega_W}\left[\sqrt{\frac{m'+1}{2}}\delta_{m,m'+1} + \sqrt{\frac{m'}{2}}\delta_{m,m'-1}\right]\delta_{n,n'}\right. \\
&\left.- ie_y\left[-\sqrt{\frac{m'+1}{2}}\delta_{m,m'+1} + \sqrt{\frac{m'}{2}}\delta_{m,m'-1}\right]\delta_{n,n'}\right)
\end{aligned}
\tag{3.64}
$$

if $n + n'$ is even, where we have used Eq. (3.20), Eq. (3.15), Eq. (3.11), Eq. (3.30) and Eq. (3.19). Similarly, Eq. (3.61) is given by

$$
\begin{aligned}
\langle m,n,\sigma| \hat{\tilde{g}} |m',n',\sigma'\rangle =& \delta_{\sigma,\sigma'} \frac{eA\hbar}{m^*ca_W} \left(-e_x^* \frac{\omega_c}{\Omega_W} \left[\sqrt{\frac{m'+1}{2}} \delta_{m,m'+1} + \sqrt{\frac{m'}{2}} \delta_{m,m'-1} \right] \delta_{n,n'} \right. \\
& - ie_y^* \left[-\sqrt{\frac{m'+1}{2}} \delta_{m,m'+1} + \sqrt{\frac{m'}{2}} \delta_{m,m'-1} \right] \delta_{n,n'} \\
& \left. - ie_x^* a_W \frac{4n'n(-1)^{\frac{n+n'-1}{2}}}{L_x(n^2-n'^2)} \delta_{m,m'} \right)
\end{aligned}
\tag{3.65}
$$

if $n + n'$ is odd and by

$$
\begin{aligned}
\langle m,n,\sigma| \hat{\tilde{g}} |m',n',\sigma'\rangle =& \delta_{\sigma,\sigma'} \frac{eA\hbar}{m^*ca_W} \left(-e_x^* \frac{\omega_c}{\Omega_W} \left[\sqrt{\frac{m'+1}{2}} \delta_{m,m'+1} + \sqrt{\frac{m'}{2}} \delta_{m,m'-1} \right] \delta_{n,n'} \right. \\
& \left. - ie_y^* \left[-\sqrt{\frac{m'+1}{2}} \delta_{m,m'+1} + \sqrt{\frac{m'}{2}} \delta_{m,m'-1} \right] \delta_{n,n'} \right)
\end{aligned}
\tag{3.66}
$$

if $n + n'$ is even. Equation (3.59) must be transformed from the Fock space to the ME space and then the matrix elements in the product space of the photon and ME space can be calculated.

3.4. Hamiltonian of the leads

We connect two leads $l \in \{L, R\}$ (left ($x < 0$) and right ($x > 0$) lead) opposite to each other to the central system, which are parabolically confined in the y-direction and infinitely extended in the x-direction (except at the ends, which are connected to the central system). The leads are electrically biased and therefore can drive a charge current through the central system. The leads can be considered as electron baths or the environment in the dynamical description of an open system. For reasons of simplicity, we neglect the Coulomb interaction of the electrons. Furthermore, we assume that the electromagnetic field of the photon cavity is not interacting with the electrons of the leads. The lead Hamiltonian is

$$
\hat{H}_l\left(\hat{\mathbf{p}}_l(\mathbf{r}), \mathbf{r}\right) = \frac{\hat{\mathbf{p}}_l^2(\mathbf{r})}{2m^*} + V_l(\mathbf{r}) + H_Z + \hat{H}_R(\hat{\mathbf{p}}_l(\mathbf{r})) + \hat{H}_D(\hat{\mathbf{p}}_l(\mathbf{r})).
\tag{3.67}
$$

with the momentum operator containing the kinetic momentum and the vector potential describing the magnetic field (but not the photon field)

$$
\hat{\mathbf{p}}_l(\mathbf{r}) = \frac{\hbar}{i}\nabla + \frac{e}{c}\mathbf{A}(\mathbf{r}).
\tag{3.68}
$$

Equation (3.67) contains the lead potential

$$V_l(\mathbf{r}) = \frac{1}{2} m^* \Omega_l^2 y^2 \tag{3.69}$$

that confines the electrons parabolically in y-direction in the leads with the characteristic energy $\hbar\Omega_l$. Furthermore, it contains the Zeeman term (Eq. (3.3)) and Rashba (Eq. (3.4)) and Dresselhaus (Eq. (3.5)) SOI provided that these terms are also present in the central system. The Hamiltonian in Eq. (3.67) can be written

$$\hat{H}_l\left(\hat{\mathbf{p}}_l(\mathbf{r}), \mathbf{r}\right) = -\frac{\hbar^2}{2m^*}\nabla^2 + \frac{1}{2}m^*\tilde{\Omega}_l^2 y^2 + \frac{i\hbar^2}{m^* l^2} y \frac{\partial}{\partial x} + H_Z + \hat{H}_R(\hat{\mathbf{p}}_l(\mathbf{r})) + \hat{H}_D(\hat{\mathbf{p}}_l(\mathbf{r})) \tag{3.70}$$

with the magnetic length l and $\tilde{\Omega}_l := \sqrt{\Omega_l^2 + \omega_c^2}$. The first two terms of the right hand side of Eq. (3.70) have the eigenspectrum

$$E_l(m, q) = \hbar\tilde{\Omega}_l\left(m + \frac{1}{2} + \frac{q^2\tilde{a}_l^2}{2}\right), \tag{3.71}$$

where the discrete quantum number m describes the harmonic modes in the y-direction and the continuous wave number q describes the motion in the x-direction in the semi-infinite lead l. In Eq. (3.71), the modified magnetic length is $\tilde{a}_l := \sqrt{\hbar/(m^*\tilde{\Omega}_l)}$. The eigenfunctions of the first two terms of the right hand side of Eq. (3.70) are

$$\psi_{m,q}(x, y) = \psi_q(x)\phi_m(y) \tag{3.72}$$

with $\phi_m(y)$ given in Eq. (3.35), but with another modified magnetic length $\tilde{a}_l$ instead of a_W and

$$\psi_q(x) = \sqrt{\frac{2}{\pi}} \sin\left(q\left(x \pm \frac{L_x}{2}\right)\right), \tag{3.73}$$

where the "plus"-sign refers to the left lead $l = L$ and the "minus"-sign refers to the right lead $l = R$. In fact, the spectrum in Eq. (3.71) and eigenfunctions in Eq. (3.72) are unchanged if the third term on the right hand side of Eq. (3.70) is added. This is shown in detail in the Appendix C.

Using the representation Eq. (3.26) for the Hamiltonian Eq. (3.67), we get the following structure

$$\langle m, q, \sigma|\, \hat{H}_l\, |m', q', \sigma'\rangle$$
$$= \begin{pmatrix} \left(E_l(m, q) + \frac{\hbar\omega_c m^* g_S}{4m_e}\right)\delta_{m,m'}\delta(q - q') & A_{m,n,m',n'} \\ A^*_{m',n',m,n} & \left(E_l(m, q) - \frac{\hbar\omega_c m^* g_S}{4m_e}\right)\delta_{m,m'}\delta(q - q') \end{pmatrix} \tag{3.74}$$

with

$$A_{m,n,m',n'} = (\beta - i\alpha)\langle m, n|\, \partial_y\, |m', n'\rangle - (i\alpha + \beta)\frac{eB}{c\hbar}\langle m, n|\, y\, |m', n'\rangle, \tag{3.75}$$

3. Hamiltonian of the central system and the leads

where the matrix elements given in Eq. (3.30) and Eq. (3.20). The reason that the matrix elements $(\alpha - i\beta) \langle m, n| \partial_x |m', n'\rangle$ can be skipped in Eq. (3.75) follows the path of the arguments in the Appendix C. To see this, the eigenfunction expansion, Eq. (C.6), has to be replaced by

$$|m, q, \sigma\rangle = \sum_{\sigma'} \sum_{m'} \int_0^\infty dq' \, C_{m,m',\sigma,\sigma'}(q, q') \, |m', q', \sigma'\rangle_2 , \qquad (3.76)$$

where $|m, q, \sigma\rangle$ are the eigenfunctions of the Hamiltonian Eq. (3.67) and $|m, q, \sigma\rangle_2$ are the eigenfunctions of the Hamiltonian Eq. (3.74). Similarly, Eq. (C.7) has to be replaced by the equation

$$\sum_{\sigma'} \sum_{m'} \int_0^\infty dq' \, _2\langle m'', q'', \sigma''| \hat{H}_l |m', q', \sigma'\rangle_2 \, C_{m,m',\sigma,\sigma'}(q, q')$$
$$= E_{l,2}(m, q, \sigma) C_{m,m'',\sigma,\sigma''}(q, q''), \qquad (3.77)$$

where $E_{l,2}(m, q, \sigma)$ are the eigenvalues of the Hamiltonian Eq. (3.74). For $\hat{H}_l = (i\alpha\sigma_y - i\beta\sigma_x)\partial_x$, the following equations of the Appendix C apply accordingly. Therefore, we find

$$C_{m,m'',\sigma,\sigma''}(q, q'') = \delta_{m,m''}\delta(q - q'')\delta_{\sigma,\sigma''} \qquad (3.78)$$

and

$$E_l(m, q, \sigma) = E_{l,2}(m, q, \sigma) \qquad (3.79)$$

meaning that the term $(i\alpha\sigma_y - i\beta\sigma_x)\partial_x$ can be neglected in Eq. (3.67) because it does not change the eigenvalues and eigenvectors of the Hamiltonian. Thus, the expression Eq. (3.75) is correct with

$$A_{m,n,m',n'} = -(\beta - i\alpha)\,\delta_{n,n'}\frac{1}{a_W\sqrt{2}}\left(\sqrt{m'+1}\delta_{m,m'+1} - \sqrt{m'}\delta_{m,m'-1}\right)$$
$$-(i\alpha + \beta)\frac{\hbar\omega_c}{\hbar\Omega_W a_W\sqrt{2}}\delta_{n,n'}\left(\sqrt{m'}\delta_{m,m'-1} + \sqrt{m'+1}\delta_{m,m'+1}\right). \qquad (3.80)$$

4. Time-dependent densities

In this Chapter, we describe the time-dependent density and current density for the charge and spin. In addition, we describe the spin source densities, which appear since the spin density does not satisfy a conservation law [39, 105]. First, we will derive the operators for the time-dependent densities using the Heisenberg picture and second quantization. Second, we will show how we implement the densities in our program by calculating the mean values of the MB matrix elements of the operators. We have used and simplified the expressions for the density operators also to calculate analytical results for a 1D Rashba or Dresselhaus ring (see Ref. [106]).

4.1. Derivation

In second quantization the MB system Hamiltonian, Eq. (3.57), is

$$
\hat{H}_S = \int d^2r \; \hat{\boldsymbol{\Psi}}^\dagger(\mathbf{r}) \left[\left(\frac{(\hat{\mathbf{p}}^{\text{ph}})^2}{2m^*} + V_S(\mathbf{r}) \right) + H_Z + \hat{H}_R(\mathbf{r}) + \hat{H}_D(\mathbf{r}) \right] \hat{\boldsymbol{\Psi}}(\mathbf{r})
$$
$$
+ \hat{H}_{ee} + \hbar\omega \hat{a}^\dagger \hat{a}, \tag{4.1}
$$

with the spinor

$$
\hat{\boldsymbol{\Psi}}(\mathbf{r}) = \left(\begin{array}{c} \hat{\Psi}(\uparrow, \mathbf{r}) \\ \hat{\Psi}(\downarrow, \mathbf{r}) \end{array} \right) \tag{4.2}
$$

and

$$
\hat{\boldsymbol{\Psi}}^\dagger(\mathbf{r}) = \left(\; \hat{\Psi}^\dagger(\uparrow, \mathbf{r}), \quad \hat{\Psi}^\dagger(\downarrow, \mathbf{r}) \; \right), \tag{4.3}
$$

where $\hat{\Psi}(x)$ is the field operator defined in Eq. (3.38), $x \equiv (\mathbf{r}, \sigma)$ and the spin $\sigma \in \{\uparrow, \downarrow\}$. The charge density operator

$$
\hat{n}^c(\mathbf{r}) = e\hat{\boldsymbol{\Psi}}^\dagger(\mathbf{r})\hat{\boldsymbol{\Psi}}(\mathbf{r}) \tag{4.4}
$$

and the spin polarization density operator for spin polarization S_i $(i = x, y, z)$

$$
\hat{n}^i(\mathbf{r}) = \frac{\hbar}{2}\hat{\boldsymbol{\Psi}}^\dagger(\mathbf{r})\sigma_i\hat{\boldsymbol{\Psi}}(\mathbf{r}). \tag{4.5}
$$

4. Time-dependent densities

We transform the field operators from the Schrödinger picture to the Heisenberg picture to make them time-dependent in order to be able to calculate the time derivative of Eq. (4.4) and Eq. (4.5). The Heisenberg field operator is

$$\hat{\Psi}_H(x,t) = \hat{U}^\dagger(t)\hat{\Psi}(x)\hat{U}(t), \tag{4.6}$$

where $\hat{U}(t)$ is given by

$$i\hbar\frac{\partial}{\partial t}\hat{U}(t) = \hat{H}_S\hat{U}(t), \tag{4.7}$$

i.e. $\hat{U}(t) = \exp(-\frac{it\hat{H}_S}{\hbar})$. In the Heisenberg picture, the charge density operator

$$\hat{n}_H^c(\mathbf{r},t) = e\hat{\Psi}_H^\dagger(\mathbf{r},t)\hat{\Psi}_H(\mathbf{r},t) \tag{4.8}$$

and the spin polarization density operator for spin polarization S_i $(i = x, y, z)$

$$\hat{n}_H^i(\mathbf{r},t) = \frac{\hbar}{2}\hat{\Psi}_H^\dagger(\mathbf{r},t)\sigma_i\hat{\Psi}_H(\mathbf{r},t). \tag{4.9}$$

Using the equation of motion for the Heisenberg field operator

$$i\hbar\frac{\partial}{\partial t}\hat{\Psi}_H(x,t) = [\hat{\Psi}_H(x,t), \hat{H}_S] \tag{4.10}$$

we can apply the continuity equation

$$\frac{\partial}{\partial t}\hat{n}_H^c(\mathbf{r},t) = \frac{e}{i\hbar}\left[\hat{\Psi}_H^\dagger(\mathbf{r},t)\hat{\Psi}_H(\mathbf{r},t)\hat{H}_S - \hat{H}_S\hat{\Psi}_H^\dagger(\mathbf{r},t)\hat{\Psi}_H(\mathbf{r},t)\right] = -\nabla\hat{\mathbf{j}}_H^c(\mathbf{r},t) \tag{4.11}$$

or

$$\begin{aligned}
\frac{\partial}{\partial t}\hat{n}_H^i(\mathbf{r},t) &= \frac{1}{2i}\left[\hat{\Psi}_H^\dagger(\mathbf{r},t)\sigma_i\hat{\Psi}_H(\mathbf{r},t)\hat{H}_S - \hat{H}_S\hat{\Psi}_H^\dagger(\mathbf{r},t)\sigma_i\hat{\Psi}_H(\mathbf{r},t)\right] \\
&= -\nabla\hat{\mathbf{j}}_H^i(\mathbf{r},t) + \hat{s}_H^i(\mathbf{r},t)
\end{aligned} \tag{4.12}$$

to find the charge current density operator $\hat{\mathbf{j}}_H^c(\mathbf{r},t)$, spin polarization current density operators $\hat{\mathbf{j}}_H^i(\mathbf{r},t)$ and spin polarization source operators $\hat{s}_H^i(\mathbf{r},t)$. In Eq. (4.8), Eq. (4.9), Eq. (4.11) and Eq. (4.12), the spinors

$$\hat{\boldsymbol{\Psi}}_H(\mathbf{r},t) = \begin{pmatrix} \hat{\Psi}_H(\uparrow, \mathbf{r}, t) \\ \hat{\Psi}_H(\downarrow, \mathbf{r}, t) \end{pmatrix} \tag{4.13}$$

and

$$\hat{\boldsymbol{\Psi}}_H^\dagger(\mathbf{r},t) = \begin{pmatrix} \hat{\Psi}_H^\dagger(\uparrow, \mathbf{r}, t), & \hat{\Psi}_H^\dagger(\downarrow, \mathbf{r}, t) \end{pmatrix} \tag{4.14}$$

and $\hat{H}_S = \hat{U}^\dagger(t)\hat{H}_S\hat{U}(t)$ could be transformed to the Heisenberg picture without any change. However, parts of the Hamiltonian $\hat{H}_S$ might be different in the different pictures. We will therefore consistently consider the parts of $\hat{H}_S$ after their transformation to the Heisenberg picture.

It is sufficient to consider the Hamiltonian

$$\hat{H}_{S,1}(t) = \int dx'' \int dx' \, \hat{\Psi}_H^\dagger(x',t)\delta(\mathbf{r}' - \mathbf{r}'')$$

$$\times \left\{ \left[\frac{1}{2m^*} \left(\frac{\hbar}{i}\nabla'' + \frac{e}{c}\hat{\mathbf{A}}^H(\mathbf{r}'',t) \right)^2 + V_S(\mathbf{r}'') + \frac{\mu_B g_S B}{2}(1 - 2\delta_{\sigma'',\downarrow}) \right] \delta_{\sigma',\sigma''} \right.$$

$$+ \frac{\alpha}{\hbar} \left((\delta_{\sigma',\uparrow}\delta_{\sigma'',\downarrow} + \delta_{\sigma',\downarrow}\delta_{\sigma'',\uparrow}) \left[\frac{\hbar}{i}\frac{\partial}{\partial y''} + \frac{e}{c}\hat{A}_y^H(\mathbf{r}'',t) \right] \right.$$

$$- (-i\delta_{\sigma',\uparrow}\delta_{\sigma'',\downarrow} + i\delta_{\sigma',\downarrow}\delta_{\sigma'',\uparrow}) \left[\frac{\hbar}{i}\frac{\partial}{\partial x''} + \frac{e}{c}\hat{A}_x^H(\mathbf{r}'',t) \right] \right)$$

$$+ \frac{\beta}{\hbar} \left((\delta_{\sigma',\uparrow}\delta_{\sigma'',\downarrow} + \delta_{\sigma',\downarrow}\delta_{\sigma'',\uparrow}) \left[\frac{\hbar}{i}\frac{\partial}{\partial x''} + \frac{e}{c}\hat{A}_x^H(\mathbf{r}'',t) \right] \right.$$

$$\left. \left. - (-i\delta_{\sigma',\uparrow}\delta_{\sigma'',\downarrow} + i\delta_{\sigma',\downarrow}\delta_{\sigma'',\uparrow}) \left[\frac{\hbar}{i}\frac{\partial}{\partial y''} + \frac{e}{c}\hat{A}_y^H(\mathbf{r}'',t) \right] \right) \right\} \hat{\Psi}_H(x'',t), \quad (4.15)$$

instead of the Hamiltonian in Eq. (4.1), where the photon bath and the Coulomb interaction are omitted, because the commutators

$$\left[\hbar\omega \hat{U}^\dagger(t)\hat{a}^\dagger\hat{a}\hat{U}(t), \hat{\Psi}_H^\dagger(x,t)\hat{\Psi}_H(\mathbf{r},\sigma''',t) \right] = 0 \qquad (4.16)$$

and

$$\left[\hat{H}_{ee}, \hat{\Psi}_H^\dagger(x,t)\hat{\Psi}_H(\mathbf{r},\sigma''',t) \right] = 0, \qquad (4.17)$$

which appear in Eq. (4.11) and Eq. (4.12) due to specific parts of the Hamiltonian $\hat{H}_S$ are vanishing. In our convention to transform the parts of the Hamiltonian Eq. (4.1) to the Heisenberg picture, we replace the Schrödinger field operators in Eq. (4.1) by the Heisenberg field operators and the Schrödinger vector potential $\hat{\mathbf{A}}(\mathbf{r})$, which may include photon operators, by the Heisenberg vector potential

$$\hat{\mathbf{A}}^H(\mathbf{r},t) = \hat{U}^\dagger(t)\hat{\mathbf{A}}(\mathbf{r})\hat{U}(t). \qquad (4.18)$$

Similarly, $\hat{H}_{ee}$ in Eq. (4.17) has to be understood such that the Schrödinger field operators in Eq. (3.37) are to be replaced by the Heisenberg ones. Equation (4.16) is valid as

$$\left[\hbar\omega\hat{a}^\dagger\hat{a}, \hat{\Psi}^\dagger(x)\hat{\Psi}(\mathbf{r},\sigma''') \right] = 0 \qquad (4.19)$$

since the field operator operates in a different space (electron space) than the photon creation and annihilation operators, $\hat{a}^\dagger$ and $\hat{a}$. Equation (4.16) is obtained when Eq. (4.19) is transformed to the Heisenberg picture. The proof for Eq. (4.17) can be found in the Appendix D.

In this thesis, we show only the derivation of the spin polarization current density operator for S_x and S_y spin polarization and the spin polarization source operator for S_x and S_y spin polarization in the Appendix E. We derived the charge current density

4. Time-dependent densities

operator, the spin polarization current density operator for S_z spin polarization and the spin polarization source operator for S_z spin polarization in complete analogy. The component labeled with $j \in \{x, y\}$ of the charge current density operator is given by

$$
\hat{j}_j^c(\mathbf{r}) = \frac{e\hbar}{2m^*i}\left[\hat{\boldsymbol{\Psi}}^\dagger(\mathbf{r})\nabla_j\hat{\boldsymbol{\Psi}}(\mathbf{r}) - \left(\nabla_j\hat{\boldsymbol{\Psi}}^\dagger(\mathbf{r})\right)\hat{\boldsymbol{\Psi}}(\mathbf{r})\right] + \frac{e^2}{m^*c}\hat{A}_j(\mathbf{r})\hat{\boldsymbol{\Psi}}^\dagger(\mathbf{r})\hat{\boldsymbol{\Psi}}(\mathbf{r})
$$
$$
+ \frac{e}{\hbar}\hat{\boldsymbol{\Psi}}^\dagger(\mathbf{r})(\beta\sigma_x - \alpha\sigma_y)\hat{\boldsymbol{\Psi}}(\mathbf{r})\delta_{x,j} + \frac{e}{\hbar}\hat{\boldsymbol{\Psi}}^\dagger(\mathbf{r})(\alpha\sigma_x - \beta\sigma_y)\hat{\boldsymbol{\Psi}}(\mathbf{r})\delta_{y,j}. \tag{4.20}
$$

The current density operator for the j-component and S_x spin polarization

$$
\hat{j}_j^x(\mathbf{r}) = \frac{\hbar^2}{4m^*i}\left[\hat{\boldsymbol{\Psi}}^\dagger(\mathbf{r})\sigma_x\nabla_j\hat{\boldsymbol{\Psi}}(\mathbf{r}) - \left(\nabla_j\hat{\boldsymbol{\Psi}}^\dagger(\mathbf{r})\right)\sigma_x\hat{\boldsymbol{\Psi}}(\mathbf{r})\right]
$$
$$
+ \frac{e\hbar}{2m^*c}\hat{A}_j(\mathbf{r})\hat{\boldsymbol{\Psi}}^\dagger(\mathbf{r})\sigma_x\hat{\boldsymbol{\Psi}}(\mathbf{r}) + \frac{\beta\delta_{x,j} + \alpha\delta_{y,j}}{2}\hat{\boldsymbol{\Psi}}^\dagger(\mathbf{r})\hat{\boldsymbol{\Psi}}(\mathbf{r}). \tag{4.21}
$$

the current density operator for S_y spin polarization

$$
\hat{j}_j^y(\mathbf{r}) = \frac{\hbar^2}{4m^*i}\left[\hat{\boldsymbol{\Psi}}^\dagger(\mathbf{r})\sigma_y\nabla_j\hat{\boldsymbol{\Psi}}(\mathbf{r}) - \left(\nabla_j\hat{\boldsymbol{\Psi}}^\dagger(\mathbf{r})\right)\sigma_y\hat{\boldsymbol{\Psi}}(\mathbf{r})\right]
$$
$$
+ \frac{e\hbar}{2m^*c}\hat{A}_j(\mathbf{r})\hat{\boldsymbol{\Psi}}^\dagger(\mathbf{r})\sigma_y\hat{\boldsymbol{\Psi}}(\mathbf{r}) - \frac{\alpha\delta_{x,j} + \beta\delta_{y,j}}{2}\hat{\boldsymbol{\Psi}}^\dagger(\mathbf{r})\hat{\boldsymbol{\Psi}}(\mathbf{r}). \tag{4.22}
$$

and S_z spin polarization

$$
\hat{j}_j^z(\mathbf{r}) = \frac{\hbar^2}{4m^*i}\left[\hat{\boldsymbol{\Psi}}^\dagger(\mathbf{r})\sigma_z\nabla_j\hat{\boldsymbol{\Psi}}(\mathbf{r}) - \left(\nabla_j\hat{\boldsymbol{\Psi}}^\dagger(\mathbf{r})\right)\sigma_z\hat{\boldsymbol{\Psi}}(\mathbf{r})\right]
$$
$$
+ \frac{e\hbar}{2m^*c}\hat{A}_j(\mathbf{r})\hat{\boldsymbol{\Psi}}^\dagger(\mathbf{r})\sigma_z\hat{\boldsymbol{\Psi}}(\mathbf{r}). \tag{4.23}
$$

The spin polarization source operator for S_x spin polarization

$$
\hat{s}^x(\mathbf{r}) = -\frac{\mu_B g_S B}{2}\hat{\boldsymbol{\Psi}}^\dagger(\mathbf{r})\sigma_y\hat{\boldsymbol{\Psi}}(\mathbf{r}) - \frac{i\alpha}{2}\left[\frac{\partial}{\partial x}\left(\hat{\boldsymbol{\Psi}}^\dagger(\mathbf{r})\right)\sigma_z\hat{\boldsymbol{\Psi}}(\mathbf{r}) - \hat{\boldsymbol{\Psi}}^\dagger(\mathbf{r})\sigma_z\frac{\partial}{\partial x}\hat{\boldsymbol{\Psi}}(\mathbf{r})\right]
$$
$$
- \frac{i\beta}{2}\left[\frac{\partial}{\partial y}\left(\hat{\boldsymbol{\Psi}}^\dagger(\mathbf{r})\right)\sigma_z\hat{\boldsymbol{\Psi}}(\mathbf{r}) - \hat{\boldsymbol{\Psi}}^\dagger(\mathbf{r})\sigma_z\frac{\partial}{\partial y}\hat{\boldsymbol{\Psi}}(\mathbf{r})\right]
$$
$$
- \frac{e\alpha}{c\hbar}\hat{A}_x(\mathbf{r})\hat{\boldsymbol{\Psi}}^\dagger(\mathbf{r})\sigma_z\hat{\boldsymbol{\Psi}}(\mathbf{r}) - \frac{e\beta}{c\hbar}\hat{A}_y(\mathbf{r})\hat{\boldsymbol{\Psi}}^\dagger(\mathbf{r})\sigma_z\hat{\boldsymbol{\Psi}}(\mathbf{r}), \tag{4.24}
$$

S_y spin polarization

$$
\hat{s}^y(\mathbf{r}) = \frac{\mu_B g_S B}{2}\hat{\boldsymbol{\Psi}}^\dagger(\mathbf{r})\sigma_x\hat{\boldsymbol{\Psi}}(\mathbf{r}) - \frac{i\beta}{2}\left[\frac{\partial}{\partial x}\left(\hat{\boldsymbol{\Psi}}^\dagger(\mathbf{r})\right)\sigma_z\hat{\boldsymbol{\Psi}}(\mathbf{r}) - \hat{\boldsymbol{\Psi}}^\dagger(\mathbf{r})\sigma_z\frac{\partial}{\partial x}\hat{\boldsymbol{\Psi}}(\mathbf{r})\right]
$$
$$
- \frac{i\alpha}{2}\left[\frac{\partial}{\partial y}\left(\hat{\boldsymbol{\Psi}}^\dagger(\mathbf{r})\right)\sigma_z\hat{\boldsymbol{\Psi}}(\mathbf{r}) - \hat{\boldsymbol{\Psi}}^\dagger(\mathbf{r})\sigma_z\frac{\partial}{\partial y}\hat{\boldsymbol{\Psi}}(\mathbf{r})\right]
$$
$$
- \frac{e\beta}{c\hbar}\hat{A}_x(\mathbf{r})\hat{\boldsymbol{\Psi}}^\dagger(\mathbf{r})\sigma_z\hat{\boldsymbol{\Psi}}(\mathbf{r}) - \frac{e\alpha}{c\hbar}\hat{A}_y(\mathbf{r})\hat{\boldsymbol{\Psi}}^\dagger(\mathbf{r})\sigma_z\hat{\boldsymbol{\Psi}}(\mathbf{r}) \tag{4.25}
$$

and S_z spin polarization

$$
\begin{aligned}
\hat{s}^z(\mathbf{r}) = &\frac{1}{2}\left[\frac{\partial}{\partial x}\left(\hat{\boldsymbol{\Psi}}^\dagger(\mathbf{r})\right)(i\alpha\sigma_x + i\beta\sigma_y)\,\hat{\boldsymbol{\Psi}}(\mathbf{r}) - \hat{\boldsymbol{\Psi}}^\dagger(\mathbf{r})\,(i\alpha\sigma_x + i\beta\sigma_y)\frac{\partial}{\partial x}\hat{\boldsymbol{\Psi}}(\mathbf{r})\right] \\
&+\frac{1}{2}\left[\frac{\partial}{\partial y}\left(\hat{\boldsymbol{\Psi}}^\dagger(\mathbf{r})\right)(i\beta\sigma_x + i\alpha\sigma_y)\,\hat{\boldsymbol{\Psi}}(\mathbf{r}) - \hat{\boldsymbol{\Psi}}^\dagger(\mathbf{r})\,(i\beta\sigma_x + i\alpha\sigma_y)\frac{\partial}{\partial y}\hat{\boldsymbol{\Psi}}(\mathbf{r})\right] \\
&+\frac{e}{ic\hbar}\hat{A}_x(\mathbf{r})\hat{\boldsymbol{\Psi}}^\dagger(\mathbf{r})\,(i\alpha\sigma_x + i\beta\sigma_y)\,\hat{\boldsymbol{\Psi}}(\mathbf{r}) \\
&+\frac{e}{ic\hbar}\hat{A}_y(\mathbf{r})\hat{\boldsymbol{\Psi}}^\dagger(\mathbf{r})\,(i\beta\sigma_x + i\alpha\sigma_y)\,\hat{\boldsymbol{\Psi}}(\mathbf{r}).
\end{aligned}
\tag{4.26}
$$

4.2. Implementation

We calculate the time-dependent densities (charge and spin polarization density, charge and spin polarization current density, spin polarization source density) in two main steps. First, we calculate the matrix elements of the corresponding operators in the truncated MB space in order to represent them in the same basis as the RDO. Second, we calculate the time-dependent expectation values of the operators using the time-dependent RDO of the system Eq. (2.8). Here, we shall demonstrate this for the example of a particular component of a particular density, namely the x-component of the current density for S_x spin polarization (Eq. (4.21) for $j = x$).

4. Time-dependent densities

The matrix element of the corresponding operator in the truncated MB space is

$$
(\nu|\hat{j}_x^x(\mathbf{r})|\mu) = \sum_{a,b}^{N_{\mathrm{SES}}} \left\{ \left[\left(\frac{\hbar^2}{4m^*i} \left[\psi_a^{S*}(\mathbf{r},\uparrow)(\partial_x \psi_b^S(\mathbf{r},\downarrow)) - (\partial_x \psi_a^{S*}(\mathbf{r},\uparrow))\psi_b^S(\mathbf{r},\downarrow) \right] \right. \right. \right.
$$

$$
- \frac{eB\hbar}{2m^*c} \psi_a^{S*}(\mathbf{r},\uparrow)\psi_b^S(\mathbf{r},\downarrow)y \bigg)
$$

$$
+ \left(\frac{\hbar^2}{4m^*i} \left[\psi_a^{S*}(\mathbf{r},\downarrow)(\partial_x \psi_b^S(\mathbf{r},\uparrow)) - (\partial_x \psi_a^{S*}(\mathbf{r},\downarrow))\psi_b^S(\mathbf{r},\uparrow) \right] \right.
$$

$$
- \frac{eB\hbar}{2m^*c} \psi_a^{S*}(\mathbf{r},\downarrow)\psi_b^S(\mathbf{r},\uparrow)y \bigg)
$$

$$
+ \frac{\beta}{2} \left(\psi_a^{S*}(\mathbf{r},\uparrow)\psi_b^S(\mathbf{r},\uparrow) + \psi_a^{S*}(\mathbf{r},\downarrow)\psi_b^S(\mathbf{r},\downarrow) \right) \bigg]
$$

$$
\times \sum_{\tau,\sigma}^{N_{\mathrm{prod}}} W_{\nu,\tau}^\dagger \delta_{g(\tau),g(\sigma)} \sum_{m,n}^{N_{\mathrm{Fock}}} V_{f(\tau),m}^\dagger \langle m| \hat{C}_a^\dagger \hat{C}_b |n\rangle V_{n,f(\sigma)} W_{\sigma,\mu} \Bigg\}
$$

$$
+ \sum_{a,b}^{N_{\mathrm{SES}}} \left\{ \left[\psi_a^{S*}(\mathbf{r},\uparrow)\psi_b^S(\mathbf{r},\downarrow) + \psi_a^{S*}(\mathbf{r},\downarrow)\psi_b^S(\mathbf{r},\uparrow) \right] \right.
$$

$$
\times \sum_{\tau,\sigma}^{N_{\mathrm{prod}}} \left[W_{\nu,\tau}^\dagger \frac{e\hbar}{2m^*c} A \left(e_x^* \sqrt{g(\sigma)+1}\, \delta_{g(\tau),g(\sigma)+1} + e_x \sqrt{g(\sigma)}\, \delta_{g(\tau),g(\sigma)-1} \right) \right.
$$

$$
\left. \left. \times \sum_{m,n}^{N_{\mathrm{Fock}}} V_{f(\tau),m}^\dagger \langle m| \hat{C}_a^\dagger \hat{C}_b |n\rangle V_{n,f(\sigma)} W_{\sigma,\mu} \right] \right\}. \tag{4.27}
$$

In Eq. (4.27), the MB states are indicated by the ket $|\mu)$ and the states indicated by the common ket $|m\rangle$ are Fock states. The matrix $V_{m,n}$ describes the transformation between the Fock and the ME basis

$$
|m\} = \sum_{n=1}^{N_{\mathrm{Fock}}} V_{m,n}^\dagger |n\rangle, \tag{4.28}
$$

where the ket $|m\}$ indicates a ME state. Similarly, the matrix $W_{m,n}$ describes the transformation between the product space of the ME and photon basis and the MB basis. Due to the truncation of the ME and MB eigenfunctions, the matrices $V_{m,n}$ and $W_{m,n}$ are not square matrices. The maps f and g appearing in indexes of Eq. (4.27) map from the product space of the ME and photon basis to either the ME (in case of f) or photon space (in case of g). The expectation value of the x-component of the current density operator for S_x spin polarization is

$$
j_x^x(\mathbf{r},t) = \mathrm{Tr}\left[\hat{\rho}_S(t)\hat{j}_x^x(\mathbf{r}) \right] = \sum_{\mu,\nu}^{N_{\mathrm{MBS}}} (\mu|\hat{\rho}_S(t)|\nu)(\nu|\hat{j}_x^x(\mathbf{r})|\mu), \tag{4.29}
$$

which is a function of space and time. The other time-dependent densities can be implemented similarly.

5. Summary of the results

The main results of this work can be found in the attached papers. In this Chapter, we will provide some additional results and summarize the main results of the papers.

5.1. Photon-electron interaction and occupation of MB states

Here, we will present a few supplemental plots to the attached papers to elucidate the effect of the photon-electron interaction on the photon content of the MB states and the photon number relaxation in the central system. It becomes clear that we are describing the non-equilibrium physics of the transport through the quantum ring. Furthermore, we discuss the distribution of the occupation of the MB states.

Figure 5.1 shows the deviation of the photon content of the MB states from an integer value averaged over the truncated MB states N_{MBS},

$$\chi := \frac{1}{N_{\mathrm{MBS}}} \sum_{n=1}^{N_{\mathrm{MBS}}} \chi_n - [\chi_n] \tag{5.1}$$

with $[\chi_n]$ being the nearest integer function, which return the nearest integer to χ_n and χ_n being the photon content of the MB state $|n\rangle$. The deviation χ (Eq. (5.1)) is shown for x- or y-polarization as a function of the magnetic field in Fig. 5.1. A value of 0 for χ would indicate integer photon content and a value of 0.25 would indicate that the photon contents are arbitrarily distributed over the MB states. The parameters for the calculations are identical with the parameters from Ref. [96]. The deviation from integer numbers of the photon content of the MB states is correlated to the strength of the coupling between the electrons and the photons. If the photons would not couple to the electrons, the photon content of the MB states would be integer numbers. For a large magnetic field, the electron-photon coupling becomes less relevant relative to the kinetic term. Therefore, the photon numbers are closer to integers for large magnetic field as can be seen in Fig. 5.1.

Figure 5.2 shows the time evolution of the photon number $N_{\mathrm{ph}}(t)$ in the central
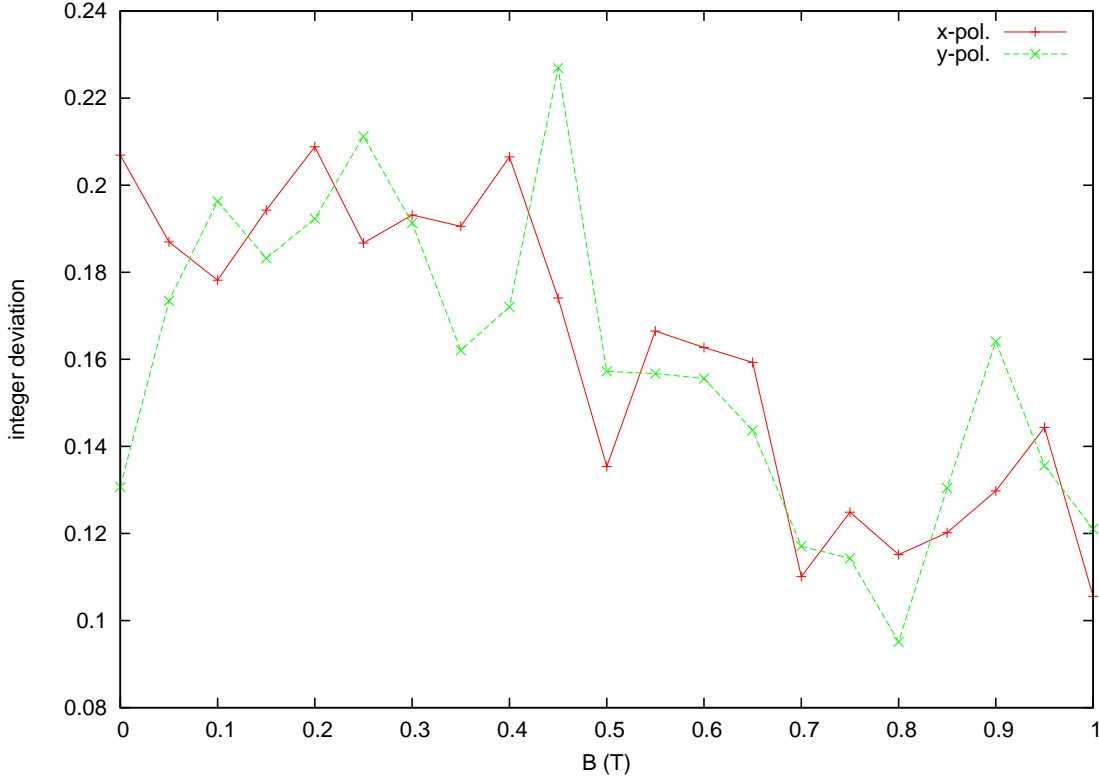
5. Summary of the results

Figure 5.1: (Color online) Average deviation from integer MB state photon content for x- or y-polarization as a function of the magnetic field. A value of 0.25 would indicate a complete deviation from integer numbers.

system (quantum ring) in the case that the photon field is x-polarized. The initial photon number (at $t = 0$) is varied. The initial photon number $N_{\mathrm{ph,init}}$ are integers as the initial MB state is selected to be a pure photon state with $N_{\mathrm{e,init}} = 0$. The graphs are shown for (a) a small magnetic field $B = 0.05$ T and (b) a large magnetic field $B = 1$ T It becomes clear from the graphs that the photon number has not yet reached its equilibrium value. However, it approaches much faster its equilibrium value for the smaller magnetic field. This is in agreement with the conclusion drawn from Fig. 5.1 that the smaller magnetic field would be associated with a higher electron-photon coupling drawing the photon number stronger to its equilibrium position. From the time range, for which we got converged results, we can only assume that the equilibrium photon number is below 1 independent of the initial photon number.

Figure 5.3 shows the occupation of the MB states as a function of the magnetic field and the energy of the MB states for x-polarized photon field. The occupation is shown at the time when the charge of the central system $Q = 0.8e$ meaning that the sum over the occupations for a specific magnetic field is 0.8. The leads are electrically biased with the chemical potential $\mu_L = 2.0$ meV of the left lead and $\mu_R = 0.9$ meV
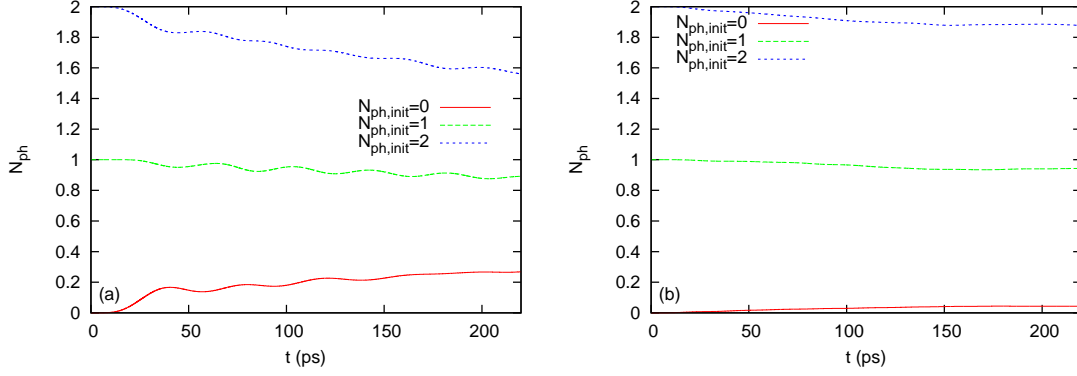
Figure 5.2: (Color online) Photon number N_{ph} as a function of time when the initial MB state is selected to be with $N_{\mathrm{e,init}} = 0$ and $N_{\mathrm{ph,init}} = 0, 1, 2$. The photon field is x-polarized. The magnetic field is (a) $B = 0.05$ T or (b) $B = 1$ T.

of the right lead. It is clear from Fig. 5.3 that only two MB states contain usually more than 50 % of the electron content. The energetic distance of these states oscillates in accordance with the AB phase as a function of the magnetic field. For large magnetic field $B \approx 1$ T, these states lie higher in energy and the contribution of other MB states to the occupation distribution increases. It is important to note that the fact that the occupation is mainly restricted to two MB states helps us to understand the underlying physics. However, it is also clear that the more realistic situation that we describe in our model is more complicated and that the restriction to a two-level system would not in all cases be appropriate.
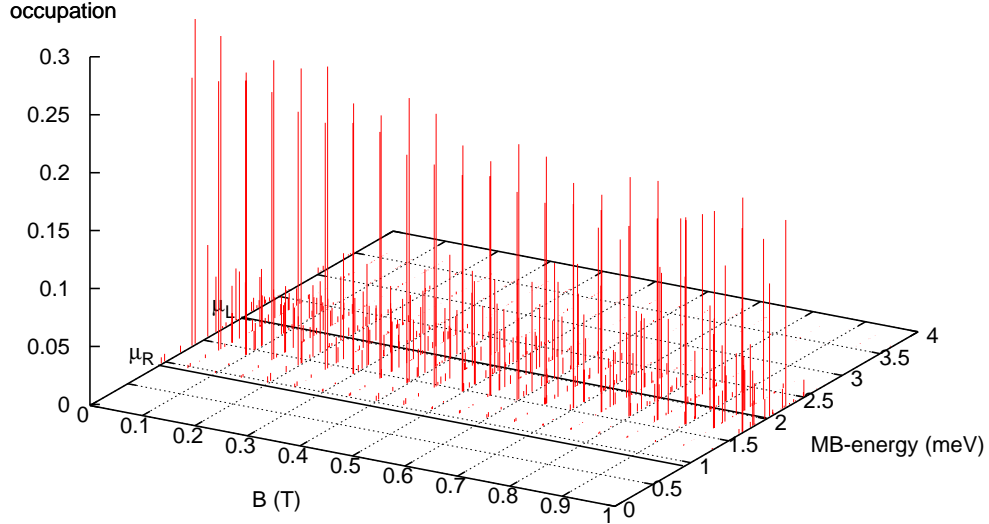
Figure 5.3: (Color online) Occupation of the MB states at time t_c, for which the charge of the central system $Q(t_c) = 0.8e$, as a function of the magnetic field and the energy of the MB states. The bias window $[\mu_R, \mu_L]$ is indicated by solid black lines in the base. The photon field is x-polarized.

5.2. Conclusions

Here, we summarize the results of the papers that are attached to this thesis, where we have used a time-convolutionless, non-Markovian generalized master equation formalism to calculate the non-equilibrium transport of Coulomb and spin-orbit interacting electrons through a broad quantum ring in a photon cavity under the influence of a uniform perpendicular magnetic field. The central quantum ring 1ESs are charged quickly. Electron-electron correlation and sequential tunneling slow down the 2ES charging in the long-time response regime.

Aharonov-Bohm charge current oscillations can be recognized in the long-time response regime with magnetic field period $B_0 = \Phi_0/A$, which is related to the flux quantum Φ_0 and ring area A. In the case of x-polarized photon field, we have found charge oscillations between the left and right part of the quantum ring when the magnetic field is associated with integer flux quanta. The oscillation frequency agrees well with the energy difference of the two mostly occupied states. The rela-

tively high energy difference for x-polarized photons is related to a relatively high transient current through the ring. The amplitude of the charge oscillations through the quantum ring is decreasing in time due to dissipation effects caused by the coupling to the leads. Usually, the "persistent" circular local current is larger than the total local charge current through both ring arms from the left to the right. The persistent current shows a periodic behavior with magnetic field, but with a tendency to clockwise rotation due to the contact region vortex structure. In the case of y-polarized photon field, the magnetic field dependence of the left and right charge current exhibits a pronounced dip at magnetic field $B = 0.425$ T corresponding to two flux quanta that is therefore clearly not related to the Aharonov-Bohm effect. The dip is associated with a degeneracy of the two mostly occupied MB states at magnetic field associated with two flux quanta. The additional level crossing appears only for y-polarized photons, but influences the spatial distribution of the charge density and flow similarly to any other MB degeneracy. The generally lower energy difference of the two mostly occupied MB states in the case of y-polarization perturbs the constructive phase interference condition for the bias driven charge flow through the quantum device and decreases the persistent current magnitude. We have demonstrated for our ring geometry that y-polarized photons perturb our system stronger than x-polarized photons, suppressing or enhancing magnetic field induced and bias-driven currents and perturbing flux periodicity beyond finite width effects. The relatively strong influence of the y-polarized photon field on the electronic transport is due to the closeness of the photon mode energy $\hbar\omega = 0.4$ meV to the characteristic electronic excitation energy in y-direction (the confinement energy $\hbar\Omega_0 = 1.0$ meV is reduced due to the ring geometry).

A pronounced AC charge current dip at the critical value of the Rashba coefficient α^c can be recognized in the TL current flowing from the higher-biased lead through the ring to the lower-biased lead at the position of the Rashba coefficient that a simpler 1D model predicts. The critical Rashba coefficient is related to two experimentally adjustable parameters, the ring radius and the gate voltage leading to the average electric field causing the Rashba effect. The dip structure is linked to crossings in the ME spectrum and can be removed partly by embedding the ring system in a photon cavity of preferably y-polarized photons. The currents in a 1D ring with Rashba or Dresselhaus SOI can be calculated analytically. For zero temperature and divisibility of the electron number by 4, we predict a finite spin current of non-interacting electrons in the limit of the electric field causing the Rashba effect approaching zero. The current for the S_z spin polarization is flowing homogeneously around the ring, but the currents for the other spin polarizations flow from a local source to a local sink. The spin polarization currents of the more complicated 2D ring agree qualitatively in the kind (total local or circular local) and spin polarization (S_x, S_y or S_z), the position of sign changes with respect to the Rashba parameter and the geometric shape of the current flow distribution to the spin polarization currents of the simpler 1D ring. Quantitatively, it is preferable to choose a narrow ring of weakly correlated electrons to obtain a strong spin polarization current. The

5. Summary of the results

linearly polarized photon field interacting with the electrons suppresses in general the charge current but enhances the spin polarization current in the small Rashba coefficient regime. Therefore, the linearly polarized photon field might be used to restore to some extent the strong spin polarization current for S_z spin polarization in the small Rashba coefficient regime, which is suppressed for the broad ring with electron correlations and coupling to the leads. This information could be very useful for experiments with spin polarization currents (for suggestions to measure it, see Refs. [39, 40]) since the number of materials with a strong spin current could be considerably enhanced (without the requirement of a gate). Specific symmetry relations of the spin polarization currents between the Rashba and Dresselhaus ring remain valid for a finite-width ring of correlated electrons connected to electrically biased leads via a spin-conserving coupling tensor. Furthermore, switching on the cavity photon field does not destroy the symmetry relations.

The spin polarization in a ring, which is connected to leads and mirror symmetric with respect to the transport axis, is perpendicular to the transport direction. A linearly polarized photon field with polarization in or perpendicular to the transport direction, increases only the magnitude of the spin polarization while keeping the direction of the spin polarization vector uninfluenced. The spin polarization accumulates to larger magnitudes when the transport of electrons is suppressed by a destructive AC phase. The circularly polarized photon field enhances the spin polarization much more than the linearly polarized photon field. Furthermore, the spin polarization vector is no longer bound to a specific direction as the circularly polarized photon field excites the orbital angular motion of the electrons around the ring and pronounced vortices of the charge current density of smaller spatial scale. The circulation direction of the vortices is found to depend on the handedness of the photon field and the value of the Rashba coefficient α relative to α^c.

The charge current from the left lead into the quantum ring device and out to the right lead shows three AC dips around α^c instead of one for the circularly polarized photon field. The reason for it is a small splitting of degenerate states by the interaction of the angular momentum of the electrons and the spin angular momentum of light, which leads to MB crossings at three different values of the Rashba coefficient. The distance in α between the dips increases with the number of photons in the system due to the larger spin angular momentum of light. The charge photocurrent from the left to the right side of the quantum ring is usually negative meaning that the photon cavity suppresses the charge transport thus increasing the device resistance (except close to α^c, where the AC phase interference is destructive). The circulating part of the charge photocurrent can only be excited by the circularly polarized photon field. The handedness of the circulation depends on the handedness of the light. This way, it is possible to confine the charge transport through the ring to one ring arm (upper or lower). The circular charge photocurrent is suppressed in a wide range of the Rashba coefficient around $\alpha = \alpha^c$ and might therefore serve as a reliable quantity to detect destructive AC phases. The spin photocurrents are

44

especially strong around $\alpha = \alpha^c$ (due to the longer electron dwell time) and for circular polarization (for geometrical reasons). The handedness of the light does not influence the spin polarization current including the current for S_z spin polarization, which circulates around the ring.

Our results are crucial to know for the development of spin-optoelectronic quantum devices in the field of quantum information processing. For instance, interest might arise to build a spintronic device, which breaks (blocks) an electrical circuit if the gate voltage is very close to a specific, critical value, which corresponds to the magnitude of the electric field leading to a destructive AC phase interference in a ring interferometer. Thus, our device could be used as a quantum switch, which is extremely sensitive to the gate voltage. The critical gate potential of the quantum switch could be tuned with the ring radius. A possible experimental approach to determine the ring radius would be to measure the circular charge current around the ring (for example indirectly by its induced magnetic field) that is caused by a circularly polarized cavity photon field. We predict that this approach is better than direct resistance measurements of the quantum switch without the photon cavity. This is because the data that a certain number of measurements with the circularly polarized cavity photon field yields are more relevant for suggesting the proper ring radius due to the broadness of the corresponding Aharonov-Casher feature in the Rashba coefficient.

A. Calculation of the integrals in Eq. (3.16)

We have to distinguish four cases according to whether $\rho_\mu(x)$ (and $\rho_{\mu'}(x)$) is odd (denoted by $\mu = \tilde{n}$) or even (denoted by $\mu = n$). In the odd-odd case

$$
\begin{aligned}
\int dx \, \rho_{\tilde{n}}^*(x) \frac{\partial}{\partial x} \rho_{\tilde{n}'}(x) &= -\frac{2\tilde{n}'\pi}{L_x^2} \int_{-\frac{L_x}{2}}^{\frac{L_x}{2}} dx \, \cos\left(\frac{\tilde{n}\pi x}{L_x}\right) \sin\left(\frac{\tilde{n}'\pi x}{L_x}\right) \\
&= -\frac{\tilde{n}'\pi}{L_x^2} \int_{-\frac{L_x}{2}}^{\frac{L_x}{2}} dx \, \left[\sin\left(\frac{\pi}{L_x}(\tilde{n}+\tilde{n}')x\right) - \sin\left(\frac{\pi}{L_x}(\tilde{n}-\tilde{n}')x\right)\right] \\
&= \frac{\tilde{n}'\pi}{L_x^2} \left[\frac{\cos\left(\frac{\pi}{L_x}(\tilde{n}+\tilde{n}')x\right)}{\frac{\pi}{L_x}(\tilde{n}+\tilde{n}')} - \frac{\cos\left(\frac{\pi}{L_x}(\tilde{n}-\tilde{n}')x\right)}{\frac{\pi}{L_x}(\tilde{n}-\tilde{n}')}\right]_{-\frac{L_x}{2}}^{\frac{L_x}{2}} \\
&= \frac{\tilde{n}'\pi}{L_x^2} \left[\frac{0}{\frac{\pi}{L_x}(\tilde{n}+\tilde{n}')} - \frac{0}{\frac{\pi}{L_x}(\tilde{n}-\tilde{n}')}\right] = 0. \quad\quad\quad\quad \text{(A.1)}
\end{aligned}
$$

A. Calculation of the integrals in Eq. (3.16)

In the odd-even case

$$
\begin{aligned}
\int dx \, \rho_{\tilde{n}}^*(x) \frac{\partial}{\partial x} \rho_{n'}(x) =& \frac{2n'\pi}{L_x^2} \int_{-\frac{L_x}{2}}^{\frac{L_x}{2}} dx \, \cos\left(\frac{\tilde{n}\pi x}{L_x}\right) \cos\left(\frac{n'\pi x}{L_x}\right) \\
=& \frac{n'\pi}{L_x^2} \int_{-\frac{L_x}{2}}^{\frac{L_x}{2}} dx \, \left[\cos\left(\frac{\pi}{L_x}(\tilde{n}+n')x\right) + \cos\left(\frac{\pi}{L_x}(\tilde{n}-n')x\right)\right] \\
=& \frac{n'\pi}{L_x^2} \left[\frac{\sin\left(\frac{\pi}{L_x}(\tilde{n}+n')x\right)}{\frac{\pi}{L_x}(\tilde{n}+n')} + \frac{\sin\left(\frac{\pi}{L_x}(\tilde{n}-n')x\right)}{\frac{\pi}{L_x}(\tilde{n}-n')}\right]_{-\frac{L_x}{2}}^{\frac{L_x}{2}} \\
=& \frac{n'\pi}{L_x^2} \left[\frac{2(-1)^{\frac{\tilde{n}+n'-1}{2}}}{\frac{\pi}{L_x}(\tilde{n}+n')} + \frac{2(-1)^{\frac{\tilde{n}-n'-1}{2}}}{\frac{\pi}{L_x}(\tilde{n}-n')}\right] \\
=& \frac{n'}{L_x} \left[\frac{2(\tilde{n}-n')(-1)^{\frac{\tilde{n}+n'-1}{2}} + 2(\tilde{n}+n')(-1)^{\frac{\tilde{n}+n'-1}{2}}}{\tilde{n}^2 - n'^2}\right] \\
=& \frac{n'}{L_x} \left[\frac{4\tilde{n}(-1)^{\frac{\tilde{n}+n'-1}{2}}}{\tilde{n}^2 - n'^2}\right].
\end{aligned}
\tag{A.2}
$$

In the even-odd case

$$
\begin{aligned}
\int dx \, \rho_n^*(x) \frac{\partial}{\partial x} \rho_{\tilde{n}'}(x) =& -\frac{2\tilde{n}'\pi}{L_x^2} \int_{-\frac{L_x}{2}}^{\frac{L_x}{2}} dx \, \sin\left(\frac{n\pi x}{L_x}\right) \sin\left(\frac{\tilde{n}'\pi x}{L_x}\right) \\
=& \frac{\tilde{n}'\pi}{L_x^2} \int_{-\frac{L_x}{2}}^{\frac{L_x}{2}} dx \, \left[\cos\left(\frac{\pi}{L_x}(n+\tilde{n}')x\right) - \cos\left(\frac{\pi}{L_x}(n-\tilde{n}')x\right)\right] \\
=& \frac{\tilde{n}'\pi}{L_x^2} \left[\frac{\sin\left(\frac{\pi}{L_x}(n+\tilde{n}')x\right)}{\frac{\pi}{L_x}(n+\tilde{n}')} - \frac{\sin\left(\frac{\pi}{L_x}(n-\tilde{n}')x\right)}{\frac{\pi}{L_x}(n-\tilde{n}')}\right]_{-\frac{L_x}{2}}^{\frac{L_x}{2}} \\
=& \frac{\tilde{n}'\pi}{L_x^2} \left[\frac{2(-1)^{\frac{n+\tilde{n}'-1}{2}}}{\frac{\pi}{L_x}(n+\tilde{n}')} - \frac{2(-1)^{\frac{n-\tilde{n}'-1}{2}}}{\frac{\pi}{L_x}(n-\tilde{n}')}\right] \\
=& \frac{\tilde{n}'\pi}{L_x^2} \left[\frac{2(-1)^{\frac{n+\tilde{n}'-1}{2}}}{\frac{\pi}{L_x}(n+\tilde{n}')} + \frac{2(-1)^{\frac{n+\tilde{n}'-1}{2}}}{\frac{\pi}{L_x}(n-\tilde{n}')}\right] \\
=& \frac{\tilde{n}'}{L_x} \left[\frac{2(n-\tilde{n}')(-1)^{\frac{n+\tilde{n}'-1}{2}} + 2(n+\tilde{n}')(-1)^{\frac{n+\tilde{n}'-1}{2}}}{n^2 - \tilde{n}'^2}\right] \\
=& \frac{\tilde{n}'}{L_x} \left[\frac{4n(-1)^{\frac{n+\tilde{n}'-1}{2}}}{n^2 - \tilde{n}'^2}\right].
\end{aligned}
\tag{A.3}
$$

48

And in the even-even case

$$
\begin{aligned}
\int dx\; \rho_n^*(x)\frac{\partial}{\partial x}\rho_{n'}(x) =& \frac{2n'\pi}{L_x^2}\int_{-\frac{L_x}{2}}^{\frac{L_x}{2}} dx\; \sin\left(\frac{n\pi x}{L_x}\right)\cos\left(\frac{n'\pi x}{L_x}\right)\\
=& \frac{n'\pi}{L_x^2}\int_{-\frac{L_x}{2}}^{\frac{L_x}{2}} dx\; \left[\sin\left(\frac{\pi}{L_x}(n'+n)x\right) - \sin\left(\frac{\pi}{L_x}(n'-n)x\right)\right]\\
=& -\frac{n'\pi}{L_x^2}\left[\frac{\cos\left(\frac{\pi}{L_x}(n'+n)x\right)}{\frac{\pi}{L_x}(n'+n)} - \frac{\cos\left(\frac{\pi}{L_x}(n'-n)x\right)}{\frac{\pi}{L_x}(n'-n)}\right]_{-\frac{L_x}{2}}^{\frac{L_x}{2}}\\
=& -\frac{n'\pi}{L_x^2}\left[\frac{0}{\frac{\pi}{L_x}(n'+n)} - \frac{0}{\frac{\pi}{L_x}(n'-n)}\right] = 0. \qquad (A.4)
\end{aligned}
$$

Summarizing the results of Eqs. (A.1) – (A.4), we find

$$
\int dx\; \rho_\mu^*(x)\frac{\partial}{\partial x}\rho_{\mu'}(x) = \begin{cases} \frac{4\mu'\mu(-1)^{\frac{\mu+\mu'-1}{2}}}{L_x(\mu^2-\mu'^2)} & \text{if } \mu+\mu'=3,5,7,\ldots \\ 0 & \text{if } \mu+\mu'=2,4,6,\ldots \end{cases}. \qquad (A.5)
$$

B. Calculation of the integral in Eq. (3.36)

The integral in Eq. (3.36) can be calculated analytically using the definitions $u := y/a_W$, $c := 1 + \gamma_{yi}$, $w := \sqrt{c}u$ and the integral 7.374.9 from Ref. [107].

$$\int_{-\infty}^{\infty} dy\, \phi_m^*(y) \exp\left[-\gamma_{yi}(u - u_{0i})^2\right] \phi_{m'}(y)$$

$$= \int_{-\infty}^{\infty} du\, \frac{\exp\left(-\frac{u^2}{2}\right)}{\sqrt{2^m \sqrt{\pi} m!}} H_m(u) \exp\left[-\gamma_{yi}(u - u_{0i})^2\right] \frac{\exp\left(-\frac{u^2}{2}\right)}{\sqrt{2^{m'} \sqrt{\pi} m'!}} H_{m'}(u)$$

$$= \int_{-\infty}^{\infty} du\, \frac{\exp\left[-u^2 - \gamma_{yi}(u - u_{0i})^2\right]}{\sqrt{2^{m+m'} \pi m! m'!}} H_m(u) H_{m'}(u)$$

$$= \exp\left(\frac{u_{0i}^2 \gamma_{yi}^2}{c} - u_{0i}^2 \gamma_{yi}\right) \int_{-\infty}^{\infty} du\, \frac{\exp\left[-c\left(u - \frac{u_{0i}\gamma_{yi}}{c}\right)^2\right]}{\sqrt{2^{m+m'} \pi m! m'!}} H_m(u) H_{m'}(u)$$

$$= \exp\left(-\frac{\gamma_{yi} u_{0i}^2}{1 + \gamma_{yi}}\right) \int_{-\infty}^{\infty} \frac{dw}{\sqrt{c}}\, \frac{\exp\left[-\left(w - \frac{u_{0i}\gamma_{yi}}{\sqrt{c}}\right)^2\right]}{\sqrt{2^{m+m'} \pi m! m'!}} H_m\left(\frac{w}{\sqrt{c}}\right) H_{m'}\left(\frac{w}{\sqrt{c}}\right)$$

$$= \frac{\exp\left(-\frac{\gamma_{yi} u_{0i}^2}{1 + \gamma_{yi}}\right)}{(c 2^{m+m'} \pi m! m'!)^{\frac{1}{2}}} \int_{-\infty}^{\infty} dw\, \exp\left[-\left(w - \frac{u_{0i}\gamma_{yi}}{\sqrt{c}}\right)^2\right] H_m\left(\frac{w}{\sqrt{c}}\right) H_{m'}\left(\frac{w}{\sqrt{c}}\right)$$

$$= \frac{\exp\left(-\frac{\gamma_{yi} u_{0i}^2}{1 + \gamma_{yi}}\right)}{(c 2^{m+m'} \pi m! m'!)^{\frac{1}{2}}} \sqrt{\pi}$$

$$\times \sum_{k=0}^{\min(m, m')} 2^k k! \binom{m}{k} \binom{m'}{k} \left(\frac{\gamma_{yi}}{1 + \gamma_{yi}}\right)^{\frac{m+m'}{2} - k} H_{m+m'-2k}\left(\frac{\gamma_{yi}^{\frac{1}{2}} u_{0i}}{(1 + \gamma_{yi})^{\frac{1}{2}}}\right), \quad \text{(B.1)}$$

B. Calculation of the integral in Eq. (3.36)

$$\int_{-\infty}^{\infty} dy \; \phi_m^*(y) \exp\left[-\gamma_{yi}(u - u_{0i})^2\right] \phi_{m'}(y)$$

$$= \frac{\exp\left(-\frac{\gamma_{yi} u_{0i}^2}{1+\gamma_{yi}}\right)}{(2^{m+m'} m! m'! (1 + \gamma_{yi}))^{\frac{1}{2}}}$$

$$\times \sum_{k=0}^{\min(m,m')} 2^k k! \begin{pmatrix} m \\ k \end{pmatrix} \begin{pmatrix} m' \\ k \end{pmatrix} \left(\frac{\gamma_{yi}}{1+\gamma_{yi}}\right)^{\frac{m+m'}{2}-k} H_{m+m'-2k}\left(\frac{\gamma_{yi}^{\frac{1}{2}} u_{0i}}{(1+\gamma_{yi})^{\frac{1}{2}}}\right). \quad \text{(B.2)}$$

C. Influence of the third term of the right hand side of Eq. (3.70) on the eigenvalues Eq. (3.71) and eigenvectors Eq. (3.72)

We want to find the eigenvalues of eigenfunctions of the first three parts of the Hamiltonian Eq. (3.70)

$$\hat{H}_{l,1}\left(\hat{\mathbf{p}}_l(\mathbf{r}), \mathbf{r}\right) = -\frac{\hbar^2}{2m^*}\nabla^2 + \frac{1}{2}m^*\tilde{\Omega}_l^2 y^2 + \frac{i\hbar^2}{m^*l^2}y\frac{\partial}{\partial x}. \tag{C.1}$$

The eigenvalues and eigenfunctions of the two first terms on the right hand side of Eq. (C.1) are assumed to be known and are given in Eq. (3.71) and Eq. (3.72). We start with calculating the matrix elements of the term $i\hbar^2/(m^*l^2) \times y\partial_x$ in the eigenfunctions Eq. (3.72) and begin here with the continuous modes in x-direction Eq. (3.73). We show the calculation here for the case of the left lead $l = L$ and use the formula

$$\zeta(x) := -i\int_0^\infty dt\ \exp(ixt) = \frac{\mathfrak{P}}{x} - i\pi\delta(x) \tag{C.2}$$

in Ref. [108] on page 164 and $u := x + L_x/2$ to find

$$\int_{-\infty}^{-\frac{L_x}{2}} dx\ \psi_q(x)i\frac{\partial}{\partial x}\psi_{q'}(x) = \frac{2}{\pi}\int_{-\infty}^{-\frac{L_x}{2}} dx\ \sin\left(q\left(x + \frac{L_x}{2}\right)\right)\cos\left(q'\left(x + \frac{L_x}{2}\right)\right)iq'$$

$$= \frac{2iq'}{\pi}\int_{-\infty}^0 du\ \sin(qu)\cos(q'u) = \frac{iq'}{\pi}\int_{-\infty}^0 du\ \sin(u(q+q')) + \sin(u(q-q'))$$

$$= \frac{q'}{2\pi}\int_0^\infty du\ [\exp(-iu(q+q')) - \exp(iu(q+q'))$$

$$+ \exp(-iu(q-q')) - \exp(iu(q-q'))]$$

$$= \frac{iq'}{2\pi}\left[\zeta(-q-q') - \zeta(q+q') + \zeta(q'-q) - \zeta(q-q')\right] = \frac{iq'}{\pi}\left[-\frac{\mathfrak{P}}{q+q'} + \frac{\mathfrak{P}}{q'-q}\right]$$

$$= -\frac{2iqq'}{\pi}\frac{\mathfrak{P}}{q^2 - q'^2} =: I_{qq'}. \tag{C.3}$$

C. Influence of the third term of the right hand side of Eq. (3.70)

The complete matrix elements are then using Eq. (3.8), Eq. (3.11) and Eq. (3.20) with $\tilde{a}_l$ instead of a_W

$$\langle m, q| \hat{H}_{l,1} |m', q'\rangle$$
$$= \delta_{m,m'}\delta(q - q')E_l(m, q) + \left[\sqrt{\frac{m'}{2}}\delta_{m,m'-1} + \sqrt{\frac{m'+1}{2}}\delta_{m,m'+1}\right]\hbar\omega_c\tilde{a}_l I_{qq'}. \quad \text{(C.4)}$$

We denote the eigenfunctions and eigenvalues of Hamiltonian Eq. (C.1) that we are searching for by $|q, m\rangle_1$ and $E_{l,1}$ such that we can state our eigenvalue problem as

$$\hat{H}_{l,1} |m, q\rangle_1 = E_{l,1}(m, q) |m, q\rangle_1 \quad \text{(C.5)}$$

and expand $|q, m\rangle_1$ in the eigenfunctions of the two first terms on the right hand side of Eq. (C.1)

$$|m, q\rangle_1 = \sum_{m'} \int_0^\infty dq' \, C_{m,m'}(q, q') |m', q'\rangle \quad \text{(C.6)}$$

leading to

$$\sum_{m'} \int_0^\infty dq' \, \langle m'', q''|\hat{H}_{l,1}|m', q'\rangle C_{m,m'}(q, q') = E_{l,1}(m, q)C_{m,m''}(q, q''). \quad \text{(C.7)}$$

From the left side of Eq. (C.7), an integral of the form

$$-\int_0^\infty dq' \, \frac{2iq''q'}{\pi} \frac{\mathfrak{P}}{q''^2 - q'^2} C_{m,m'}(q, q') = \frac{2iq''}{\pi} \int_0^\infty dq' \, \frac{\mathfrak{P}q'}{q'^2 - q''^2} C_{m,m'}(q, q') \quad \text{(C.8)}$$

appears. The integral

$$\int_0^\infty dq' \, \frac{\mathfrak{P}q'C_{m,m'}(q, q')}{q'^2 - q''^2} = \frac{1}{2}\int_{-\infty}^\infty dq' \, \frac{\mathfrak{P}|q'|C_{m,m'}(q, |q'|)}{q'^2 - q''^2}$$
$$= \frac{1}{2}\int_{-\infty}^\infty dq' \, \mathfrak{P}|q'|C_{m,m'}(q, |q'|)\left[\frac{1}{q' - q''} - \frac{1}{q' + q''}\right]\frac{1}{2q''}$$
$$= \pi i \left[\frac{1}{2}\frac{|q''|C_{m,m'}(q, |q''|)}{2q''} - \frac{1}{2}\frac{|q''|C_{m,m'}(q, |q''|)}{2q''}\right] = 0 \quad \text{(C.9)}$$

due to the residue theorem noticing that the integral along a curved contour $\mathfrak{C}$ in the complex space with $q' = |q'| \exp(i\varphi)$ and $0 \leq \varphi \leq \pi$ of the integral

$$\frac{1}{2}\int_{\mathfrak{C}} dq' \, \frac{|q'|C_{m,m'}(q, |q'|)}{q'^2 - q''^2} = \frac{1}{2}\int_0^\pi d\varphi|q'| \frac{|q'|C_{m,m'}(q, |q'|)}{|q'|^2 \exp(2i\varphi) - q''^2}$$
$$= \int_0^\pi d\varphi \, \frac{C_{m,m'}(q, |q'|)}{2\left(\exp(2i\varphi) - \frac{q''^2}{|q'|^2}\right)} \quad \text{(C.10)}$$

54

vanishes for $|q'| \to \infty$. As a consequence, we get for Eq. (C.7)

$$\sum_{m'} \int_0^\infty dq' \, \delta_{m'',m'} \delta(q'' - q') E_l(m', q') C_{m,m'}(q, q') = E_{l,1}(m, q) C_{m,m''}(q, q'') \quad \text{(C.11)}$$

or

$$E_l(m'', q'') C_{m,m''}(q, q'') = E_{l,1}(m, q) C_{m,m''}(q, q''). \quad \text{(C.12)}$$

This can only be satisfied when

$$C_{m,m''}(q, q'') = \delta_{m,m''} \delta(q - q'') \quad \text{(C.13)}$$

and

$$E_{l,1}(m, q) = E_l(m, q) \quad \text{(C.14)}$$

since $E_l(m'', q'')$ depends on both m'' and q''. As the coefficient matrix Eq. (C.13) for the transformation between the eigenfunctions is found to be the identity matrix, we conclude together with Eq. (C.14) that the third term of the right hand side of Eq. (3.70) leaves the eigenvalues Eq. (3.71) and eigenvectors Eq. (3.72) invariant.

D. Proof of Eq. (4.17)

First, we note that it is enough to show

$$\left[\hat{H}_{ee}, \hat{\Psi}^\dagger(x)\hat{\Psi}(\mathbf{r}, \sigma''')\right] = 0, \tag{D.1}$$

with $\hat{H}_{ee}$ being written with Schrödinger field operators, i. e. exactly as proposed in Eq. (3.37). Equation (4.17) follows then from the transformation of Eq. (D.1) to the Heisenberg picture. Using Eq. (3.37), the term

$$\hat{H}_{ee}\hat{\Psi}^\dagger(x)\hat{\Psi}(\mathbf{r}, \sigma''') = \frac{e^2}{2\kappa}\int dx' \int dx'' \frac{1}{\sqrt{|\mathbf{r}'' - \mathbf{r}'|^2 + \eta^2}}$$
$$\left[\hat{A}^1(x', x'', \mathbf{r}, \sigma, \sigma''') + \hat{A}^2(x', x'', \mathbf{r}, \sigma, \sigma''') + \hat{A}^3(x', x'', \mathbf{r}, \sigma, \sigma''') + \right.$$
$$\left. \hat{A}^4(x', x'', \mathbf{r}, \sigma, \sigma''') + \hat{A}^5(x', x'', \mathbf{r}, \sigma, \sigma''')\right] \tag{D.2}$$

with

$$\hat{A}^1(x', x'', \mathbf{r}, \sigma, \sigma''') := \hat{\Psi}^\dagger(x'')\hat{\Psi}^\dagger(x')\hat{\Psi}(x')\delta(x - x'')\hat{\Psi}(\mathbf{r}, \sigma'''), \tag{D.3}$$

$$\hat{A}^2(x', x'', \mathbf{r}, \sigma, \sigma''') := -\hat{\Psi}^\dagger(x'')\hat{\Psi}^\dagger(x')\delta(x - x')\hat{\Psi}(x'')\hat{\Psi}(\mathbf{r}, \sigma'''), \tag{D.4}$$

$$\hat{A}^3(x', x'', \mathbf{r}, \sigma, \sigma''') := \hat{\Psi}^\dagger(x)\hat{\Psi}^\dagger(x'')\delta(\mathbf{r} - \mathbf{r}')\delta_{\sigma''',\sigma'}\hat{\Psi}(x')\hat{\Psi}(x''), \tag{D.5}$$

$$\hat{A}^4(x', x'', \mathbf{r}, \sigma, \sigma''') := -\hat{\Psi}^\dagger(x)\delta(\mathbf{r}'' - \mathbf{r})\delta_{\sigma'',\sigma'''}\hat{\Psi}^\dagger(x')\hat{\Psi}(x')\hat{\Psi}(x'') \tag{D.6}$$

and

$$\hat{A}^5(x', x'', \mathbf{r}, \sigma, \sigma''') := \hat{\Psi}^\dagger(x)\hat{\Psi}(\mathbf{r}, \sigma''')\hat{\Psi}^\dagger(x'')\hat{\Psi}^\dagger(x')\hat{\Psi}(x')\hat{\Psi}(x''). \tag{D.7}$$

We can calculate the term connected to $\hat{A}^1(x', x'', \mathbf{r}, \sigma, \sigma''')$,

$$\int dx' \int dx'' \frac{1}{\sqrt{|\mathbf{r}'' - \mathbf{r}'|^2 + \eta^2}}\hat{A}^1(x', x'', \mathbf{r}, \sigma, \sigma''')$$
$$= \int dx' \frac{1}{\sqrt{|\mathbf{r} - \mathbf{r}'|^2 + \eta^2}}\hat{\Psi}^\dagger(x)\hat{\Psi}^\dagger(x')\hat{\Psi}(x')\hat{\Psi}(\mathbf{r}, \sigma'''), \tag{D.8}$$

D. Proof of Eq. (4.17)

to $\hat{A}^2(x', x'', \mathbf{r}, \sigma, \sigma''')$,

$$\int dx' \int dx'' \frac{1}{\sqrt{|\mathbf{r}'' - \mathbf{r}'|^2 + \eta^2}} \hat{A}^2(x', x'', \mathbf{r}, \sigma, \sigma''')$$
$$= -\int dx'' \frac{1}{\sqrt{|\mathbf{r}'' - \mathbf{r}|^2 + \eta^2}} \hat{\Psi}^\dagger(x'') \hat{\Psi}^\dagger(x) \hat{\Psi}(x'') \hat{\Psi}(\mathbf{r}, \sigma''')$$
$$= -\int dx' \frac{1}{\sqrt{|\mathbf{r}' - \mathbf{r}|^2 + \eta^2}} \hat{\Psi}^\dagger(x') \hat{\Psi}^\dagger(x) \hat{\Psi}(x') \hat{\Psi}(\mathbf{r}, \sigma'''), \tag{D.9}$$

to $\hat{A}^3(x', x'', \mathbf{r}, \sigma, \sigma''')$,

$$\int dx' \int dx'' \frac{1}{\sqrt{|\mathbf{r}'' - \mathbf{r}'|^2 + \eta^2}} \hat{A}^3(x', x'', \mathbf{r}, \sigma, \sigma''')$$
$$= \int dx'' \frac{1}{\sqrt{|\mathbf{r}'' - \mathbf{r}|^2 + \eta^2}} \hat{\Psi}^\dagger(x) \hat{\Psi}^\dagger(x'') \hat{\Psi}(\mathbf{r}, \sigma''') \hat{\Psi}(x'')$$
$$= \int dx' \frac{1}{\sqrt{|\mathbf{r}' - \mathbf{r}|^2 + \eta^2}} \hat{\Psi}^\dagger(x) \hat{\Psi}^\dagger(x') \hat{\Psi}(\mathbf{r}, \sigma''') \hat{\Psi}(x'), \tag{D.10}$$

and to $\hat{A}^4(x', x'', \mathbf{r}, \sigma, \sigma''')$,

$$\int dx' \int dx'' \frac{1}{\sqrt{|\mathbf{r}'' - \mathbf{r}'|^2 + \eta^2}} \hat{A}^4(x', x'', \mathbf{r}, \sigma, \sigma''')$$
$$= -\int dx' \frac{1}{\sqrt{|\mathbf{r} - \mathbf{r}'|^2 + \eta^2}} \hat{\Psi}^\dagger(x) \hat{\Psi}^\dagger(x') \hat{\Psi}(x') \hat{\Psi}(\mathbf{r}, \sigma'''). \tag{D.11}$$

Equation (D.8) and Eq. (D.10) cancel. Furthermore, Eq. (D.9) and Eq. (D.11) cancel. Therefore,

$$\hat{H}_{ee} \hat{\Psi}^\dagger(x) \hat{\Psi}(\mathbf{r}, \sigma''') = \hat{\Psi}^\dagger(x) \hat{\Psi}(\mathbf{r}, \sigma''') \hat{H}_{ee}, \tag{D.12}$$

which is equivalent to Eq. (D.1).

E. Derivation of the current density operator for S_x and S_y (Eq. (4.21) and Eq. (4.22)) and the source operator for S_x and S_y spin polarization (Eq. (4.24) and Eq. (4.25))

To simplify our derivation, we split the Hamiltonian Eq. (4.15) in two parts

$$
\hat{H}_{S,2}(t) = \int dx'' \int dx' \, \hat{\Psi}_H^\dagger(x',t) \delta(\mathbf{r}' - \mathbf{r}'')
$$

$$
\times \left[\frac{1}{2m^*} \left(\frac{\hbar}{i} \nabla'' + \frac{e}{c} \hat{\mathbf{A}}^H(\mathbf{r}'',t) \right)^2 + V_S(\mathbf{r}'') \right.
$$

$$
\left. + \frac{\mu_B g_S B}{2} (1 - 2\delta_{\sigma'',\downarrow}) \right] \delta_{\sigma',\sigma''} \hat{\Psi}_H(x'',t)
$$

$$
= \int dx'' \int dx' \, \hat{\Psi}_H^\dagger(x',t) \delta(\mathbf{r}' - \mathbf{r}'') \hat{\mathcal{H}}_{S,2}(x'',t) \delta_{\sigma',\sigma''} \hat{\Psi}_H(x'',t)
$$

$$
= \int dx'' \, \hat{\Psi}_H^\dagger(x'',t) \hat{\mathcal{H}}_{S,2}(x'',t) \hat{\Psi}_H(x'',t) \tag{E.1}
$$

with

$$
\hat{\mathcal{H}}_{S,2}(x'',t) = \frac{1}{2m^*} \left(\frac{\hbar}{i} \nabla'' + \frac{e}{c} \hat{\mathbf{A}}^H(\mathbf{r}'',t) \right)^2 + V_S(\mathbf{r}'') + \frac{\mu_B g_S B}{2} (1 - 2\delta_{\sigma'',\downarrow}) \tag{E.2}
$$

E. Derivation of Eq. (4.21), Eq. (4.22), Eq. (4.24) and Eq. (4.25)

and

$$
\begin{aligned}
\hat{H}_{S,3}(t) =& \int dx'' \int dx' \, \hat{\Psi}_H^\dagger(x',t)\delta(\mathbf{r}' - \mathbf{r}'') \\
&\times \left\{ \frac{\alpha}{\hbar} \left((\delta_{\sigma',\uparrow}\delta_{\sigma'',\downarrow} + \delta_{\sigma',\downarrow}\delta_{\sigma'',\uparrow}) \left[\frac{\hbar}{i}\frac{\partial}{\partial y''} + \frac{e}{c}\hat{A}_y^H(\mathbf{r}'',t) \right] \right. \right. \\
&\left. - (-i\delta_{\sigma',\uparrow}\delta_{\sigma'',\downarrow} + i\delta_{\sigma',\downarrow}\delta_{\sigma'',\uparrow}) \left[\frac{\hbar}{i}\frac{\partial}{\partial x''} + \frac{e}{c}\hat{A}_x^H(\mathbf{r}'',t) \right] \right) \\
&+ \frac{\beta}{\hbar} \left((\delta_{\sigma',\uparrow}\delta_{\sigma'',\downarrow} + \delta_{\sigma',\downarrow}\delta_{\sigma'',\uparrow}) \left[\frac{\hbar}{i}\frac{\partial}{\partial x''} + \frac{e}{c}\hat{A}_x^H(\mathbf{r}'',t) \right] \right. \\
&\left. \left. - (-i\delta_{\sigma',\uparrow}\delta_{\sigma'',\downarrow} + i\delta_{\sigma',\downarrow}\delta_{\sigma'',\uparrow}) \left[\frac{\hbar}{i}\frac{\partial}{\partial y''} + \frac{e}{c}\hat{A}_y^H(\mathbf{r}'',t) \right] \right) \right\} \hat{\Psi}_H(x'',t) \\
=& \int dx'' \int dx' \, \hat{\Psi}_H^\dagger(x',t)\delta(\mathbf{r}' - \mathbf{r}'')\hat{\mathcal{H}}_{S,3}(\mathbf{r}'',\sigma',\sigma'',t)\hat{\Psi}_H(x'',t) \qquad \text{(E.3)}
\end{aligned}
$$

with

$$
\begin{aligned}
\hat{\mathcal{H}}_{S,3}(\mathbf{r}'',\sigma',\sigma'',t) =& \frac{\alpha}{\hbar} \left((\delta_{\sigma',\uparrow}\delta_{\sigma'',\downarrow} + \delta_{\sigma',\downarrow}\delta_{\sigma'',\uparrow}) \left[\frac{\hbar}{i}\frac{\partial}{\partial y''} + \frac{e}{c}\hat{A}_y^H(\mathbf{r}'',t) \right] \right. \\
&\left. - (-i\delta_{\sigma',\uparrow}\delta_{\sigma'',\downarrow} + i\delta_{\sigma',\downarrow}\delta_{\sigma'',\uparrow}) \left[\frac{\hbar}{i}\frac{\partial}{\partial x''} + \frac{e}{c}\hat{A}_x^H(\mathbf{r}'',t) \right] \right) \\
&+ \frac{\beta}{\hbar} \left((\delta_{\sigma',\uparrow}\delta_{\sigma'',\downarrow} + \delta_{\sigma',\downarrow}\delta_{\sigma'',\uparrow}) \left[\frac{\hbar}{i}\frac{\partial}{\partial x''} + \frac{e}{c}\hat{A}_x^H(\mathbf{r}'',t) \right] \right. \\
&\left. - (-i\delta_{\sigma',\uparrow}\delta_{\sigma'',\downarrow} + i\delta_{\sigma',\downarrow}\delta_{\sigma'',\uparrow}) \left[\frac{\hbar}{i}\frac{\partial}{\partial y''} + \frac{e}{c}\hat{A}_y^H(\mathbf{r}'',t) \right] \right). \qquad \text{(E.4)}
\end{aligned}
$$

We furthermore assume that $\left[\hat{\mathbf{A}}(\mathbf{r}), \hat{\Psi}^\dagger(x')\right] = 0$ and $\left[\hat{\mathbf{A}}(\mathbf{r}), \hat{\Psi}(x')\right] = 0$. As a consequence, $\left[\hat{\mathbf{A}}^H(\mathbf{r},t), \hat{\Psi}_H^\dagger(x',t)\right] = 0$ and $\left[\hat{\mathbf{A}}^H(\mathbf{r},t), \hat{\Psi}_H(x',t)\right] = 0$.

To treat both the case of S_x and the case of S_y spin polarization, we generalize and define

$$
\mu := \begin{cases} 1, & S_x \text{ spin polarization} \\ -i, & S_y \text{ spin polarization} \end{cases} \qquad \text{(E.5)}
$$

and

$$
\nu := \begin{cases} 1, & S_x \text{ spin polarization} \\ i, & S_y \text{ spin polarization} \end{cases}. \qquad \text{(E.6)}
$$

E.1. Contribution of the first part (Hamiltonian Eq. (E.1))

Using the commutation relations for the Heisenberg field operators

$$\left\{\hat{\Psi}_H(\mathbf{r},\sigma,t),\hat{\Psi}_H^\dagger(\mathbf{r}',\sigma',t)\right\} = \hat{U}^\dagger(t)\left\{\hat{\Psi}(\mathbf{r},\sigma),\hat{\Psi}^\dagger(\mathbf{r}',\sigma')\right\}\hat{U}(t) = \delta_{\sigma,\sigma'}\delta(\mathbf{r}-\mathbf{r}'), \quad \text{(E.7)}$$

$$\left\{\hat{\Psi}_H(\mathbf{r},\sigma,t),\hat{\Psi}_H(\mathbf{r}',\sigma',t)\right\} = \hat{U}^\dagger(t)\left\{\hat{\Psi}(\mathbf{r},\sigma),\hat{\Psi}(\mathbf{r}',\sigma')\right\}\hat{U}(t) = 0 \quad \text{(E.8)}$$

and

$$\left\{\hat{\Psi}_H^\dagger(\mathbf{r},\sigma,t),\hat{\Psi}_H^\dagger(\mathbf{r}',\sigma',t)\right\} = \hat{U}^\dagger(t)\left\{\hat{\Psi}^\dagger(\mathbf{r},\sigma),\hat{\Psi}^\dagger(\mathbf{r}',\sigma')\right\}\hat{U}(t) = 0 \quad \text{(E.9)}$$

and defining

$$\hat{\tilde{\mathcal{H}}}_{S,2}(x) := \frac{1}{2m^*}\left(\frac{\hbar}{i}\nabla'' - \frac{e}{c}\hat{\mathbf{A}}^H(\mathbf{r}'',t)\right)^2 + V_S(\mathbf{r}'') + \frac{\mu_B g_S B}{2}(1 - 2\delta_{\sigma'',\downarrow}) \quad \text{(E.10)}$$

and assuming that the field operators are vanishing when the space coordinates go to infinity (confinement of the system), we consider the contribution of Hamiltonian Eq. (E.1) in Eq. (4.12) and get

$$\begin{aligned}
\frac{\partial}{\partial t}\hat{n}_{H,2}^{x,y}(\mathbf{r},t) =& \sum_\sigma\sum_{\sigma'}(\mu\delta_{\sigma,\uparrow}\delta_{\sigma',\downarrow} + \nu\delta_{\sigma,\downarrow}\delta_{\sigma',\uparrow})\\
&\times\frac{1}{2i}\left[\hat{\Psi}_H^\dagger(\mathbf{r},\sigma,t)\hat{\Psi}_H(\mathbf{r},\sigma',t)\hat{H}_{S,2}(t) - \hat{H}_{S,2}(t)\hat{\Psi}_H^\dagger(\mathbf{r},\sigma,t)\hat{\Psi}_H(\mathbf{r},\sigma',t)\right]\\
=& \sum_\sigma\sum_{\sigma'}(\mu\delta_{\sigma,\uparrow}\delta_{\sigma',\downarrow} + \nu\delta_{\sigma,\downarrow}\delta_{\sigma',\uparrow})\\
&\times\frac{1}{2i}\int dx''\left[\hat{\Psi}_H^\dagger(\mathbf{r},\sigma,t)\hat{\Psi}_H(\mathbf{r},\sigma',t)\hat{\Psi}_H^\dagger(x'',t)\hat{\tilde{\mathcal{H}}}_{S,2}(x'',t)\hat{\Psi}_H(x'',t)\right.\\
&\left. - \hat{\Psi}_H^\dagger(x'',t)\hat{\tilde{\mathcal{H}}}_{S,2}(x'',t)\hat{\Psi}_H(x'',t)\hat{\Psi}_H^\dagger(\mathbf{r},\sigma,t)\hat{\Psi}_H(\mathbf{r},\sigma',t)\right]\\
=& \sum_\sigma\sum_{\sigma'}(\mu\delta_{\sigma,\uparrow}\delta_{\sigma',\downarrow} + \nu\delta_{\sigma,\downarrow}\delta_{\sigma',\uparrow})\\
&\times\frac{1}{2i}\int dx''\left[\hat{\Psi}_H^\dagger(\mathbf{r},\sigma,t)\hat{\Psi}_H(\mathbf{r},\sigma',t)\hat{\Psi}_H^\dagger(x'',t)\hat{\tilde{\mathcal{H}}}_{S,2}(x'',t)\hat{\Psi}_H(x'',t)\right.\\
&- \hat{\Psi}_H^\dagger(x'',t)\hat{\tilde{\mathcal{H}}}_{S,2}(x'',t)\delta(x - x'')\hat{\Psi}_H(\mathbf{r},\sigma',t)\\
&\left.+ \hat{\Psi}_H^\dagger(x'',t)\hat{\tilde{\mathcal{H}}}_{S,2}(x'',t)\hat{\Psi}_H^\dagger(\mathbf{r},\sigma,t)\hat{\Psi}_H(x'',t)\hat{\Psi}_H(\mathbf{r},\sigma',t)\right], \quad \text{(E.11)}
\end{aligned}$$

E. Derivation of Eq. (4.21), Eq. (4.22), Eq. (4.24) and Eq. (4.25)

$$
\begin{aligned}
\frac{\partial}{\partial t}\hat{n}_{H,2}^{x,y}(\mathbf{r},t) = &\sum_{\sigma}\sum_{\sigma'}(\mu\delta_{\sigma,\uparrow}\delta_{\sigma',\downarrow} + \nu\delta_{\sigma,\downarrow}\delta_{\sigma',\uparrow}) \\
&\times \frac{1}{2i}\int dx'' \left[\hat{\Psi}_H^\dagger(\mathbf{r},\sigma,t)\hat{\Psi}_H(\mathbf{r},\sigma',t)\hat{\Psi}_H^\dagger(x'',t)\hat{\mathcal{H}}_{S,2}(x'',t)\hat{\Psi}_H(x'',t) \right. \\
&\quad - \hat{\Psi}_H^\dagger(x'',t)\hat{\mathcal{H}}_{S,2}(x'',t)\delta(x-x'')\hat{\Psi}_H(\mathbf{r},\sigma',t) \\
&\quad \left. + \hat{\Psi}_H^\dagger(\mathbf{r},\sigma,t)\hat{\Psi}_H^\dagger(x'',t)\hat{\mathcal{H}}_{S,2}(x'',t)\hat{\Psi}_H(\mathbf{r},\sigma',t)\hat{\Psi}_H(x'',t) \right] \\
= &\sum_{\sigma}\sum_{\sigma'}(\mu\delta_{\sigma,\uparrow}\delta_{\sigma',\downarrow} + \nu\delta_{\sigma,\downarrow}\delta_{\sigma',\uparrow}) \\
&\times \frac{1}{2i}\int dx'' \left[\hat{\Psi}_H^\dagger(\mathbf{r},\sigma,t)\hat{\Psi}_H(\mathbf{r},\sigma',t)\hat{\Psi}_H^\dagger(x'',t)\hat{\mathcal{H}}_{S,2}(x'',t)\hat{\Psi}_H(x'',t) \right. \\
&\quad - \hat{\Psi}_H^\dagger(x'',t)\hat{\mathcal{H}}_{S,2}(x'',t)\delta(x-x'')\hat{\Psi}_H(\mathbf{r},\sigma',t) \\
&\quad + \hat{\Psi}_H^\dagger(\mathbf{r},\sigma,t)\delta(\mathbf{r}-\mathbf{r}'')\delta_{\sigma',\sigma''}\hat{\mathcal{H}}_{S,2}(x'',t)\hat{\Psi}_H(x'',t) \\
&\quad \left. - \hat{\Psi}_H^\dagger(\mathbf{r},\sigma,t)\hat{\Psi}_H(\mathbf{r},\sigma',t)\hat{\Psi}_H^\dagger(x'',t)\hat{\mathcal{H}}_{S,2}(x'',t)\hat{\Psi}_H(x'',t) \right] \\
= &\sum_{\sigma}\sum_{\sigma'}(\mu\delta_{\sigma,\uparrow}\delta_{\sigma',\downarrow} + \nu\delta_{\sigma,\downarrow}\delta_{\sigma',\uparrow}) \\
&\times \frac{1}{2i}\int dx'' \left[-\hat{\Psi}_H^\dagger(x'',t)\hat{\mathcal{H}}_{S,2}(x'',t)\delta(x-x'')\hat{\Psi}_H(\mathbf{r},\sigma',t) \right. \\
&\quad \left. + \hat{\Psi}_H^\dagger(\mathbf{r},\sigma,t)\delta(\mathbf{r}-\mathbf{r}'')\delta_{\sigma',\sigma''}\hat{\mathcal{H}}_{S,2}(x'',t)\hat{\Psi}_H(x'',t) \right] \\
= &\sum_{\sigma}\sum_{\sigma'}(\mu\delta_{\sigma,\uparrow}\delta_{\sigma',\downarrow} + \nu\delta_{\sigma,\downarrow}\delta_{\sigma',\uparrow}) \\
&\times \frac{1}{2i}\int dx'' \left[-\delta(x-x'')\hat{\bar{\mathcal{H}}}_{S,2}(x'')\hat{\Psi}_H^\dagger(x'',t)\hat{\Psi}_H(\mathbf{r},\sigma',t) \right. \\
&\quad \left. + \hat{\Psi}_H^\dagger(\mathbf{r},\sigma,t)\delta(\mathbf{r}-\mathbf{r}'')\delta_{\sigma',\sigma''}\hat{\mathcal{H}}_{S,2}(x'',t)\hat{\Psi}_H(x'',t) \right] \\
= &\sum_{\sigma}\sum_{\sigma'}(\mu\delta_{\sigma,\uparrow}\delta_{\sigma',\downarrow} + \nu\delta_{\sigma,\downarrow}\delta_{\sigma',\uparrow}) \\
&\times \frac{1}{2i}\int dx'' \left[-\delta(x-x'')\hat{\bar{\mathcal{H}}}_{S,2}(x'')\hat{\Psi}_H^\dagger(x'',t)\hat{\Psi}_H(\mathbf{r},\sigma',t) \right. \\
&\quad \left. + \hat{\Psi}_H^\dagger(\mathbf{r},\sigma,t)\delta(\mathbf{r}-\mathbf{r}'')\delta_{\sigma',\sigma''}\hat{\mathcal{H}}_{S,2}(x'',t)\hat{\Psi}_H(x'',t) \right] \\
= &\sum_{\sigma}\sum_{\sigma'}(\mu\delta_{\sigma,\uparrow}\delta_{\sigma',\downarrow} + \nu\delta_{\sigma,\downarrow}\delta_{\sigma',\uparrow}) \\
&\times \frac{1}{2i}\left[-\left(\hat{\bar{\mathcal{H}}}_{S,2}(x)\hat{\Psi}_H^\dagger(\mathbf{r},\sigma,t) \right)\hat{\Psi}_H(\mathbf{r},\sigma',t) \right. \\
&\quad \left. + \hat{\Psi}_H^\dagger(\mathbf{r},\sigma,t)\hat{\mathcal{H}}_{S,2}(\mathbf{r},\sigma',t)\hat{\Psi}_H(\mathbf{r},\sigma',t) \right],
\end{aligned}
\tag{E.12}
$$

$$\frac{\partial}{\partial t}\hat{n}_{H,2}^{x,y}(\mathbf{r},t) = \sum_{\sigma}\sum_{\sigma'}(\mu\delta_{\sigma,\uparrow}\delta_{\sigma',\downarrow} + \nu\delta_{\sigma,\downarrow}\delta_{\sigma',\uparrow})$$

$$\times\frac{1}{2i}\left\{-\left(\left[\frac{1}{2m^*}\left(-\hbar^2\nabla^2 - \frac{e\hbar}{ic}\left[\nabla\hat{\mathbf{A}}^H(\mathbf{r},t) + \hat{\mathbf{A}}^H(\mathbf{r},t)\nabla\right]\right)\right.\right.$$

$$\left.\left.- \mu_B g_S B\delta_{\sigma,\downarrow}\right]\hat{\Psi}_H^\dagger(\mathbf{r},\sigma,t)\right)$$

$$\times\hat{\Psi}_H(\mathbf{r},\sigma',t) + \hat{\Psi}_H^\dagger(\mathbf{r},\sigma,t)$$

$$\times\left[\frac{1}{2m^*}\left(-\hbar^2\nabla^2 + \frac{e\hbar}{ic}\left[\nabla\hat{\mathbf{A}}^H(\mathbf{r},t) + \hat{\mathbf{A}}^H(\mathbf{r},t)\nabla\right]\right)\right.$$

$$\left.- \mu_B g_S B\delta_{\sigma',\downarrow}\right]\hat{\Psi}_H(\mathbf{r},\sigma',t)\Bigg\}$$

$$= -\sum_{\sigma}\sum_{\sigma'}(\mu\delta_{\sigma,\uparrow}\delta_{\sigma',\downarrow} + \nu\delta_{\sigma,\downarrow}\delta_{\sigma',\uparrow})$$

$$\times\left\{\nabla\left[\frac{\hbar^2}{4m^*i}\left(\hat{\Psi}_H^\dagger(\mathbf{r},\sigma,t)\nabla\hat{\Psi}_H(\mathbf{r},\sigma',t) - \left[\nabla\hat{\Psi}_H^\dagger(\mathbf{r},\sigma,t)\right]\hat{\Psi}_H(\mathbf{r},\sigma',t)\right)\right.\right.$$

$$\left.+ \frac{e\hbar}{2m^*c}\hat{\mathbf{A}}^H(\mathbf{r},t)\hat{\Psi}_H^\dagger(\mathbf{r},\sigma,t)\hat{\Psi}_H(\mathbf{r},\sigma',t)\right]$$

$$\left.+ \frac{\mu_B g_S B}{2i}(\delta_{\sigma',\downarrow} - \delta_{\sigma,\downarrow})\hat{\Psi}_H^\dagger(\mathbf{r},\sigma,t)\hat{\Psi}_H(\mathbf{r},\sigma',t)\right\}. \tag{E.13}$$

After performing the inverse transformation back to the Schrödinger picture, we find the contribution of Hamiltonian Eq. (E.1) of the current density operator for S_x spin polarization

$$\hat{\mathbf{j}}_2^x(\mathbf{r}) = \frac{\hbar^2}{4m^*i}\left[\hat{\Psi}^\dagger(\mathbf{r},\uparrow)\nabla\hat{\Psi}(\mathbf{r},\downarrow) - \left[\nabla\hat{\Psi}^\dagger(\mathbf{r},\uparrow)\right]\hat{\Psi}(\mathbf{r},\downarrow)\right] + \frac{e\hbar}{2m^*c}\hat{\mathbf{A}}(\mathbf{r})\hat{\Psi}^\dagger(\mathbf{r},\uparrow)\hat{\Psi}(\mathbf{r},\downarrow)$$

$$+ \frac{\hbar^2}{4m^*i}\left[\hat{\Psi}^\dagger(\mathbf{r},\downarrow)\nabla\hat{\Psi}(\mathbf{r},\uparrow) - \left[\nabla\hat{\Psi}^\dagger(\mathbf{r},\downarrow)\right]\hat{\Psi}(\mathbf{r},\uparrow)\right]$$

$$+ \frac{e\hbar}{2m^*c}\hat{\mathbf{A}}(\mathbf{r})\hat{\Psi}^\dagger(\mathbf{r},\downarrow)\hat{\Psi}(\mathbf{r},\uparrow) \tag{E.14}$$

and the y-component of the current density operator for S_y spin polarization

$$\hat{\mathbf{j}}_2^y(\mathbf{r}) = -\frac{\hbar^2}{4m^*}\left[\hat{\Psi}^\dagger(\mathbf{r},\uparrow)\nabla\hat{\Psi}(\mathbf{r},\downarrow) - \left[\nabla\hat{\Psi}^\dagger(\mathbf{r},\uparrow)\right]\hat{\Psi}(\mathbf{r},\downarrow)\right] - \frac{ie\hbar}{2m^*c}\hat{\mathbf{A}}(\mathbf{r})\hat{\Psi}^\dagger(\mathbf{r},\uparrow)\hat{\Psi}(\mathbf{r},\downarrow)$$

$$+ \frac{\hbar^2}{4m^*}\left[\hat{\Psi}^\dagger(\mathbf{r},\downarrow)\nabla\hat{\Psi}(\mathbf{r},\uparrow) - \left[\nabla\hat{\Psi}^\dagger(\mathbf{r},\downarrow)\right]\hat{\Psi}(\mathbf{r},\uparrow)\right]$$

$$+ \frac{ie\hbar}{2m^*c}\hat{\mathbf{A}}(\mathbf{r})\hat{\Psi}^\dagger(\mathbf{r},\downarrow)\hat{\Psi}(\mathbf{r},\uparrow). \tag{E.15}$$

In the Schrödinger picture, the contribution of Hamiltonian Eq. (E.1) to the spin

E. Derivation of Eq. (4.21), Eq. (4.22), Eq. (4.24) and Eq. (4.25)

polarization source operators is

$$
\hat{s}_2^{x,y}(\mathbf{r}) = \sum_\sigma \sum_{\sigma'} (\mu \delta_{\sigma,\uparrow} \delta_{\sigma',\downarrow} + \nu \delta_{\sigma,\downarrow} \delta_{\sigma',\uparrow}) \frac{\mu_B g_S B}{2i} (\delta_{\sigma,\downarrow} - \delta_{\sigma',\downarrow}) \hat{\Psi}^\dagger(\mathbf{r},\sigma) \hat{\Psi}(\mathbf{r},\sigma')
$$

$$
= \sum_\sigma \sum_{\sigma'} (-\mu \delta_{\sigma,\uparrow} \delta_{\sigma',\downarrow} + \nu \delta_{\sigma,\downarrow} \delta_{\sigma',\uparrow}) \frac{\mu_B g_S B}{2i} \hat{\Psi}^\dagger(\mathbf{r},\sigma) \hat{\Psi}(\mathbf{r},\sigma') \tag{E.16}
$$

leading to the source operator for S_x spin polarization

$$
\hat{s}_2^x(\mathbf{r}) = \frac{\mu_B g_S B}{2i} \left[-\hat{\Psi}^\dagger(\mathbf{r},\uparrow)\hat{\Psi}(\mathbf{r},\downarrow) + \hat{\Psi}^\dagger(\mathbf{r},\downarrow)\hat{\Psi}(\mathbf{r},\uparrow) \right] \tag{E.17}
$$

and S_y spin polarization

$$
\hat{s}_2^y(\mathbf{r}) = \frac{\mu_B g_S B}{2} \left[\hat{\Psi}^\dagger(\mathbf{r},\uparrow)\hat{\Psi}(\mathbf{r},\downarrow) + \hat{\Psi}^\dagger(\mathbf{r},\downarrow)\hat{\Psi}(\mathbf{r},\uparrow) \right]. \tag{E.18}
$$

E.2. Contribution of the second part (Hamiltonian Eq. (E.3))

Using the commutation relations for the Heisenberg field operators Eq. (E.7), Eq. (E.8) and Eq. (E.9) and defining

$$
\hat{\tilde{\mathcal{H}}}_{S,3}(\mathbf{r}'',\sigma',\sigma'',t) := \frac{\alpha}{\hbar} \left((\delta_{\sigma',\uparrow}\delta_{\sigma'',\downarrow} + \delta_{\sigma',\downarrow}\delta_{\sigma'',\uparrow}) \left[-\frac{\hbar}{i}\frac{\partial}{\partial y''} + \frac{e}{c}\hat{A}_y^H(\mathbf{r}'',t) \right] \right.
$$
$$
\left. - (-i\delta_{\sigma',\uparrow}\delta_{\sigma'',\downarrow} + i\delta_{\sigma',\downarrow}\delta_{\sigma'',\uparrow}) \left[-\frac{\hbar}{i}\frac{\partial}{\partial x''} + \frac{e}{c}\hat{A}_x^H(\mathbf{r}'',t) \right] \right)
$$
$$
+ \frac{\beta}{\hbar} \left((\delta_{\sigma',\uparrow}\delta_{\sigma'',\downarrow} + \delta_{\sigma',\downarrow}\delta_{\sigma'',\uparrow}) \left[-\frac{\hbar}{i}\frac{\partial}{\partial x''} + \frac{e}{c}\hat{A}_x^H(\mathbf{r}'',t) \right] \right.
$$
$$
\left. - (-i\delta_{\sigma',\uparrow}\delta_{\sigma'',\downarrow} + i\delta_{\sigma',\downarrow}\delta_{\sigma'',\uparrow}) \left[-\frac{\hbar}{i}\frac{\partial}{\partial y''} + \frac{e}{c}\hat{A}_y^H(\mathbf{r}'',t) \right] \right). \tag{E.19}
$$

and assuming that the field operators are vanishing when the space coordinates go to infinity, we consider the contribution of Hamiltonian Eq. (E.3) in Eq. (4.12) and get

$$
\frac{\partial}{\partial t}\hat{n}_{H,3}^{x,y}(\mathbf{r},t) = \sum_\sigma \sum_{\sigma'} (\mu \delta_{\sigma,\uparrow}\delta_{\sigma',\downarrow} + \nu \delta_{\sigma,\downarrow}\delta_{\sigma',\uparrow}) \frac{1}{2i} \left[\hat{\Psi}_H^\dagger(\mathbf{r},\sigma,t)\hat{\Psi}_H(\mathbf{r},\sigma',t)\hat{H}_{S,3} \right.
$$
$$
\left. - \hat{H}_{S,3}\hat{\Psi}_H^\dagger(\mathbf{r},\sigma,t)\hat{\Psi}_H(\mathbf{r},\sigma',t) \right], \tag{E.20}
$$

$$\frac{\partial}{\partial t}\hat{n}_{H,3}^{x,y}(\mathbf{r},t) = \sum_{\sigma}\sum_{\sigma'}(\mu\delta_{\sigma,\uparrow}\delta_{\sigma',\downarrow} + \nu\delta_{\sigma,\downarrow}\delta_{\sigma',\uparrow})\frac{1}{2i}\int dx''' \int dx'' \,\delta(\mathbf{r}''-\mathbf{r}''')$$

$$\times\left[\hat{\Psi}_H^\dagger(\mathbf{r},\sigma,t)\hat{\Psi}_H(\mathbf{r},\sigma',t)\hat{\Psi}_H^\dagger(x'',t)\hat{\mathcal{H}}_{S,3}(\mathbf{r}''',\sigma'',\sigma''',t)\hat{\Psi}_H(x''',t)\right.$$

$$\left. - \hat{\Psi}_H^\dagger(x'',t)\hat{\mathcal{H}}_{S,3}(\mathbf{r}''',\sigma'',\sigma''',t)\hat{\Psi}_H(x''',t)\hat{\Psi}_H^\dagger(\mathbf{r},\sigma,t)\hat{\Psi}_H(\mathbf{r},\sigma',t)\right]$$

$$= \sum_{\sigma}\sum_{\sigma'}(\mu\delta_{\sigma,\uparrow}\delta_{\sigma',\downarrow} + \nu\delta_{\sigma,\downarrow}\delta_{\sigma',\uparrow})\frac{1}{2i}\int dx''' \int dx'' \,\delta(\mathbf{r}''-\mathbf{r}''')$$

$$\times\left[\hat{\Psi}_H^\dagger(\mathbf{r},\sigma,t)\hat{\Psi}_H(\mathbf{r},\sigma',t)\hat{\Psi}_H^\dagger(x'',t)\hat{\mathcal{H}}_{S,3}(\mathbf{r}''',\sigma'',\sigma''',t)\hat{\Psi}_H(x''',t)\right.$$

$$- \hat{\Psi}_H^\dagger(x'',t)\hat{\mathcal{H}}_{S,3}(\mathbf{r}''',\sigma'',\sigma''',t)\delta(x-x''')\hat{\Psi}_H(\mathbf{r},\sigma',t)$$

$$\left. + \hat{\Psi}_H^\dagger(\mathbf{r},\sigma,t)\hat{\Psi}_H^\dagger(x'',t)\hat{\mathcal{H}}_{S,3}(\mathbf{r}''',\sigma'',\sigma''',t)\hat{\Psi}_H(\mathbf{r},\sigma',t)\hat{\Psi}_H(x''',t)\right]$$

$$= \sum_{\sigma}\sum_{\sigma'}(\mu\delta_{\sigma,\uparrow}\delta_{\sigma',\downarrow} + \nu\delta_{\sigma,\downarrow}\delta_{\sigma',\uparrow})\frac{1}{2i}\int dx''' \int dx'' \,\delta(\mathbf{r}''-\mathbf{r}''')$$

$$\times\left[-\hat{\Psi}_H^\dagger(x'',t)\hat{\mathcal{H}}_{S,3}(\mathbf{r}''',\sigma'',\sigma''',t)\delta(x-x'')\hat{\Psi}_H(\mathbf{r},\sigma',t)\right.$$

$$\left. + \hat{\Psi}_H^\dagger(\mathbf{r},\sigma,t)\delta(\mathbf{r}-\mathbf{r}'')\delta_{\sigma',\sigma''}\hat{\mathcal{H}}_{S,3}(\mathbf{r}''',\sigma'',\sigma''',t)\hat{\Psi}_H(x''',t)\right]$$

$$= \sum_{\sigma}\sum_{\sigma'}(\mu\delta_{\sigma,\uparrow}\delta_{\sigma',\downarrow} + \nu\delta_{\sigma,\downarrow}\delta_{\sigma',\uparrow})\frac{1}{2i}\sum_{\sigma'''}\int dx''$$

$$\times\left[-\hat{\Psi}_H^\dagger(x'',t)\hat{\mathcal{H}}_{S,3}(\mathbf{r}'',\sigma'',\sigma''',t)\delta(\mathbf{r}-\mathbf{r}'')\delta_{\sigma,\sigma'''}\hat{\Psi}_H(\mathbf{r},\sigma',t)\right.$$

$$\left. + \hat{\Psi}_H^\dagger(\mathbf{r},\sigma,t)\delta(\mathbf{r}-\mathbf{r}'')\delta_{\sigma',\sigma''}\hat{\mathcal{H}}_{S,3}(\mathbf{r}'',\sigma'',\sigma''',t)\hat{\Psi}_H(\mathbf{r}'',\sigma''',t)\right]$$

$$= \sum_{\sigma}\sum_{\sigma'}(\mu\delta_{\sigma,\uparrow}\delta_{\sigma',\downarrow} + \nu\delta_{\sigma,\downarrow}\delta_{\sigma',\uparrow})\frac{1}{2i}\sum_{\sigma'''}\int dx''$$

$$\times\left[-\delta(\mathbf{r}-\mathbf{r}'')\hat{\bar{\mathcal{H}}}_{S,3}(\mathbf{r}'',\sigma'',\sigma''',t)\hat{\Psi}_H^\dagger(x'',t)\delta_{\sigma,\sigma'''}\hat{\Psi}_H(\mathbf{r},\sigma',t)\right.$$

$$\left. + \hat{\Psi}_H^\dagger(\mathbf{r},\sigma,t)\delta(\mathbf{r}-\mathbf{r}'')\delta_{\sigma',\sigma''}\hat{\mathcal{H}}_{S,3}(\mathbf{r}'',\sigma'',\sigma''',t)\hat{\Psi}_H(\mathbf{r}'',\sigma''',t)\right]$$

$$= \sum_{\sigma}\sum_{\sigma'}(\mu\delta_{\sigma,\uparrow}\delta_{\sigma',\downarrow} + \nu\delta_{\sigma,\downarrow}\delta_{\sigma',\uparrow})$$

$$\times\frac{1}{2i}\sum_{\sigma'''}\sum_{\sigma''}\left[-\left\{\hat{\bar{\mathcal{H}}}_{S,3}(\mathbf{r},\sigma'',\sigma''',t)\hat{\Psi}_H^\dagger(\mathbf{r},\sigma'',t)\right\}\delta_{\sigma,\sigma'''}\hat{\Psi}_H(\mathbf{r},\sigma',t)\right.$$

$$\left. + \hat{\Psi}_H^\dagger(\mathbf{r},\sigma,t)\delta_{\sigma',\sigma''}\hat{\mathcal{H}}_{S,3}(\mathbf{r},\sigma'',\sigma''',t)\hat{\Psi}_H(\mathbf{r},\sigma''',t)\right]$$

$$= \sum_{\sigma}\sum_{\sigma'}(\mu\delta_{\sigma,\uparrow}\delta_{\sigma',\downarrow} + \nu\delta_{\sigma,\downarrow}\delta_{\sigma',\uparrow})$$

$$\times\frac{1}{2i}\sum_{\sigma''}\left[-\left\{\hat{\bar{\mathcal{H}}}_{S,3}(\mathbf{r},\sigma'',\sigma,t)\hat{\Psi}_H^\dagger(\mathbf{r},\sigma'',t)\right\}\hat{\Psi}_H(\mathbf{r},\sigma',t)\right.$$

$$\left. + \hat{\Psi}_H^\dagger(\mathbf{r},\sigma,t)\hat{\mathcal{H}}_{S,3}(\mathbf{r},\sigma',\sigma'',t)\hat{\Psi}_H(\mathbf{r},\sigma'',t)\right]$$

$$=: \hat{A}_1^{x,y}(\mathbf{r},t) + \hat{A}_2^{x,y}(\mathbf{r},t) + \hat{A}_3^{x,y}(\mathbf{r},t) + \hat{A}_4^{x,y}(\mathbf{r},t). \tag{E.21}$$

65

E. Derivation of Eq. (4.21), Eq. (4.22), Eq. (4.24) and Eq. (4.25)

Before we continue, we split the intermediate result in four terms:

$$
\begin{aligned}
\hat{A}_1^{x,y}(\mathbf{r},t) :=& \frac{1}{2i} \sum_\sigma \sum_{\sigma'} (\mu \delta_{\sigma,\uparrow}\delta_{\sigma',\downarrow} + \nu \delta_{\sigma,\downarrow}\delta_{\sigma',\uparrow}) \sum_{\sigma''} \left\{ \frac{\hbar}{i}\frac{\partial}{\partial x}\left[\hat{\Psi}_H^\dagger(\mathbf{r},\sigma'',t)\right] \right. \\
& \times \left[-\frac{\alpha}{\hbar}(-i\delta_{\sigma'',\uparrow}\delta_{\sigma,\downarrow} + i\delta_{\sigma'',\downarrow}\delta_{\sigma,\uparrow}) + \frac{\beta}{\hbar}(\delta_{\sigma'',\uparrow}\delta_{\sigma,\downarrow} + \delta_{\sigma'',\downarrow}\delta_{\sigma,\uparrow}) \right] \hat{\Psi}_H(\mathbf{r},\sigma',t) \\
& + \hat{\Psi}_H^\dagger(\mathbf{r},\sigma,t)\left[-\frac{\alpha}{\hbar}(-i\delta_{\sigma',\uparrow}\delta_{\sigma'',\downarrow} + i\delta_{\sigma',\downarrow}\delta_{\sigma'',\uparrow}) \right. \\
& \left. \left. + \frac{\beta}{\hbar}(\delta_{\sigma',\uparrow}\delta_{\sigma'',\downarrow} + \delta_{\sigma',\downarrow}\delta_{\sigma'',\uparrow}) \right] \frac{\hbar}{i}\frac{\partial}{\partial x}\hat{\Psi}_H(\mathbf{r},\sigma'',t) \right\},
\end{aligned}
\tag{E.22}
$$

$$
\begin{aligned}
\hat{A}_2^{x,y}(\mathbf{r},t) :=& \frac{1}{2i} \sum_\sigma \sum_{\sigma'} (\mu \delta_{\sigma,\uparrow}\delta_{\sigma',\downarrow} + \nu \delta_{\sigma,\downarrow}\delta_{\sigma',\uparrow}) \sum_{\sigma''} \left\{ \frac{\hbar}{i}\frac{\partial}{\partial y}\left[\hat{\Psi}_H^\dagger(\mathbf{r},\sigma'',t)\right] \right. \\
& \times \left[-\frac{\beta}{\hbar}(-i\delta_{\sigma'',\uparrow}\delta_{\sigma,\downarrow} + i\delta_{\sigma'',\downarrow}\delta_{\sigma,\uparrow}) + \frac{\alpha}{\hbar}(\delta_{\sigma'',\uparrow}\delta_{\sigma,\downarrow} + \delta_{\sigma'',\downarrow}\delta_{\sigma,\uparrow}) \right] \hat{\Psi}_H(\mathbf{r},\sigma',t) \\
& + \hat{\Psi}_H^\dagger(\mathbf{r},\sigma,t)\left[-\frac{\beta}{\hbar}(-i\delta_{\sigma',\uparrow}\delta_{\sigma'',\downarrow} + i\delta_{\sigma',\downarrow}\delta_{\sigma'',\uparrow}) \right. \\
& \left. \left. + \frac{\alpha}{\hbar}(\delta_{\sigma',\uparrow}\delta_{\sigma'',\downarrow} + \delta_{\sigma',\downarrow}\delta_{\sigma'',\uparrow}) \right] \frac{\hbar}{i}\frac{\partial}{\partial y}\hat{\Psi}_H(\mathbf{r},\sigma'',t) \right\},
\end{aligned}
\tag{E.23}
$$

$$
\begin{aligned}
\hat{A}_3^{x,y}(\mathbf{r},t) :=& \frac{1}{2i} \sum_\sigma \sum_{\sigma'} (\mu \delta_{\sigma,\uparrow}\delta_{\sigma',\downarrow} + \nu \delta_{\sigma,\downarrow}\delta_{\sigma',\uparrow}) \sum_{\sigma''} \left\{ \frac{e}{c}\hat{A}_x^H(\mathbf{r},t)\hat{\Psi}_H^\dagger(\mathbf{r},\sigma'',t) \right. \\
& \times \left[\frac{\alpha}{\hbar}(-i\delta_{\sigma'',\uparrow}\delta_{\sigma,\downarrow} + i\delta_{\sigma'',\downarrow}\delta_{\sigma,\uparrow}) - \frac{\beta}{\hbar}(\delta_{\sigma'',\uparrow}\delta_{\sigma,\downarrow} + \delta_{\sigma'',\downarrow}\delta_{\sigma,\uparrow}) \right] \hat{\Psi}_H(\mathbf{r},\sigma',t) + \\
& + \hat{\Psi}_H^\dagger(\mathbf{r},\sigma,t)\left[-\frac{\alpha}{\hbar}(-i\delta_{\sigma',\uparrow}\delta_{\sigma'',\downarrow} + i\delta_{\sigma',\downarrow}\delta_{\sigma'',\uparrow}) \right. \\
& \left. \left. + \frac{\beta}{\hbar}(\delta_{\sigma',\uparrow}\delta_{\sigma'',\downarrow} + \delta_{\sigma',\downarrow}\delta_{\sigma'',\uparrow}) \right] \frac{e}{c}\hat{A}_x^H(\mathbf{r},t)\hat{\Psi}_H(\mathbf{r},\sigma'',t) \right\}
\end{aligned}
\tag{E.24}
$$

and

$$
\begin{aligned}
\hat{A}_4^{x,y}(\mathbf{r},t) :=& \frac{1}{2i} \sum_\sigma \sum_{\sigma'} (\mu \delta_{\sigma,\uparrow}\delta_{\sigma',\downarrow} + \nu \delta_{\sigma,\downarrow}\delta_{\sigma',\uparrow}) \sum_{\sigma''} \left\{ \frac{e}{c}\hat{A}_y^H(\mathbf{r},t)\hat{\Psi}_H^\dagger(\mathbf{r},\sigma'',t) \right. \\
& \times \left[\frac{\beta}{\hbar}(-i\delta_{\sigma'',\uparrow}\delta_{\sigma,\downarrow} + i\delta_{\sigma'',\downarrow}\delta_{\sigma,\uparrow}) - \frac{\alpha}{\hbar}(\delta_{\sigma'',\uparrow}\delta_{\sigma,\downarrow} + \delta_{\sigma'',\downarrow}\delta_{\sigma,\uparrow}) \right] \hat{\Psi}_H(\mathbf{r},\sigma',t) + \\
& \times \hat{\Psi}_H^\dagger(\mathbf{r},\sigma,t)\left[-\frac{\beta}{\hbar}(-i\delta_{\sigma',\uparrow}\delta_{\sigma'',\downarrow} + i\delta_{\sigma',\downarrow}\delta_{\sigma'',\uparrow}) \right. \\
& \left. \left. + \frac{\alpha}{\hbar}(\delta_{\sigma',\uparrow}\delta_{\sigma'',\downarrow} + \delta_{\sigma',\downarrow}\delta_{\sigma'',\uparrow}) \right] \frac{e}{c}\hat{A}_y^H(\mathbf{r},t)\hat{\Psi}_H(\mathbf{r},\sigma'',t) \right\}.
\end{aligned}
\tag{E.25}
$$

To simplify our calculations, we note that the term $\hat{A}_1^{x,y}(\mathbf{r},t)$ (Eq. (E.22)) differs from $\hat{A}_2^{x,y}(\mathbf{r},t)$ (Eq. (E.23)) by swapping (a) α and β and (b) $\frac{\partial}{\partial x}$ and $\frac{\partial}{\partial y}$. We note also

that the term $\hat{A}_3^{x,y}(\mathbf{r}, t)$ (Eq. (E.24)) differs from $\hat{A}_4^{x,y}(\mathbf{r}, t)$ (Eq. (E.25)) by swapping (a) α and β and (b) $\hat{A}_x(\mathbf{r}, t)$ by $\hat{A}_y(\mathbf{r}, t)$. Therefore, it is sufficient to look only at the terms $\hat{A}_1^{x,y}(\mathbf{r})$ (Eq. (E.22)) and $\hat{A}_3^{x,y}(\mathbf{r})$ (Eq. (E.24)). Equation (E.22) can be simplified

$$
\begin{aligned}
\hat{A}_1^{x,y}(\mathbf{r}, t) = -\frac{1}{2} \Bigg\{ & (i\alpha + \beta)\, \nu \frac{\partial}{\partial x} \left[\hat{\Psi}_H^\dagger(\mathbf{r}, \uparrow, t) \right] \hat{\Psi}_H(\mathbf{r}, \uparrow, t) \\
& + (-i\alpha + \beta)\, \mu \frac{\partial}{\partial x} \left[\hat{\Psi}_H^\dagger(\mathbf{r}, \downarrow, t) \right] \hat{\Psi}_H(\mathbf{r}, \downarrow, t) \\
& + (i\alpha + \beta)\, \nu \hat{\Psi}_H^\dagger(\mathbf{r}, \downarrow, t) \frac{\partial}{\partial x} \hat{\Psi}_H(\mathbf{r}, \downarrow, t) \\
& + (-i\alpha + \beta)\, \mu \hat{\Psi}_H^\dagger(\mathbf{r}, \uparrow, t) \frac{\partial}{\partial x} \hat{\Psi}_H(\mathbf{r}, \uparrow, t) \Bigg\}.
\end{aligned}
\tag{E.26}
$$

For S_x spin polarization, the term $\hat{A}_1^x(\mathbf{r}, t)$ is

$$
\begin{aligned}
\hat{A}_1^x(\mathbf{r}, t) = -\frac{1}{2} \Bigg\{ & (i\alpha + \beta)\, \frac{\partial}{\partial x} \left[\hat{\Psi}_H^\dagger(\mathbf{r}, \uparrow, t) \right] \hat{\Psi}_H(\mathbf{r}, \uparrow, t) \\
& + (-i\alpha + \beta)\, \frac{\partial}{\partial x} \left[\hat{\Psi}_H^\dagger(\mathbf{r}, \downarrow, t) \right] \hat{\Psi}_H(\mathbf{r}, \downarrow, t) \\
& + (i\alpha + \beta)\, \hat{\Psi}_H^\dagger(\mathbf{r}, \downarrow, t) \frac{\partial}{\partial x} \hat{\Psi}_H(\mathbf{r}, \downarrow, t) + (-i\alpha + \beta)\, \hat{\Psi}_H^\dagger(\mathbf{r}, \uparrow, t) \frac{\partial}{\partial x} \hat{\Psi}_H(\mathbf{r}, \uparrow, t) \Bigg\} \\
= -\frac{\partial}{\partial x} & \left\{ \frac{\beta}{2} \left[\hat{\Psi}_H^\dagger(\mathbf{r}, \uparrow, t) \hat{\Psi}_H(\mathbf{r}, \uparrow, t) + \hat{\Psi}_H^\dagger(\mathbf{r}, \downarrow, t) \hat{\Psi}_H(\mathbf{r}, \downarrow, t) \right] \right\} \\
- \frac{1}{2} \Bigg\{ & i\alpha \frac{\partial}{\partial x} \left[\hat{\Psi}_H^\dagger(\mathbf{r}, \uparrow, t) \right] \hat{\Psi}_H(\mathbf{r}, \uparrow, t) - i\alpha \frac{\partial}{\partial x} \left[\hat{\Psi}_H^\dagger(\mathbf{r}, \downarrow, t) \right] \hat{\Psi}_H(\mathbf{r}, \downarrow, t) \\
& + i\alpha \hat{\Psi}_H^\dagger(\mathbf{r}, \downarrow, t) \frac{\partial}{\partial x} \hat{\Psi}_H(\mathbf{r}, \downarrow, t) - i\alpha \hat{\Psi}_H^\dagger(\mathbf{r}, \uparrow, t) \frac{\partial}{\partial x} \hat{\Psi}_H(\mathbf{r}, \uparrow, t) \Bigg\}
\end{aligned}
\tag{E.27}
$$

E. Derivation of Eq. (4.21), Eq. (4.22), Eq. (4.24) and Eq. (4.25)

and for S_y spin polarization, the term $\hat{A}_1^y(\mathbf{r}, t)$ is

$$
\begin{aligned}
\hat{A}_1^y(\mathbf{r}, t) = & -\frac{1}{2}\left\{(-\alpha + i\beta)\frac{\partial}{\partial x}\left[\hat{\Psi}_H^\dagger(\mathbf{r}, \uparrow, t)\right]\hat{\Psi}_H(\mathbf{r}, \uparrow, t)\right. \\
& + (-\alpha - i\beta)\frac{\partial}{\partial x}\left[\hat{\Psi}_H^\dagger(\mathbf{r}, \downarrow, t)\right]\hat{\Psi}_H(\mathbf{r}, \downarrow, t) \\
& + (-\alpha + i\beta)\hat{\Psi}_H^\dagger(\mathbf{r}, \downarrow, t)\frac{\partial}{\partial x}\hat{\Psi}_H(\mathbf{r}, \downarrow, t) \\
& \left. + (-\alpha - i\beta)\hat{\Psi}_H^\dagger(\mathbf{r}, \uparrow, t)\frac{\partial}{\partial x}\hat{\Psi}_H(\mathbf{r}, \uparrow, t)\right\} \\
= & -\frac{\partial}{\partial x}\left\{-\frac{\alpha}{2}\left[\hat{\Psi}_H^\dagger(\mathbf{r}, \uparrow, t)\hat{\Psi}_H(\mathbf{r}, \uparrow, t) + \hat{\Psi}_H^\dagger(\mathbf{r}, \downarrow, t)\hat{\Psi}_H(\mathbf{r}, \downarrow, t)\right]\right\} \\
& -\frac{1}{2}\left\{i\beta\frac{\partial}{\partial x}\left[\hat{\Psi}_H^\dagger(\mathbf{r}, \uparrow, t)\right]\hat{\Psi}_H(\mathbf{r}, \uparrow, t) - i\beta\frac{\partial}{\partial x}\left[\hat{\Psi}_H^\dagger(\mathbf{r}, \downarrow, t)\right]\hat{\Psi}_H(\mathbf{r}, \downarrow, t)\right. \\
& \left. + i\beta\hat{\Psi}_H^\dagger(\mathbf{r}, \downarrow, t)\frac{\partial}{\partial x}\hat{\Psi}_H(\mathbf{r}, \downarrow, t) - i\beta\hat{\Psi}_H^\dagger(\mathbf{r}, \uparrow, t)\frac{\partial}{\partial x}\hat{\Psi}_H(\mathbf{r}, \uparrow, t)\right\}. \quad \text{(E.28)}
\end{aligned}
$$

Equation (E.24) can be simplified

$$
\begin{aligned}
\hat{A}_3^{x,y}(\mathbf{r}, t) = & \frac{e}{2ic\hbar}\hat{A}_x^H(\mathbf{r}, t)\left\{-(i\alpha + \beta)\nu\hat{\Psi}_H^\dagger(\mathbf{r}, \uparrow, t)\hat{\Psi}_H(\mathbf{r}, \uparrow, t)\right. \\
& - (-i\alpha + \beta)\mu\hat{\Psi}_H^\dagger(\mathbf{r}, \downarrow, t)\hat{\Psi}_H(\mathbf{r}, \downarrow, t) \\
& + (i\alpha + \beta)\nu\hat{\Psi}_H^\dagger(\mathbf{r}, \downarrow, t)\hat{\Psi}_H(\mathbf{r}, \downarrow, t) \\
& \left. + (-i\alpha + \beta)\mu\hat{\Psi}_H^\dagger(\mathbf{r}, \uparrow, t)\hat{\Psi}_H(\mathbf{r}, \uparrow, t)\right\}. \quad \text{(E.29)}
\end{aligned}
$$

For S_x spin polarization, the term $\hat{A}_3^x(\mathbf{r}, t)$ is

$$
\begin{aligned}
\hat{A}_3^x(\mathbf{r}, t) = & \frac{e}{2ic\hbar}\hat{A}_x^H(\mathbf{r}, t)\left[-(i\alpha + \beta)\hat{\Psi}_H^\dagger(\mathbf{r}, \uparrow, t)\hat{\Psi}_H(\mathbf{r}, \uparrow, t)\right. \\
& - (-i\alpha + \beta)\hat{\Psi}_H^\dagger(\mathbf{r}, \downarrow, t)\hat{\Psi}_H(\mathbf{r}, \downarrow, t) \\
& \left. + (i\alpha + \beta)\hat{\Psi}_H^\dagger(\mathbf{r}, \downarrow, t)\hat{\Psi}_H(\mathbf{r}, \downarrow, t) + (-i\alpha + \beta)\hat{\Psi}_H^\dagger(\mathbf{r}, \uparrow, t)\hat{\Psi}_H(\mathbf{r}, \uparrow, t)\right] \\
= & \frac{e\alpha}{c\hbar}\hat{A}_x^H(\mathbf{r}, t)\left[-\hat{\Psi}_H^\dagger(\mathbf{r}, \uparrow, t)\hat{\Psi}_H(\mathbf{r}, \uparrow, t) + \hat{\Psi}_H^\dagger(\mathbf{r}, \downarrow, t)\hat{\Psi}_H(\mathbf{r}, \downarrow, t)\right] \quad \text{(E.30)}
\end{aligned}
$$

and for S_y spin polarization, the term $\hat{A}_3^y(\mathbf{r}, t)$ is

$$
\begin{aligned}
\hat{A}_3^y(\mathbf{r}, t) = & \frac{e}{2ic\hbar}\hat{A}_x^H(\mathbf{r}, t)\left[(\alpha - i\beta)\hat{\Psi}_H^\dagger(\mathbf{r}, \uparrow, t)\hat{\Psi}_H(\mathbf{r}, \uparrow, t)\right. \\
& + (\alpha + i\beta)\hat{\Psi}_H^\dagger(\mathbf{r}, \downarrow, t)\hat{\Psi}_H(\mathbf{r}, \downarrow, t) \\
& \left. + (-\alpha + i\beta)\hat{\Psi}_H^\dagger(\mathbf{r}, \downarrow, t)\hat{\Psi}_H(\mathbf{r}, \downarrow, t) + (-\alpha - i\beta)\hat{\Psi}_H^\dagger(\mathbf{r}, \uparrow, t)\hat{\Psi}_H(\mathbf{r}, \uparrow, t)\right] \\
= & \frac{e\beta}{c\hbar}\hat{A}_x^H(\mathbf{r}, t)\left[-\hat{\Psi}_H^\dagger(\mathbf{r}, \uparrow, t)\hat{\Psi}_H(\mathbf{r}, \uparrow, t) + \hat{\Psi}_H^\dagger(\mathbf{r}, \downarrow, t)\hat{\Psi}_H(\mathbf{r}, \downarrow, t)\right]. \quad \text{(E.31)}
\end{aligned}
$$

After performing the inverse transformation back to the Schrödinger picture, we find the contribution of Hamiltonian Eq. (E.3) of the current density operator for S_x spin polarization

$$\hat{\mathbf{j}}_3^x(\mathbf{r}) = \frac{\beta \mathbf{e}_x + \alpha \mathbf{e}_y}{2} \left[\hat{\Psi}^\dagger(\mathbf{r}, \uparrow)\hat{\Psi}(\mathbf{r}, \uparrow) + \hat{\Psi}^\dagger(\mathbf{r}, \downarrow)\hat{\Psi}(\mathbf{r}, \downarrow) \right] \tag{E.32}$$

and the y-component of the current density operator for S_y spin polarization

$$\hat{\mathbf{j}}_3^y(\mathbf{r}) = -\frac{\alpha \mathbf{e}_x + \beta \mathbf{e}_y}{2} \left[\hat{\Psi}^\dagger(\mathbf{r}, \uparrow)\hat{\Psi}(\mathbf{r}, \uparrow) + \hat{\Psi}^\dagger(\mathbf{r}, \downarrow)\hat{\Psi}(\mathbf{r}, \downarrow) \right], \tag{E.33}$$

where we have to consider all the terms $\hat{A}_1^{x,y}(\mathbf{r})$, $\hat{A}_2^{x,y}(\mathbf{r})$, $\hat{A}_3^{x,y}(\mathbf{r})$ and $\hat{A}_4^{x,y}(\mathbf{r})$. In the Schrödinger picture, the contribution of Hamiltonian Eq. (E.3) to the source operator for S_x spin polarization

$$
\begin{aligned}
\hat{s}_3^x(\mathbf{r}) = &-\frac{1}{2}\left\{ i\alpha \frac{\partial}{\partial x}\left[\hat{\Psi}^\dagger(\mathbf{r}, \uparrow)\right]\hat{\Psi}(\mathbf{r}, \uparrow) - i\alpha \frac{\partial}{\partial x}\left[\hat{\Psi}^\dagger(\mathbf{r}, \downarrow)\right]\hat{\Psi}(\mathbf{r}, \downarrow) \right. \\
&\left. + i\alpha\hat{\Psi}^\dagger(\mathbf{r}, \downarrow)\frac{\partial}{\partial x}\hat{\Psi}(\mathbf{r}, \downarrow) - i\alpha\hat{\Psi}^\dagger(\mathbf{r}, \uparrow)\frac{\partial}{\partial x}\hat{\Psi}(\mathbf{r}, \uparrow) \right\} \\
&-\frac{1}{2}\left\{ i\beta \frac{\partial}{\partial y}\left[\hat{\Psi}^\dagger(\mathbf{r}, \uparrow)\right]\hat{\Psi}(\mathbf{r}, \uparrow) - i\beta \frac{\partial}{\partial y}\left[\hat{\Psi}^\dagger(\mathbf{r}, \downarrow)\right]\hat{\Psi}(\mathbf{r}, \downarrow) \right. \\
&\left. + i\beta\hat{\Psi}^\dagger(\mathbf{r}, \downarrow)\frac{\partial}{\partial y}\hat{\Psi}(\mathbf{r}, \downarrow) - i\beta\hat{\Psi}^\dagger(\mathbf{r}, \uparrow)\frac{\partial}{\partial y}\hat{\Psi}(\mathbf{r}, \uparrow) \right\} \\
&+ \frac{e}{c\hbar}(\alpha\hat{A}_x(\mathbf{r}) + \beta\hat{A}_y(\mathbf{r}))\left[-\hat{\Psi}^\dagger(\mathbf{r}, \uparrow)\hat{\Psi}(\mathbf{r}, \uparrow) + \hat{\Psi}^\dagger(\mathbf{r}, \downarrow)\hat{\Psi}(\mathbf{r}, \downarrow)\right] \tag{E.34}
\end{aligned}
$$

and S_y spin polarization

$$
\begin{aligned}
\hat{s}_3^y(\mathbf{r}) = &-\frac{1}{2}\left\{ i\beta \frac{\partial}{\partial x}\left[\hat{\Psi}^\dagger(\mathbf{r}, \uparrow)\right]\hat{\Psi}(\mathbf{r}, \uparrow) - i\beta \frac{\partial}{\partial x}\left[\hat{\Psi}^\dagger(\mathbf{r}, \downarrow)\right]\hat{\Psi}(\mathbf{r}, \downarrow) \right. \\
&\left. + i\beta\hat{\Psi}^\dagger(\mathbf{r}, \downarrow)\frac{\partial}{\partial x}\hat{\Psi}(\mathbf{r}, \downarrow) - i\beta\hat{\Psi}_H^\dagger(\mathbf{r}, \uparrow)\frac{\partial}{\partial x}\hat{\Psi}(\mathbf{r}, \uparrow) \right\} \\
&-\frac{1}{2}\left\{ i\alpha \frac{\partial}{\partial y}\left[\hat{\Psi}^\dagger(\mathbf{r}, \uparrow)\right]\hat{\Psi}(\mathbf{r}, \uparrow) - i\alpha \frac{\partial}{\partial y}\left[\hat{\Psi}^\dagger(\mathbf{r}, \downarrow)\right]\hat{\Psi}(\mathbf{r}, \downarrow) \right. \\
&\left. + i\alpha\hat{\Psi}^\dagger(\mathbf{r}, \downarrow)\frac{\partial}{\partial y}\hat{\Psi}(\mathbf{r}, \downarrow) - i\alpha\hat{\Psi}^\dagger(\mathbf{r}, \uparrow)\frac{\partial}{\partial y}\hat{\Psi}(\mathbf{r}, \uparrow) \right\} \\
&+ \frac{e}{c\hbar}(\beta\hat{A}_x(\mathbf{r}) + \alpha\hat{A}_y(\mathbf{r}))\left[-\hat{\Psi}^\dagger(\mathbf{r}, \uparrow)\hat{\Psi}(\mathbf{r}, \uparrow) + \hat{\Psi}^\dagger(\mathbf{r}, \downarrow)\hat{\Psi}(\mathbf{r}, \downarrow)\right]. \tag{E.35}
\end{aligned}
$$

Finally, we note that the addition of the contributions of the Hamiltonian Eq. (E.1) and the Hamiltonian Eq. (E.3) yields the expression for the current density operator for S_x spin polarization Eq. (4.21) by addition of Eq. (E.14) and Eq. (E.32), the current density operator for S_y spin polarization Eq. (4.22) by addition of Eq. (E.15) and Eq. (E.33), the source operator for S_x spin polarization Eq. (4.24) by addition of Eq. (E.17) and Eq. (E.34) and the source operator for S_y spin polarization Eq. (4.25) by addition of Eq. (E.18) and Eq. (E.35).

Bibliography

[1] Heinz-Peter Breuer and Francesco Petruccione. *The theory of open quantum systems*. Oxford University Press, 2002.

[2] E. Buks, R. Schuster, M. Heiblum, D. Mahalu, and V. Umansky. Dephasing in electron interference by a 'which-path' detector. *Nature (London)*, 391:871, 1998.

[3] D. Sprinzak, E. Buks, M. Heiblum, and H. Shtrikman. Controlled dephasing of electrons via a phase sensitive detector. *Phys. Rev. Lett.*, 84:5820, 2000.

[4] A. Bertoni, P. Bordone, R. Brunetti, C. Jacoboni, and S. Reggiani. Quantum logic gates based on coherent electron transport in quantum wires. *Phys. Rev. Lett.*, 84:5912, 2000.

[5] V. Gudmundsson and C.-S. Tang. Magnetotransport in a double quantum wire: Modeling using a scattering formalism built on the lippmann-schwinger equation. *Phys. Rev. B*, 74:125302, 2006.

[6] Kensuke Kobayashi, Hisashi Aikawa, Akira Sano, Shingo Katsumoto, and Yasuhiro Iye. Fano resonance in a quantum wire with a side-coupled quantum dot. *Phys. Rev. B*, 70:035319, Jul 2004.

[7] O. Valsson, C.-S. Tang, and V. Gudmundsson. Coherent switching by detuning a side-coupled quantum-dot system. *Phys. Rev. B*, 78:165318, 2008.

[8] C. C. Eugster and J. A. del Alamo. Tunneling spectroscopy of an electron waveguide. *Phys. Rev. Lett.*, 67:3586, 1991.

[9] D. M. Schroer, A. K. Huttel, K. Eberl, S. Ludwig, M. N. Kiselev, and B. L. Altshuler. Kondo effect in a one-electron double quantum dot: Oscillations of the kondo current in a weak magnetic field. *Phys. Rev. B*, 74:233301, 2006.

[10] B. Szafran and F. M. Peeters. Time dependent simulations of electron transport through a quantum ring: effect of the lorentz force. *Phys. Rev. B*, 72:165301, 2005.

[11] Sven S. Buchholz, Saskia F. Fischer, Ulrich Kunze, Matthew Bell, Dirk Reuter, and Andreas D. Wieck. Control of the transmission phase in an asymmetric four-terminal aharonov-bohm interferometer. *Phys. Rev. B*, 82:045432, 2010.

[12] Ho-Fai Cheung, Yuval Gefen, Eberhard K. Riedel, and Wei-Heng Shih. Persistent currents in small one-dimensional metal rings. *Phys. Rev. B*, 37:6050–6062, Apr 1988.

[13] Y. Aharonov and D. Bohm. Significance of electromagnetic potentials in the quantum theory. *Phys. Rev.*, 115:485–491, Aug 1959.

[14] M. Büttiker, Y. Imry, and M. Ya. Azbel. Quantum oscillations in one-dimensional normal-metal rings. *Phys. Rev. A*, 30:1982–1989, Oct 1984.

[15] R. A. Webb, S. Washburn, C. P. Umbach, and R. B. Laibowitz. Observation of $\frac{h}{e}$ aharonov-bohm oscillations in normal-metal rings. *Phys. Rev. Lett.*, 54:2696–2699, Jun 1985.

[16] A. Tonomura, N. Osakabe, T. Matsuda, T. Kawasaki, J. Endo, S. Yano, and H. Yamada. Electron resonant tunneling through a circle-ring multicomponent quantum system. *Phys. Rev. Lett.*, 56:792, 1986.

[17] Konstantin N. Pichugin and Almas F. Sadreev. Aharanov-bohm oscillations of conductance in two-dimensional rings. *Phys Rev. B*, 56:9662, 1997.

[18] N. Byers and C. N. Yang. Theoretical considerations concerning quantized magnetic flux in superconducting cylinders. *Phys. Rev. Lett.*, 7:46–49, Jul 1961.

[19] S. Viefers, P. Koskinen, P. Singha Deo, and M. Manninen. Quantum rings for beginners: energy spectra and persistent currents. *Physica E: Low-dimensional Systems and Nanostructures*, 21(1):1 – 35, 2004.

[20] W.-C. Tan and J. C. Inkson. Magnetization, persistent currents, and their relation in quantum rings and dots. *Phys. Rev. B*, 60(8):5626, August 15 1999.

[21] Thorsten Arnold, Marc Siegmund, and Oleg Pankratov. Exact-exchange spin-density functional theory of Wigner localization and phase transitions in quantum rings. *Journal of Physics: Condensed Matter*, 23(33), AUG 24 2011.

[22] W-C Tan and J C Inkson. Electron states in a two-dimensional ring - an exactly soluble model. *Semiconductor Science and Technology*, 11(11):1635, 1996.

[23] A. Fuhrer, P. Brusheim, T. Ihn, M. Sigrist, K. Ensslin, W. Wegscheider, and M. Bichler. Fano effect in a quantum-ring-quantum-dot system with tunable coupling. *Phys. Rev. B*, 73:205326, 2006.

[24] Junsaku Nitta and Tobias Bergsten. Time reversal aharonov-casher effect using rashba spin-orbit interaction. *New Journal of Physics*, 9(9):341, 2007.

[25] Yu A Bychkov and E I Rashba. Oscillatory effects and the magnetic susceptibility of carriers in inversion layers. *Journal of Physics C: Solid State Physics*, 17(33):6039, 1984.

[26] Y. Aharonov and A. Casher. Topological quantum effects for neutral particles. *Phys. Rev. Lett.*, 53:319–321, Jul 1984.

[27] Y. Aharonov and J. Anandan. Phase change during a cyclic quantum evolution. *Phys. Rev. Lett.*, 58:1593–1596, Apr 1987.

[28] David J. Griffiths. *Introductin to Quantum Mechanics*. Pearson Education, 2005.

[29] F. Nagasawa, D. Frustaglia, H. Saarikoski, K. Richter, and J. Nitta. Control of the spin geometric phase in semiconductor quantum rings. *Nat. Commun.*, 4:2526, 2013.

[30] Stefan Filipp. *New Aspects of the Quantum Geometric Phase*. PhD thesis, Technischen Universität Wien, 2006.

[31] M. V. Berry. Quantal phase factors accompanying adiabatic changes. *Proc. R. Soc. Lond. A*, 392:45–57, 1984.

[32] Sangchul Oh and Chang-Mo Ryu. Persistent spin currents induced by the aharonov-casher effect in mesoscopic rings. *Phys. Rev. B*, 51:13441–13448, May 1995.

[33] G. Dresselhaus. Spin-orbit coupling effects in zinc blende structures. *Phys. Rev.*, 100:580–586, Oct 1955.

[34] Daniel Loss, Paul Goldbart, and A. V. Balatsky. Berry's phase and persistent charge and spin currents in textured mesoscopic rings. *Phys. Rev. Lett.*, 65:1655–1658, Sep 1990.

[35] A. V. Balatsky and B. L. Altshuler. Persistent spin and mass currents and aharonov-casher effect. *Phys. Rev. Lett.*, 70:1678–1681, Mar 1993.

[36] Alexey A. Kovalev, M. F. Borunda, T. Jungwirth, L. W. Molenkamp, and Jairo Sinova. Aharonov-casher effect in a two-dimensional hole ring with spin-orbit interaction. *Phys. Rev. B*, 76:125307, Sep 2007.

[37] Santanu K. Maiti, Moumita Dey, Shreekantha Sil, Arunava Chakrabarti, and S. N. Karmakar. Magneto-transport in a mesoscopic ring with rashba and dresselhaus spin-orbit interactions. *EPL (Europhysics Letters)*, 95(5):57008, 2011.

[38] Janine Splettstoesser, Michele Governale, and Ulrich Zülicke. Persistent current in ballistic mesoscopic rings with rashba spin-orbit coupling. *Phys. Rev. B*, 68:165341, Oct 2003.

[39] Qing-feng Sun, X. C. Xie, and Jian Wang. Persistent spin current in nanodevices and definition of the spin current. *Phys. Rev. B*, 77:035327, Jan 2008.

[40] E. B. Sonin. Proposal for measuring mechanically equilibrium spin currents in the rashba medium. *Phys. Rev. Lett.*, 99:266602, Dec 2007.

[41] J. S. Sheng and Kai Chang. Spin states and persistent currents in mesoscopic rings: Spin-orbit interactions. *Phys. Rev. B*, 74:235315, Dec 2006.

[42] Diego Frustaglia and Klaus Richter. Spin interference effects in ring conductors subject to rashba coupling. *Phys. Rev. B*, 69:235310, Jun 2004.

[43] Gao Ying-Fang, Zhang Yong-Ping, and Liang Jiu-Qing. Transport of spin-polarized current through a mesoscopic ring with two leads induced by aharonov-bohm and aharonov-casher phases. *Chinese Physics Letters*, 21(11):2093, 2004.

[44] Ya-Sha Yi, Tie-Zheng Qian, and Zhao-Bin Su. Spin precession and time-reversal symmetry breaking in quantum transport of electronsthrough mesoscopic rings. *Phys. Rev. B*, 55:10631–10637, Apr 1997.

[45] A. G. Aronov and Y. B. Lyanda-Geller. Spin-orbit berry phase in conducting rings. *Phys. Rev. Lett.*, 70:343–346, Jan 1993.

[46] X. F. Wang and P. Vasilopoulos. Spin-dependent magnetotransport through a mesoscopic ring in the presence of spin-orbit interaction. *Phys. Rev. B*, 72:165336, Oct 2005.

[47] C. S. Tang and C. S. Chu. Quantum transport in the presence of a finite-range time-modulated potential. *Phys. Rev. B*, 53:4838, 1996.

[48] M. Ahsan Zeb, K. Sabeeh, and M. Tahir. Chiral tunneling through a time-periodic potential in monolayer graphene. *Phys. Rev B*, 78:165420, 2008.

[49] Diego Kienle and François Léonard. Terahertz response of carbon nanotube transistors. *Phys. Rev. Lett.*, 103:026601, 2009.

[50] Chi-Shung Tang, Kristinn Torfason, and Vidar Gudmundsson. Magnetotransport in a time-modulated double quantum point contact system. *Computer Physics Communications*, 182:65, 2011.

[51] C. S. Tang and C. S. Chu. Coherent quantum transport in narrow constrictions in the presence of a finite-range longitudinally polarized time-dependent field. *Phys. Rev. B*, 60:1830, 1999.

[52] Guanghui Zhou and Yuan Li. Floquet scattering approach to electron transport for a quantum wire under longitudinally polarized electromagnetic field irradiation. *J. Phys.: Condens. Matter*, 17:6663, 2005.

[53] Jin-Wook Jung, Kyungsun Na, and L. E. Reichl. Scattering from radiation-induced entangled states. *Phys. Rev. A*, 85:023420, 2012.

[54] C. S. Tang and C. S. Chu. Coherent quantum transport in the presence of a finite-range transversely polarized time-dependent field. *Physica B*, 292:127, 2000.

[55] Guanghui Zhou, Mou Yang, Xianbo Xiao, and Yuan Li. Electronic transport in a quantum wire under external terahertz electromagnetic irradiation. *Phys. Rev. B*, 68:155309, 2003.

[56] Petri Myöhänen, Adrian Stan, Gianluca Stefanucci, and Robert van Leeuwen. Kadanoff-baym approach to quantum transport through interacting nanoscale systems: From the transient to the steady-state regime. *Phys. Rev. B*, 80:115107, 2009.

[57] Gianluca Stefanucci, Enrico Perfetto, and Michele Cini. Time-dependent quantum transport with superconducting leads: A discrete-basis kohn-sham formulation and propagation scheme. *Phys. Rev. B*, 81:115446, 2010.

[58] M. Tahir and A. MacKinnon. Time-dependent quantum transport in a resonant tunnel junction coupled to a nanomechanical oscillator. *Phys. Rev. B*, 81:195444, 2010.

[59] Po-Wen Chen, Chung-Chin Jian, and Hsi-Sheng Goan. Non-markovian dynamics of a nanomechanical resonator measured by a quantum point contact. *Phys. Rev. B*, 83:115439, 2011.

[60] S. A. Gurvitz and Ya. S. Prager. Microscopic derivation of rate equations for quantum transport. *Phys. Rev. B*, 53:15932, 1996.

[61] N. G. van Kampen. *Stochastic Processes in Physics and Chemistry*. North-Holland, Amsterdam, 2nd ed. edition, 2001.

[62] U. Harbola, M. Esposito, and S. Mukamel. Quantum master equation for electron transport through quantum dots and single molecules. *Phys. Rev. B*, 74:235309, 2006.

[63] Herbert Walther, Benjamin T H Varcoe, Berthold-Georg Englert, and Thomas Becker. Cavity quantum electrodynamics. *Reports on Progress in Physics*, 69(5):1325, 2006.

[64] R Miller, T E Northup, K M Birnbaum, A Boca, A D Boozer, and H J Kimble. Trapped atoms in cavity qed: coupling quantized light and matter. *Journal of Physics B: Atomic, Molecular and Optical Physics*, 38(9):S551, 2005.

[65] A. Mehdizadeh Khasraghi, S. Shojaei, A. Soltani Vala, and M. Kalafi. Coupling effects in a photonic crystal microcavity with embedded semiconductor quantum dot. *Physica E*, 47:17, 2013.

[66] A. Matos-Abiague and J. Berakdar. Photoinduced charge currents in mesoscopic rings. *Phys. Rev. Lett.*, 94:166801, Apr 2005.

[67] Yuriy V. Pershin and Carlo Piermarocchi. Laser-controlled local magnetic field with semiconductor quantum rings. *Phys. Rev. B*, 72:245331, Dec 2005.

[68] O. V. Kibis. Dissipationless electron transport in photon-dressed nanostructures. *Phys. Rev. Lett.*, 107:106802, Aug 2011.

[69] O. V. Kibis, O. Kyriienko, and I. A. Shelykh. Persistent current induced by vacuum fluctuations in a quantum ring. *Phys. Rev. B*, 87:245437, Jun 2013.

[70] Marian Nita, D. C. Marinescu, Andrei Manolescu, and Vidar Gudmundsson. Nonadiabatic generation of a pure spin current in a one-dimensional quantum ring with spin-orbit interaction. *Phys. Rev. B*, 83:155427, Apr 2011.

[71] Zhen-Gang Zhu and Jamal Berakdar. Electromagnetic pulse-driven spin-dependent currents in semiconductor quantum rings. *Journal of Physics: Condensed Matter*, 21(14):145801, 2009.

[72] Zhen-Gang Zhu and Jamal Berakdar. Photoinduced nonequilibrium spin and charge polarization in quantum rings. *Phys. Rev. B*, 77:235438, Jun 2008.

[73] A. S. Moskalenko and J. Berakdar. Polarized light bursts from kicked quantum rings. *Phys. Rev. A*, 78:051804, Nov 2008.

[74] Yan Xie, Weidong Chu, and Suqing Duan. Magnetic-field-modulated terahertz absorption spectra of a quantum ring. *Applied Physics Letters*, 93(2):023104, 2008.

[75] S. D. Ganichev, E. L. Ivchenko, S. N. Danilov, J. Eroms, W. Wegscheider, D. Weiss, and W. Prettl. Conversion of spin into directed electric current in quantum wells. *Phys. Rev. Lett.*, 86:4358–4361, May 2001.

[76] G. F. Quinteiro and J. Berakdar. Electric currents induced by twisted light in quantum rings. *Opt. Express*, 17(22):20465–20475, Oct 2009.

[77] E Räsänen, A. Castro, J. Werschnik, A. Rubio, and E. K. U. Gross. Optimal control of quantum rings by terahertz laser pulses. *Phys. Rev. Letters*, 98:157404, 2007.

[78] Olafur Jonasson, Chi-Shung Tang, Hsi-Sheng Goan, Andrei Manolescu, and Vidar Gudmundsson. Quantum magneto-electrodynamics of electrons embedded in a photon cavity. *New Journal of Physics*, 14(1):013036, 2012.

76

[79] E.T. Jaynes and F. W. Cummings. Comparison of quantum and semiclassical radiation theories with application to the beam maser. *Proceedings of the IEEE*, 51(1):89–109, 1963.

[80] Ying Wu and Xiaoxue Yang. Strong-coupling theory of periodically driven two-level systems. *Phys. Rev. Lett.*, 98:013601, Jan 2007.

[81] Andrew T. Sornborger, Andrew N. Cleland, and Michael R. Geller. Superconducting phase qubit coupled to a nanomechanical resonator: Beyond the rotating-wave approximation. *Phys. Rev. A*, 70:052315, Nov 2004.

[82] H. Spohn. Kinetic equations from hamiltonian dynamics: Markovian limits. *Rev. Mod. Phys.*, 52:569, 1980.

[83] Vidar Gudmundsson, Cosmin Gainar, Chi-Shung Tang, Valeriu Moldoveanu, and Andrei Manolescu. Time-dependent transport via the generalized master equation through a finite quantum wire with an embedded subsystem. *New Journal of Physics*, 11(11):113007, 2009.

[84] Vidar Gudmundsson, Chi-Shung Tang, Olafur Jonasson, Valeriu Moldoveanu, and Andrei Manolescu. Correlated time-dependent transport through a two-dimensional quantum structure. *Phys. Rev. B*, 81:205319, 2010.

[85] M. Helm. *Intersubband Transitions in Quantum Wells: Physics and Device Applications I.* Academic Press, 2000.

[86] Alon Gabbay, John Reno, Joel R. Wendt, Aaron Gin, Michael C. Wanke, Michael B. Sinclair, Eric Shaner, and Igal Brener. Interaction between metamaterial resonators and intersubband transitions in semiconductor quantum wells. *Appl. Phys. Lett.*, 98:203103, 2011.

[87] Cristiano Ciuti, Gérald Bastard, and Iacopo Carusotto. Quantum vacuum properties of the intersubband cavity polariton field. *Phys. Rev. B*, 72:115303, 2005.

[88] M. Devoret, S. Girvin, and R. Schoelkopf. Circuit-qed: How strong can the coupling between a josephson. *Ann. Phys.*, 16:767, 2007.

[89] Abdufarrukh A. Abdumalikov, Oleg Astafiev, Yasunobu Nakamura, Yuri A. Pashkin, and Jaw Shen Tsai. Vacuum rabi splitting due to strong coupling of a flux qubit and a coplanar-waveguide resonator. *Phys. Rev. B*, 78:180502(R), 2008.

[90] F. De Zela, E. Solano, and A. Gago. Micromaser without the rotating-wave approximation: The bloch-siegert shift and related effects. *Optics Communications*, 142:106, 1997.

[91] E. K. Irish. Generalized rotating-wave approximation for arbitrarily large coupling. *Phys. Rev. Lett.*, 99:173601, 2007.

[92] C. Bruder and H. Schoeller. Charging effects in ultrasmall quantum dots in the presence of time-varing fields. *Phys. Rev. Lett.*, 72:1076–1079, Feb 1994.

[93] A. Braggio, J. König, and R. Fazio. Full counting statistics in strongly interacting systems: Non-markovian effects. *Phys. Rev. Lett.*, 96:026805, 2006.

[94] Valeriu Moldoveanu, Andrei Manolescu, and Vidar Gudmundsson. Geometrical effects and signal delay in time-dependent transport at the nanoscale. *New Journal of Physics*, 11(7):073019, 2009.

[95] Heinz-Peter Breuer, Bernd Kappler, and Francesco Petruccione. Stochastic wave-function method for non-markovian quantum master equations. *Phys. Rev. A*, 59:1633–1643, Feb 1999.

[96] Thorsten Arnold, Chi-Shung Tang, Andrei Manolescu, and Vidar Gudmundsson. Magnetic-field-influenced nonequilibrium transport through a quantum ring with correlated electrons in a photon cavity. *Phys. Rev. B*, 87:035314, Jan 2013.

[97] R. Graham and F. Haake. *Quantum Statistics in Optics and Solid-State Physics*. Springer, 1973.

[98] I. Knezevic and B. Novakovic. Time-dependent transport in open systems based on quantum master equations. *Journal of Computational Electronics*, 12(3):363–374, 2013.

[99] S. Nakajima. On quantum theory of transport phenomena. *Prog. Theor. Phys.*, 20:948, 1958.

[100] R. Zwanzig. Ensemble method in the theory of irreversibility. *J. Chem. Phys.*, 33:1338, 1960.

[101] Vidar Gudmundsson, Olafur Jonasson, Chi-Shung Tang, Hsi-Sheng Goan, and Andrei Manolescu. Time-dependent transport of electrons through a photon cavity. *Phys. Rev. B*, 85:075306, 2012.

[102] Vidar Gudmundsson, Cosmin Gainar, Chi-Shung Tang, Valeriu Moldoveanu, and Andrei Manolescu. Time-dependent transport via the generalized master equation through a finite quantum wire with an embedded subsystem. *New Journal of Physics*, 11(11):113007, 2009.

[103] Roland Winkler. *Spin-orbit coupling effects in two-dimensional electron and hole systems*. Springer, 2003.

[104] Olafur Jonasson. Nonperturbative approach to circuit quantum electrodynamics. Master's thesis, School of Engineering and Natural Sciences, University of Iceland, 2012.

[105] Federico Bottegoni, Henri-Jean Drouhin, Guy Fishman, and Jean-Eric Wegrowe. Probability- and spin-current operators for effective hamiltonians. *Phys. Rev. B*, 85:235313, Jun 2012.

[106] Thorsten Arnold, Chi-Shung Tang, Andrei Manolescu, and Vidar Gudmundsson. Effects of geometry and linearly polarized cavity photons on charge and spin currents in a quantum ring with spin-orbit interactions. *The European Physical Journal B*, 87(5):1–20, 2014.

[107] I. S. Gradshteyn and I. M. Ryshik, editors. *Table of Integrals, Series and Products*. Academic Press, Florida, 1982.

[108] W. Heitler. *The Quantum Theory of Radiation*. Oxford University Press, 1984.

Magnetic-field-influenced nonequilibrium transport through a quantum ring with correlated electrons in a photon cavity

Thorsten Arnold,[1,*] Chi-Shung Tang,[2,†] Andrei Manolescu,[3] and Vidar Gudmundsson[1,‡]

[1]*Science Institute, University of Iceland, Dunhaga 3, IS-107 Reykjavik, Iceland*
[2]*Department of Mechanical Engineering, National United University, 1, Lienda, Miaoli 36003, Taiwan*
[3]*Reykjavik University, School of Science and Engineering, Menntavegur 1, IS-101 Reykjavik, Iceland*

We investigate magnetic-field-influenced time-dependent transport of Coulomb interacting electrons through a two-dimensional quantum ring in an electromagnetic cavity under nonequilibrium conditions described by a time-convolutionless non-Markovian master equation formalism. We take into account the full electromagnetic interaction of electrons and cavity photons. A bias voltage is applied to semi-infinite leads along the x axis, which are connected to the quantum ring. The magnetic field is tunable to manipulate the time-dependent electron transport coupled to a photon field with either x or y polarization. We find that the lead-system-lead current is strongly suppressed by the y-polarized photon field at magnetic field with two flux quanta due to a degeneracy of the many-body energy spectrum of the mostly occupied states. On the other hand, the lead-system-lead current can be significantly enhanced by the y-polarized field at magnetic field with half-integer flux quanta. Furthermore, the y-polarized photon field perturbs the periodicity of the persistent current with the magnetic field and suppresses the magnitude of the persistent current. The spatial and temporal density distributions reflect the characteristics of the many-body spectrum. The vortex formation in the contact areas to the leads influences the charge circulation in the ring.

I. INTRODUCTION

Quantum interference phenomena are essential when developing quantum devices. Quantum confined geometries conceived for such studies may consist of which-path interferometers,[1,2] coupled quantum wires,[3,4] side-coupled quantum dots,[5,6] or quantum rings.[7,8] These coupled quantum systems have captured interest due to their potential applications in electronic spectroscopy tools[9] and quantum information processing.[10] Furthermore, the magnetic flux through the ring system can drive persistent currents[11] and lead to the topological quantum interference phenomenon known as the Aharonov-Bohm (AB) effect.[12–16] Both, the persistent current and ring conductance show characteristic oscillations with period of one flux quantum, $\Phi_0 = hc/e$. The free spectrum of the one-dimensional quantum ring exhibits level crossings at half-integer and integer multiples of Φ_0.[17,18] The persistent current dependence on the magnetic field[19] and electron-electron interaction strength[20] has been investigated adopting a two-dimensional quantum ring model with analytically known noninteracting properties.[21] Varying either the magnetic field or the electrostatic confining potentials allows the quantum interference to be tuned.[22]

There has been considerable interest in the study of electronic transport through a quantum system in a strong system-lead coupling regime driven by periodic time-dependent potentials,[23–26] longitudinally polarized fields,[27–29] or transversely polarized fields.[30,31] On the other hand, quantum transport driven by a transient time-dependent potential enables development of switchable quantum devices, in which the interplay of the electronic system with external perturbation plays an important role.[32–35] These systems are usually operated in the weak system-lead coupling regime and described within the wide-band or the Markovian approximation.[36–38] Within this approximation, the energy dependence of the electron tunneling rate or the memory effect in the system are neglected by assuming that the correlation time of the electrons in the leads is much shorter than the typical response time of the central system. However, the transient transport is intrinsically linked to the coherence and relaxation dynamics and cannot generally be described in the Markovian approximation. The energy-dependent spectral density in the leads has to be included for accurate numerical calculation.

In order to explicitly explore the transport dynamics with the electron-photon coupling and the transient system-lead coupling, a non-Markovian density-matrix formalism involving the energy-dependent coupled elements should be considered based on the generalized master equation (GME).[39–42] How to appropriately describe the carrier dynamics under nonequilibrium conditions with realistic device geometries is a challenging problem.[43,44] More recently, manipulation of electron-photon coupled quantum systems embedded in an electromagnetic cavity has become one of the most promising applications in quantum information processing devices. Utilizing the giant dipole moments of intersubband transitions in quantum wells[45,46] enables researchers to reach the ultrastrong electron-photon coupling regime.[47–49] In this regime, the dynamical electron-photon coupling mechanism has to be explored beyond the wide-band and rotating-wave approximations.[50–52] Nevertheless, time-dependent transport of Coulomb interacting electrons through a topologically nontrivial broad ring geometry in an electromagnetic cavity with quantized photon modes remains unexplored beyond the Markovian approximation.

In the present work, we explore the transient effects of electronic transport through a broad quantum ring in a linearly polarized electromagnetic cavity coupled to electrically biased leads. This electron-photon coupled system under investigation can be manipulated by tuning the applied magnetic field and the polarization of the photon field. A time-convolutionless

(TCL) version of the GME is utilized to project the time evolution onto the central system by taking trace with respect to the operators in the leads.[53–55] We demonstrate the transient transport properties by showing the many-body (MB) energy spectra, the time-dependence of the electric charge, the magnetic-field dependence of the total charge current with (w) or without (w/o) photon cavity, the charge density distribution, the normalized current density distribution and the local current coming from an occupation redistribution of the MB states in the central quantum ring system.

The paper is organized as follows. In Sec. II, the theoretical model is described. The electron system is embedded in an electromagnetic cavity by coupling a many-level electron system with photons using the full photon energy spectrum of a single cavity mode. In Sec. III, we show the numerical results for the dynamical transient transport properties for different magnetic field and photon field polarization. The influence of the photon field polarization on the magnetic field dependence of the lead-system-lead and persistent current is illustrated in detail and connected with the properties of the many-body spectrum. It is further shown how the photon field influenced many-body spectrum affects the spatial charge arrangement and flow inside the ring. Concluding remarks will be presented in Sec. IV.

II. MODEL AND THEORY

In this section, we describe the central system potential V_S for the broad quantum ring and its connection to the leads. The electronic ring system is embedded in an electromagnetic cavity by coupling a many-level electron system with photons using the full photon energy spectrum of a single cavity mode. The central ring system is described by an MB system Hamiltonian $\hat{H}_S$ with a uniform perpendicular magnetic field in which the electron-electron interaction and the electron-photon coupling to the x- or y-polarized photon field is explicitly taken into account. We employ the TCL-GME approach to explore the nonequilibrium electronic transport when the system is coupled to leads by a transient switching potential.

A. Quantum ring connected to leads

The system under investigation is a broad quantum ring connected to left and right leads $l \in \{L, R\}$ with identical parabolic confining potentials

$$V_l(\mathbf{r}) = \tfrac{1}{2} m^* \Omega_0^2 y^2 \tag{1}$$

in which the characteristic energy of the confinement is $\hbar\Omega_0 = 1.0\,\text{meV}$ and $m^* = 0.067 m_e$ is the effective mass of an electron in GaAs-based material.

The quantum ring is embedded in the central system of length $L_x = 300$ nm situated between two contact areas that will be coupled to the external leads, as is depicted in Fig. 1. The system potential is described by

$$V_S(\mathbf{r}) = \sum_{i=1}^{6} V_i \exp\{-[\beta_{xi}(x - x_0)]^2 - (\beta_{yi} y)^2\} + \tfrac{1}{2} m^* \Omega_0^2 y^2, \tag{2}$$
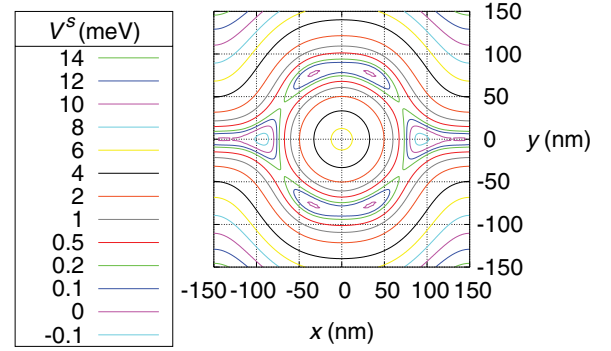
with parameters from Table I.

FIG. 1. (Color online) Equipotential lines in the central ring system connected to the left and right leads. Note that the isolines are refined close to the bottom of the ring structure.

B. Central system Hamiltonian

The time evolution of the closed system with respect to $t = 0$,

$$\hat{U}_S(t) = \exp\left(-\frac{i}{\hbar} \hat{H}_S t\right), \tag{3}$$

is governed by the MB system Hamiltonian[56]

$$\hat{H}_S = \int d^2r\, \hat{\psi}^\dagger(\mathbf{r}) \left[\frac{1}{2m^*} \left\{ \frac{\hbar}{i}\nabla + \frac{e}{c}[\mathbf{A}(\mathbf{r}) + \hat{\mathbf{A}}^{\text{ph}}(\mathbf{r})] \right\}^2 \right.$$
$$\left. + V_S(\mathbf{r}) \right] \hat{\psi}(\mathbf{r}) + \hat{H}_{\text{ee}} + \hbar\omega \hat{a}^\dagger \hat{a}. \tag{4}$$

The first term includes a constant magnetic field $\mathbf{B} = B\hat{z}$, in Landau gauge being represented by $\mathbf{A}(\mathbf{r}) = -By\hat{x}$. The second term is the exactly treated electron-electron interaction

$$\hat{H}_{\text{ee}} = \int d^2r \int d^2r' \hat{\psi}^\dagger(\mathbf{r})\hat{\psi}^\dagger(\mathbf{r}') V_{\text{ee}}(\mathbf{r},\mathbf{r}')\hat{\psi}(\mathbf{r}')\hat{\psi}(\mathbf{r}), \tag{5}$$

where

$$V_{\text{ee}}(\mathbf{r},\mathbf{r}') = \frac{e^2}{2\kappa\sqrt{|\mathbf{r} - \mathbf{r}'|^2 + \eta^2}} \tag{6}$$

with $e > 0$ being the magnitude of the electron charge and $\eta = 1.0 \times 10^{-15}$ nm being a numerical regularization parameter. In addition, the last term in Eq. (4) indicates the quantized photon field, where $\hat{a}$ and $\hat{a}^\dagger$ are the photon annihilation and creation operators, respectively, and $\hbar\omega$ is the photon excitation energy. The photon field interacts with the electron system via the vector potential

$$\hat{\mathbf{A}}^{\text{ph}}(\mathbf{r}) = A(\hat{a} + \hat{a}^\dagger) \begin{cases} \mathbf{e}_x, & \text{TE}_{011}, \\ \mathbf{e}_y, & \text{TE}_{101}, \end{cases} \tag{7}$$

TABLE I. Parameters of the central region ring potential.

i	V_i (meV)	β_{xi} (nm^{-1})	x_0 (nm)	β_{yi} (nm^{-1})
1	9.6	0.014	150	0
2	9.6	0.014	−150	0
3	11.1	0.0165	0	0.0165
4	−4.7	0.02	149	0.02
5	−4.7	0.02	−149	0.02
6	−4.924	0	0	0

for a longitudinally polarized (x-polarized) photon field (TE$_{011}$) or a transversely polarized (y-polarized) photon field (TE$_{101}$). The electron-photon coupling constant $g^{\text{EM}} = eAa_w\Omega_w/c$ scales with the amplitude A of the electromagnetic field. For reasons of comparison, we also consider results without photons in the system. In this case, $\hat{\mathbf{A}}^{\text{ph}}(\mathbf{r})$ and $\hbar\omega\hat{a}^\dagger\hat{a}$ drop out from the MB system Hamiltonian in Eq. (4).

C. Time-convolutionless generalized master equation approach

The TCL-GME[55] is an alternative non-Markovian master equation to the Nakajima-Zwanzig (NZ) equation,[57–60] which is *local* in time. We assume that the initial total statistical density matrix can be written as a product of the system and leads density matrices, before switching on the coupling to the leads,

$$\hat{W}(0) = \hat{\rho}_L \otimes \hat{\rho}_R \otimes \hat{\rho}_S(0), \qquad (8)$$

with ρ_l, $l \in \{L,R\}$, being the normalized density matrices of the leads. The coupling Hamiltonian between the central system and the leads reads

$$\hat{H}_T(t) = \sum_{l=L,R} \int dq \, \chi^l(t)[\hat{\mathfrak{T}}^l(q)\hat{C}_{ql} + \hat{C}_{ql}^\dagger\hat{\mathfrak{T}}^{l\dagger}(q)]. \quad (9)$$

Here, $\hat{C}_{ql}^\dagger$ is the electron creation operator for state q and lead l and

$$\hat{\mathfrak{T}}^l(q) = \sum_{\alpha\beta} |\alpha)(\beta| \sum_a T_{qa}^l(\alpha|\hat{C}_a^\dagger|\beta) \qquad (10)$$

with the creation operator $\hat{C}_a^\dagger$ for the single-electron state (SES) a in the central system, i.e., the eigenstate a of the first term of Eq. (4) with $\hat{\mathbf{A}}^{\text{ph}}(\mathbf{r}) = 0$. The coupling is switched on at $t = 0$ via the switching function

$$\chi^l(t) = 1 - \frac{2}{e^{\alpha^l t} + 1} \qquad (11)$$

with switching parameter α^l. Equation (10) is written in the system Hamiltonian MB eigenbasis $\{|\alpha)\}$. The coupling tensor[56]

$$T_{qa}^l = \int_{\Omega_S^l} d^2r \int_{\Omega_l} d^2r' \, \psi_{ql}^*(\mathbf{r}') g_{aq}^l(\mathbf{r},\mathbf{r}')\psi_a^S(\mathbf{r}) \qquad (12)$$

couples the extended lead SES $\{\psi_{ql}(\mathbf{r})\}$ with energy spectrum $\{\epsilon^l(q)\}$ to the system SES $\{\psi_a^S(\mathbf{r})\}$ with energy spectrum $\{E_a\}$ that reach into the contact regions,[59] Ω_S^l and Ω_l, of system and lead l, respectively, and

$$g_{aq}^l(\mathbf{r},\mathbf{r}') = g_0^l \exp[-\delta_x^l(x-x')^2 - \delta_y^l(y-y')^2]$$
$$\times \exp\left[-\frac{|E_a - \epsilon^l(q)|}{\Delta_E^l}\right]. \qquad (13)$$

Here, g_0^l is the lead coupling strength. In addition, δ_x^l and δ_y^l are the contact region parameters for lead l in x and y directions, respectively. Moreover, Δ_E^l denotes the affinity constant between the central system SES energy levels $\{E_a\}$ and the lead energy levels $\{\epsilon^l(q)\}$.

In this work, we derive the TCL-GME[55] in the Schrödinger picture. In this picture, the reduced density operator (RDO) of

the system,

$$\hat{\rho}_S(t) = \text{Tr}_L\text{Tr}_R[\hat{W}(t)], \qquad (14)$$

evolves to second order in the lead coupling strength in time via

$$\dot{\hat{\rho}}_S(t) = -\frac{i}{\hbar}[\hat{H}_S, \hat{\rho}_S(t)] - \left[\sum_{l=L,R}\int dq \, (\hat{\mathfrak{T}}^l(q), \hat{\Omega}^l(q,t)\hat{\rho}_S(t)\right.$$
$$\left. - f[\epsilon^l(q)]\{\hat{\rho}_S(t), \hat{\Omega}^l(q,t)\}) + \text{H.c.}\right] \qquad (15)$$

with

$$\hat{\Omega}^l(q,t) = \frac{1}{\hbar^2}\chi^l(t)\exp\left[-\frac{i}{\hbar}t\epsilon^l(q)\right]\hat{U}_S(t)\hat{\Pi}^l(q,t)\hat{U}_S^\dagger(t), \qquad (16)$$

$$\hat{\Pi}^l(q,t) = \int_0^t dt' \left\{\exp\left[\frac{i}{\hbar}t'\epsilon^l(q)\right]\chi^l(t')\hat{U}_S^\dagger(t')\hat{\mathfrak{T}}^{l\dagger}(q)\hat{U}_S(t')\right\}, \qquad (17)$$

and $f(E)$ being the Fermi distribution function.

Comparing this equation to the corresponding NZ equation,[57–60]

$$\dot{\hat{\rho}}_S^{\text{NZ}}(t) = -\frac{i}{\hbar}[\hat{H}_S, \hat{\rho}_S^{\text{NZ}}(t)]$$
$$- \left\{\sum_{l=L,R}\int dq \, [\hat{\mathfrak{T}}^l(q), \hat{\Omega}^l(q,t)] + \text{H.c.}\right\} \quad (18)$$

with

$$\hat{\Omega}^l(q,t) = \frac{1}{\hbar^2}\chi^l(t)\hat{U}_S(t)\int_0^t dt' \left\{\exp\left[\frac{i}{\hbar}(t'-t)\epsilon^l(q)\right]\right.$$
$$\left. \times \chi^l(t')\hat{\Pi}^l(q,t')\right\}\hat{U}_S^\dagger(t) \qquad (19)$$

and

$$\hat{\Pi}^l(q,t') = \hat{U}_S^\dagger(t')(\hat{\mathfrak{T}}^{l\dagger}(q)\hat{\rho}_S^{\text{NZ}}(t')$$
$$- f[\epsilon^l(q)]\{\hat{\rho}_S^{\text{NZ}}(t'), \hat{\mathfrak{T}}^{l\dagger}(q)\})\hat{U}_S(t'), \qquad (20)$$

we note that we reobtain the TCL equation, if we set

$$\hat{\rho}_S^{\text{NZ}}(t') = \hat{U}_S^\dagger(t-t')\hat{\rho}_S(t)\hat{U}_S(t-t'), \qquad (21)$$

in Eq. (20) [which enters the kernel of Eq. (18)], but let $\hat{\rho}_S^{\text{NZ}}(t) = \hat{\rho}_S(t)$ in the first term of Eq. (18). In other words, in the Schrödinger picture, the NZ kernel takes the central system time propagated RDO (which lets it become convoluted), while the TCL kernel takes just the unpropagated RDO. The deviation between the two approaches is therefore only of relevance when the central system is far from a steady state and when the coupling to the leads is strong. It is our experience that the positivity conditions[61] for the MB state occupation probabilities in the RDO are satisfied to a higher system-lead coupling strength in the TCL case. The more involved quantum structure demands a stronger system-lead coupling than in our earlier work.[56] The numerical effort of the two approaches is of similar magnitude. Both cases allow for a t-independent inner time integral over t', which can be integrated successively

with increasing t (increasing integration domain).[62] The RDO is inside (NZ) or outside (TCL) of the inner time integral, but the required number of matrix multiplications is equal.

III. NONEQUILIBRIUM TRANSPORT PROPERTIES

In this section, we investigate the nonequilibrium electron transport properties through a quantum ring system, which is situated in a photon cavity and weakly coupled to leads. We assume GaAs-based material with electron effective mass $m^* = 0.067 m_e$ and background relative dielectric constant $\kappa = 12.4$. We consider a single cavity mode with fixed photon excitation energy $\hbar\omega = 0.4$ meV. The electron-photon coupling constant in the central system is $g^{\mathrm{EM}} = 0.1$ meV. Before switching on the coupling, we assume the central system to be in the pure initial state with electron occupation number $N_{e,\mathrm{init}} = 0$ and photon occupation number $N_{\mathrm{ph,init}} = 1$ of the electromagnetic field.

An external perpendicular uniform magnetic field is applied through the central ring system and the lead reservoirs. The area of the central ring system is $A \approx 2 \times 10^4$ nm^2 so that the magnetic field corresponding to the flux quantum Φ_0 is $B_0 = \Phi_0/A \approx 0.2$ T. The temperature of the reservoirs is assumed to be $T = 0.5$ K. The chemical potentials in the leads are $\mu_L = 2$ meV and $\mu_R = 0.9$ meV leading to a source-drain bias window $\Delta\mu = 1.1$ meV. We let the affinity constant $\Delta_E^l = 0.25$ meV to be close to the characteristic electronic excitation energy in x direction. In addition, we let the contact region parameters for lead $l \in \{L,R\}$ in x and y directions be $\delta_x^l = \delta_y^l = 4.39 \times 10^{-4}$ nm^{-2}. The system-lead coupling strength $g_0^l = 0.2058$ meV nm$^{-3/2}$.

There are several relevant length and time scales that should be mentioned. The two-dimensional magnetic length is $l = [c\hbar/(eB)]^{1/2} = 25.67[B(\mathrm{T})]^{-1/2}$ nm. The ring system is parabolically confined in the y direction with characteristic energy $\hbar\Omega_0 = 1.0$ meV leading to a modified magnetic length scale

$$
\begin{aligned}
a_w &= \left(\frac{\hbar}{m^*\Omega_0}\right)^{1/2} \frac{1}{\sqrt[4]{1 + [eB/(m^* c\Omega_0)]^2}} \\
&= \frac{33.74}{\sqrt[4]{1 + 2.982[B(\mathrm{T})]^2}} \text{ nm}.
\end{aligned} \tag{22}
$$

Correspondingly, the system-lead coupling strength is then $g_0^l a_w^{3/2} = 39.85$ meV for magnetic field $B = 0.1$ T and $g_0^l a_w^{3/2} = 38.22$ meV for magnetic field $B = 0.225$ T. The time scale for the switching on of the system-lead coupling is $(\alpha^l)^{-1} = 3.291$ ps, the single-electron state (1ES) charging time scale $\tau_{\mathrm{1ES}} \approx 30$ ps, and the two-electron state (2ES) charging time scale $\tau_{\mathrm{2ES}} \gg 200$ ps described in the sequential tunneling regime. We study the transport properties for $0 \leqslant t < \tau_{\mathrm{2ES}}$, when the system has not yet reached a steady state.

In order to understand the nonequilibrium dynamical behavior of the charge distribution in the system, we define the time-dependent magnitude of charge on the left part ($x < 0$) of the ring,

$$
Q_S^L(t) = \int_{-\frac{L_x}{2}}^{0} dx \int_{-\infty}^{\infty} dy \, \rho(\mathbf{r},t), \tag{23}
$$

and the time-dependent magnitude of charge on the right part ($x > 0$) of the ring

$$
Q_S^R(t) = \int_{0}^{\frac{L_x}{2}} dx \int_{-\infty}^{\infty} dy \, \rho(\mathbf{r},t). \tag{24}
$$

The space- and time-dependent charge density,

$$
\rho(\mathbf{r},t) = \mathrm{Tr}[\hat{\rho}_S(t)\hat{\rho}(\mathbf{r})], \tag{25}
$$

is the expectation value of the charge density operator

$$
\hat{\rho}(\mathbf{r}) = e\hat{\psi}^\dagger(\mathbf{r})\hat{\psi}(\mathbf{r}). \tag{26}
$$

In order to explore the magnetic field influence on the charge currents from and into the leads, we define the charge current from the left lead into the system by

$$
I_L(t) = \mathrm{Tr}[\dot{\rho}_S^L(t)\hat{Q}]. \tag{27}
$$

Here, $\hat{Q} = e\hat{N}$ is the charge operator with number operator $\hat{N}$ and the time derivative of the RDO in the MB basis due to the coupling to the lead $l \in \{L,R\}$:

$$
\dot{\rho}_S^l(t) = \int dq \, [\mathfrak{T}^l(q), (\Omega^l(q,t)\rho_S(t) \\
- f[\epsilon^l(q)]\{\rho_S(t),\Omega^l(q,t)\})] + \mathrm{H.c.}. \tag{28}
$$

Similarly, the charge current from the system into the right lead can be expressed as

$$
I_R(t) = -\mathrm{Tr}[\dot{\rho}_S^R(t)\hat{N}]. \tag{29}
$$

To get more insight into the local current flow in the ring system, we define the top local charge current through the upper arm ($y > 0$) of the ring

$$
I_{\mathrm{top}}(t) = \int_{0}^{\infty} dy \, j_x(x=0,y,t) \tag{30}
$$

and the bottom local charge current through the lower arm ($y < 0$) of the ring

$$
I_{\mathrm{bottom}}(t) = \int_{-\infty}^{0} dy \, j_x(x=0,y,t). \tag{31}
$$

Here, the charge current density,

$$
\mathbf{j}(\mathbf{r},t) = \begin{pmatrix} j_x(\mathbf{r},t) \\ j_y(\mathbf{r},t) \end{pmatrix} = \mathrm{Tr}[\hat{\rho}_S(t)\hat{\mathbf{j}}(\mathbf{r})], \tag{32}
$$

is given by the expectation value of the charge current density operator,

$$
\hat{\mathbf{j}}(\mathbf{r}) = \hat{\mathbf{j}}_p(\mathbf{r}) + \hat{\mathbf{j}}_d(\mathbf{r}), \tag{33}
$$

decomposed into the paramagnetic charge current density operator,

$$
\hat{\mathbf{j}}_p(\mathbf{r}) = \frac{e\hbar}{2mi}\{\hat{\psi}^\dagger(\mathbf{r})[\nabla\hat{\psi}(\mathbf{r})] - [\nabla\hat{\psi}^\dagger(\mathbf{r})]\hat{\psi}(\mathbf{r})\}, \tag{34}
$$

and the diamagnetic charge current density operator,

$$
\hat{\mathbf{j}}_d(\mathbf{r}) = \hat{\mathbf{j}}_d^{\mathrm{mag}}(\mathbf{r}) + \hat{\mathbf{j}}_d^{\mathrm{ph}}(\mathbf{r}). \tag{35}
$$

The latter consists of a magnetic component,

$$
\hat{\mathbf{j}}_d^{\mathrm{mag}}(\mathbf{r}) = \frac{e^2}{m}\mathbf{A}(\mathbf{r})\hat{\psi}^\dagger(\mathbf{r})\hat{\psi}(\mathbf{r}), \tag{36}
$$

and photonic component,

$$\hat{\mathbf{j}}_d^{ph}(\mathbf{r}) = \frac{e^2}{m}\hat{\mathbf{A}}^{ph}(\mathbf{r})\hat{\psi}^\dagger(\mathbf{r})\hat{\psi}(\mathbf{r}). \qquad (37)$$

Furthermore, to understand better the driving schemes of the dynamical transport features, we define the total local charge current

$$I_{tl}(t) = I_{top}(t) + I_{bottom}(t) \qquad (38)$$

and circular local charge current

$$I_{cl}(t) = \tfrac{1}{2}[I_{top}(t) - I_{bottom}(t)]. \qquad (39)$$

Below, we shall explore the influence of the applied magnetic field and the photon field polarization on the nonequilibrium quantum transport in terms of the above time-dependent charges and currents in the broad quantum ring system connected to leads.

A. Photons with *x* polarization

In this section, we focus on our results for *x*-polarized photon field. Figure 2 shows the MB energy spectrum of the system Hamiltonian $\hat{H}_S$ including the electron-electron and electron-photon interactions. The MB-energy levels are assigned different colors according to their electron content N_e. The bias window (solid black lines) contains $(\mu_L - \mu_R)/(\hbar\omega)$ zero-electron states (green dots) and several SESs (red dots). However, even in the sequential tunneling regime, SESs outside the bias window can contribute to the transport due to the photon perturbation and the time dependency of the coupling to the leads. In order to estimate the energetic
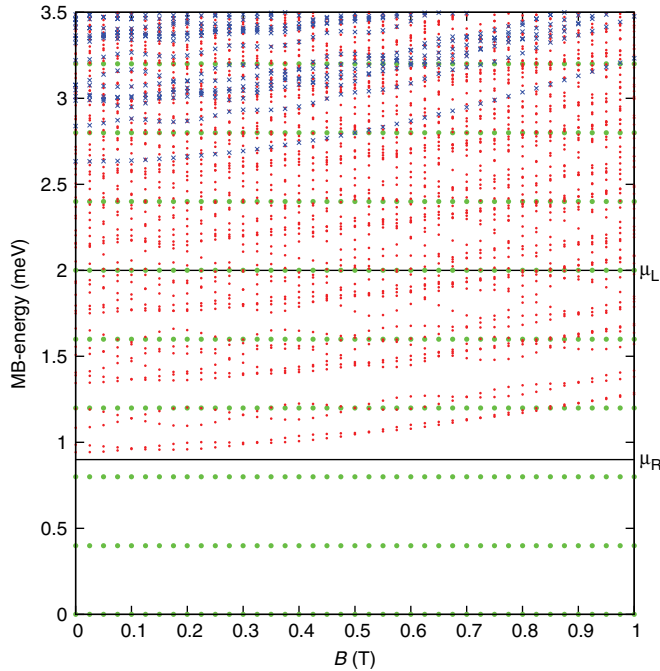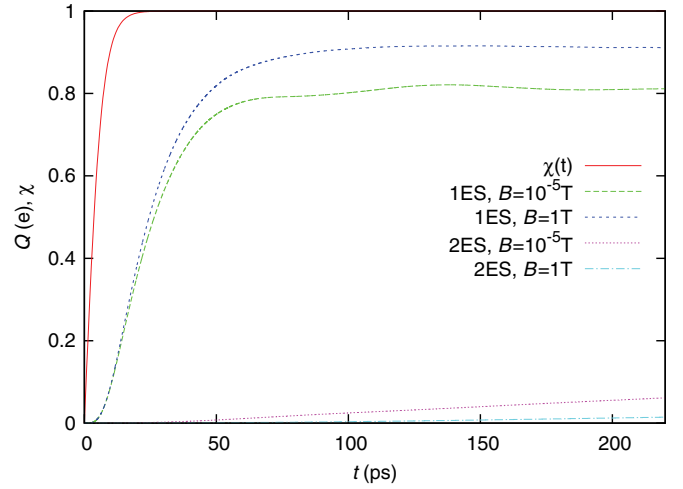
FIG. 3. (Color online) Switching function $\chi^l(t)$ (solid red), charge of all 1ES for $B = 10^{-5}$ T (long-dashed green) and $B = 1.0$ T (short-dashed blue), and charge of all 2ES for $B = 10^{-5}$ T (dotted purple) and $B = 1.0$ T (dash-dotted cyan) as a function of time. The photon field is *x*-polarized.

capability of the two electron states (2ES, blue crosses) to contribute to the transport, their energy difference to the SES has to be considered. This energy difference can fall into the bias window.

Our specific ring geometry has two main effects on the spectrum. First, the rotation symmetry violation due to the contact regions leads to avoided crossings at integer flux quanta leaving only the half-integer flux quanta crossings. For the latter, wave functions of odd and even quantum numbers of magnetic moment[18] cross, which therefore have opposite and equal phases at the contact regions, respectively, thus leaving them uninfluenced by the rotation symmetry violation. It can be seen from an analysis of the wave functions with magnetic flux that the magnetic moment remains unchanged and clearly defined for the crossings at half-integer flux quantum, while a gradual change in the magnetic moment quantum number by an even number is observable at the avoided crossings. Second, the finite ring width allows for small state-dependent variations of the crossing period B_0.

Figure 3 illustrates the central region charging of 1ES and 2ES as a function of time. It demonstrates the earlier mentioned time scales $(\alpha^l)^{-1} = 3.291$ ps, $\tau_{1ES} \approx 30$ ps and $\tau_{2ES} \gg 200$ ps. The 2ES are occupied slower than the 1ES indicating the sequential tunneling processes and the 2ES energetic shift by the Coulomb interaction. The effect is more pronounced for higher magnetic field due to the larger energy difference of the 2ES with respect to the 1ES (see Fig. 2). The total charging has slowed down by more than one order of magnitude around $t = 200$ ps.

In Fig. 4, we show the current from the left lead into the ring system I_L (solid red curve) and the current from the ring system to the right lead I_R (long-dashed green curve) as a function of magnetic field at time $t = 200$ ps. The similar values of $I_L(B)$ and $I_R(B)$ indicate the slow down in the total charging. We see clear oscillations of the current with period $B_0 \approx 0.2$ T: the first minimum current at $B = 0.1$ T corresponds to the situation of a half-flux quantum, while the maximum current

FIG. 2. (Color online) MB energy spectrum of system Hamiltonian $\hat{H}_S$ vs magnetic field B in units of tesla (T). The states are differentiated according to their electron content N_e: zero-electron states ($N_e = 0$, 0ES, green dots), single-electron states ($N_e = 1$, 1ES, red dots) and two-electron states ($N_e = 2$, 2ES, blue crosses). The photon field is *x* polarized.
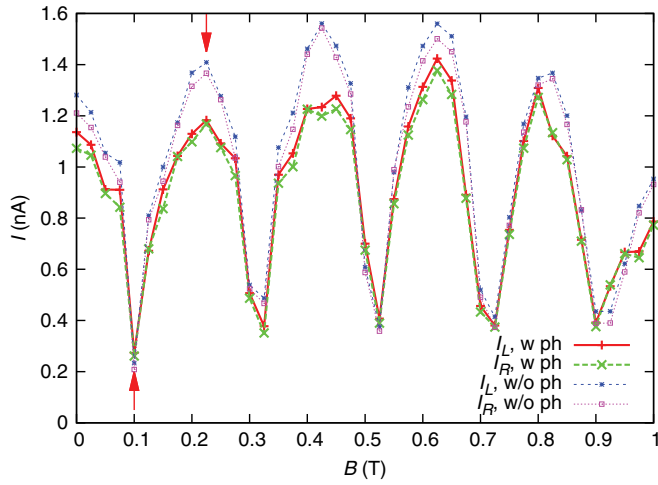
FIG. 4. (Color online) The left charge current I_L (solid red) and the right charge current I_R (long-dashed green) vs the magnetic field with (w) x-polarized photon field at $t = 200$ ps. For comparison: left charge current I_L (short-dashed blue) and right charge current I_R (dotted purple) in a purely electronic central system, i.e., without (w/o) photon cavity.

at $B = 0.225$ T is corresponding to the case of one flux quantum. Although the oscillations could be classified as being of Aharonov-Bohm (AB) type,[12–14] modifications by the electron-electron correlation effects and the nonequilibrium situation may not be neglected. In addition, the electron-photon coupling suppresses the constructive interference of AB phases in the integer flux quantum situation as can be seen from a comparison with the purely electronic system results in Fig. 4 (short-dashed blue and dotted purple curve).

In Fig. 5, we illustrate the normalized charge current density vector field $\mathbf{j}(\mathbf{r},t)$ in the central quantum ring system in the long-time response regime $t = 200$ ps, i.e., when the 2ES get charged. For magnetic field $B = 0.1$ T, a clear counterclockwise vortex located close to the left lead can be found dominating the current flow pattern in the central ring system as shown in Fig. 5(a).[16] The vortex circulation direction is determined by the Lorentz force, while the vortex area is too small to see effects of the threaded magnetic flux. It is important to realize that the vortex circulation direction in combination with the geometrical position of the vortex and the current continuity condition, favors clockwise current direction for the ring system. For magnetic field $B = 0.225$ T, the counterclockwise vortex appears relatively weak being present at both left and right lead connection areas as shown in Fig. 5(b), while the total local current through the whole central system from the left to the right lead is large. Additionally, for a later comparison with the y-polarized photon field, Fig. 5(c) shows the current density for $B = 0.425$ T (two flux quanta), which is similar to Fig. 5(b) (one flux quanta).

Figure 6 illustrates the time-dependent charge on the left part of the ring $Q_S^L(t)$ and the time-dependent charge on the right part of the ring $Q_S^R(t)$. In the half-integer flux quantum case $B = 0.1$ T shown in Fig. 6(a), both Q_S^L and Q_S^R are increasing almost monotonically in time. In the long-time response regime $t = 200$ ps, $Q_S^L(t) = 0.742e$ is much higher than $Q_S^R(t) = 0.234e$.
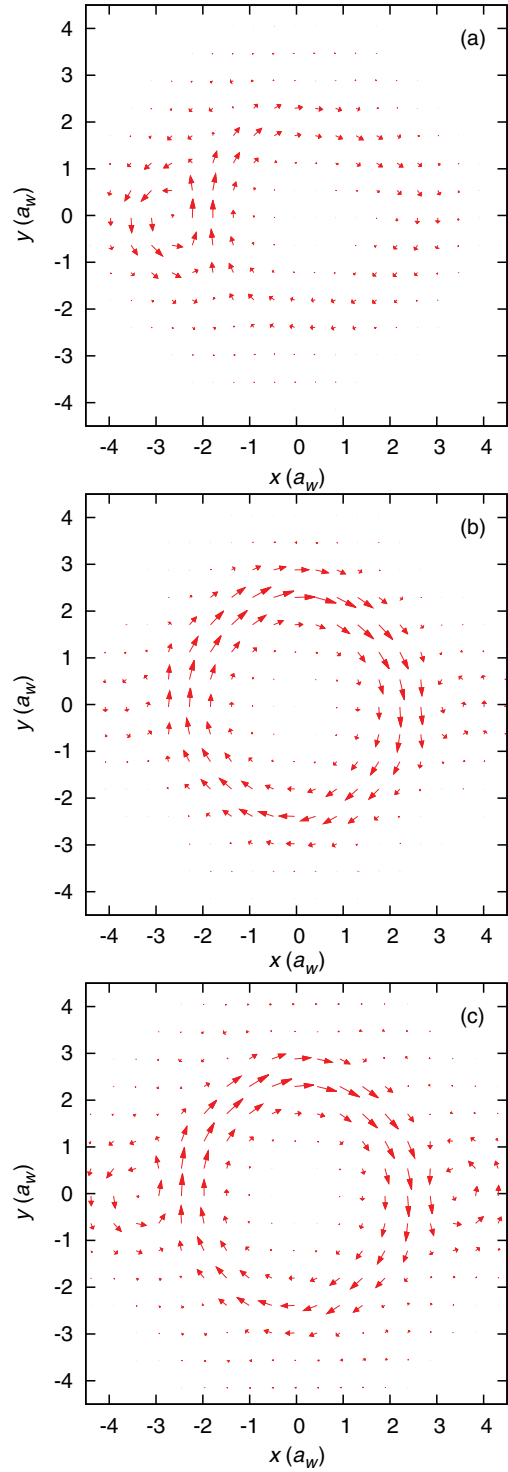

FIG. 5. (Color online) Normalized charge current density vector field in the central system for (a) $B = 0.1$ T, (b) $B = 0.225$ T, and (c) $B = 0.425$ T at $t = 200$ ps in the case of x-polarized photon field.

In the integer flux quantum case $B = 0.225$ T shown in Fig. 6(b), we find oscillating behavior of the charge between the left and right parts of the quantum ring. The oscillation amplitude is decreasing in time due to the dissipation effects caused by the coupling to the leads. In the long-time response regime $t = 200$ ps, $Q_S^L(t) = 0.423e$ is of similar magnitude as $Q_S^R(t) = 0.446e$ differently from the half-integer flux quantum
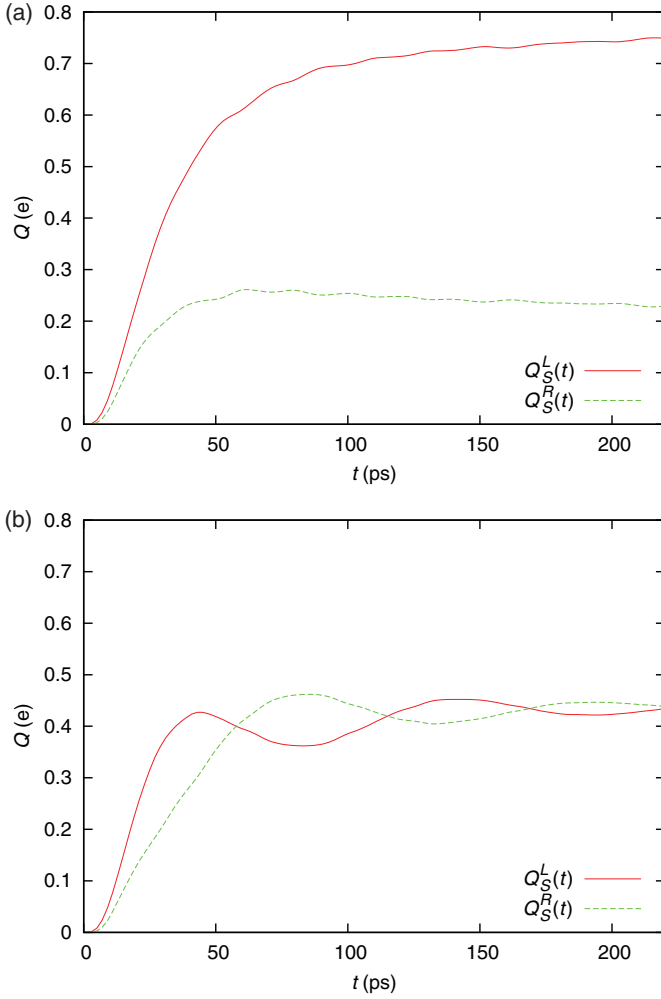
FIG. 6. (Color online) Charge in the left $[Q_S^L(t)]$ or right $[Q_S^R(t)]$ half of the central quantum ring system as a function of time for (a) $B = 0.1$ and (b) 0.225 T. The photon field is x-polarized.
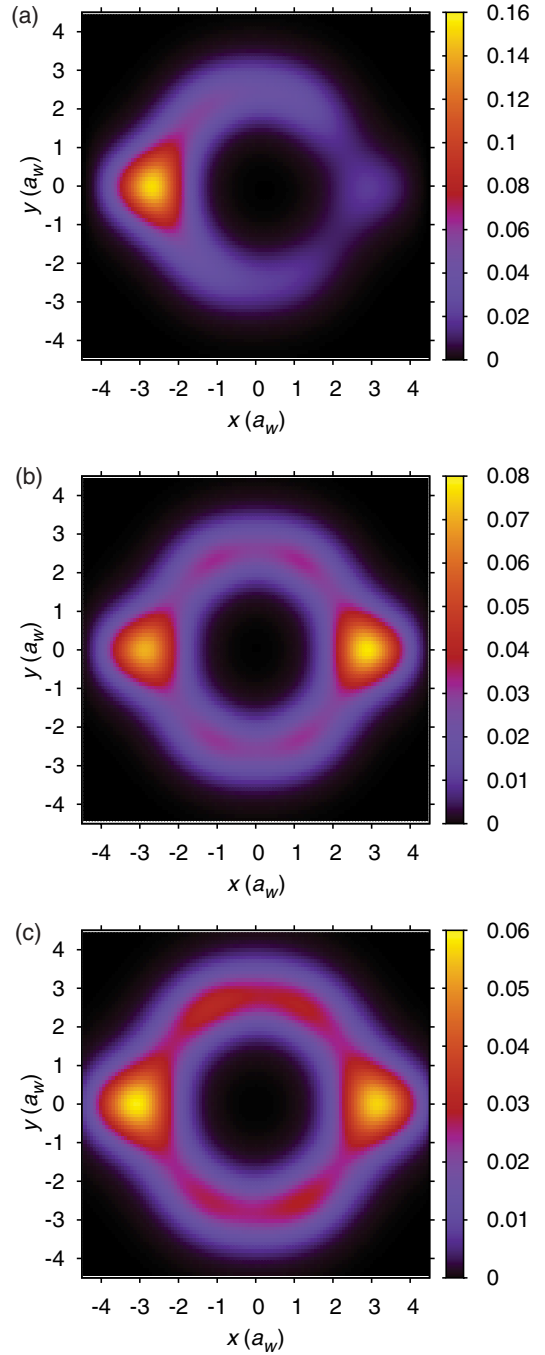

FIG. 7. (Color online) Charge density distribution $\rho(\mathbf{r},t)$ (e/a_w^2) in the central system for (a) $B = 0.1$, (b) 0.225, and (c) 0.425 T in the x-polarized photon field case at $t = 200$ ps.

case. The characteristic energy $\delta E_Q \approx 0.04$ meV of the charge oscillating period $\tau \approx 100$ ps agrees well with the MB energy difference of the mostly occupied MB states. As we find these MB states not only to correspond to the elements of the RDO causing this oscillation, but also to influence the current magnitude both due to AB and photon effects, we consider these states to be of particular interest. The MB energy levels are $E_{10}^x = 1.4038$ meV and $E_9^x = 1.3664$ meV such that $\Delta E_{9,10}^x = 0.0374$ meV. The corresponding two-level (TL) oscillation period of the closed system would be $\tau_{TL}^0 = 111$ ps. In the nonequilibrium open system, the TL oscillation period is $\tau_{TL}^L = 94$ ps or $\tau_{TL}^R = 100$ ps when we take the time intervals between the first and second maxima of $Q_S^L(t)$ and $Q_S^R(t)$, respectively. The full numerical calculation including all MB levels shown in Fig. 6(b) yields the left and right charge oscillation periods, $\tau^L = 96$ ps and $\tau^R = 110$ ps, respectively. The system is far from equilibrium at the earlier maximum, thus reducing, in particular, the left period τ^L with respect to τ_{TL}^0. Furthermore, we find that also the other MB states change the periods when comparing τ^L with τ_{TL}^L and τ^R with τ_{TL}^R.

Figure 7 shows the charge density distribution in the central quantum ring system with the magnetic field (a) $B = 0.1$,

(b) 0.225, and (c) 0.425 T at $t = 200$ ps. In the case of $B = 0.1$ T (half-flux quantum) shown in Fig. 6(a), the electrons are highly accumulated on the left-hand side of the quantum ring with very weak coupling to the right lead, and hence strongly blocking the left charge current and suppressing the right charge current, as it was shown previously in Fig. 4 (marked by the up arrow). The electron dwell time on the left-hand side of the ring is enhanced relative to the electron dwell time on the right-hand side of the ring due to destructive
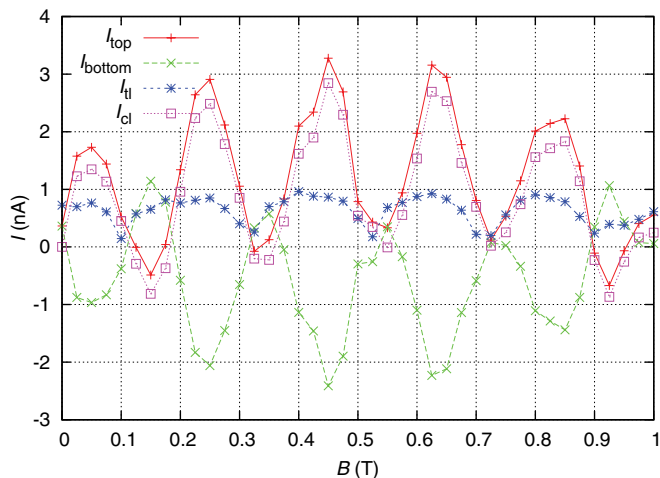
FIG. 8. (Color online) Local current through the top arm of the ring I_{top} (solid red), local current through the bottom arm of the ring I_{bottom} (long-dashed green), total local current I_{tl} (short-dashed blue), and the circular local current I_{cl} (dotted purple) versus the magnetic field averaged over the time interval [180,220] ps in the case of x-polarized photon field.

phase interference on the right-hand side suppressing also the evoked vortex there [see Fig. 5(a)].

In the $B = 0.225$ T case (one flux quantum) shown in Fig. 7(b), the electrons are nearly equally well accumulated on both sides of the quantum ring. This phenomenon is related to the manifestation of current peaks observed in Fig. 4 (marked by the down arrow) as the constructive phase interference enhances the likelihood for electrons to flow through the quantum ring to the right-hand side of the central system and further to the right lead. Additionally, for a later comparison, Fig. 7(c) shows the charge density for $B = 0.425$ T (two flux quanta), which is similar to Fig. 7(b) (one flux quantum).

In Fig. 8, we show the magnetic field dependence of the partial local currents I_{top} and I_{bottom} through the top and bottom arms, the total local current I_{tl} across $x = 0$, and the circular local current I_{cl}, which are convenient tools to study the relative importance of local "persistent" current flows induced by the magnetic field in the long-time response transient time regime. We would like to bring attention to the fact that charge balances like $\dot{Q}_L = I_L - I_{tl}$ and $\dot{Q}_R = I_{tl} - I_R$ would not be satisfied for the local current I_{tl}. This is because the SES that are filled from the left lead or emptied to the right lead are in general not restricted to a single half of the central system, but extended over the whole system. The total local current (short-dashed blue) through the two current arms, I_{tl}, is strongly suppressed in the case of half-integer flux quanta showing a very similar behavior to the nonlocal currents I_L and I_R (see Fig. 4). This is because the destructive interference in the quantum ring enhances the back scattering for magnetic flux with half-integer quanta.

The "persistent" circular local current (dotted purple) is usually larger in magnitude than the total local current leading to a different top and bottom local flow direction. In the absence of magnetic field $B = 0$, the circular current, however, is identical to zero due to the symmetric situation for both ring arms. It is interesting to note that the circular local

current I_{cl} reaches 1.347 nA for less than half a flux quantum (at $B = 0.05$ T), increases further until $B = 0.45$ T with a maximum value max $|I_{cl}| = 2.844$ nA and decreases again for $B > 0.45$ T. The magnetic component of the diamagnetic part of the circular local current increases linearly with the magnetic field B, but the paramagnetic part guarantees a behavior, which is closer to being periodic with the flux quantum. The periodic structure appears also for a ring of infinitesimal width,[17] but is shifted here toward clockwise circulation due to the vortices in Fig. 5. In the case of high magnetic field regime ($B > 0.45$ T), a comparison with Fig. 2 shows that the different flux periods of different MB-states in the finite-width ring lead to destructive interference effects reducing the periodic oscillations considerably.

B. Photons with y polarization

In this section, we focus on the y-polarized photon field situation and compare with the results for the x-polarized photon field. Figure 9 shows the MB energy spectra of the system Hamiltonian $\hat{H}_S$ in the case of (a) x-polarized and (b) y-polarized photon field. We note in passing that Fig. 9(a) magnifies a part of the MB spectrum of Fig. 2. The mostly occupied levels are the two levels around 1.4 meV. In the cases of both x- and y-polarized photon field, we see the MB energy degeneracy around $B = 0.1$ and 0.325 T related to the destructive AB phase interference. However, in the case of y polarization, an extra MB energy degeneracy is found at $B = 0.425$ T. This degeneracy is related to a current dip coming from *photonic* suppression, i.e., it is not related to AB oscillations.
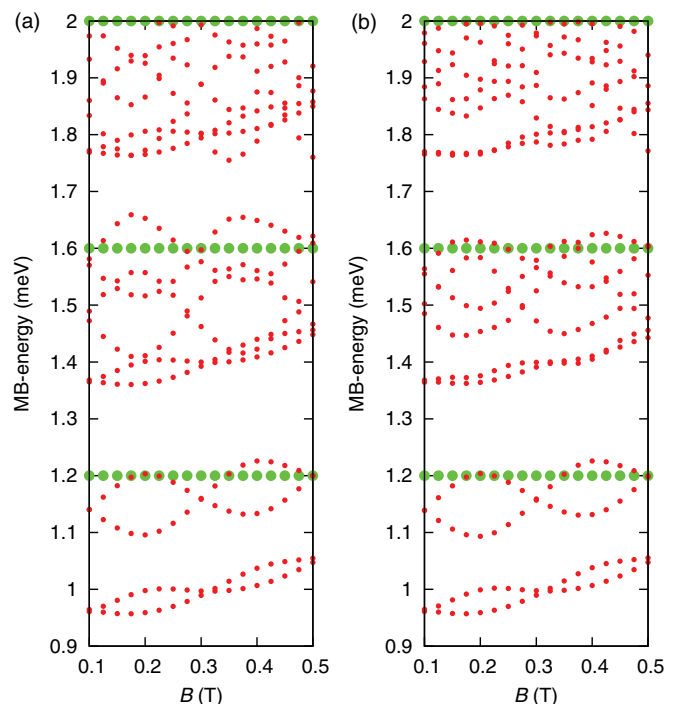

FIG. 9. (Color online) MB energy spectrum of the system Hamiltonian $\hat{H}_S$ vs magnetic field B within the bias window energy range for (a) x-polarized and (b) y-polarized photon field. The states are differentiated according to their electron content N_e: zero-electron ($N_e = 0$, 0ES, green dots) and single-electron ($N_e = 1$, 1ES, red dots) states.
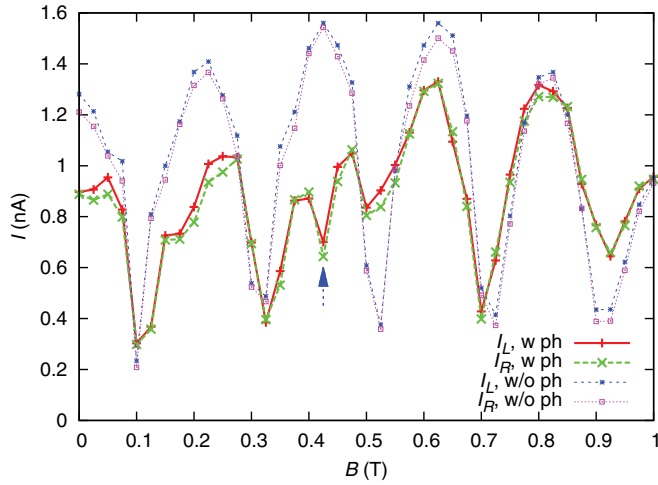
FIG. 10. (Color online) Left charge current I_L (solid red) and right charge current I_R (long-dashed green) vs the magnetic field with (w) y-polarized photon field at $t = 200$ ps. For comparison: left charge current I_L (short-dashed blue) and right charge current I_R (dotted purple) in a purely electronic central system, i.e., without (w/o) photon cavity.

Figure 10 shows the left charge current I_L (solid red) and the right charge current I_R (long-dashed green) as a function of magnetic field at $t = 200$ ps. It is eye catching that the oscillation amplitude and extrema positions show more unexpected features than in the case of x-polarized photon field. In particular, we would like to point out that the magnetic field dependence of the charge current exhibits a pronounced dip at $B = 0.425$ T (two flux quanta) in the case of a y-polarized photon field that is not present in the case of an x-polarized photon field. The dip structure is due to the above mentioned extra degeneracy of the MB energy spectrum, which strongly suppresses the photon-assisted tunneling properties. Furthermore, the charge current can be enhanced by the y-polarized photon field at magnetic field with half-integer flux quantum.

Figure 11 shows the normalized charge current density vector field $\mathbf{j}(\mathbf{r},t)$ in the central ring system for the magnetic field, (a) $B = 0.1$, (b) 0.225, and (c) 0.425 T, in the long-time response regime $t = 200$ ps. For magnetic field $B = 0.1$ T, a clear counterclockwise vortex can be found being associated with a long-living localized state, which is strongly dominating the current flow pattern in the central ring system, as is shown in Fig. 11(a). However, for magnetic field $B = 0.225$ T, this counterclockwise vortex appears weaker relative to the total local current, but is present at both contact regions as shown in Fig. 11(b). Figures 11(a) and 11(b) are similar to Figs. 5(a) and 5(b) meaning that the local current flow is mainly governed by AB interference with the photon polarization having only a minor effect.

Figure 11(c) shows the current density field for $B = 0.425$ T (two flux quanta), which is similar to the half-integer flux quanta case Fig. 11(a) and not to the integer flux quanta case Fig. 11(b). This similarity is only found for y polarization. [Instead for x polarization, the integer flux quanta cases Figs. 5(a) and 5(b) are found to be similar.] The charge flow at $B = 0.425$ T for y polarization is therefore not predicted by the AB effect, but is caused by the influence of the y-polarized
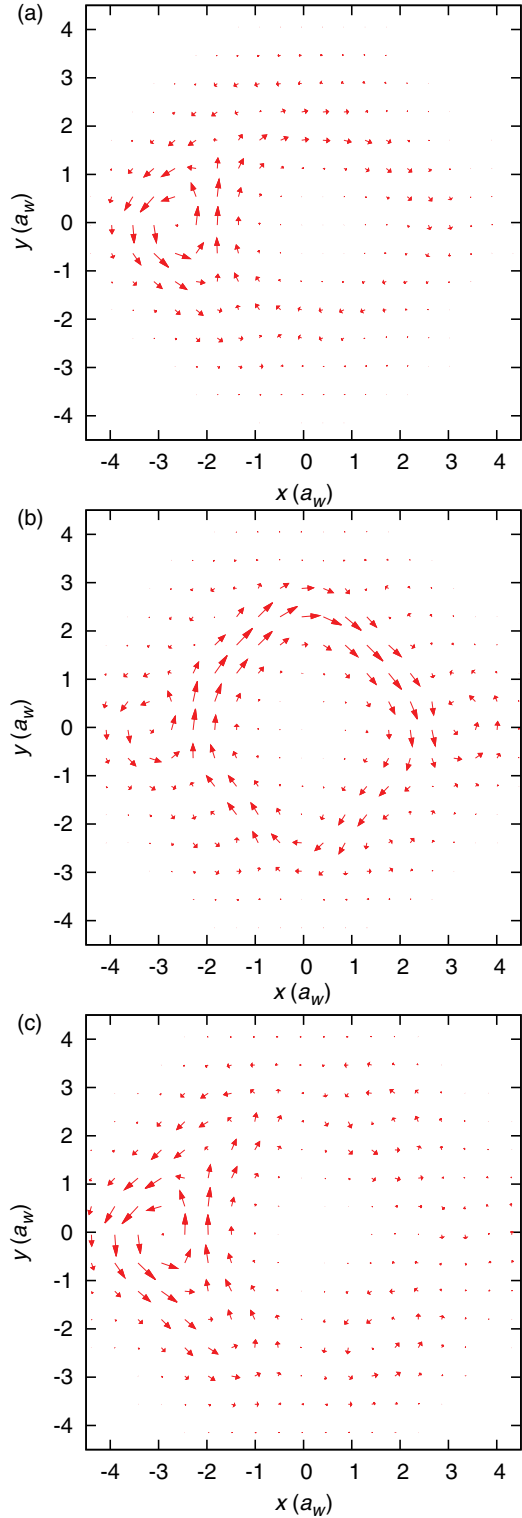
FIG. 11. (Color online) Normalized charge current density vector field in the central system for (a) $B = 0.1$, (b) 0.225, and (c) 0.425 T at $t = 200$ ps in the case of y-polarized photon field.

photons. However, any MB spectrum degeneracy of the mostly occupied MB states [see Fig. 9(b)], whether it originates from the AB effect [see Fig. 11(a)] or the photons [see Fig. 11(c)], influences the local current flow structure in a similar way.
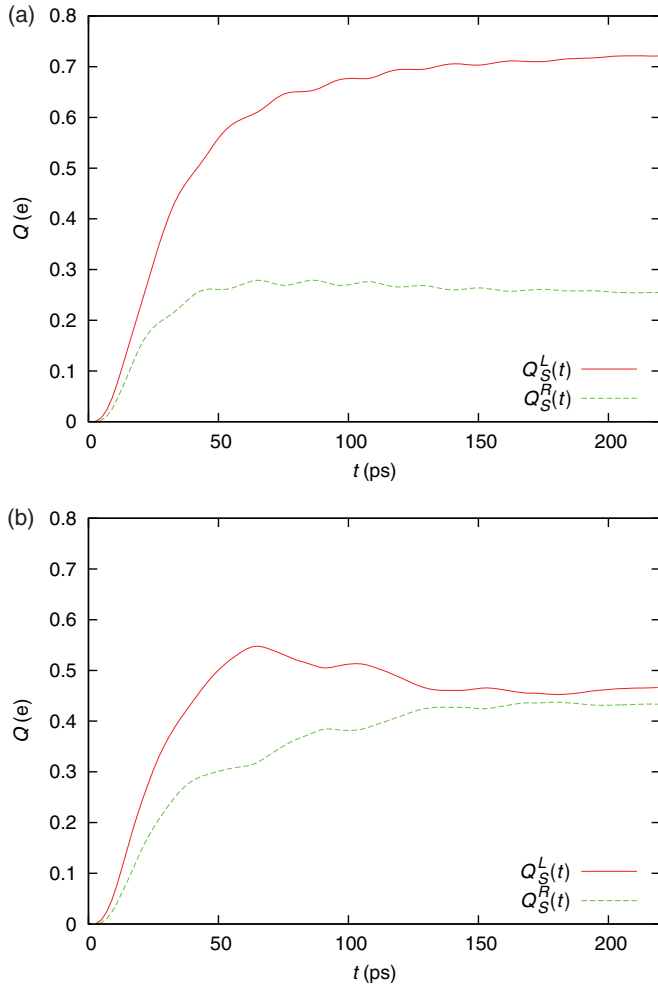
FIG. 12. (Color online) Charge in the left $[Q_S^L(t)]$ or right $[Q_S^R(t)]$ half of the central system as a function of time for (a) $B = 0.1$ T and (b) $B = 0.225$ T. The photon field is y polarized.

Figure 12 shows the time evolution of $Q_S^L(t)$ and $Q_S^R(t)$. In the long-time response regime at time $t = 200$ ps, the picture is very similar to the x-polarized photon field case: for $B = 0.1$ T, the charge is mainly accumulated at the left-hand side, $Q_S^L = 0.720e$ and $Q_S^R = 0.256e$ and for $B = 0.225$ T, the left and right charges are of similar magnitude, $Q_S^L = 0.462e$ and $Q_S^R = 0.431e$. However, in the $B = 0.225$ T case, the MB energies of the mostly occupied MB levels are $E_{10}^y = 1.3846$ meV and $E_9^y = 1.3683$ meV such that $\Delta E_{9,10}^y = 0.0163$ meV. Thus the energy level difference of the mostly occupied MB levels is only 44% of the case of x-polarized photon field: $E_{9,10}^y \approx 0.44 \times E_{9,10}^x$. The corresponding TL oscillation period of the closed system would be $\tau_{TL}^0 = 254$ ps. The oscillation period is too long to be observed clearly in Fig. 12(b), but we know from the analysis of the TL system defined by the two mostly occupied states that the low-frequency oscillation starts with its first maximum of $Q_S^L(t)$ at $t = 65$ ps. Our findings suggest that the energy difference of the two mostly occupied levels controls not only the charge distribution, but also photonic suppressions of the AB current. The different connectivity (probability density on the left or right ring part) to the leads found within the TL dynamic suggests that the
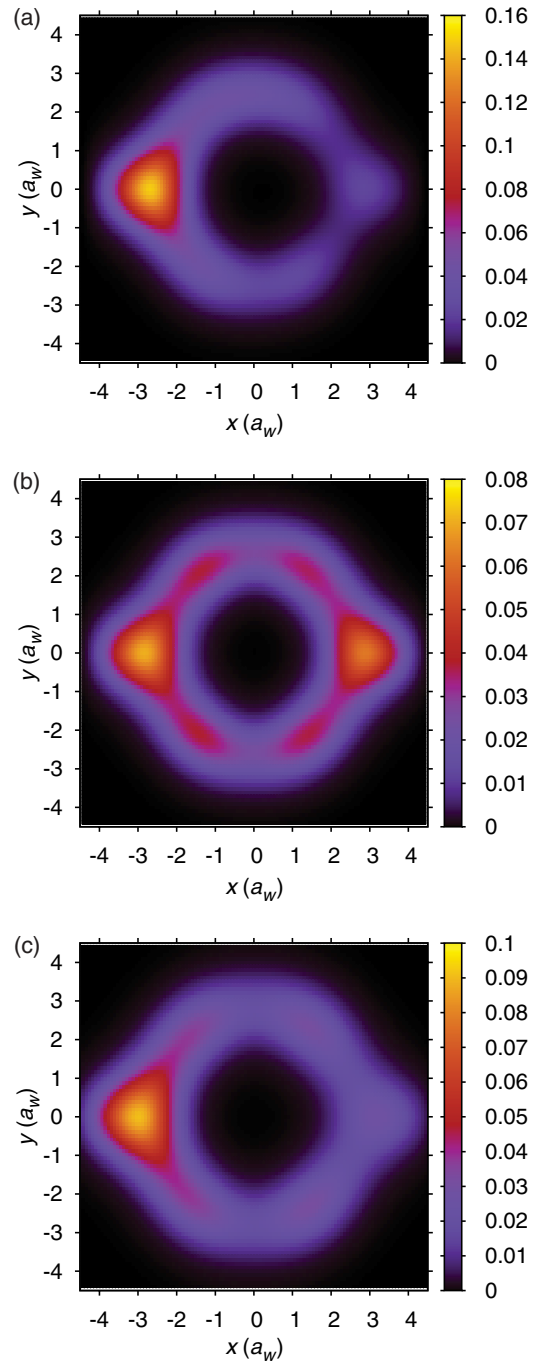
FIG. 13. (Color online) Charge density distribution $\rho(\mathbf{r},t)$ (e/a_w^2) in the central system for (a) $B = 0.1$, (b) 0.225, and (c) 0.425 T in the y-polarized photon field case at $t = 200$ ps.

probability of a photon coupled electron transition between these levels plays a major role in understanding the photonic modifications of the AB current pattern.

Figure 13 shows the charge density distribution in the central ring system for magnetic field (a) $B = 0.1$, 0.225, and (c) 0.425 T at $t = 200$ ps. In the case of $B = 0.1$ T shown in Fig. 13(a), the electrons are highly accumulated on the left-hand side of the quantum ring with very weak coupling to the right lead, and hence strongly blocking the left charge current and suppressing the right charge current.
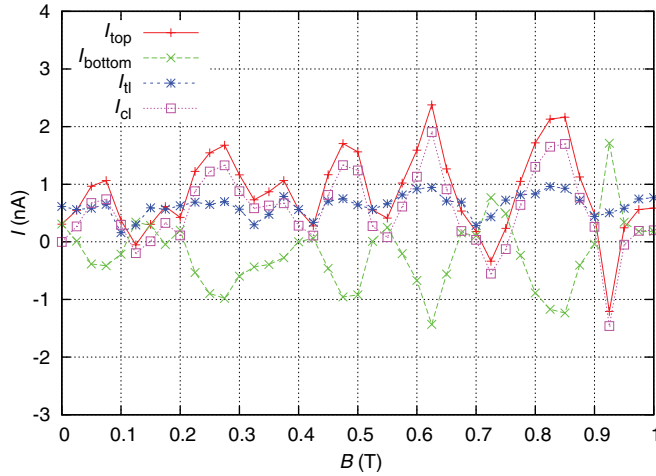
FIG. 14. (Color online) Local current through the top I_{top} (solid red) and bottom I_{bottom} (long-dashed green) ring arms and total I_{tl} (short-dashed blue) and circular I_{cl} (dotted purple) local currents vs the magnetic field and averaged over the time interval [180,220] ps in the case of y-polarized photon field.

In the integer flux quanta case of $B = 0.225$ T shown in Fig. 13(b), the electrons are equally well accumulated on both sides of the quantum ring. This situation is related to the manifestation of the current peaks observed in Fig. 10 by enhancement of the likelihood for electrons to flow through the quantum ring to the right-hand side of the central system and further to the right lead.

Figure 13(c) shows the charge density for $B = 0.425$ T (two flux quanta), which is similar to the half-integer flux quanta case Fig. 13(a). This feature is therefore not predicted by the AB effect, but is caused by the influence of the y-polarized photons. However, any MB spectrum degeneracy of the mostly occupied MB states [see Fig. 9(b)], whether it originates from the AB effect [see Fig. 13(a)] or the photons [see Fig. 13(c)], influences the density distribution in a similar way.

In Fig. 14, we show the magnetic field dependence of the local currents I_{top} and I_{bottom} through the top and bottom arms, respectively, the total local current I_{tl} across $x = 0$, and the circular local current I_{cl}. The local current through the two current arms, I_{tl}, is suppressed in the case of half-integer flux quanta showing a similar behavior to the nonlocal currents I_L and I_R (see Fig. 10). We find more irregularities due to the stronger effective influence of the y-polarized photon field than for x polarization. It is interesting to note that the current suppression dip at $B = 0.425$ T (marked by the blue arrow in Fig. 10) appears also in the local current (blue short-dashed curve) flowing through both ring arms from the left to the right.

The "persistent" circular local current reaches a maximum absolute value of max $|I_{cl}| = 1.905$ nA at $B = 0.625$ T, which is by 0.939 nA smaller than for x polarization. It is clearly visible from a comparison of Figs. 14 and 8 that the circular current is considerably smaller than in the x-polarized photon case, while the total local current is of the same order. Thus the capability of the magnetic field to drive a rotational ring current is weakened by having the electromagnetic field y-polarized. In particular, this can be said about the diamagnetic part of the

circular local current leading to the much smaller value $I_{cl} = 0.675$ nA at low magnetic field $B = 0.05$ T. The periodicity of the circular local current is preserved better for x-polarized photon field as is for the total local current emphasizing the perturbing influence of the y-polarized photon field.

IV. CONCLUDING REMARKS

We have presented a time-convolutionless generalized master equation formalism that allows us to calculate the nonequilibrium transport of Coulomb interacting electrons through a broad quantum ring in a photon cavity under the influence of a uniform perpendicular magnetic field. The topologically nontrivial broad ring geometry allows for substantial electron-electron correlations relative to their kinetic energy and, hence, a large basis is required for sufficient numerical accuracy. The central quantum ring 1ES are charged quickly. Electron-electron correlation and sequential tunneling slow down the 2ES charging in the long-time response regime. Aharonov-Bohm charge current oscillations can be recognized in the long-time response regime with magnetic field period $B_0 = \Phi_0/A$, which is related to the flux quantum Φ_0 and ring area A.

In the case of x-polarized photon field, we have found charge oscillations between the left and right parts of the quantum ring when the magnetic field is associated with integer flux quanta. The oscillation frequency agrees well with the energy difference of the two mostly occupied states. The relatively high energy difference for x-polarized photons is related to a relatively high transient current through the ring. The amplitude of the charge oscillations through the quantum ring is decreasing in time due to dissipation effects caused by the coupling to the leads. Usually, the local current through the upper ring arm exhibits opposite sign to the local current through the lower ring arm. Hence the "persistent" circular local current is usually larger than the total local charge current through both ring arms from the left to the right. The persistent current shows a periodic behavior with magnetic field, but with a tendency to clockwise rotation due to the contact region vortex structure.

In the case of y-polarized photon field, the magnetic field dependence of the left and right charge current exhibits a pronounced dip at magnetic field $B = 0.425$ T corresponding to two flux quanta that is therefore clearly not related to the Aharonov-Bohm effect. The dip is associated with a degeneracy of the two mostly occupied MB states at magnetic field associated with two flux quanta. The additional level crossing appears only for y-polarized photons, but influences the spatial distribution of the charge density and flow similarly to any other MB degeneracy. The generally lower energy difference of the two mostly occupied MB states in the case of y polarization perturbs the constructive phase interference condition for the bias driven charge flow through the quantum device and decreases the persistent current magnitude.

In conclusion, we have demonstrated for our ring geometry that y-polarized photons perturb our system stronger than x-polarized photons, suppressing or enhancing magnetic field induced and bias-driven currents and perturbing flux periodicity beyond finite width effects. It is interesting to compare these findings to the quantum wire case, where it was

found that mainly x-polarized photons attenuate the central system charging due to a closer agreement of the photon mode energy and the characteristic electronic excitation energy in x direction.[56] In this paper, we have considered a more complex geometry, which reduces effectively the y-confinement energy $\hbar\Omega_0 = 1.0$ meV. The characteristic electronic excitation energy in y direction may therefore be much closer to the photon mode energy $\hbar\omega = 0.4$ meV, thus leading to a relatively strong influence of the y-polarized photon field on the electronic transport. Transient spectroscopy has been applied to semiconductor microstructures.[63,64] We can only speculate that methods from quantum optics combined with methods developed for time-dependent electron transport can be used to make the time scale in our nanostructures accessible.

The conceived magnetic field influenced quantum ring system in a photon cavity could serve as an elementary quantum device for optoelectronic applications and quantum information processing with unique characteristics by controlling the applied magnetic field and the polarization of the photon field.

*tla1@hi.is

†cstang@nuu.edu.tw

‡vidar@hi.is

[1] E. Buks, R. Schuster, M. Heiblum, D. Mahalu, and V. Umansky, Nature (London) **391**, 871 (1998).

[2] D. Sprinzak, E. Buks, M. Heiblum, and H. Shtrikman, Phys. Rev. Lett. **84**, 5820 (2000).

[3] A. Bertoni, P. Bordone, R. Brunetti, C. Jacoboni, and S. Reggiani, Phys. Rev. Lett. **84**, 5912 (2000).

[4] V. Gudmundsson and C.-S. Tang, Phys. Rev. B **74**, 125302 (2006).

[5] K. Kobayashi, H. Aikawa, A. Sano, S. Katsumoto, and Y. Iye, Phys. Rev. B **70**, 035319 (2004).

[6] O. Valsson, C.-S. Tang, and V. Gudmundsson, Phys. Rev. B **78**, 165318 (2008).

[7] B. Szafran and F. M. Peeters, Phys. Rev. B **72**, 165301 (2005).

[8] S. S. Buchholz, S. F. Fischer, U. Kunze, M. Bell, D. Reuter, and A. D. Wieck, Phys. Rev. B **82**, 045432 (2010).

[9] C. C. Eugster and J. A. del Alamo, Phys. Rev. Lett. **67**, 3586 (1991).

[10] D. M. Schroer, A. K. Huttel, K. Eberl, S. Ludwig, M. N. Kiselev, and B. L. Altshuler, Phys. Rev. B **74**, 233301 (2006).

[11] H.-F. Cheung, Y. Gefen, E. K. Riedel, and W.-H. Shih, Phys. Rev. B **37**, 6050 (1988).

[12] Y. Aharonov and D. Bohm, Phys. Rev. **115**, 485 (1959).

[13] M. Büttiker, Y. Imry, and M. Y. Azbel, Phys. Rev. A **30**, 1982 (1984).

[14] R. A. Webb, S. Washburn, C. P. Umbach, and R. B. Laibowitz, Phys. Rev. Lett. **54**, 2696 (1985).

[15] A. Tonomura, N. Osakabe, T. Matsuda, T. Kawasaki, J. Endo, S. Yano, and H. Yamada, Phys. Rev. Lett. **56**, 792 (1986).

[16] K. N. Pichugin and A. F. Sadreev, Phys Rev B **56**, 9662 (1997).

[17] N. Byers and C. N. Yang, Phys. Rev. Lett. **7**, 46 (1961).

[18] S. Viefers, P. Koskinen, P. S. Deo, and M. Manninen, Phys. E **21**, 1 (2004).

[19] W.-C. Tan and J. C. Inkson, Phys. Rev. B **60**, 5626 (1999).

[20] T. Arnold, M. Siegmund, and O. Pankratov, J. Phys.: Condens. Matter **23**, 335601 (2011).

[21] W.-C. Tan and J. C. Inkson, Semicond. Sci. Technol. **11**, 1635 (1996).

[22] A. Fuhrer, P. Brusheim, T. Ihn, M. Sigrist, K. Ensslin, W. Wegscheider, and M. Bichler, Phys. Rev. B **73**, 205326 (2006).

[23] C. S. Tang and C. S. Chu, Phys. Rev. B **53**, 4838 (1996).

[24] M. A. Zeb, K. Sabeeh, and M. Tahir, Phys. Rev B **78**, 165420 (2008).

[25] D. Kienle and F. Léonard, Phys. Rev. Lett. **103**, 026601 (2009).

[26] C.-S. Tang, K. Torfason, and V. Gudmundsson, Comput. Phys. Commun. **182**, 65 (2011).

[27] C. S. Tang and C. S. Chu, Phys. Rev. B **60**, 1830 (1999).

[28] G. Zhou and Y. Li, J. Phys.: Condens. Matter **17**, 6663 (2005).

[29] J.-W. Jung, K. Na, and L. E. Reichl, Phys. Rev. A **85**, 023420 (2012).

[30] C. S. Tang and C. S. Chu, Physica B **292**, 127 (2000).

[31] G. Zhou, M. Yang, X. Xiao, and Y. Li, Phys. Rev. B **68**, 155309 (2003).

[32] P. Myöhänen, A. Stan, G. Stefanucci, and R. van Leeuwen, Phys. Rev. B **80**, 115107 (2009).

[33] G. Stefanucci, E. Perfetto, and M. Cini, Phys. Rev. B **81**, 115446 (2010).

[34] M. Tahir and A. MacKinnon, Phys. Rev. B **81**, 195444 (2010).

[35] P.-W. Chen, C.-C. Jian, and H.-S. Goan, Phys. Rev. B **83**, 115439 (2011).

[36] S. A. Gurvitz and Y. S. Prager, Phys. Rev. B **53**, 15932 (1996).

[37] N. G. van Kampen, *Stochastic Processes in Physics and Chemistry*, 2nd ed. (North-Holland, Amsterdam, 2001).

[38] U. Harbola, M. Esposito, and S. Mukamel, Phys. Rev. B **74**, 235309 (2006).

[39] A. Braggio, J. König, and R. Fazio, Phys. Rev. Lett. **96**, 026805 (2006).

[40] C. Emary, D. Marcos, R. Aguado, and T. Brandes, Phys. Rev. B **76**, 161404(R) (2007).

[41] A. Bednorz and W. Belzig, Phys. Rev. Lett. **101**, 206803 (2008).

[42] V. Moldoveanu, A. Manolescu, and V. Gudmundsson, New J. Phys. **11**, 073019 (2009).

[43] V. Gudmundsson, C. Gainar, C.-S. Tang, V. Moldoveanu, and A. Manolescu, New J. Phys. **11**, 113007 (2009).

[44] V. Gudmundsson, C.-S. Tang, O. Jonasson, V. Moldoveanu, and A. Manolescu, Phys. Rev. B **81**, 205319 (2010).

[45] M. Helm, *Intersubband Transitions in Quantum Wells: Physics and Device Applications I*, edited by H. C. Liu and F. Capasso (Academic Press, San Diego, CA, 2000).

[46] A. Gabbay, J. Reno, J. R. Wendt, A. Gin, M. C. Wanke, M. B. Sinclair, E. Shaner, and I. Brener, Appl. Phys. Lett. **98**, 203103 (2011).

[47] C. Ciuti, G. Bastard, and I. Carusotto, Phys. Rev. B **72**, 115303 (2005).

[48] M. Devoret, S. Girvin, and R. Schoelkopf, Ann. Phys. **16**, 767 (2007).

[49] A. A. Abdumalikov, O. Astafiev, Y. Nakamura, Y. A. Pashkin, and J. S. Tsai, Phys. Rev. B **78**, 180502(R) (2008).

[50] F. D. Zela, E. Solano, and A. Gago, Opt. Commun. **142**, 106 (1997).

[51] A. T. Sornborger, A. N. Cleland, and M. R. Geller, Phys. Rev. A **70**, 052315 (2004).

[52] E. K. Irish, Phys. Rev. Lett. **99**, 173601 (2007).

[53] E. B. Davies, *Quantum Theory of Open Systems* (Academic, London, 1976).

[54] H. Spohn, Rev. Mod. Phys. **52**, 569 (1980).

[55] H.-P. Breuer, B. Kappler, and F. Petruccione, Phys. Rev. A **59**, 1633 (1999).

[56] V. Gudmundsson, O. Jonasson, C.-S. Tang, H.-S. Goan, and A. Manolescu, Phys. Rev. B **85**, 075306 (2012).

[57] S. Nakajima, Prog. Theor. Phys. **20**, 948 (1958).

[58] R. Zwanzig, J. Chem. Phys. **33**, 1338 (1960).

[59] V. Gudmundsson, C. Gainar, C.-S. Tang, V. Moldoveanu, and A. Manolescu, New J. Phys. **11**, 113007 (2009).

[60] V. Moldoveanu, A. Manolescu, C.-S. Tang, and V. Gudmundsson, Phys. Rev. B **81**, 155442 (2010).

[61] R. S. Whitney, J. Phys. A: Math. Theor. **41**, 175304 (2008).

[62] V. Moldoveanu, A. Manolescu, and V. Gudmundsson, New J. Phys. **11**, 073019 (2009).

[63] W.-T. Lai, D. M. Kuo, and P.-W. Li, Phys. E **41**, 886 (2009).

[64] B. Naser, D. K. Ferry, J. Heeren, J. L. Reno, and J. P. Bird, Appl. Phys. Lett. **89**, 083103 (2006).

Stepwise introduction of model complexity in a generalized master equation approach to time-dependent transport

Vidar Gudmundsson[1,*]**, Olafur Jonasson**[1]**, Thorsten Arnold**[1]**, Chi-Shung Tang**[2,**]**, Hsi-Sheng Goan**[3,***]**,** and **Andrei Manolescu**[4,#]

[1] Science Institute, University of Iceland, Dunhaga 3, IS-107 Reykjavik, Iceland

[2] Department of Mechanical Engineering, National United University, 1, Lienda, Miaoli 36003, Taiwan

[3] Department of Physics and Center for Theoretical Sciences, and
  Center for Quantum Science and Engineering, National Taiwan University, Taipei 10617, Taiwan

[4] Reykjavik University, School of Science and Engineering, Menntavegur 1, IS-101 Reykjavik, Iceland

We demonstrate that with a stepwise introduction of complexity to a model of an electron system embedded in a photonic cavity and a carefully controlled stepwise truncation of the ensuing many-body space it is possible to describe the time-dependent transport of electrons through the system with a non-Markovian generalized quantum master equation. We show how this approach retains effects of the geometry of an anisotropic electronic system. The Coulomb interaction between the electrons and the full electromagnetic coupling between the electrons and the photons are treated in a non-perturbative way using "exact numerical diagonalization".

1 Introduction

Advances in techniques constructing and experimenting with quantum electrodynamic circuits have resulted in systems with very strong electron-photon coupling [1–3]. Traditionally, some version of the Jaynes-Cummings model [4] is used to describe the energy spectrum of the closed system or its time evolution [5]. Recently, we have shown that for a strong electron-photon coupling in a semiconductor nanostructure the Jaynes-Cumming model may not be adequate and one may have to consider a model with more than two electron levels and the diamagnetic term in the coupling [6]. In continuation we have used our experience with describing the dynamics of open systems in terms of the generalized master equation (GME) [7, 8] to start the exploration of time-dependent transport properties of circuit quantum electrodynamic (circuit-QED) systems [9].

Here, we will describe our approach with a special emphasis on what we call: "A stepwise introduction of complexity to a model and a carefully controlled stepwise truncation of the ensuing many-body space". We will discuss technical issues that are common to models of different phenomena and fields, but we will use the model of Coulomb interacting electrons in a photonic cavity as an example to display our approach and findings.

*   Corresponding author   E-mail: vidar@hi.is
**   E-mail: cstang@nuu.edu.tw
*** E-mail: goan@phys.ntu.edu.tw
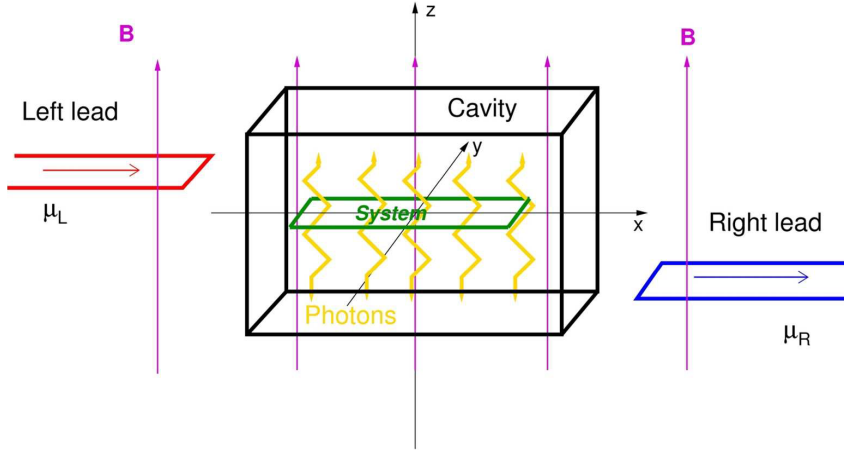\#   E-mail: manoles@ru.is

Fig. 1   (online colour at: www.fp-journal.org) A schematic view of the total system consisting of a finite quantum wire (green, the central electronic system) in a photon cavity (bold black), coupled to external left (red) and right (blue) leads at different chemical potentials, μ_L and μ_R. An external homogeneous magnetic field **B** (magenta) is perpendicular to the system and the leads. The lengths are not shown to scale. The length of the central system is 300 nm, but the characteristic lengths of the cavity are on the millimeter scale. The GaAs leads and central system contain a quasi-one-dimensional (Q1D) electron gas in 1 to 4 subbands of width 60 to 120 nm for the parameters to be introduced below. The cavity photon modes (yellow) are standing waves in the z-direction with an electric component in the x- or y-direction. The applied bias between the left and right leads is indicated by placing them at different levels with respect to the central system.

2   The model of the closed system

The closed electron-photon system is a finite quasi-one-dimensional (Q1D) quantum wire placed in the center of a rectangular photon cavity (see Fig. 1). It is described by the Hamiltonian [9]

$$
\begin{aligned}
H_0 =& \sum_i E_i d_i^\dagger d_i + \hbar\omega a^\dagger a + \frac{1}{2} \sum_{ijrs} \langle ij|V_{\text{Coul}}|rs\rangle d_i^\dagger d_j^\dagger d_s d_r \\
&+ \mathcal{E}_c \sum_{ij} d_i^\dagger d_j \, g_{ij} \left\{ a + a^\dagger \right\} \\
&+ \mathcal{E}_c \left(\frac{\mathcal{E}_c}{\hbar\Omega_w} \right) \sum_i d_i^\dagger d_i \left\{ \left(a^\dagger a + \frac{1}{2} \right) + \frac{1}{2} \left(aa + a^\dagger a^\dagger \right) \right\},
\end{aligned}
\tag{1}
$$

where E_i is the single-electron spectrum for the finite quantum wire with hard walls at $x = \pm L_x/2$ and parabolic confinement in the y-direction with characteristic energy $\hbar\Omega_0$. A static classical external magnetic field $\mathbf{B} = \nabla \times \mathbf{A}_{\text{ext}} = B\hat{z}$ renormalizes the frequency of the y-confinement $\Omega_w^2 = \omega_c^2 + \Omega_0^2$ and the natural length scale $a_w = \sqrt{\hbar/(m^*\Omega_w)}$ with the cyclotron frequency $\omega_c = eB/(m^*c)$. d_i is an annihilation operator of the non-interacting single-electron state (SES) $|i\rangle$ with energy E_i, and a is the annihilation operator for the single-photon mode with energy $\hbar\omega$. The kernel for the Coulomb interaction of the electrons is

$$
V_{\text{Coul}}(\mathbf{r} - \mathbf{r}') = \frac{e^2}{\kappa\sqrt{(x - x')^2 + (y - y')^2 + \eta^2}},
\tag{2}
$$

with the small regularization factor selected such that $\eta/a_w \approx 7.1 \times 10^{-3}$ when $a_w \approx 33.5$ nm at $B = 0.1$ T for GaAs parameters, i. e. the effective mass $m^* = 0.067 m_e$, and the dielectric constant $\kappa = 12.4$.

The second line in the Hamiltonian (1) is the paramagnetic interaction between electrons and photons $(-\int d\mathbf{r}\, \mathbf{j}\cdot\mathbf{A})/c$, and the last line stems from the diamagnetic term in the interaction $(-e\int d\mathbf{r}\, \rho A^2)/(2m^*c^2)$. In terms of the field operators the charge current density and charge density are, respectively,

$$\mathbf{j} = -\frac{e}{2m^*}\left\{\psi^\dagger\left(\boldsymbol{\pi}\psi\right) + \left(\boldsymbol{\pi}^*\psi^\dagger\right)\psi\right\},\tag{3}$$

and

$$\rho = -e\psi^\dagger\psi,\tag{4}$$

where

$$\boldsymbol{\pi} = \left(\mathbf{p} + \frac{e}{c}\mathbf{A}_{\mathrm{ext}}\right).\tag{5}$$

The photon cavity is assumed to be a rectangular box $(x,y,z) \in \{[-a_{\mathrm{c}}/2, a_{\mathrm{c}}/2] \times [-a_{\mathrm{c}}/2, a_{\mathrm{c}}/2] \times [-d_{\mathrm{c}}/2, d_{\mathrm{c}}/2]\}$ with the finite quantum wire centered in the $z = 0$ plane. In the Coulomb gauge the polarization of the electric field can be chosen parallel to the transport in the x-direction by selecting the TE_{011} mode, or perpendicular to it by selecting the TE_{101} mode

$$\mathbf{A}(\mathbf{r}) = \begin{pmatrix}\hat{\mathbf{e}}_x \\ \hat{\mathbf{e}}_y\end{pmatrix}\mathcal{A}\left\{a + a^\dagger\right\}\begin{pmatrix}\cos\left(\frac{\pi y}{a_{\mathrm{c}}}\right) \\ \cos\left(\frac{\pi x}{a_{\mathrm{c}}}\right)\end{pmatrix}\cos\left(\frac{\pi z}{d_{\mathrm{c}}}\right),\qquad \begin{matrix}\mathrm{TE}_{011} \\ \mathrm{TE}_{101}\end{matrix}.\tag{6}$$

$\mathcal{A}$ is the amplitude of the cavity vector field defining a characteristic energy scale $\mathcal{E}_{\mathrm{c}} = e\mathcal{A}\Omega_w a_w/c = g^{\mathrm{EM}}$ for the electron-photon interaction and leaving an effective dimensionless coupling tensor

$$g_{ij} = \frac{a_w}{2\hbar}\int d\mathbf{r}\,\left[\psi_i^*(\mathbf{r})\left\{(\hat{\mathbf{e}}\cdot\boldsymbol{\pi})\,\psi_j(\mathbf{r})\right\} + \left\{(\hat{\mathbf{e}}\cdot\boldsymbol{\pi})\,\psi_i(\mathbf{r})\right\}^*\psi_j(\mathbf{r})\right],\tag{7}$$

defining the coupling of individual single-electron states $|i\rangle$ and $|j\rangle$ to the photonic mode. In the calculations of the energy spectrum of the Hamiltonian (1) we will retain all resonant and antiresonant terms in the photon creation and annihilation operators so we will not use the rotating wave approximation, but in the calculations of the electron-photon coupling tensor (7) we assume $a_w, L_x << a_{\mathrm{c}}$ and approximate $\cos(\pi\{x,y\}/a_{\mathrm{c}}) \sim 1$ in Eq. (6) for the cavity vector field $\mathbf{A}$.

The energy spectrum and the states of the Hamiltonian for the closed electron-photon system have to be sought for an unspecified number of electrons as we want to open the system up for electrons from the leads later. We will be investigating systems with few electrons present in the finite quantum wire, but it is not a trivial task to construct an adequate many-body (MB) basis for the diagonalization of H_0 since in addition to geometrical and bias (set by the leads) considerations we have strong requirements set both by the Coulomb and the photon interaction. Our solution to this dilemma and a mean to keep a tight lid on the exponential growth of the size of the required many-body Fock space is to do the diagonalization in two steps.

First, we select the lowest N_{SES} single-electron states (SESs) of the finite quantum wire. These have been found by diagonalizing the Hamiltonian operator for a single electron in the Q1D confinement and in a perpendicular constant magnetic field in a large basis of oscillator-like wave functions. Originally, we constructed a many-electron Fock space with $N_{\mathrm{MES}} = 2^{N_{\mathrm{SES}}}$ states $|\mu\rangle$ [10, 11]. (We use Latin indices for the single-electron states and Greek ones for the many-electron states). This "simple binary" construction for the Fock-space does not deliver the optimal ratio of single-, two-, and higher number-of-electrons states for an interacting system when their energy is compared. Usually one ends up with too few SESs compared to the MESs. Here we will select 18 SESs and construct all possible combinations of 2-4 electron states. This can be refined further. These MESs, which are in fact Slater determinants, and which we denote as $|\mu\rangle$

(with an angular right bracket) are then used to diagonalize the part of the Hamiltonian (1) for the Coulomb interacting electrons only, supplying their spectrum $\tilde{E}_\mu$ and states $|\mu)$ (denoted now with a rounded right bracket). The eigenvectors from the diagonalization procedure define the unitary transform between the two sets of MESs, $|\mu) = \sum_\alpha \mathcal{V}_{\mu\alpha}|\alpha\rangle$. As the action of the creation and annihilation operators is only known in the non-interacting electron basis $\{|\mu\rangle\}$ we need this transform to write H_0 in the new Coulomb interacting basis $\{|\mu)\}$

$$H_0 = \sum_\mu |\mu)\tilde{E}_\mu(\mu| + \hbar\omega a^\dagger a + \mathcal{E}_c \sum_{\mu\nu ij} |\mu)\langle\mu|\mathcal{V}^+ d_i^\dagger d_j \mathcal{V}|\nu\rangle(\nu| \; g_{ij} \left\{ a + a^\dagger \right\}$$

$$+ \mathcal{E}_c \left(\frac{\mathcal{E}_c}{\hbar\Omega_w} \right) \sum_{\mu\nu i} |\mu)\langle\mu|\mathcal{V}^+ d_i^\dagger d_i \mathcal{V}|\nu\rangle(\nu| \left\{ \left(a^\dagger a + \frac{1}{2} \right) + \frac{1}{2} \left(aa + a^\dagger a^\dagger \right) \right\}. \tag{8}$$

In order to finally obtain the energy spectrum of the electron-photon Hamiltonian (8) we need to construct a MB-space $|\mu) \otimes |N_{\rm ph}\rangle \longrightarrow |\mu\rangle_{\rm e-EM}$ out of the Coulomb interacting MESs $|\mu)$ and the eigenstates of the photon number operator $|N_{\rm ph}\rangle$. To properly take account of the effects of the Coulomb interaction we selected a large basis $\{|\mu)\}$ and many photon states since the strong coupling to the cavity photons requires many states. For the system parameters to be introduced later we find that basis build up of the 64 lowest in energy Coulomb interacting MESs and 27 photon states is adequate for the transport bias windows and the electron-photon coupling to be selected later. The catch is that the unitary transform has to be performed with the full untruncated basis since $\mathcal{V}$ can not be truncated. In other words each of the 64 interacting MESs $|\mu)$ remains a superposition of all of the $2^{N_{\rm SES}}$ noninteracting MESs $|\mu\rangle$ with the same number of electrons $N_{\rm e}$, i. e. $|\mu)$ is a linear combination of a subset of $\binom{N_{\rm SES}}{N_{\rm e}}$ terms. (A similar issue is met when the dimensionless coupling tensor g_{ij} (7) is transformed from the original single-electron basis to the single-electron states $|i\rangle$).

The diagonalization of H_0 produces the new interacting electron-photon states $|\breve{\mu}) = \sum_\alpha \mathcal{W}_{\mu\alpha}|\alpha\rangle_{\rm e-EM}$ with a known integer electron content, but an indefinite number of photons, since the photon number operator does not commute with H_0. The MB energy spectra for the x- and y-polarization of the photon mode are shown in Fig. 2 in comparison with the subbandstructure of the single-electron spectrum of the leads. The difference in the energy spectra for the x- and the y-polarization stems from the anisotropic electron system. The photon mode selected with energy 0.4 meV is close to be in resonance with the motion in the x-direction, but quite far from the fundamental energy in the y-direction, 1.0 meV. The spectrum for the x-polarization thus displays stronger dispersion and interaction of levels than the spectrum for the y-polarization.

The states of the closed system in Fig. 2 have a definite number of electrons and an undetermined number of photons of one given polarization. Later when the system is coupled to the leads one can expect the electrons entering the system to radiate photons with any polarization. A preferred polarization could though be influenced by the aspect ratio of the cavity. In the treatment of the time-dependent system to follow we assume the electrons only to radiate photons with one given polarization. This is done to facilitate the numerical calculations and the analysis of a system with a strong spatial anisotropy.

3   Opening of the system, coupling to external leads

At time $t = 0$ the closed system of Coulomb interacting electrons coupled to cavity photons described by the Hamiltonian (8) is connected to two external semi-infinite quasi-one-dimensional quantum wires in a perpendicular magnetic field [8]. We use an approach introduced by Nakajima and Zwanzig to project the time evolution of the total system onto the central system by partial tracing operations with respect to the operators of the leads [12, 13]. The coupling Hamiltonian of the central system (i. e. the short Q1D wire)
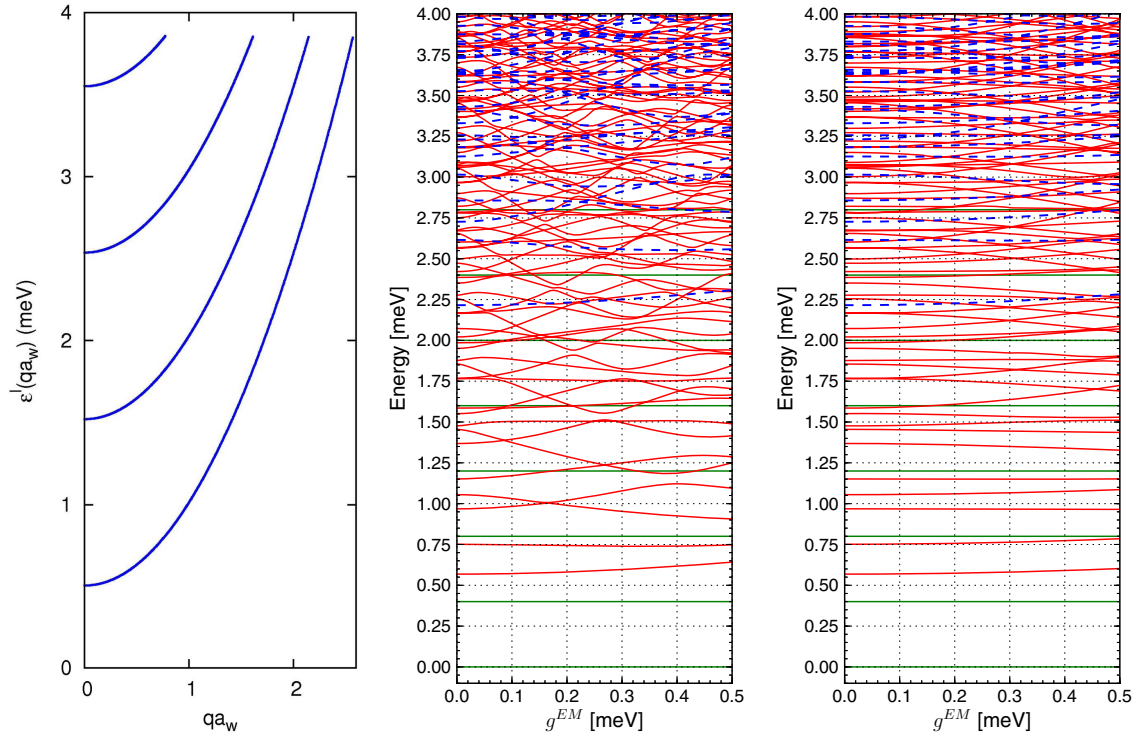
Fig. 2 (online colour at: www.fp-journal.org) The single-electron energy spectrum of the leads (left panel) versus the "subband momentum" qa_w, and the many-body energy spectra for Coulomb interacting electrons coupled to quantized cavity photon modes with the electric component polarized along the finite quantum wire (x-polarization, center panel), and perpendicular to the wire (y-polarization, right panel) versus the electron-photon coupling strength $g^{\mathrm{EM}} = \mathcal{E}_c$. In the energy range shown there are states with no electrons (horizontal solid green), one electron (solid red), and two electrons (dashed blue). In order to reach convergence for high $\mathcal{E}_c$ in this figure we use $N_{\mathrm{SES}} = 200$ here. $B = 0.1$ T, $\hbar\Omega_0 = 1.0$ meV, $\hbar\omega = 0.4$ meV, $\hbar\Omega_0^l = 1.0$ meV, $L_x = 300$ nm, $m^* = 0.067m_e$, $\kappa = 12.4$, the dielectric constant of GaAs.

to the leads is of the form

$$H_{\mathrm{T}}(t) = \sum_{i,l} \chi^l(t) \int dq \left\{ T_{qi}^l c_{ql}^\dagger d_i + (T_{qi}^l)^* d_i^\dagger c_{ql} \right\}, \tag{9}$$

where $l \in \{L, R\}$ refers to the left or the right lead, and $\chi^l(t)$ is the time-dependent switching function of the coupling. The operators c_{ql} and $c_{ql}^\dagger$ annihilate and create an electron in the l-lead with a quantum number q referring both to the continuous momentum q and the subband n^l, see Fig. 2 for the corresponding energy spectrum. To represent the geometry of the leads and the central system, the coupling tensor T_{qi}^l of single-electron states $|q\rangle$ in the lead l to single-electron states states $|i\rangle$ in the system is modeled as a non-local overlap integral of the corresponding wave functions in the contact regions of the system, Ω_S^l, and the lead l, Ω_l [11]

$$T_{iq}^l = \int_{\Omega_S^l \times \Omega_l} d\mathbf{r} d\mathbf{r}' \left[\psi_q^l(\mathbf{r}') \right]^* \psi_i^S(\mathbf{r}) \, g_{iq}^l(\mathbf{r}, \mathbf{r}'). \tag{10}$$

The function

$$g_{iq}^l(\mathbf{r}, \mathbf{r}') = g_0^l \exp \left[-\delta_1^l(x - x')^2 - \delta_2^l(y - y')^2 \right] \times \exp \left(\frac{-|E_i - \epsilon^l(q)|}{\Delta_E^l} \right) \tag{11}$$

with $\mathbf{r} \in \Omega_{\mathrm{S}}^l$ and $\mathbf{r}' \in \Omega_l$ defines the 'nonlocal Gaussian overlap' determined by the constants δ_1 and δ_2, and the affinity of the states in energy Δ_E^l. The energy spectra of the leads are represented by $\epsilon^l(q)$.

The time-evolution of the total system is determined by the Liouville-von Neumann equation

$$i\hbar \dot{W}(t) = [H(t), W(t)], \quad W(t < 0) = \rho_{\mathrm{L}} \rho_{\mathrm{R}} \rho_{\mathrm{S}}, \tag{12}$$

with W the statistical operator of the total system and ρ_l the equilibrium density operator of the disconnected lead $l \in \{L, R\}$ having chemical potential μ_l

$$\rho_l = \frac{e^{-\beta(H_l - \mu_l N_l)}}{\mathrm{Tr}_l \{ e^{-\beta(H_l - \mu_l N_l)} \}}, \tag{13}$$

where H_l is the Hamiltonian of the electrons in lead $l \in \{L, R\}$ and N_l is their number operator. The Liouville-von Neumann equation (12) is projected on the central system of coupled electrons and photons by a partial tracing operation with respect to the operators of the leads. Defining the reduced density operator (RDO) of the central system

$$\rho_{\mathrm{S}}(t) = \mathrm{Tr}_{\mathrm{L}} \mathrm{Tr}_{\mathrm{R}} W(t), \quad \rho_{\mathrm{S}}(0) = \rho_{\mathrm{S}}, \tag{14}$$

we obtain an integro-differential equation for the RDO, the generalized master equation (GME)

$$\dot{\rho}_{\mathrm{S}}(t) = -\frac{i}{\hbar} [H_{\mathrm{S}}, \rho_{\mathrm{S}}(t)] - \frac{\mathrm{Tr}_{\mathrm{LR}}}{\hbar^2} \left\{ \left[H_{\mathrm{T}}(t), \int_0^t dt' \left[U(t - t') H_{\mathrm{T}}(t') U^+(t - t'), \right. \right. \right.$$
$$\left. \left. \left. U_0(t - t') \rho_{\mathrm{S}}(t') U_0^+(t - t') \rho_{\mathrm{L}} \rho_{\mathrm{R}} \right] \right] \right\}, \tag{15}$$

where the time evolution operator for the closed systems of Coulomb interacting electrons coupled to photons on one hand, and on the other hand noninteracting electrons in the leads is given by $U(t) = \exp\{-i(H_{\mathrm{e}} + H_{\mathrm{Coul}} + H_{\mathrm{EM}} + H_{\mathrm{L}} + H_{\mathrm{R}})t/\hbar\}$, without the coupling to the leads $H_{\mathrm{T}}(t)$. Here, H_{e} is the Hamiltonian for the electrons in the central system, H_{Coul} their mutual Coulomb interaction, H_{EM} is the Hamiltonian for the photons in the cavity together with their interaction to the electrons, and $H_{\mathrm{L,R}}$ are the Hamiltonian operators for the electrons in the left and right leads. The time evolution of the closed system of Coulomb interacting electrons interacting with the photons is governed by $U_0(t) = \exp\{-iH_0 t/\hbar\}$. The GME (15) is valid in the weak system-leads coupling limit since we have only retained terms of second order in the coupling Hamiltonian H_{T} in its integral kernel. It should though be stressed that we are not approximating the GME to second order in the coupling as its integral structure effectively provides terms of any order, but with a structure reflecting the type of the integral kernel.

Commonly, the GME is written in terms of spectral densities for the states in the system instead of the coupling tensor (10). We do not make this transformation but the spectral densities for the 10 lowest SESs used in our system have been presented elsewhere [9] (Here the overall coupling is one quarter of the value used in [9]). The spectral density is a particularly useful physical concept as it demonstrates the spectral broadening of the SESs in the finite system due to the coupling to the leads.

4 Transport characteristics

The time-dependent coupling betweeen the leads and the central system is modeled by the switching functions $\chi^l(t)$. These functions may be considered input elements of the transport problem: stepwise functions, periodic, relatively phase-shifted, etc. In the following examples the left and right leads are coupled simultaneously smoothly to the central system by use of the switching function

$$\chi^l(t) = \left(1 - \frac{2}{e^{\alpha^l t} + 1} \right), \quad l \in \{L, R\} \tag{16}$$

with $\alpha^l = 0.3$ ps^{-1}. The temperature of the leads $T = 0.5$ K, and the overall coupling strength $g_0^l a_w^{3/2} = 13.3$ meV, is much lower than in our earlier calculation [9]. We choose $\delta_{1,2}^l a_w^2 = 0.4916$ meaning that states of a lead and the central system with considerable charge density within a length equivalent to $2a_w$ ($a_w \approx 33.5$ nm here) could be well coupled.

The energy of the photon mode is $\hbar\omega = 0.4$ meV, and the electron confinement in the y-direction has the energy scale $\hbar\Omega_0 = 1.0$ meV. The energy separation of the lowest states for the motion in the x-direction is lower, ~ 0.2 meV. The Coulomb interaction has a characteristic energy scale $0.5e^2/(\kappa a_w) \approx 1.7$ meV. The external magnetic field is low enough so that only the highest lying SESs show any effects of the Lorentz force. We expect thus the transport properties of the system to be anisotropic at a low energy scale with respect to polarization of the photon field along (x-direction) or perpendicular (y-direction) to the transport.
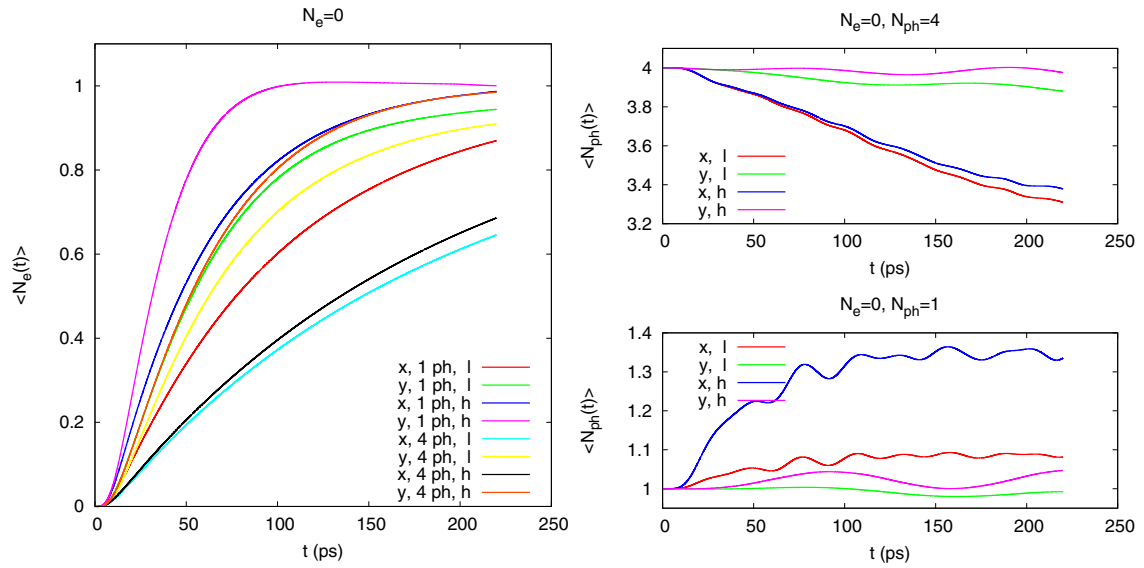

Fig. 3 (online colour at: www.fp-journal.org) The total mean number of electrons $\langle N_e(t)\rangle$ (left panel), and the total mean photon number $\langle N_{\mathrm{ph}}(t)\rangle$ (right panels) as a function of time, polarization of the photon field (x or y) and bias window low (l: $\mu_L = 2.0$ and $\mu_R = 1.4$ meV) or high (h: $\mu_L = 3.0$ and $\mu_R = 2.5$ meV). $B = 0.1$ T, $g^{\mathrm{EM}} = 0.1$ meV, $\hbar\Omega_0 = 1.0$ meV, $L_x = 300$ nm, $\hbar\omega = 0.4$ meV, $\Delta_E^l = 0.25$ meV, $g_0^l a_w^{3/2} = 13.3$ meV, $\delta_{1,2}^l a_w^2 = 0.4916$, $m^* = 0.067 m_e$, and $\kappa = 12.4$.

In the present calculations we start with a central system empty of electrons, but with one or four photons in the cavity. For $N_{\mathrm{SES}} = 18$ the state with no electron, but one photon, is $|\breve{2}\rangle$ for both polarizations. The state containing 4 photons and no electrons is $|\breve{14}\rangle$ for the x-polarization and $|\breve{15}\rangle$ in the case of the y-polarization. The time evolution of the total mean electron number $\langle N_e(t)\rangle$ is seen in the left panel of Fig. 3 and the total mean number of photons $\langle N_{\mathrm{ph}}(t)\rangle$ is displayed in the lower right panel for the case of initially one photon and in the upper panel for initially 4 photons. The charging of the system is in most cases fastest for the higher bias window as the active states of the central system are well coupled to states in the leads that carry a large current in this energy range. The presence of photons in the system sharply diminishes the charging speed, especially for their polarization along the transport direction (x-direction). The time evolution of the total mean number of photons in the system does not give much insight into what is happening in the system, but it is though clear that it varies more in case of the x-polarization.

Very similar information can be read from the graphs of the total currents in the left (L) or the right (R) leads shown in Fig. 4. The negative values for the current into the right lead indicate a flow from the lead to the central system. A note of caution here is that we are concentrating on the charging time-regime here
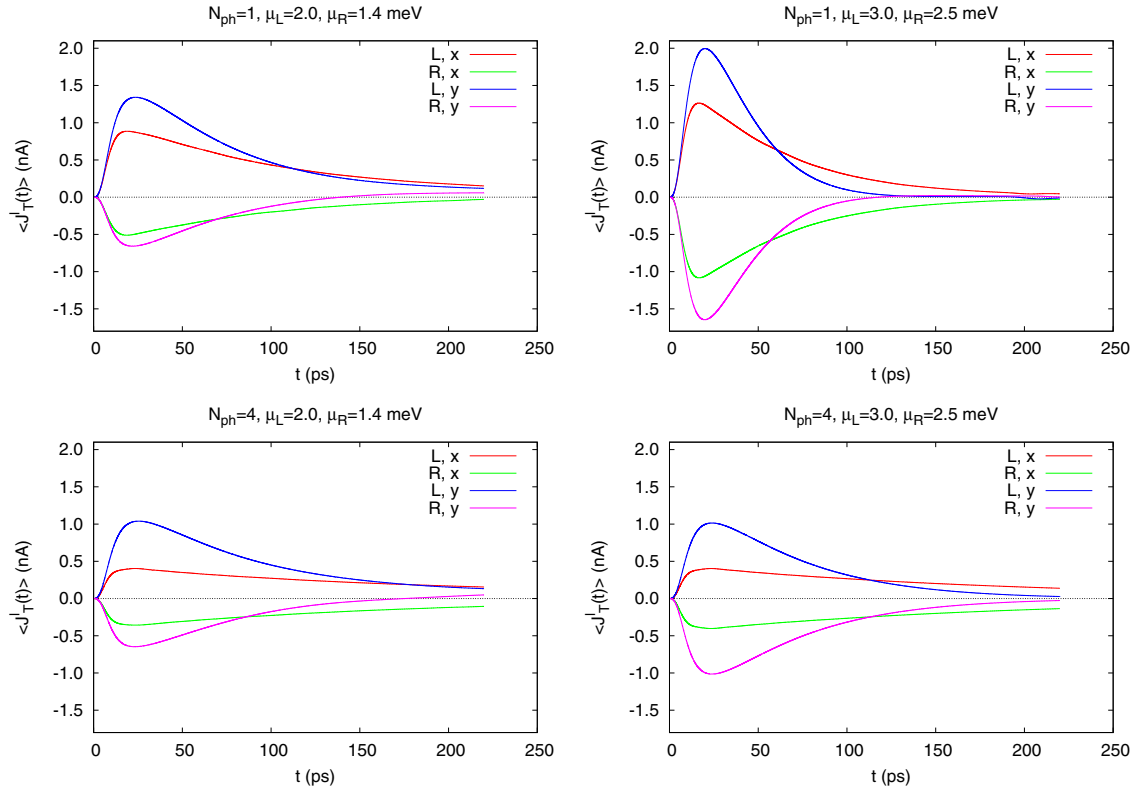
Fig. 4 (online colour at: www.fp-journal.org) The total current from the left lead (L), and into the right lead (R) as a function of time for $g^{EM} = 0.1$ meV and polarization of the photon field (x or y). Initially, at $t = 0$ there is one photon in the cavity (top panel), or 4 photons (bottom panel). The bias window is low ($\mu_L = 2.0$ and $\mu_R = 1.4$ meV) for the left panels and high ($\mu_L = 3.0$ and $\mu_R = 2.5$ meV) for the right panels. $B = 0.1$ T, $\hbar\Omega_0 = 1.0$ meV, $L_x = 300$ nm, $\hbar\omega = 0.4$ meV, $\mu_L = 2.0$ meV, $\mu_R = 1.4$ meV, $\Delta_E^l = 0.25$ meV, $g_0^l a_w^{3/2} = 13.3$ meV, $\delta_{1,2}^l a_w^2 = 0.4916$, $m^* = 0.067 m_e$, and $\kappa = 12.4$.

and we are not trying to reach a possible steady state, but clearly we are most likely in a Coulomb blocking range. It is our experience that a considerable probability for two electrons in the system is only seen after several two-electron states are in or under the bias window. The reason for this is most likely the different coupling between states in the leads and the system, how far the system is from equilibrium and, and how the coupling strength influences the rate of occupation of various dynamically correlated states. We have verified that a still higher bias leads to a nonvanishing steady state current. Here, we always have at least one photon initially in the cavity and we notice that the charging rate and the currents are mostly higher for the y-polarization. The time-scale for the charging in the x-polarization gets very long as the photon number is increased from 1 to 4. This is not a total surprise since the energy of the photons is closer to characteristic excitation energies for a motion in the x-direction.

A detailed view of the charging processes can be obtained by observing the time-dependent probabilities for occupation of the available many-body states (MBS) by electrons or photons. In Fig. 5 we see the mean charge in the MBS for the transport through the lower bias window $\mu_L = 2.0$ and $\mu_R = 1.4$ meV. The MBS $|\breve{\mu})$ are numbered according to increasing energy. We see clearly that the system is not close to equilibrium and the charge is "scattered" to more states for the x-polarization than the y-polarization. The presence of photons has large effects on the electrons in the system.
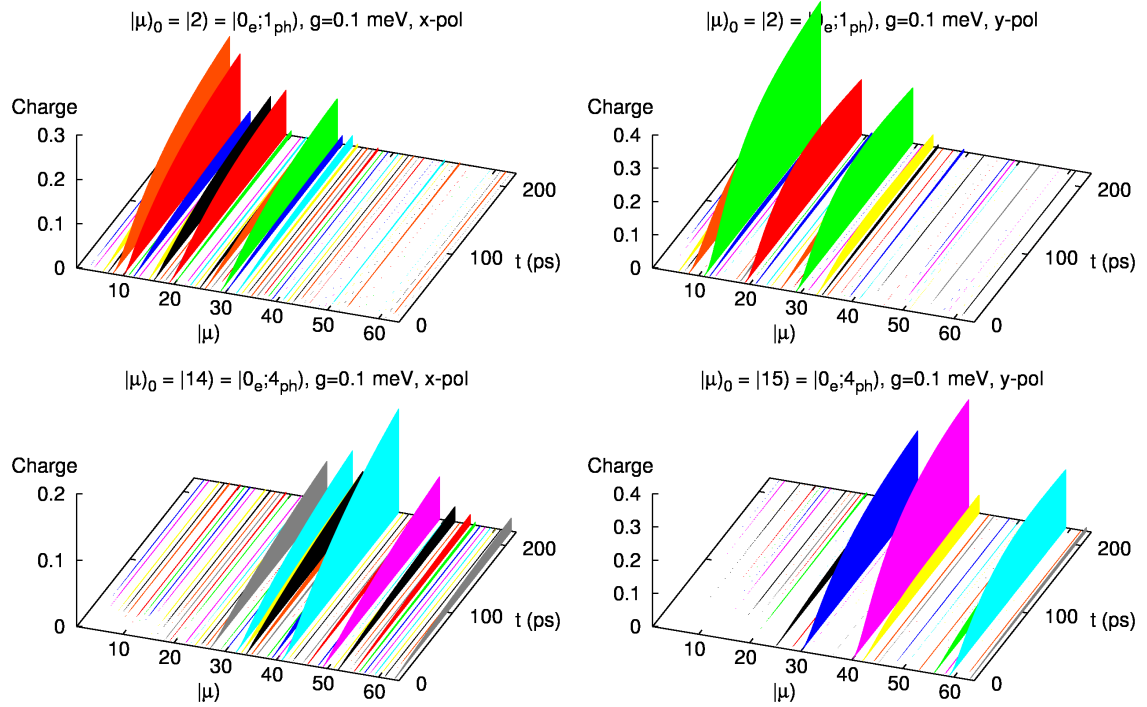
Fig. 5 (online colour at: www.fp-journal.org) The mean number of electrons $\langle N_e(t) \rangle$ in a MBS $|\breve{\mu}\rangle$ for a low bias window ($\mu_L = 2.0$ and $\mu_R = 1.4$ meV) for x-polarization (left) and y-polarization (right) as a function of time. Initially, at $t = 0$, there is one photon in the cavity (top panels), or 4 photons (bottom panels). The initial number of electrons is zero in all cases. $B = 0.1$ T, $g^{EM} = 0.10$ meV, $\hbar\omega = 0.4$ meV, $\hbar\Omega_0 = 1.0$ meV, $\Delta_E^l = 0.25$ meV, $g_0^l a_w^{3/2} = 13.3$ meV, $\delta_{1,2}^l a_w^2 = 0.4916$, $L_x = 300$ nm, $m^* = 0.067 m_e$, and $\kappa = 12.4$.

Very similar story can be said about the results for the higher bias window, $\mu_L = 3.0$ and $\mu_R = 2.5$ meV displayed in Fig. 6. Especially interesting is to see that the results for both polarizations are almost identical for the higher and lower bias window for the case of 4 photons initially in the central system. The effects of the bias window are washed out by the strong interaction with the quantized electromagnetic field in the cavity. We have though to bring in a note of caution here and admit that this effect should be studied further using a larger MB basis for the RDO.

A complete picture can not be reached without exploring the time-evolution of the mean photon number per MBS presented in Fig. 7 for the lower bias window and in 8 for the higher bias window. Again we notice that the state of the system, the distribution of the photon component into various MBS, is almost independent of the the bias window in the case of 4 photons initially in the cavity.

But, here another very important fact about the system evolution becomes evident. The occupation of the initial photon state seems to vary much faster with time than the total mean number of photons shown in Fig. 3. The slow decay of the charging current in Fig. 4 for the system with 4 photons initially might also indicate that radiation processes here are slow. Why then do we have a fast redistribution of the photon component between the available MBS initially, during the switch-on process? The resolution of this dilemma comes from remembering the structure of the interaction terms. Part of the interaction is an integral over the term $\mathbf{j} \cdot \mathbf{A}$. We have a vector field initially present in the system. The high current into the system during the transient phase, when the contacts between the leads and the central system are switched on, creates a strong interaction that can "scatter" the electrons and the photons to different MBS, few or many, depending on selections rules and resonances. This initial rushing of electrons from both ends of the finite quantum wire is a longitudinal (irrotational) current that enhances the coupling to the photon
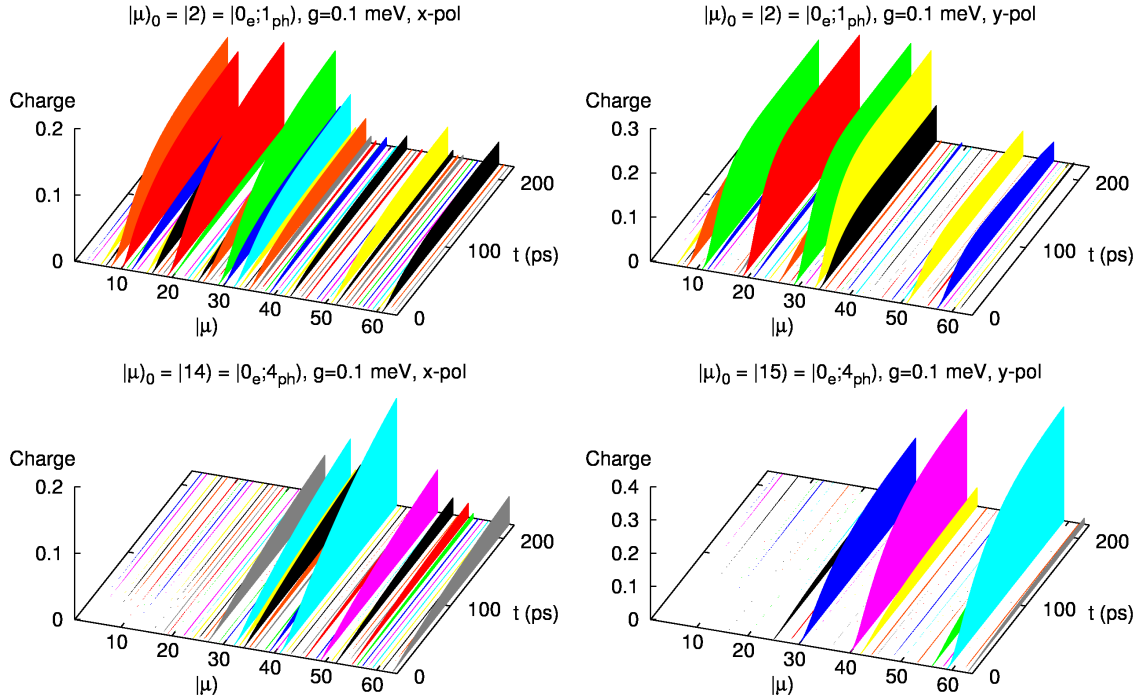
Fig. 6 (online colour at: www.fp-journal.org) The mean number of electrons $\langle N_e(t) \rangle$ in a MBS $|\breve{\mu}\rangle$ for a high bias window ($\mu_L = 3.0$ and $\mu_R = 2.5$ meV) for x-polarization (left) and y-polarization (right) as a function of time. Initially, at $t = 0$, there is one photon in the cavity (top panels), or 4 photons (bottom panels). The initial number of electrons is zero in all cases. $B = 0.1$ T, $g^{\mathrm{EM}} = 0.10$ meV, $\hbar\omega = 0.4$ meV, $\hbar\Omega_0 = 1.0$ meV, $\Delta_E^l = 0.25$ meV, $g_0^l a_w^{3/2} = 13.3$ meV, $\delta_{1,2}^l a_w^2 = 0.4916$, $L_x = 300$ nm, $m^* = 0.067 m_e$, and $\kappa = 12.4$.

field. This effect can be seen very well by comparing the photon distribution into the MBS at the low bias window and for the case of only one photon initially present in the cavity.

In case of the x-polarization we see that the system seems to develop a higher "impedance" acting against its charging as the number of photons is increased, and at the same time the electrons that enter the system are scattered to a wide range of MBS. The "impedance" has to be understood from the fact that the photon field is polarizing the electron density inside the system along the x-direction. Effectively, the states may gain coupling strength to the leads, but that works in both ways. The electrons enter the system easily and leave it equally easily at the same end before they can be transported through it. The charging of the system is counteracted by an effective scattering of a localized photon field. A phenomena that should be similar for a system with localized phonons.

5 Summary

In this publication we have shown how we have successfully been able to implement a scheme which we wish to call: "A stepwise introduction of complexity to a model description and a careful counteracting stepwise truncation of the ensuing many-body space" to describe a time-dependent transport of Coulomb interacting electrons through a photon cavity. We have used this approach to demonstrate how the geometry of a particular system leaves its fingerprints on its transport properties. We guarantee geometrical dependence by using a phenomenological description of the system-lead coupling based on a nonlocal overlap of the single-electron states in the leads and the system in the contact area, and by using a large basis of
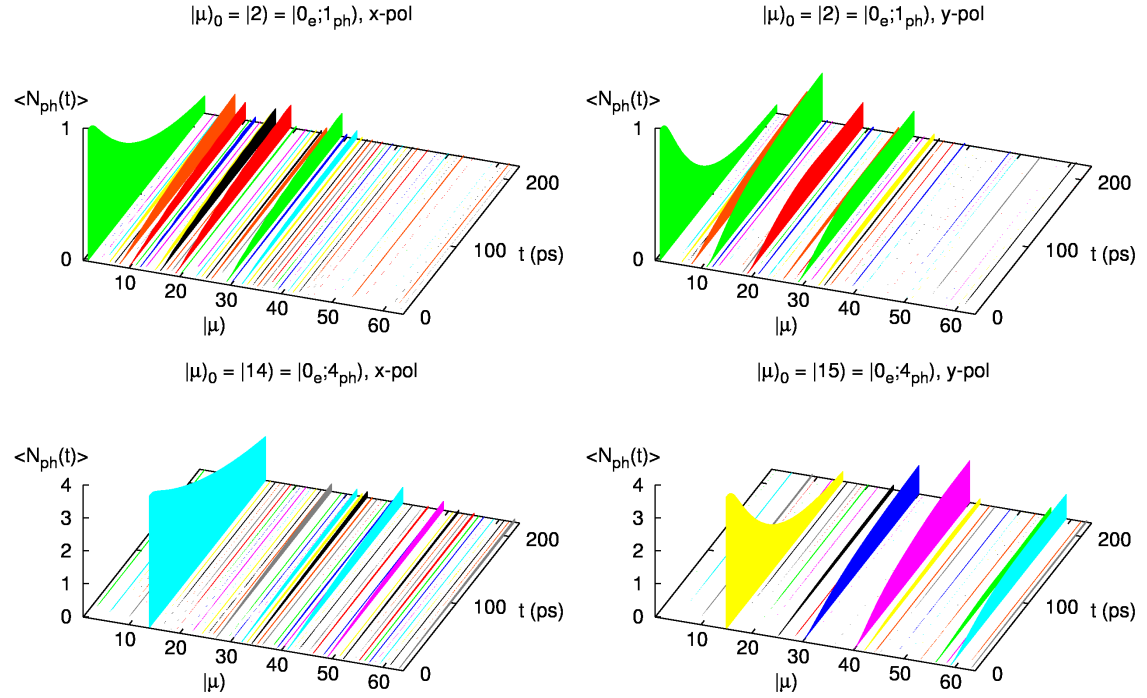
Fig. 7 (online colour at: www.fp-journal.org) The mean number of photons $\langle N_{\mathrm{ph}}(t) \rangle$ in a MBS $|\breve{\mu}\rangle$ for a low bias window ($\mu_L = 2.0$ and $\mu_R = 1.4$ meV) for x-polarization (left) and y-polarization (right) as a function of time. Initially, at $t = 0$, there is one photon in the cavity (top panels), or 4 photons (bottom panels). $B = 0.1$ T, $g^{\mathrm{EM}} = 0.1$ meV, $\hbar\omega = 0.4$ meV, $\hbar\Omega_0 = 1.0$ meV, $\Delta_E^l = 0.25$ meV, $g_0^l a_w^{3/2} = 13.3$ meV, $\delta_{1,2}^l a_w^2 = 0.4916$, $L_x = 300$ nm, $m^* = 0.067 m_e$, and $\kappa = 12.4$.

SESs in order to build our MBS. The Coulomb interaction is implemented by an "exact numerical diagonalization", and the coupling to the quantized electromagnetic cavity field of a single frequency is carried out using both the paramagnetic and the diamagnetic part of the charge current density. The coupling of the electrons and the photons is also treated by an exact numerical diagonalization without resorting to the rotating wave approximation. This approach is thus applicable for the modeling of circuit-QED elements in the strong coupling limit.

We have deployed the GME method to include memory effects without a Markov approximation. Moreover, the GME approach is utilized to describe the coupling of the electron-photon system to the external leads. At this moment in the development of the model we ignore the spin variable of freedom, but it can easily be included. The inclusion of the spin is (more or less) straight forward, but it requires a double amount of computer memory and an increased number of MBSs in the GME solver. This is work in progress now.

We concentrate our investigations on the charging regime of the system and find that it is strongly influenced by the presence of photons in the cavity, their polarization and the geometry of the system. We consider these results presented here as the mere initial steps into the exploration of a fascinating regime of circuit-QED elements.

For the numerical implementation we rely heavily on parallel processing, but we foresee further refinement in the truncation schemes for the many-body spaces and in the parallelization that will allow us to describe systems of increased complexity.
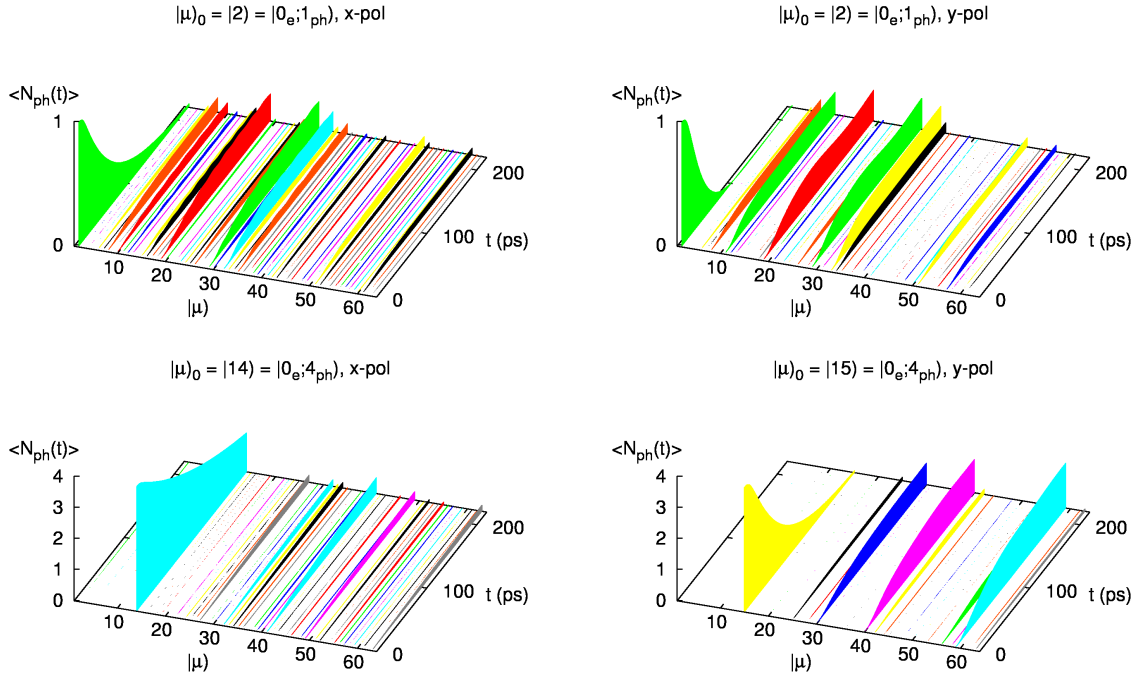
Fig. 8 (online colour at: www.fp-journal.org) The mean number of photons $\langle N_{\mathrm{ph}}(t) \rangle$ in a MBS $|\breve{\mu})$ for a high bias window ($\mu_L = 3.0$ and $\mu_R = 2.5$ meV) for x-polarization (left) and y-polarization (right) as a function of time. Initially, at $t = 0$, there is one photon in the cavity (top panels), or 4 photons (bottom panels). $B = 0.1$ T, $g^{\mathrm{EM}} = 0.1$ meV, $\hbar\omega = 0.4$ meV, $\hbar\Omega_0 = 1.0$ meV, $\Delta_E^l = 0.25$ meV, $g_0^l a_w^{3/2} = 13.3$ meV, $\delta_{1,2}^l a_w^2 = 0.4916$, $L_x = 300$ nm, $m^* = 0.067 m_e$, and $\kappa = 12.4$.

References

[1] T. Niemczyk et al., Nature (Phys. Sci.) **6**, 772 (2010).

[2] T. Frey et al., arXiv:1108.5378 (2011).

[3] M. Delbecq et al., Phys. Rev. Lett. **107**, 256804 (2011).

[4] E. T. Jaynes and F. W. Cummings, Proc. IEEE. **51**, 89 (1963).

[5] A. Joshi and S. V. Lawande, Phys. Rev. A **48**, 2276 (1993).

[6] O. Jonasson et al., New J. Phys. **14**, 013036 (2012).

[7] V. Moldoveanu, A. Manolescu, C. S. Tang, and V. Gudmundsson, Phys. Rev. B **81**, 155442 (2010).

[8] V. Gudmundsson et al., Phys. Rev. B **81**, 205319 (2010).

[9] V. Gudmundsson et al., Phys. Rev. B **85**, 075306 (2012).

[10] V. Moldoveanu, A. Manolescu, and V. Gudmundsson, New J. Phys. **11**(7), 073019 (2009).

[11] V. Gudmundsson et al., New J. Phys. **11**(11), 113007 (2009).

[12] S. Nakajima, Prog. Theor. Phys. **20**, 948 (1958).

[13] R. Zwanzig, J. Chem. Phys. **33**, 1338 (1960).
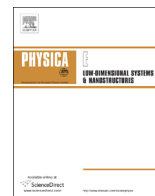
Impact of a circularly polarized cavity photon field on the charge and spin flow through an Aharonov–Casher ring

Thorsten Arnold [a,*], Chi-Shung Tang [b], Andrei Manolescu [c], Vidar Gudmundsson [a]

[a] Science Institute, University of Iceland, Dunhaga 3, IS-107 Reykjavik, Iceland
[b] Department of Mechanical Engineering, National United University, 1, Lienda, Miaoli 36003, Taiwan
[c] School of Science and Engineering, Reykjavik University, Menntavegur 1, IS-101 Reykjavik, Iceland

HIGHLIGHTS

- Transport of spin–orbit coupled electrons interacting with cavity photons.
- Photonic charge current vortices in finite-width quantum ring connected to leads.
- Circularly polarized photon field increases spin polarization and spin photocurrents.
- Threefold Aharonov–Casher charge current dip for circularly polarized photon field.
- Wide-range Aharonov–Casher phase sensitivity of the persistent charge photocurrent.

GRAPHICAL ABSTRACT
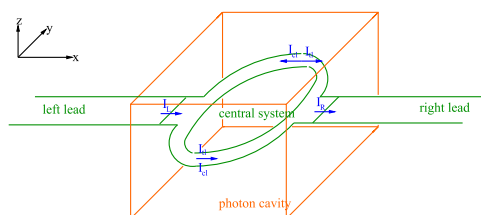
ARTICLE INFO

ABSTRACT

We explore the influence of a circularly polarized cavity photon field on the transport properties of a finite-width ring, in which the electrons are subject to spin–orbit and Coulomb interaction. The quantum ring is embedded in an electromagnetic cavity and described by "exact" numerical diagonalization. We study the case that the cavity photon field is circularly polarized and compare it to the linearly polarized case. The quantum device is moreover coupled to external, electrically biased leads. The time propagation in the transient regime is described by a non-Markovian generalized master equation. We find that the spin polarization and the spin photocurrents of the quantum ring are largest for circularly polarized photon field and destructive Aharonov–Casher (AC) phase interference. The charge current suppression dip due to the destructive AC phase becomes threefold under the circularly polarized photon field as the interaction of the electrons' angular momentum and spin angular momentum of light causes many-body level splitting leading to three many-body level crossing locations instead of one. The circular charge current inside the ring, which is induced by the circularly polarized photon field, is found to be suppressed in a much wider range around the destructive AC phase than the lead-device-lead charge current. The charge current can be directed through one of the two ring arms with the help of the circularly polarized photon field, but is superimposed by vortices of smaller scale. Unlike the charge photocurrent, the flow direction of the spin photocurrent is found to be independent of the handedness of the circularly polarized photon field.

© 2014 Elsevier B.V. All rights reserved.

* Corresponding author.: Tel.: +354 5254181.
E-mail addresses: tla1@hi.is (T. Arnold), cstang@nuu.edu.tw (C.-S. Tang), manoles@hr.is (A. Manolescu), vidar@hi.is (V. Gudmundsson).

1. Introduction

Quantum rings are interferometers with unique properties owing to their rotational symmetric geometry. Because of their non-trivially connected topology, a variety of geometrical phases can be observed [1–4], which can be tuned via the magnetic flux through the ring in the case of the Aharonov–Bohm (AB) phase, or the strength of the spin–orbit interaction (SOI) in the case of the Aharonov–Casher (AC) phase. Furthermore, the rotational symmetry of the ring resembles the characteristics of a circularly polarized photon field suggesting a strong light–matter interaction between single photons and the ring electrons. Circularly polarized light emission [5] and absorption [6] have been studied for quantum rings. Moreover, circularly polarized light has been used to generate persistent charge currents in quantum wells [7] and quantum rings [8–11]. The basic principle behind this is a change of the orbital angular momentum of the electrons in the quantum ring by the absorption or emission of a photon leading to the circular charge transport. We would like to mention that one can improve over circularly polarized light to achieve optimal optical control for a finite-width quantum ring [12]. Rather than trying to optimize quantum transitions, we are focusing here on various interesting effects that a circularly polarized photon field has on quantum rings of spin–orbit and Coulomb interacting electrons.

The transport properties of magnetic-flux threaded rings, which are connected to two leads have been investigated in detail [13,14]. The conductance of the ring shows characteristic oscillations with period $\Phi_0 = hc/e$, called AB oscillations, which were measured for the first time in 1985 [15]. The electrons' spin is not only interacting with a magnetic field via the Zeeman interaction, but also with an electric field via a so-called effective magnetic field stemming from special relativity [16]. The interaction between the spin and the electronic motion in, for example, the electric field, is called the Rashba SOI [17], which leads to the AC effect. Experimentally, the strength of the Rashba interaction can be varied by changing the magnitude of the electric field when it is oriented parallel to the central axis of the quantum ring. Another type of SOI is the Dresselhaus interaction [18], leading to the AC effect as well. The combined effects of SOI and an applied magnetic field on the electronic transport through quantum rings connected to leads have been addressed in several studies [19–23]. In this work, we use a small magnetic field outside the AB regime and a tunable Rashba or Dresselhaus SOI up to a strength corresponding to an AC phase difference $\Delta\Phi \approx 3\pi$ and use cavity quantum electrodynamics to describe the interaction of the electronic system with a circularly polarized photon field in a cavity.

While the magnetic flux through the ring causes only equilibrium persistent *charge* currents [24,25], SOI can also induce equilibrium persistent *spin* currents [26,27]. Dynamical spin currents can be obtained by two asymmetric electromagnetic pulses [28]. Optical control of the spin current can be achieved by a non-adiabatic, two-component laser pulse [29]. The persistent spin current is in general not conserved [30]. Proposals to measure persistent spin currents by the induced mechanical torque [31] or the induced electric field [30] exist.

Quantum systems embedded in an electromagnetic cavity have become one of the most promising devices for quantum information processing applications [32–34]. We are considering here the influence of the cavity photons on the spin polarization of the quantum ring and on the transient charge and spin transport inside and into and out of the ring. We treat the electron–photon interaction by using exact numerical diagonalization including many levels [35], i.e. beyond a two-level Jaynes–Cummings model or the rotating wave approximation and higher order corrections of it [36–38]. The electronic transport through a quantum system that is strongly coupled to leads has been investigated for linearly polarized electromagnetic fields [39–43]. For a weak coupling

between the system and the leads, the Markovian approximation, which neglects memory effects in the system, can be used [44–47]. To describe a stronger transient system–lead coupling, we use a non-Markovian generalized master equation [48–50] in a time-convolutionless form [51,52], which involves energy-dependent coupling elements. We used this type of master equations earlier to explore the interplay of linearly polarized cavity photons and topological phases of quantum rings for the AB [52] and AC [53] phase. The influence of a quantized cavity photon mode of *circularly* polarized light on the time-dependent transport of spin–orbit and Coulomb interacting electrons under non-equilibrium conditions through a topologically nontrivial broad ring geometry, which is connected to leads has not yet been explored beyond the Markovian approximation. We note that we can compare our results to the analytic results for a one-dimensional quantum ring with Rashba or Dresselhaus SOI [53].

The paper is organized as follows. In Section 2, we describe the Hamiltonian for the central quantum ring system including SOI, which is embedded in a photon cavity and our time-dependent generalized master equation formalism for the transient coupling to semi-infinite leads. In addition, various transport quantities that are shown in Sections 3 and 4, are here defined. Section 3 shows the numerical results concerning the spin polarization of the quantum ring, both for linear and for circular polarization. Section 4 is devoted to the transport of charge and spin. First, the non-local currents (lead-ring currents) between the leads and the system are discussed. Second, the change of the local currents inside the quantum ring due to the photon cavity (photocurrent) is considered. Finally, conclusions will be drawn in Section 5.

2. Theory, model and definitions

Here, we describe the Hamiltonian of the central system including the potential used to model the quantum ring, the Hamiltonian for the leads and the time evolution of the whole system described by a non-Markovian master equation. Furthermore, we define various quantities describing the transient charge and spin transport and their accumulation in the quantum ring and the parameters used for the numerical results.

2.1. Central system Hamiltonian

The time-evolution of the closed many-body (MB) system composed of the interacting electrons and photons relative to the initial time $t=0$,

$$\hat{U}_S(t) = \exp\left(-\frac{i}{\hbar}\hat{H}_S t\right),\tag{1}$$

is governed by the MB system Hamiltonian

$$\hat{H}_S = \int d^2r \hat{\Psi}^\dagger(\mathbf{r})\left[\left(\frac{\hat{\mathbf{p}}^2}{2m^*} + V_S(\mathbf{r})\right) + H_Z + \hat{H}_R(\mathbf{r}) + \hat{H}_D(\mathbf{r})\right]\hat{\Psi}(\mathbf{r}) + \hat{H}_{ee} + \hbar\omega\hat{a}^\dagger\hat{a},\tag{2}$$

with the spinor

$$\hat{\Psi}(\mathbf{r}) = \begin{pmatrix} \hat{\Psi}(\uparrow,\mathbf{r}) \\ \hat{\Psi}(\downarrow,\mathbf{r}) \end{pmatrix}\tag{3}$$

and

$$\hat{\Psi}^\dagger(\mathbf{r}) = \left(\hat{\Psi}^\dagger(\uparrow,\mathbf{r}), \hat{\Psi}^\dagger(\downarrow,\mathbf{r})\right),\tag{4}$$

where

$$\hat{\Psi}(x) = \sum_a \psi_a^S(x)\hat{C}_a\tag{5}$$

is the field operator with $x \equiv (\mathbf{r}, \sigma)$, $\sigma \in \{\uparrow, \downarrow\}$ and the annihilation operator, $\hat{C}_a$, for the single-electron state (SES) $\psi_a^S(x)$ in the central system. The SES $\psi_a^S(x)$ is the eigenstate labeled by a of the Hamiltonian $\hat{H}_S - \hat{H}_{ee} - \hbar\omega\hat{a}^\dagger\hat{a}$ when we set the photonic part of the vector potential $\hat{\mathbf{A}}^{ph}(\mathbf{r})$ in the momentum operator,

$$\hat{\mathbf{p}}(\mathbf{r}) = \begin{pmatrix} \hat{p}_x(\mathbf{r}) \\ \hat{p}_y(\mathbf{r}) \end{pmatrix} = \frac{\hbar}{i}\nabla + \frac{e}{c}\left[\mathbf{A}(\mathbf{r}) + \hat{\mathbf{A}}^{ph}(\mathbf{r})\right], \qquad (6)$$

to zero. The Hamiltonian in Eq. (2) includes a kinetic part, a static external magnetic field $\mathbf{B} = B\hat{z}$, in Landau gauge being represented by the vector potential $\mathbf{A}(\mathbf{r}) = -By\mathbf{e}_x$ and a photon field. Furthermore, in Eq. (2),

$$H_Z = \frac{\mu_B g_S B}{2}\sigma_z \qquad (7)$$

describes the Zeeman interaction between the spin and the magnetic field, where g_S is the electron spin g-factor and $\mu_B = e\hbar/(2m_e c)$ is the Bohr magneton. The interaction between the spin and the orbital motion is described by the Rashba part

$$\hat{H}_R(\mathbf{r}) = \frac{\alpha}{\hbar}\left(\sigma_x \hat{p}_y(\mathbf{r}) - \sigma_y \hat{p}_x(\mathbf{r})\right) \qquad (8)$$

with the Rashba coefficient α and the Dresselhaus part

$$\hat{H}_D(\mathbf{r}) = \frac{\beta}{\hbar}(\sigma_x \hat{p}_x(\mathbf{r}) - \sigma_y \hat{p}_y(\mathbf{r})) \qquad (9)$$

with the Dresselhaus coefficient β. In Eqs. (7)–(9), σ_x, σ_y and σ_z represent the spin Pauli matrices.

Eq. (2) includes the electron–electron interaction

$$\hat{H}_{ee} = \frac{e^2}{2\kappa}\int dx' \int dx \frac{\hat{\Psi}^\dagger(x)\hat{\Psi}^\dagger(x')\hat{\Psi}(x')\hat{\Psi}(x)}{\sqrt{|\mathbf{r}-\mathbf{r}'|^2 + \eta^2}} \qquad (10)$$

with $e > 0$ being the magnitude of the electron charge, which is treated numerically exactly. Only for numerical reasons, we include a small regularization parameter $\eta = 0.2387$ nm in Eq. (10). The last term in Eq. (2) indicates the quantized photon field, where $\hat{a}^\dagger$ is the photon creation operator and $\hbar\omega$ is the photon excitation energy. The photon field interacts with the electron system via the vector potential

$$\hat{\mathbf{A}}^{ph} = A(\mathbf{e}\hat{a} + \mathbf{e}^*\hat{a}^\dagger) \qquad (11)$$

with

$$\mathbf{e} = \begin{cases} \mathbf{e}_x, & \text{TE}_{011} \\ \mathbf{e}_y, & \text{TE}_{101} \\ \frac{1}{\sqrt{2}}[\mathbf{e}_x + i\mathbf{e}_y], & \text{RHcircular} \\ \frac{1}{\sqrt{2}}[\mathbf{e}_x - i\mathbf{e}_y], & \text{LHcircular} \end{cases} \qquad (12)$$

for a longitudinally-polarized (x-polarized) photon field (TE$_{011}$), transversely-polarized (y-polarized) photon field (TE$_{101}$), right-hand (RH) or left-hand (LH) circularly polarized photon field. The electron–photon coupling constant $g^{EM} = eAa_w\Omega_w/c$ scales with the amplitude A of the electromagnetic field. It is interesting to note that the photon field couples directly to the spin via Eqs. (8), (9) and (6). For reasons of comparison and to determine the photocurrents, we also consider results without photons in the system. In this case, $\hat{\mathbf{A}}^{ph}(\mathbf{r})$ and $\hbar\omega\hat{a}^\dagger\hat{a}$ drop out from the MB system Hamiltonian in Eq. (2). Our model of a photon cavity can be realized experimentally [32,33,54] by letting the photon cavity be much larger than the quantum ring (this assumption is used in the derivation of the vector potential, Eq. (11).

2.2. Quantum ring potential

The quantum ring is embedded in the central system of length $L_x = 300$ nm situated between two contact areas that will be
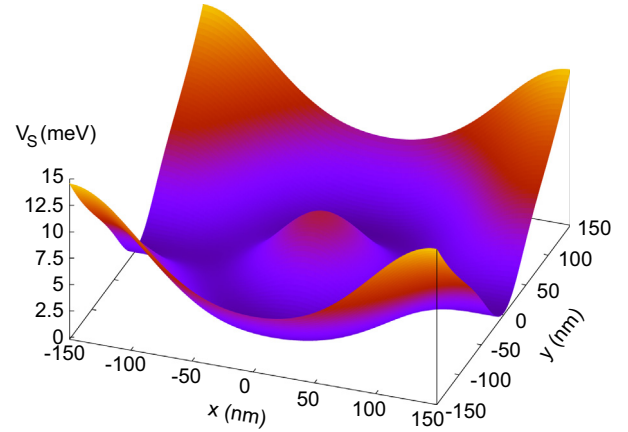
Fig. 1. System potential $V_S(\mathbf{r})$ of the central ring system connected to the left and right leads.

Table 1
Parameters of the ring potential in the central region.

i	V_i (meV)	β_{xi} (nm^{-1})	x_{0i} (nm)	β_{yi} (nm^{-1})
1	10	0.013	150	0
2	10	0.013	−150	0
3	11.1	0.0165	ϵ	0.0165
4	−4.7	0.02	149	0.02
5	−4.7	0.02	−149	0.02
6	−5.33	0	0	0

coupled to the external leads, as is depicted in Fig. 1. The system potential is described by

$$V_S(\mathbf{r}) = \sum_{i=1}^{6} V_i \exp[-(\beta_{xi}(x - x_{0i}))^2 - (\beta_{yi}y)^2] + \frac{1}{2}m^*\Omega_0^2 y^2, \qquad (13)$$

with the parameters from Table 1. $x_{03} = \epsilon$ is a small numerical symmetry breaking parameter and $|\epsilon| = 10^{-5}$ nm is enough for numerical stability. In Eq. (13), $\hbar\Omega_0 = 1.0$ meV is the characteristic energy of the confinement in the system.

2.3. Lead Hamiltonian

The Hamiltonian for the semi-infinite lead $l \in \{L, R\}$ (left or right lead),

$$\hat{H}_l = \int d^2r \int d^2r' \hat{\Psi}_l^\dagger(\mathbf{r}')\delta(\mathbf{r}' - \mathbf{r})\left[\left(\frac{\hat{\mathbf{p}}_l^2}{2m^*} + V_l(\mathbf{r})\right)\right.$$
$$\left. + H_Z + \hat{H}_R(\mathbf{r}) + \hat{H}_D(\mathbf{r})\right]\hat{\Psi}_l(\mathbf{r}), \qquad (14)$$

with the momentum operator containing the kinetic momentum and the vector potential leading only to the magnetic field (i.e. not to the photon field)

$$\hat{\mathbf{p}}_l(\mathbf{r}) = \frac{\hbar}{i}\nabla + \frac{e}{c}\mathbf{A}(\mathbf{r}). \qquad (15)$$

We remind the reader that the Rashba part, $\hat{H}_R(\mathbf{r})$, (Eq. (8)) and the Dresselhaus part, $\hat{H}_D(\mathbf{r})$, (Eq. (9)) of the SOI are momentum-dependent. For the leads, the momentum from Eq. (15), is used for the Rashba and Dresselhaus terms in Eq. (14). Eq. (14) contains the lead field operator

$$\hat{\Psi}_l(x) = \sum_q \psi_{ql}(x)\hat{C}_{ql} \qquad (16)$$

in the spinor

$$\hat{\Psi}_l(\mathbf{r}) = \begin{pmatrix} \hat{\Psi}_l(\uparrow, \mathbf{r}) \\ \hat{\Psi}_l(\downarrow, \mathbf{r}) \end{pmatrix} \tag{17}$$

and a corresponding definition to Eq. (4) for the Hermitian conjugate of $\hat{\Psi}_l(\mathbf{r})$ in Eq. (17). In Eq. (16), $\psi_{ql}(x)$ is a SES in the lead l (eigenstate with quantum number q of the Hamiltonian of Eq. (14)) and $\hat{C}_{ql}$ is the associated electron annihilation operator. The lead potential

$$V_l(\mathbf{r}) = \tfrac{1}{2} m^* \Omega_l^2 y^2 \tag{18}$$

confines the electrons parabolically in the y-direction in the leads with the characteristic energy $\hbar \Omega_l = 2.0$ meV.

2.4. Time-convolutionless generalized master equation approach

We use the time-convolutionless generalized master equation [51] (TCL-GME), which is a non-Markovian master equation that is local in time. This master equation satisfies the positivity conditions [55] for the MB state occupation probabilities in the reduced density operator (RDO) usually to a relatively strong system–lead coupling [52]. We assume the initial total statistical density matrix to be a product state of the system and leads density matrices, before we switch on the coupling to the leads,

$$\hat{W}(0) = \hat{\rho}_L \otimes \hat{\rho}_R \otimes \hat{\rho}_S(0), \tag{19}$$

with ρ_l, $l \in \{L, R\}$, being the normalized density matrices of the leads. The coupling Hamiltonian between the central system and the leads reads

$$\hat{H}_T(t) = \sum_{l=L,R} \int dq \chi^l(t) \left[\hat{\mathfrak{T}}^l(q) \hat{C}_{ql} + \hat{C}_{ql}^\dagger \hat{\mathfrak{T}}^{l\dagger}(q) \right]. \tag{20}$$

The coupling is switched on at $t=0$ via the switching function

$$\chi^l(t) = 1 - \frac{2}{e^{\alpha^l t} + 1} \tag{21}$$

with a switching parameter α^l and

$$\hat{\mathfrak{T}}^l(q) = \sum_{\alpha\beta} |\alpha)(\beta| \sum_a T_{qa}^l(\alpha|\hat{C}_a^\dagger|\beta). \tag{22}$$

Eq. (22) is written in the MB eigenbasis $\{|\alpha)\}$ of the system Hamiltonian, Eq. (2). The coupling tensor [56]

$$T_{qa}^l = \sum_\sigma \sum_{\sigma'} \int_{\Omega^l} d^2r \int_{\Omega_S^l} d^2r' \psi_{ql}^*(\mathbf{r}, \sigma) \times g_{aq}^l(\mathbf{r}, \mathbf{r}', \sigma, \sigma') \psi_a^S(\mathbf{r}', \sigma') \tag{23}$$

couples the lead SES $\{\psi_{ql}(\mathbf{r}, \sigma)\}$ with energy spectrum $\{\epsilon^l(q)\}$ to the system SES $\{\psi_a^S(\mathbf{r}, \sigma)\}$ with energy spectrum $\{E_a\}$ that reaches into the contact regions [57], Ω_S^l and Ω_l, of system and lead l, respectively, and the coupling kernel

$$g_{aq}^l(\mathbf{r}, \mathbf{r}', \sigma, \sigma') = g_0^l \delta_{\sigma,\sigma'} \exp\left[-\delta_x^l(x-x')^2\right] \times \exp\left[-\delta_y^l(y-y')^2\right] \times \exp\left(-\frac{|E_a - \epsilon^l(q)|}{\Delta_E^l}\right) \tag{24}$$

suppresses different-spin coupling. Note that the meaning of x in Eq. (24) is $\mathbf{r} = (x, y)$ and not $x = (\mathbf{r}, \sigma)$. In Eq. (24), g_0^l is the lead coupling strength and δ_x^l and δ_y^l are the contact region parameters for lead l in x- and y-directions, respectively. Moreover, Δ_E^l denotes the affinity constant between the central system SES energy levels $\{E_a\}$ and the lead energy levels $\{\epsilon^l(q)\}$.

When propagated with the TCL-GME [51,52], the RDO of the system,

$$\hat{\rho}_S(t) = \mathrm{Tr}_L \mathrm{Tr}_R[\hat{W}(t)], \tag{25}$$

evolves to second order in the lead coupling strength via

$$\dot{\hat{\rho}}_S(t) = -\frac{i}{\hbar}[\hat{H}_S, \hat{\rho}_S(t)] - \left[\sum_{l=L,R} \int dq [\hat{\mathfrak{T}}^l(q), \hat{\Omega}^l(q,t)\hat{\rho}_S(t) - f(\epsilon^l(q))\{\hat{\rho}_S(t), \hat{\Omega}^l(q,t)\}] + \mathrm{H.c.} \right] \tag{26}$$

with the Fermi distribution function $f(E)$,

$$\hat{\Omega}^l(q,t) = \frac{1}{\hbar^2} \chi^l(t) \exp\left(-\frac{i}{\hbar} t \epsilon^l(q)\right) \times \hat{U}_S(t) \hat{\Pi}^l(q,t) \hat{U}_S^\dagger(t) \tag{27}$$

and

$$\hat{\Pi}^l(q,t) = \int_0^t dt' \left[\exp\left(\frac{i}{\hbar} t' \epsilon^l(q)\right) \chi^l(t') \times \hat{U}_S^\dagger(t') \hat{\mathfrak{T}}^{l\dagger}(q) \hat{U}_S(t') \right]. \tag{28}$$

2.5. Transport quantities used in the numerical results

We investigate numerically the non-equilibrium electron transport properties through a quantum ring system, which is situated in a photon cavity and weakly coupled to leads for the parameters given in Appendix A. To explore the influence of the circularly polarized photon field and the Rashba and Dresselhaus coupling on the non-local charge and the spin polarization current from and into the leads, we define the non-local right-going charge current $I_l^c(t)$ (lead-ring charge current) in lead $l=L,R$ by

$$I_l^c(t) = c_l \mathrm{Tr}[\dot{\hat{\rho}}_S^l(t)\hat{Q}] \tag{29}$$

with $c_L = 1$ and $c_R = -1$, with the charge operator

$$\hat{Q} = \int d^2r \hat{n}^c(\mathbf{r}) \tag{30}$$

and the time-derivative of the RDO in the MB basis due to the coupling of the lead $l \in \{L, R\}$

$$\dot{\hat{\rho}}_S^l(t) = -\int dq [\mathfrak{T}^l(q), [\Omega^l(q,t)\rho_S(t) - f(\epsilon^l(q))\{\rho_S(t), \Omega^l(q,t)\}]] + \mathrm{H.c.} \tag{31}$$

The charge density operator $\hat{n}^c(\mathbf{r})$ in Eq. (30) is given in Appendix B, Eq. (B.1). Similarly, we define the non-local right-going spin polarization current $I_l^i(t)$ for S_i spin polarization (lead-ring spin polarization current) in lead $l=L,R$ by

$$I_l^i(t) = c_l \mathrm{Tr}[\dot{\hat{\rho}}_S^l(t)\hat{S}_i] \tag{32}$$

with $i=x,y,z$ and the spin polarization operator for S_i spin polarization

$$\hat{S}_i = \int d^2r \, \hat{n}^i(\mathbf{r}), \tag{33}$$

where the spin polarization density operator for spin polarization S_i, $\hat{n}^i(\mathbf{r})$, is defined in Eq. (B.2) in Appendix B. To get more insight into the local current flow in the ring system, we define the top local charge ($\gamma=c$) and the spin ($\gamma=x,y,z$, where γ describes the spin polarization) current through the upper arm ($y > 0$) of the ring

$$I_{\mathrm{top}}^\gamma(t) = \int_0^\infty dy j_x^\gamma(x=0, y, t) \tag{34}$$

and the bottom local charge and the spin polarization current through the lower arm ($y < 0$) of the ring

$$I_{\mathrm{bottom}}^\gamma(t) = \int_{-\infty}^0 dy j_x^\gamma(x=0, y, t). \tag{35}$$

Here, the charge and spin polarization current density

$$\mathbf{j}^\gamma(\mathbf{r}, t) = \begin{pmatrix} j_x^\gamma(\mathbf{r}, t) \\ j_y^\gamma(\mathbf{r}, t) \end{pmatrix} = \mathrm{Tr}[\hat{\rho}_S(t)\hat{\mathbf{j}}^\gamma(\mathbf{r})], \tag{36}$$

is given by the expectation value of the charge and spin polarization current density operator, (Eqs. (B.3), B.5), (B.6) and (B.7) in Appendix B. We note that while the charge density is satisfying the continuity equation

$$\frac{\partial}{\partial t} n^c(\mathbf{r}, t) + \nabla \mathbf{j}^c(\mathbf{r}, t) = 0, \tag{37}$$

the continuity equation for the spin polarization density includes in general the source terms

$$s^i(\mathbf{r}, t) = \frac{\partial}{\partial t} n^i(\mathbf{r}, t) + \nabla \mathbf{j}^i(\mathbf{r}, t). \tag{38}$$

The definition for the spin polarization current density ((Eqs. (B.5), B.6) and (B.7) from the appendix) corresponds to the minimal (simplest) expression for the source operator [53] and agrees with the definition of the Rashba current when we limit ourselves to the case without magnetic and photon field and without Dresselhaus SOI [58,59]. Furthermore, to distinguish better the structure of the dynamical transport features, it is convenient to define the total local (TL) charge or the spin polarization current

$$I_{tl}^\gamma(t) = I_{top}^\gamma(t) + I_{bottom}^\gamma(t) \tag{39}$$

and circular local (CL) charge or spin polarization current

$$I_{cl}^\gamma(t) = \frac{1}{2}[I_{bottom}^\gamma(t) - I_{top}^\gamma(t)], \tag{40}$$

which is positive if the electrons move counter-clockwise in the ring. The TL charge current is usually bias driven while the CL charge current can be driven by the circularly polarized photon field (or a strong magnetic field). The TL spin polarization current is usually related to non-vanishing spin polarization sources while a CL spin polarization current can exist without such sources.

To explore the influence of the photon field, we define the TL charge or spin photocurrent

$$I_{ph,tl}^{\gamma,p}(t) = I_{tl}^{\gamma,p}(t) - I_{tl}^{\gamma,0}(t) \tag{41}$$

and CL charge or spin photocurrent

$$I_{ph,cl}^{\gamma,p}(t) = I_{cl}^{\gamma,p}(t) - I_{cl}^{\gamma,0}(t), \tag{42}$$

which are given by the difference of the associated local currents with ($I^{\gamma,p}(t)$) and without ($I^{\gamma,0}(t)$) photons, where $p = x, y, r, l$ denotes the polarization of the photon field (x: x-polarization, y: y-polarization, r: RH circular polarization, l: LH circular polarization). The total charge of the central system is given by

$$Q(t) = \text{Tr}[\hat{\rho}_S(t)\hat{Q}] \tag{43}$$

and the spin polarization of the central system

$$S_i(t) = \text{Tr}[\hat{\rho}_S(t)\hat{S}_i]. \tag{44}$$

3. Spin polarization

In this section, we show the spin polarization of the central ring system for linearly or circularly polarized photon field as a function of the Rashba or Dresselhaus parameter. The ring is connected to leads, in which a chemical potential bias is maintained. The spin polarization $\mathbf{S} = (S_x, S_y, S_z)$ is a three-dimensional vector, which, in the Rashba case, is influenced by the effective magnetic field associated with the Rashba effect.

3.1. Linear photon field polarization

Here, we will compare the spin polarization in the central system for x- or y-polarization of the photon field with the spin polarization in the case that the photon cavity is removed. Fig. 2 shows the spin polarization as a function of the Rashba coefficient. The critical value of the Rashba coefficient, which describes the
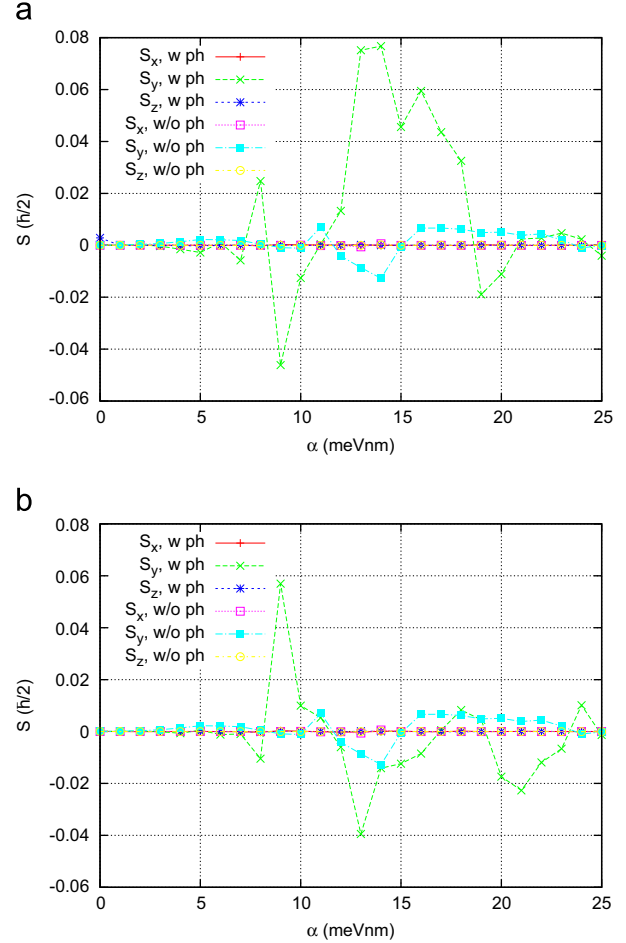
Fig. 2. Spin polarization $\mathbf{S} = (S_x, S_y, S_z)$ of the central system versus the Rashba coefficient α averaged over the time interval [180,220] ps with (w) (a) x-polarized photon field and (b) y-polarized photon field or without (w/o) photon cavity ($\beta = 0$ and $B = 10^{-5}$ T).

position of the destructive AC interference is $\alpha^c \approx 13$ meV nm, where the TL charge current has a pronounced minimum [53]. The spin polarization is largest around $\alpha = \alpha^c$ due to spin accumulation in the current suppressed regime. For $\alpha \to 0$, the spin polarization should vanish, except for the minor spin polarization in S_z due to the Zeeman interaction with the small magnetic field. Apart from that, only the S_y spin polarization seems to be significant in Fig. 2.

The direction of the spin polarization vector can be explained with the concept of the effective magnetic field,

$$\hat{\mathbf{B}}_R = -\frac{\hat{\mathbf{p}} \times \mathbf{E}}{m^*c}, \tag{45}$$

occurring due to the electronic motion in the electric field $\mathbf{E} = E\mathbf{e}_z$. Consequently, we can write the Rashba term

$$\hat{H}_R = \frac{\alpha'}{\hbar}\boldsymbol{\sigma} \cdot (\hat{\mathbf{p}} \times \mathbf{E}) = -\frac{\alpha' m^* c}{\hbar}\boldsymbol{\sigma} \cdot \hat{\mathbf{B}}_R \tag{46}$$

with $\alpha' = \alpha/E$. The spin polarization densities vanish in a one-dimensional (1D) ring with only Rashba SOI due to Kramers degeneracy for the time-reversal symmetric system (see also Ref. [53]). It is therefore clear that the spin polarization densities in the case without photon cavity result only from the geometric deviations from the 1D ring model, for example, the contact regions. The main transport and canonical momentum in the contact regions are along the x-direction. As a consequence, the Rashba effective magnetic field, $\hat{\mathbf{B}}_R$, should be parallel to the y-direction and induce a spin polarization in mainly the y-direction as is in fact depicted in

Fig. 2. With photon cavity, the *x*-polarized photons should lead to an additional kinetic momentum of the electrons in the *x*-direction increasing the S_y spin polarization further. This is also very well in agreement with Fig. 2(a). However, it is interesting that the *y*-polarized photons do *not* induce an S_x spin polarization although the vector potential contribution to the kinetic momentum would suggest this. Here, the reason for the vanishing S_x and S_z spin polarization is that the spin polarization density distribution for the S_x and S_z spin polarization is constrained to an antisymmetric function in *y* around the *x*-axis ($y=0$) for any time *t*, when the central system is initially empty ($N_{e,\text{init}} = 0$). The spin polarization density distribution for spin polarization S_y is symmetric around $y=0$ permitting the non-vanishing spin-polarization S_y. As a result, the *y*-polarized photon field increases only the S_y spin polarization, but less than in the *x*-polarized case (Fig. 2(b)). The symmetry properties and, as a consequence, the non-vanishing components of the spin polarization change if $N_{e,\text{init}} > 0$. Alternatively, $S_x \not\approx 0$ and $S_z \not\approx 0$ could be achieved with a circularly polarized photon field.

3.2. Circular photon field polarization

The circularly polarized photon field has a non-vanishing spin angular momentum perturbing the angular orbital motion of the electrons. Electrons in a 1D ring geometry (as an approximation of our geometry) do not show a circular charge current for vanishing magnetic field [53], but placing them in a photon cavity with circularly polarized photon field would let them move around the ring due to the spin angular momentum of light. The circular motion is a much stronger perturbation of the ring electrons than the perturbation caused by the linearly polarized photon field. The angular electronic motion in the electric field causes an effective magnetic field and a local spin polarization in the radial direction. In our 2D geometry, we will see that the circularly polarized photon field induces also vortices of the size of the ring width. As a consequence, the spin polarization is not only a local quantity. It should be substantially larger than for linear polarization due to the strong perturbation of the circularly polarized photon field with the electronic system.

Fig. 3 shows the spin polarization for (a) LH circularly polarized photon field and (b) and (c) RH circularly polarized photon field. Different from all other subfigures of Figs. 2 and 3, 3c shows the spin polarization as a function of the Dresselhaus instead of the Rashba coefficient. The spin polarization is indeed substantially larger for circular polarization than for linear polarization, Fig. 2. Furthermore, the spin polarization could take any direction due to spin precession. This is a fundamental difference between the linearly and circularly polarized photon field, where only the S_y spin polarization was substantially different from zero. Only the circularly polarized photon field can induce S_x spin polarization although the *y*-polarized photon field leads to an effective magnetic field in the *x*-direction.

It might seem surprising that the S_y spin polarization is relatively small for the circularly polarized photon field. Fig. 4 shows the normalized vector field for the charge current density $\mathbf{j}^c(x,y)$ for RH circularly polarized photon field and two values of the Rashba coefficient, symmetrically located around $\alpha = \alpha^c$. The vortices disappear or are much weaker without photon cavity or with linearly polarized photon field. They are also weaker for circularly polarized photon field and Rashba coefficient values, which are associated with a smaller spin polarization. The charge current density is in general a complicated superposition of many vortices. We would like to mention that it is important that we have used a ring geometry with a finite width. Otherwise, our numerical calculations would not give a realistic picture of the spin polarization. The relatively strong vortices in Fig. 4, which are located close to the contact regions to the leads, are usually not as
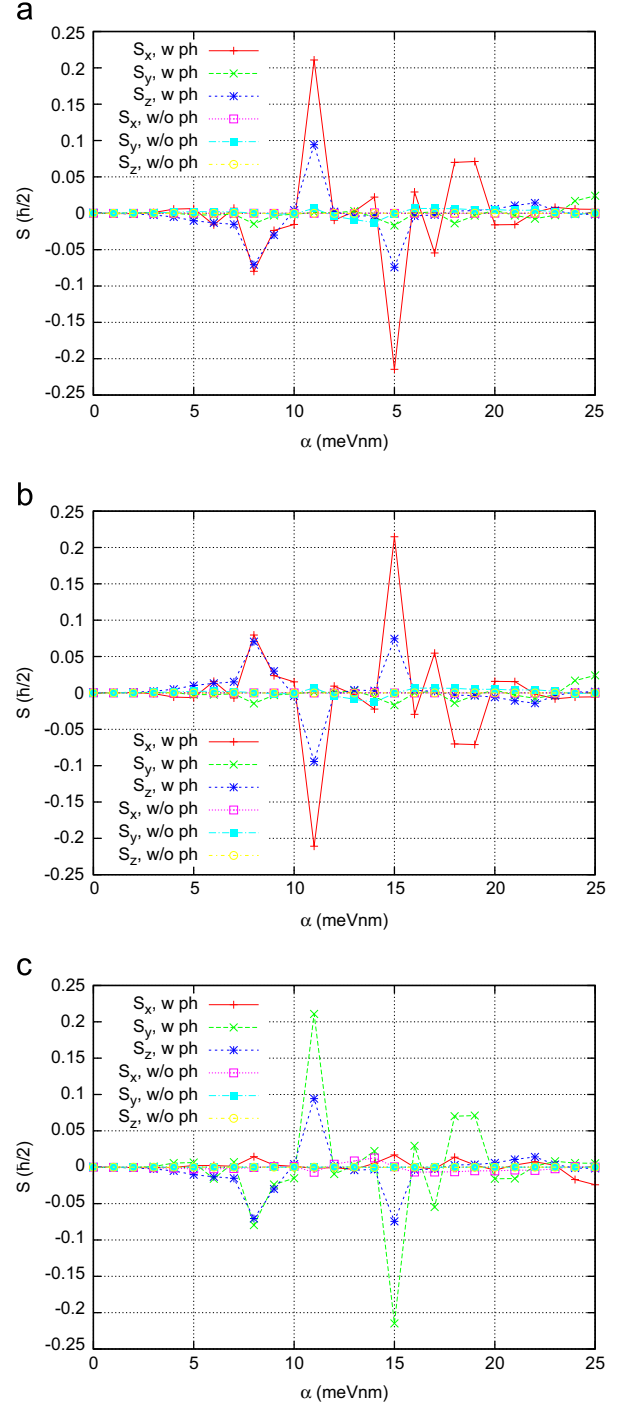
Fig. 3. Spin polarization $\mathbf{S} = (S_x, S_y, S_z)$ of the central system averaged over the time interval [180,220] ps with (w) or without (w/o) photon cavity and (a) LH circularly polarized photon field versus the Rashba coefficient α ($\beta = 0$), (b) RH circularly polarized photon field versus the Rashba coefficient α ($\beta = 0$) and (c) RH circularly polarized photon field versus the Dresselhaus coefficient β ($\alpha = 0$).

symmetric in the *x*-direction around their center than they are in the *y*-direction. Correspondingly, there is often a relatively strong net *y*-component of the canonical momentum leading to a Rashba effective magnetic field in the *x*-direction and a much stronger S_x spin polarization than S_y spin polarization.

It is in particular interesting to observe the local antisymmetric behavior of the *x*- and *z*-component of the spin polarization around the level crossings at $\alpha = \alpha^c$ (Fig. 3(b)), which are the spin polarizations induced by the circularly polarized photon field. By
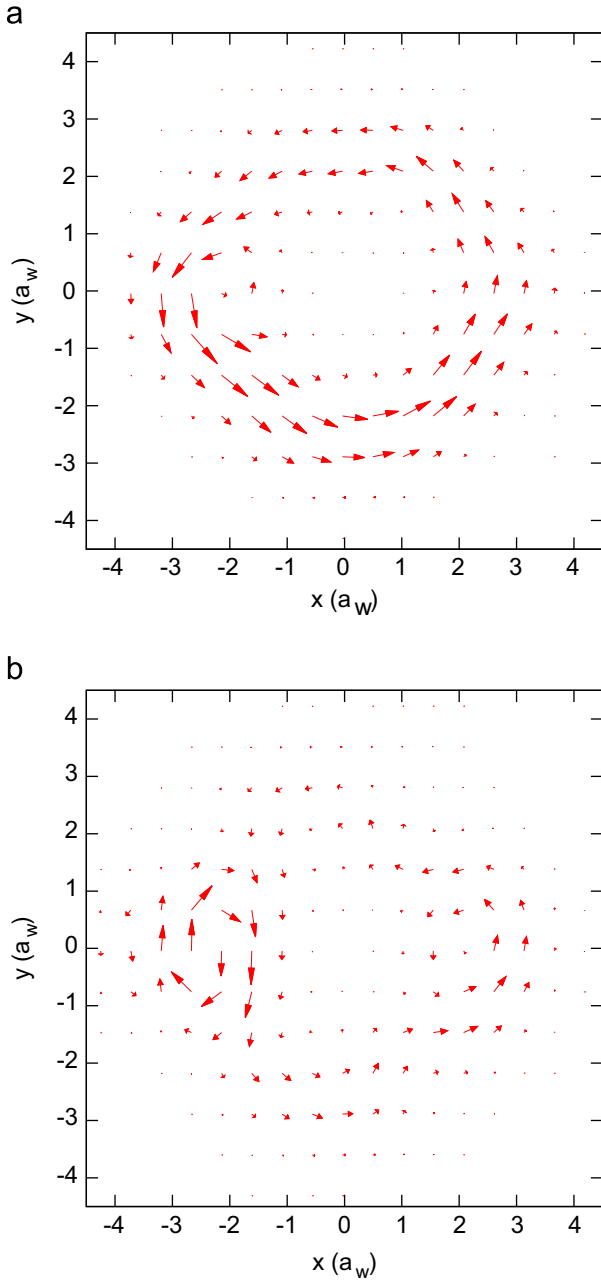
Fig. 4. Normalized vector fields of the charge current density $\mathbf{j}^c(x,y)$ in the central system for (a) the Rashba coefficient $\alpha=11$ meV nm and (b) $\alpha=15$ meV nm at $t=200$ ps with RH circularly polarized photon field and Dresselhaus coefficient $\beta=0$.

contrast, the S_y spin polarization is clearly not antisymmetric around $\alpha=\alpha^c$ for the linearly polarized photon field (see Fig. 2). It can be seen from a comparison of Fig. 4(a), where $\alpha<\alpha^c$, and Fig. 4(b), where $\alpha>\alpha^c$, that the circulation direction of the strong vortex at the left contact region is inversed. This leads to the local antisymmetric behavior of the S_x and S_z spin polarization around $\alpha=\alpha^c$. Since the pronounced vortex structure is mainly due to the circular polarization of the photon field, only the components of the spin polarization, which are induced by the circularly polarized cavity photon field show the local antisymmetric behavior. The fact that the S_y spin polarization is not antisymmetric for linear photon field polarization can be understood as follows: qualitatively, as said before, only the canonical momentum due to the deviations from the 1D ring geometry (and the photon cavity, which is unimportant for S_y in the case of circular photon field polarization) allows for spin polarization in the central system. The

contact regions in the x-direction cause only smaller perturbations of the central system spectrum beyond the level-crossing structure from the 1D ring geometry (in which only the circularly polarized photon field can perturb). It is not likely that these smaller perturbations would lead to additional level-crossings around $\alpha\approx 13$ meV nm, which we have found to be responsible for the antisymmetric behavior of S_x and S_z for circular polarization. Therefore, a local antisymmetry of S_y around $\alpha\approx 13$ meV nm cannot be found.

The x- and z-components of the spin polarization are also antisymmetric with respect to the handedness of the circularly polarized light (Fig. 3(a) in comparison with Fig. 3(b)). As the S_x and S_z spin polarizations are a direct and pure consequence of circular polarization meaning that they are vanishing in the case without photon cavity and in the case with linear polarized photon field, it is understandable that a sign change in the handedness would follow a sign change in the effective magnetic field and spin polarization. In fact, also the vortex circulation direction is inversed by an inversion of the handedness of the circularly polarized photon field. The situation is different for the S_y spin polarization, which is different from zero in the absence of photons. The circularly polarized photon field changes the S_y spin polarization only slightly. Furthermore, comparing the Rashba and Dresselhaus case for RH circularly polarized photon field (Fig. 3(b) and (c)), we can verify the spin polarization symmetries

$$\begin{pmatrix} S_{xD} \\ S_{yD} \\ S_{zD} \end{pmatrix} = - \begin{pmatrix} S_{yR} \\ S_{xR} \\ S_{zR} \end{pmatrix} \qquad (47)$$

due to the structure of the Rashba and Dresselhaus Hamiltonian.

4. Charge and spin polarization currents

Here, we show our numerical results for the charge and spin polarization currents, both between the leads and the system and in the system (quantum ring) itself. Emphasis is laid on the phenomena caused by the photon cavity with a focus on the circularly polarized photon field.

4.1. Non-local currents

Fig. 5 shows the non-local (lead-ring) charge currents from the left lead into the system and further into the right lead as a function of the Rashba coefficient α at time $t=200$ ps and circularly polarized photon field. We note in passing that the result depends not on the handedness of the circularly polarized light. Left- or right-handedness would only interchange the meaning of the otherwise indifferent upper and lower ring arm. With increasing initial number of photons the current tends to get suppressed due to the in general smaller energy differences between the MB levels and the fact that the states having a larger photon content lie in general higher in energy. However, more interestingly, we observe two additional current dips for smaller and larger α, while the current dip at $\alpha=\alpha^c$ appears weaker. With increasing number of initial photons, the two dips for smaller or larger Rashba coefficient move to even smaller ($\alpha\approx\{11,8,3\}$ meV nm) or larger ($\alpha\approx\{15,16.5,18.5\}$ meV nm) Rashba coefficients, respectively, as the initial photon number increases ($N_{ph,init}=\{1,2,3\}$). The dips are indicated in Fig. 5 by arrows in the color of the charge current from the left lead, I_L^c. The circularly polarized photon field has a spin angular momentum, which is proportional to the number of photons in the system. The spin angular momentum of the photons interacts with the total (orbital and spin) angular momentum of the electrons in the ring. For a one-dimensional ring of radius a with only Rashba interaction [53] the electron states are fourfold degenerate at $\alpha=0$ and in general
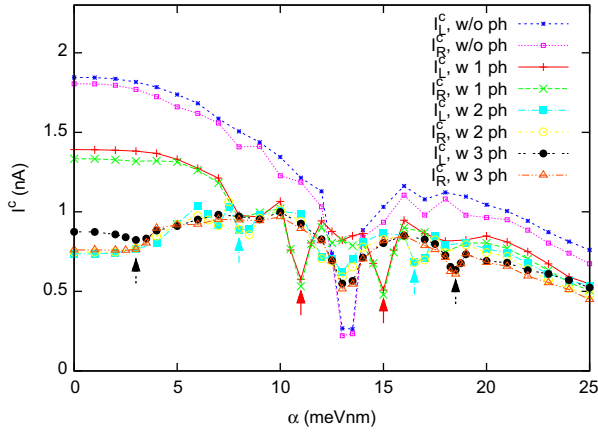
Fig. 5. Non-local lead-system charge currents I_L^c and I_R^c versus the Rashba coefficient α at time $t=200$ ps and with RH circularly polarized photon field for different initial number of photons $N_{ph,init} = 0, 1, 2, 3$. The Dresselhaus coefficient $\beta=0$.

twofold degenerate for $\alpha > 0$, as will be explained here in detail. The eigenstates are

$$\Psi_{\nu n}^R(\varphi) = \begin{pmatrix} \Psi_{\nu n}^R(\varphi, \uparrow) \\ \Psi_{\nu n}^R(\varphi, \downarrow) \end{pmatrix} = \frac{\exp(in\varphi)}{\sqrt{2\pi a}} \begin{pmatrix} A_{\nu,1}^R \\ A_{\nu,2}^R \exp(i\varphi) \end{pmatrix} \quad (48)$$

with the 2×2 coefficient matrix

$$A^R = \begin{pmatrix} A_{\nu,1}^R & A_{\nu,2}^R \end{pmatrix} = \begin{pmatrix} \cos\left(\frac{\theta_R}{2}\right) & \sin\left(\frac{\theta_R}{2}\right) \\ \sin\left(\frac{\theta_R}{2}\right) & -\cos\left(\frac{\theta_R}{2}\right) \end{pmatrix}, \quad (49)$$

$$\tan\left(\frac{\theta_R}{2}\right) = \frac{1 - \sqrt{1+x_R^2}}{x_R} \quad (50)$$

and the dimensionless Rashba parameter, x_R (and Dresselhaus parameter, x_D) is defined by

$$\begin{pmatrix} x_R \\ x_D \end{pmatrix} := \frac{2m^*a}{\hbar^2} \begin{pmatrix} \alpha \\ \beta \end{pmatrix}. \quad (51)$$

We remind the reader that a is the ring radius. We call n the total angular momentum quantum number and $\nu = \pm 1$ the spin quantum number (the latter according to the cardinality of the set of possible values). One can show that n describes indeed the total (i.e. spin and orbital) angular momentum:

$$\langle \nu n | \hat{J}_z | \nu n \rangle = \langle \nu n | \hat{L}_z + S_z | \nu n \rangle = \left\langle \nu n \left| \frac{\hbar}{i} \frac{\partial}{\partial \varphi} + \frac{\hbar}{2} \sigma_z \right| \nu n \right\rangle = \hbar \left(n + \frac{1}{2}\right). \quad (52)$$

In the Dresselhaus case, $\langle \nu n | \hat{J}_z | \nu n \rangle$ in Eq. (52) would depend on n and x_D since $[\hat{J}_z, \hat{H}_D] \neq 0$. We note in passing that $[\hat{J}_z, \hat{H}_R] = 0$ such that, in the Rashba case, $J_z = n + 1/2$ is indeed a "good" quantum number (constant). Furthermore, one can define a quantum number

$$m := \nu\left(n + \frac{1}{2}\right) + \frac{1}{2} = \nu\frac{\langle \nu n | \hat{J}_z | \nu n \rangle}{\hbar} + \frac{1}{2}. \quad (53)$$

While the exact physical meaning of m and ν remains unclear, these quantum numbers are convenient to describe the degeneracies in the 1D Rashba ring. (We assume that they both contain angular momentum and therefore reflect the spin angular momentum of light.) States with the same m, but different ν are degenerate for all α. Additional degeneracies in m appear at $\alpha=0$ and further single points, where the states are fourfold degenerate in total.

How can the degeneracy in ν be lifted? As said before, most likely, the spin quantum number ν contains inherently also orbital angular momentum. It is though clear that it contains angular momentum of some kind. As a consequence, we expect that the circularly polarized photon field would have a different influence

on states of different ν (because of the different angular momentum content), which would imply that it could lift the degeneracy. However, we would not expect that the linearly polarized photon field could lift the degeneracy, as it couples not to the angular momentum. Only the circularly polarized photon field with a non-vanishing spin angular momentum can therefore lift the degeneracy in ν. It is interesting to note that for the two-dimensional ring without photons (Fig. 6(a)) or linearly polarized photons (Fig. 6(b)), the states are in general double degenerate for all values of α except single crossing points. The m-degeneracy at $\alpha=0$ is split due to the 2D geometry. The ν-degeneracy and its energy splitting for $\alpha > 0$ by the circularly polarized photon field are here of main interest (Fig. 6). We would like to draw the attention of the reader to a subtle difference between the 1D and 2D case. First, we consider the 1D case with two states with different m, which are split in energy for $\alpha > 0$. Second, we consider the 2D case with circularly polarized photon field with two states with different ν, which are split in energy for $\alpha > 0$. In both cases, we look at the crossings at $\alpha > 0$ around the critical values in α corresponding to the AC phase differences $\Delta\Phi = n\pi$ with $n=1,2,\ldots$. Then, the difference can be stated as follows: in the 1D case one state crosses with a state that is lower, and the other state, with a state that is higher in energy at $\alpha=0$; in the 2D case the two states cross also with two other states, but here the latter are degenerate at $\alpha=0$.

To understand the three dips in the non-local (lead-ring) charge current better, we take a look at the MB spectrum. Fig. 6 shows the energy spectrum of the central system versus the Rashba coefficient. We note that Fig. 6(c) is independent of the handedness of the circularly polarized photon field. The state crossing of the mostly occupied states leading to dips in the non-local charge current are shown by dotted black lines. These states include at least about 50% of the charge in the central quantum ring system. The zero-electron states are shown by filled squares and the SES by filled circles. The photon content, which can be a fractional number due to the light–matter coupling is shown by a continuous range of colors. A photon content of $N_{ph}=0$ is shown in blue, $N_{ph}=1.5$ is shown in red and $N_{ph}=3$ is shown in yellow. $N_{ph}=4$ is shown in green color. When we start with one photon initially, $N_{ph,init}=1$, the MB spectrum for the linearly and circularly polarized fields shown in Fig. 6(b) and (c) leads to the situation that the mostly occupied states are states with a photon content $N_{ph} \approx 1$. These states have a color close to purple or violet red and lie 0.4 meV higher in the spectrum than the mostly occupied states without photon cavity (which have of course photon content $N_{ph}=0$), see Fig. 6(a).

In the case without photons, Fig. 6(a), and with linearly polarized photon field, Fig. 6(b), the SES are double degenerate, but become split for $\alpha > 0$ in the case of circularly polarized photon field, Fig. 6(c). Consequently, without photon cavity or for linearly polarized photons, the four crossings of the four mostly occupied states are at one value of $\alpha = \alpha^c$. With circularly polarized photon field, the four crossings of the four mostly occupied states become to lie at three different values of α. Two crossings are at the intermediate α-value, which is located close to α^c, the third crossing is at $\alpha < \alpha^c$ and the fourth is at $\alpha > \alpha^c$. The three MB crossing locations in the circularly polarized photon field case are the reason for the three dips of the non-local (lead-ring) charge current. To summarize the essence of Fig. 6, each Rashba coefficient α with a crossing of the mostly occupied states is corresponding to a dip of the non-local charge current. Without photon cavity or for linearly polarization of the photon field, we have one Rashba coefficient, α^c, with crossings and therefore one dip—for circular polarization, we have three values of the Rashba coefficient with crossings and therefore three dips.

Fig. 7 shows the non-local (lead-ring) spin polarization currents for (a) x-polarized photon field and (b) y-polarized photon field
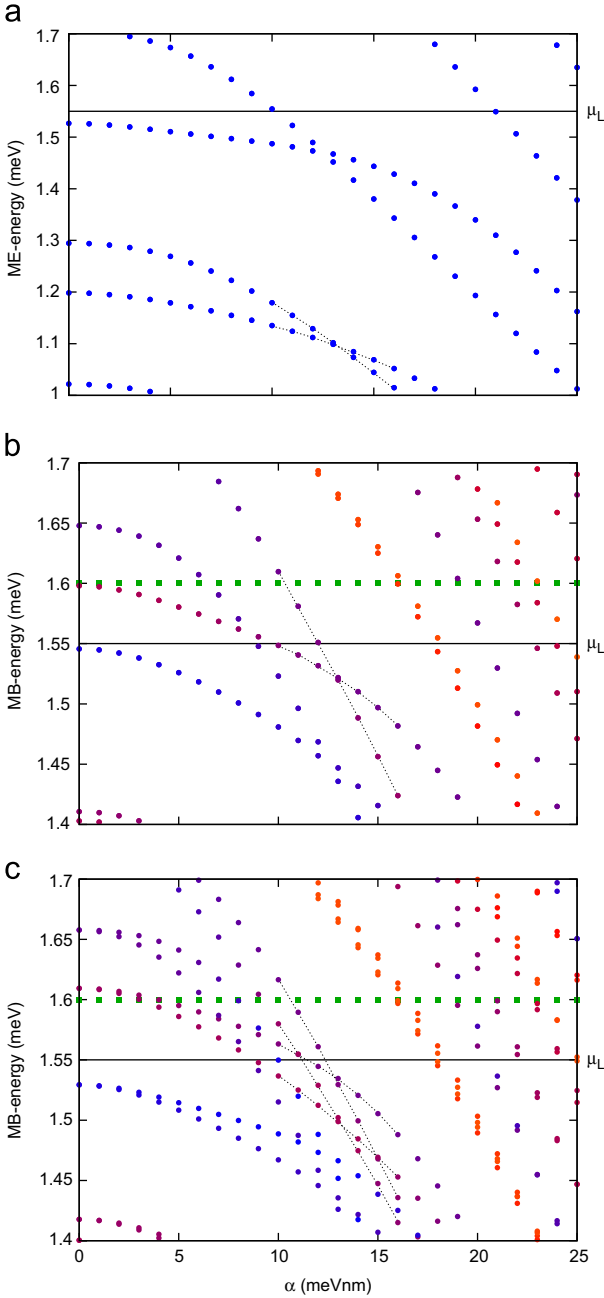
a

b

c

Fig. 6. Many-electron (ME) or many-body (MB) energy spectrum of the system Hamiltonian Eq. (2) versus the Rashba coefficient α (a) without photon cavity, (b) with x-polarized photon field and (c) with RH circularly polarized photon field. The states are differentiated according to their electron content N_e by the shape of the dots and according to their fractional photon content N_{ph} by their color. Zero-electron states ($N_e=0$, 0ES) are represented as filled squares (the green color means that $N_{ph}=4$) and single electron states ($N_e=1$, SES) as filled circles with the continuous color spectrum from blue over red to yellow corresponding to the range $N_{ph} \in [0, 3]$. The chemical potential μ_L of the left lead is shown by a solid black line. The mostly occupied states, which contribute to the current dips, are connected by black dotted lines close to their crossings as a guide to the eye. Note that the spectra are shown for different energy ranges. (For interpretation of the references to color in this figure caption, the reader is referred to the web version of this paper.)

from the left lead into the system $\mathbf{I}_L = (I_L^x, I_L^y, I_L^z)$ or from the system to the right lead $\mathbf{I}_R = (I_R^x, I_R^y, I_R^z)$. Similar to the spin polarization, Fig. 2, the y-polarized photons do *not* induce a non-local current for S_x spin polarization neither from the left nor to the right lead. Also the non-local current for S_z spin polarization is vanishing. In the strong Rashba regime $\alpha \in [19, 24]$ meV nm, the S_y spin polarization is overall emptied in the system without photon cavity
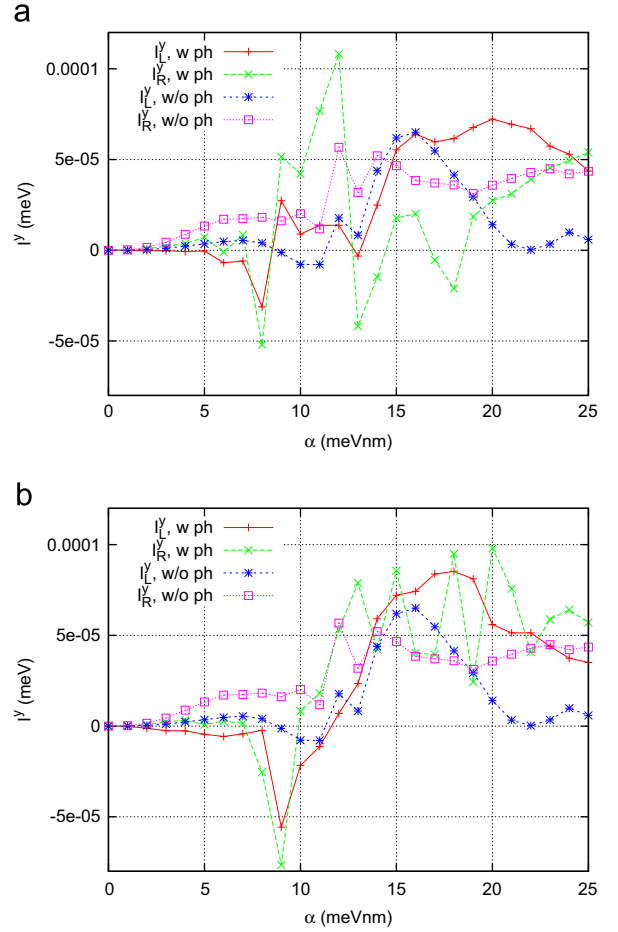
a

b

Fig. 7. Non-local spin polarization currents I_L^y and I_R^y into and out of the central system versus the Rashba coefficient α averaged over the time interval [180,220] ps with (w) (a) x-polarized photon field and (b) y-polarized photon field or without (w/o) photon cavity. I_L^x, I_L^z, I_R^x and I_R^z are not shown as they are vanishing. The Dresselhaus coefficient $\beta=0$.

meaning that $I_L^y < I_R^y$, however, with x-polarized photon field, we observe in total S_y spin injection ($I_L^y > I_R^y$). The y-polarized photon field is not in general able to invert the spin emptying into spin injection in the strong Rashba regime given above.

4.2. Local photocurrents

Fig. 8 shows the TL and CL charge photocurrents. The photon cavity reduces in general the TL charge current (Fig. 8(a)) (negative photocurrent). However, at the destructive AC interference at $\alpha = \alpha^c$, the TL charge current is enhanced in particular for the circularly polarized photon field. By the photonic perturbation of the AC phase difference, the electrons can flow more freely through the ring and the electron dwell time is reduced. In the case of the circularly polarized photon field, at the smaller and larger values $\alpha \approx \{11, 15\}$ meV nm, where the additional non-local (lead-ring) charge current dips appear (Fig. 5), the TL charge photocurrent is very negative. This gives some further evidence about the photonic nature of the additional non-local charge current dips. The TL current is independent of the handedness of the circularly polarized photon field since the ring is otherwise symmetric with respect to the x-axis. The CL charge photocurrent has different sign for RH or LH circularly polarized photon field since the circular motion of electrons changes with the spin angular momentum of the photons in sign (Fig. 8(b)). In contrast, the CL charge current remains uninfluenced by the linearly polarized photon field. With the aid of the angular motion of
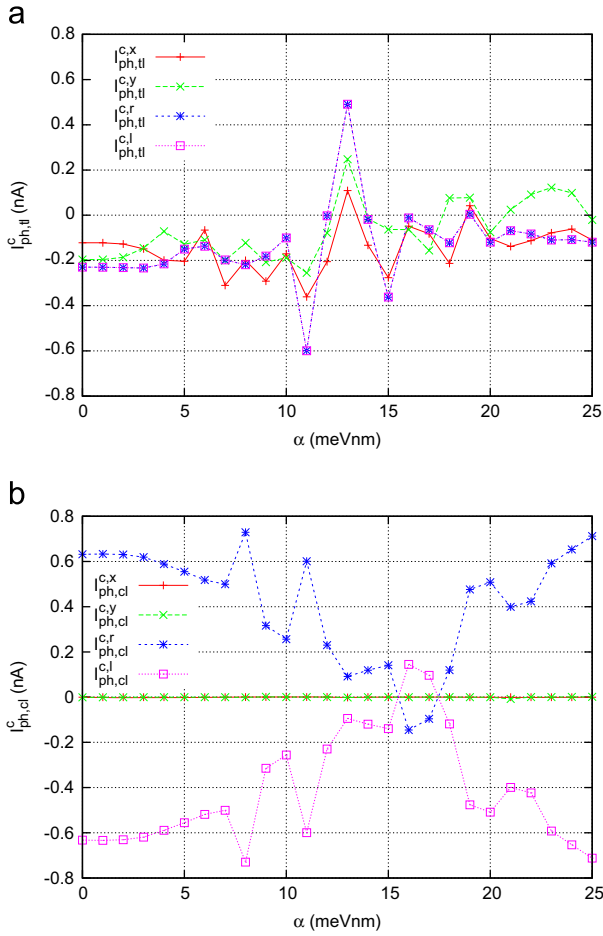
a

b

Fig. 8. (a) TL and (b) CL charge photocurrents $I_{ph,tl}^{c,p}$ versus the Rashba coefficient α averaged over the time interval [180,220] ps with ($p=x$) x-polarized photon field, ($p=y$) y-polarized photon field, ($p=r$) RH circularly polarized photon field and ($p=l$) LH circularly polarized photon field. The Dresselhaus coefficient $\beta=0$.

a

b

Fig. 9. (a) TL spin photocurrents for spin polarization S_y, $I_{ph,tl}^y$ and (b) CL spin photocurrents for spin polarization S_z, $I_{ph,cl}^z$, versus the Rashba coefficient α averaged over the time interval [180,220] ps with ($p=x$) x-polarized photon field, ($p=y$) y-polarized photon field, ($p=r$) RH circularly polarized photon field and ($p=l$) LH circularly polarized photon field. The Dresselhaus coefficient $\beta=0$.

electrons induced by the circularly polarized photon field, the charge flow can be controlled to pass through the upper or lower ring arm. Around the destructive AC interference, the CL charge photon current gets suppressed due to the unfavorable phase relation. The suppression spans a relatively wide region $\alpha \in$ [9, 23] meV nm when compared to the non-local charge current dip. The CL charge photon current might therefore serve as an alternative tool to detect AC phase interference phenomena, which minimizes the likelihood to overlook an AC destructive phase interference because of the narrowness of the non-local charge current dip in the parameter space (consider for example the dip at $\alpha = \alpha^c$ in Fig. 5). We note that the TL and CL charge current is independent from the kind of SOI, i.e. Rashba or Dresselhaus, as it is a spin-independent quantity.

Fig. 9 shows the TL spin photocurrent for the spin polarization S_y and the CL spin photocurrent for the spin polarization S_z. As opposed to the charge photocurrents, the spin photocurrents drop to zero for the Rashba coefficient $\alpha \to 0$ (when only a very weak Zeeman term distinguishes the spin). The influence of the circularly polarized photon field is strong in a relatively wide range around the position of the destructive AC phase at $\alpha = \alpha^c$ and weak around the constructive AC phases ($\alpha=0$ meV nm and $\alpha \approx 21$ meV nm). For the destructive AC phase, the reduced electron mobility increases the electron dwell time leading to the strong spin photocurrents. In general, the influence of the circularly polarized photon field is a bit stronger than the influence of the linearly polarized photon field. We note in passing that the other

spin photocurrents, which are not shown, $I_{ph,tl}^x$, $I_{ph,cl}^x$, $I_{ph,cl}^y$ and $I_{ph,tl}^z$, are about one order of magnitude smaller than $I_{ph,tl}^y$ and $I_{ph,cl}^z$. The local spin polarization currents without photons, $I_{tl}^{y,0}$ and $I_{cl}^{z,0}$, were also much larger than $I_{tl}^{x,0}$, $I_{cl}^{x,0}$, $I_{tl}^{y,0}$ and $I_{tl}^{z,0}$, meaning that the photon cavity is not changing the set of major local spin polarization currents. It is interesting to note that the handedness of the circularly polarized photon field does *not* affect the major spin photocurrents including even the CL spin photocurrent $I_{ph,cl}^z$.

5. Conclusions

The interaction between spin–orbit coupled electrons in a quantum ring interferometer and a circularly polarized electromagnetic field shows a variety of interesting effects, which do not appear for linear polarization of the photon field. The AC phase that controls the transport of electrons in such a quantum device is influenced by the photons. We found that the spin polarization in a ring, which is connected to leads and mirror symmetric with respect to the transport axis, is perpendicular to the transport direction. A linearly polarized photon field with polarization in or perpendicular to the transport direction, increases only the magnitude of the spin polarization while keeping the direction of the spin polarization vector uninfluenced. The spin polarization accumulates to larger magnitudes when the transport of electrons is

suppressed by a destructive AC phase. The circularly polarized photon field enhances the spin polarization much more than the linearly polarized photon field. Furthermore, the spin polarization vector is no longer bound to a specific direction as the circularly polarized photon field excites the orbital angular motion of the electrons around the ring and pronounced vortices of the charge current density of smaller spatial scale. The latter show the importance to resolve the finite width of our ring as we did in our model. The circulation direction of the vortices is found to depend on the handedness of the photon field and the value of the Rashba coefficient α relative to α^c.

The charge current from the left lead into the quantum ring device and out to the right lead shows three AC dips around α^c instead of one for the circularly polarized photon field. The reason for it is a small splitting of degenerate states by the interaction of the angular momentum of the electrons and the spin angular momentum of light, which leads to MB crossings at three different values of the Rashba coefficient. The distance in α between the dips increases with the number of photons in the system due to the larger spin angular momentum of light. The charge photo-current from the left to the right side of the quantum ring is usually negative meaning that the photon cavity suppresses the charge transport thus increasing the device resistance (except close to α^c, where the AC phase interference is destructive). The circulating part of the charge photocurrent can only be excited by the circularly polarized photon field. The handedness of the circulation depends on the handedness of the light. This way, it is possible to confine the charge transport through the ring to one ring arm (upper or lower). The circular charge photocurrent is suppressed in a wide range of the Rashba coefficient around $\alpha = \alpha^c$ and might therefore serve as a reliable quantity to detect destructive AC phases. The spin photocurrents are especially strong around $\alpha = \alpha^c$ (due to the longer electron dwell time) and for circular polarization (for geometrical reasons). The handedness of the light does not influence the spin polarization current including the current for S_z spin polarization, which circulates around the ring.

In summary, strong spin polarization, spin photocurrents and charge current vortices as well as splitting of the AC charge current dip into three dips and control over the local charge flow through the ring arms are important effects that only appear for circularly polarized photon field. These effects are crucial to know about for the development of spin-optoelectronic quantum devices in the field of quantum information processing. For instance, interest might arise to build a spintronic device, which can break (block) an electrical circuit at a specific, sharply defined (critical) gate potential, which corresponds to the magnitude of the electric field leading to a destructive AC phase interference in a ring inter-ferometer. The critical gate potential of the quantum switch could be adjusted by variation of the ring radius [53]. A possible experimental approach to determine the ring radius would be to measure the circular charge current around the ring (for example indirectly by its induced magnetic field) that is caused by a circularly polarized cavity photon field. We predict that this approach is better than direct resistance measurements of the quantum switch without the photon cavity. This is because the data that a certain number of measurements with the circularly polarized cavity photon field yields are more relevant for suggesting the proper ring radius due to the broadness of the corresponding Aharonov–Casher feature in the Rashba coefficient.

Acknowledgments

Appendix A. Parameters used for the numerical results

We assume GaAs-based material with electron effective mass $m^* = 0.067 m_e$ and background relative dielectric constant $\kappa = 12.4$. As stated earlier, the Rashba coefficient α can be tuned by changing the magnitude of an electric field, which is perpendicular to the plane containing the quantum ring structure. The range of α investigated in this paper is about one order of magnitude larger than typical values of α for GaAs. However, we point out that the predicted features are at fixed positions in x_R (Eq. (51)) and not in α. Therefore, by increasing the ring radius, experiments could be performed in a smaller range of the Rashba coefficient if it seems difficult to increase the electric field sufficiently by a gate. For our numerical calculations, it is inconvenient to increase the ring radius further, as we would have to consider a larger number of many-body states to get converged results. With the state of the art computational facilities, however, we are limited to about 200 MB states for our numerically exact approach. Alternatively, other materials as InAs could be used, for which the Rashba coefficient is about one order of magnitude larger [60]. The Dresselhaus coefficient β is determined by the bulk properties of the material and could only be changed by using a different material. The value for GaAs would be $\beta = 3.0$ meV nm. When using $\beta > 0$, we would also decrease slightly the α-range for which our features due to the destructive AC phase appear. However, our features would become more complex when both Rashba and Dresselhaus spin–orbit interaction are present [23].

We consider a single photon cavity mode with fixed photon excitation energy $\hbar\omega = 0.4$ meV. The electron–photon coupling constant in the central system $g^{EM} = 0.1$ meV. The temperature of the reservoirs is $T = 0.5$ K. The chemical potentials in the leads are $\mu_L = 1.55$ meV and $\mu_R = 0.7$ meV leading to a source-drain electrical bias window $\Delta\mu = 0.85$ meV.

A very small external uniform magnetic field $B = 10^{-5}$ T is applied through the central ring system and the lead reservoirs to lift the spin degeneracy in the numerical calculations. The applied magnetic field $B < B_0 = \Phi_0/A \approx 0.2$ T is order of magnitudes out-side the AB regime. The two-dimensional magnetic length would be very large: $l = [c\hbar/(eB)]^{1/2} = 8.12$ μm. However, the parabolic confinement of the ring system in the y-direction leads to the much shorter magnetic length scale

$$a_w = \left(\frac{\hbar}{m^*\Omega_0}\right)^{1/2} \frac{1}{\sqrt[4]{1 + [eB/(m^* c \Omega_0)]^2}}$$

$$\approx \left(\frac{\hbar}{m^*\Omega_0}\right)^{1/2} = 33.7 \text{ nm}. \tag{A.1}$$

To model the coupling between the system and the leads, we let the affinity constant $\Delta_E^l = 0.25$ meV to be close to the char-acteristic electronic excitation energy in the x-direction. In addi-tion, we let the contact region parameters for lead $l \in \{L, R\}$ in x- and y-directions be $\delta_x^l = \delta_y^l = 4.39 \times 10^{-4}$ nm^{-2}. The system–lead coupling strength $g_0^l = 1.371 \times 10^{-3}$ meV/nm$^{3/2}$. Before switching on the system–lead coupling at $t = 0$ with the time-scale $(\alpha^l)^{-1} = 3.291$ ps, we assume the central system to be in the pure state with electron occupation number $N_{e,\text{init}} = 0$ and—unless otherwise stated—photon occupation number $N_{\text{ph,init}} = 1$. The SES charging time-scale $\tau_{SES} \approx 30$ ps, and the two-electron state (2ES) charging time-scale $\tau_{2ES} > 200$ ps, which is described in the sequential tunneling regime. We study the non-equilibrium transport properties around $t = 200$ ps, when the system has not yet reached a steady state. Some dynamical observables are averaged over the time interval

[180,220] ps to give a more representative picture in the transient regime. The charge in the quantum ring system at $t=200$ ps is typically of the order of $Q(t=200 \text{ ps}) \approx 1e$.

Appendix B. Operators for the charge and spin polarization density and charge and spin polarization current density

The charge density operator

$$\hat{n}^c(\mathbf{r}) = e\hat{\Psi}^\dagger(\mathbf{r})\hat{\Psi}(\mathbf{r}) \tag{B.1}$$

and the spin polarization density operator for spin polarization S_i

$$\hat{n}^i(\mathbf{r}) = \frac{\hbar}{2}\hat{\Psi}^\dagger(\mathbf{r})\sigma_i\hat{\Psi}(\mathbf{r}). \tag{B.2}$$

The component labeled with $j \in \{x, y\}$ of the charge current density operator

$$
\begin{aligned}
\hat{j}^c_j(\mathbf{r}) = &\frac{e\hbar}{2m^*i}[\hat{\Psi}^\dagger(\mathbf{r})\nabla_j\hat{\Psi}(\mathbf{r}) - (\nabla_j\hat{\Psi}^\dagger(\mathbf{r}))\hat{\Psi}(\mathbf{r})] \\
&+ \frac{e^2}{m^*c}\hat{A}_j(\mathbf{r})\hat{\Psi}^\dagger(\mathbf{r})\hat{\Psi}(\mathbf{r}) \\
&+ \frac{e}{\hbar}\hat{\Psi}^\dagger(\mathbf{r})(\beta\sigma_x - \alpha\sigma_y)\hat{\Psi}(\mathbf{r})\delta_{x,j} \\
&+ \frac{e}{\hbar}\hat{\Psi}^\dagger(\mathbf{r})(\alpha\sigma_x - \beta\sigma_y)\hat{\Psi}(\mathbf{r})\delta_{y,j}
\end{aligned} \tag{B.3}
$$

with the space-dependent vector potential including the static magnetic field and cavity photon field part

$$\hat{\mathbf{A}}(\mathbf{r}) = \mathbf{A}(\mathbf{r}) + \hat{\mathbf{A}}^{ph}(\mathbf{r}). \tag{B.4}$$

The current density operator for the j-component and S_x spin polarization

$$
\begin{aligned}
\hat{j}^x_j(\mathbf{r}) = &\frac{\hbar^2}{4m^*i}[\hat{\Psi}^\dagger(\mathbf{r})\sigma_x\nabla_j\hat{\Psi}(\mathbf{r}) \\
&- (\nabla_j\hat{\Psi}^\dagger(\mathbf{r}))\sigma_x\hat{\Psi}(\mathbf{r})] \\
&+ \frac{e\hbar}{2m^*c}\hat{A}_j(\mathbf{r})\hat{\Psi}^\dagger(\mathbf{r})\sigma_x\hat{\Psi}(\mathbf{r}) \\
&+ \frac{\beta\delta_{x,j} + \alpha\delta_{y,j}}{2}\hat{\Psi}^\dagger(\mathbf{r})\hat{\Psi}(\mathbf{r}).
\end{aligned} \tag{B.5}
$$

the current density operator for S_y spin polarization

$$
\begin{aligned}
\hat{j}^y_j(\mathbf{r}) = &\frac{\hbar^2}{4m^*i}[\hat{\Psi}^\dagger(\mathbf{r})\sigma_y\nabla_j\hat{\Psi}(\mathbf{r}) \\
&- (\nabla_j\hat{\Psi}^\dagger(\mathbf{r}))\sigma_y\hat{\Psi}(\mathbf{r})] \\
&+ \frac{e\hbar}{2m^*c}\hat{A}_j(\mathbf{r})\hat{\Psi}^\dagger(\mathbf{r})\sigma_y\hat{\Psi}(\mathbf{r}) \\
&- \frac{\alpha\delta_{x,j} + \beta\delta_{y,j}}{2}\hat{\Psi}^\dagger(\mathbf{r})\hat{\Psi}(\mathbf{r}).
\end{aligned} \tag{B.6}
$$

and S_z spin polarization

$$
\begin{aligned}
\hat{j}^z_j(\mathbf{r}) = &\frac{\hbar^2}{4m^*i}[\hat{\Psi}^\dagger(\mathbf{r})\sigma_z\nabla_j\hat{\Psi}(\mathbf{r}) \\
&- (\nabla_j\hat{\Psi}^\dagger(\mathbf{r}))\sigma_z\hat{\Psi}(\mathbf{r})] \\
&+ \frac{e\hbar}{2m^*c}\hat{A}_j(\mathbf{r})\hat{\Psi}^\dagger(\mathbf{r})\sigma_z\hat{\Psi}(\mathbf{r}).
\end{aligned} \tag{B.7}
$$

References

[1] Y. Aharonov, D. Bohm, Phys. Rev. 115 (1959) 485, http://dx.doi.org/10.1103/PhysRev.115.485.
[2] Y. Aharonov, A. Casher, Phys. Rev. Lett. 53 (1984) 319, http://dx.doi.org/10.1103/PhysRevLett.53.319.
[3] Y. Aharonov, J. Anandan, Phys. Rev. Lett. 58 (1987) 1593, http://dx.doi.org/10.1103/PhysRevLett.58.1593.
[4] M.V. Berry, Proc. R. Soc. Lond. A 392 (1984) 45.
[5] A.S. Moskalenko, J. Berakdar, Phys. Rev. A 78 (2008) 051804, http://dx.doi.org/10.1103/PhysRevA.78.051804.

[6] Y. Xie, W. Chu, S. Duan, Appl. Phys. Lett. 93 (2008) 023104, URL: ⟨http://search.ebscohost.com/login.aspx?direct=true&db=aph&AN=33361228&site=ehost-live⟩.
[7] S.D. Ganichev, E.L. Ivchenko, S.N. Danilov, J. Eroms, W. Wegscheider, D. Weiss, W. Prettl, Phys. Rev. Lett. 86 (2001) 4358, http://dx.doi.org/10.1103/PhysRevLett.86.4358.
[8] G.F. Quinteiro, J. Berakdar, Opt. Express 17 (2009) 20465, http://dx.doi.org/10.1364/OE.17.020465, URL: ⟨http://www.opticsexpress.org/abstract.cfm?URI=oe-17-22-20465⟩.
[9] Y.V. Pershin, C. Piermarocchi, Phys. Rev. B 72 (2005) 245331, http://dx.doi.org/10.1103/PhysRevB.72.245331.
[10] O.V. Kibis, Phys. Rev. Lett. 107 (2011) 106802, http://dx.doi.org/10.1103/PhysRevLett.107.106802.
[11] O.V. Kibis, O. Kyriienko, I.A. Shelykh, Phys. Rev. B 87 (2013) 245437, http://dx.doi.org/10.1103/PhysRevB.87.245437.
[12] E. Räsänen, A. Castro, J. Werschnik, A. Rubio, E.K.U. Gross, Phys. Rev. Lett. 98 (2007) 157404.
[13] B. Szafran, F.M. Peeters, Phys. Rev. B 72 (2005) 165301, http://dx.doi.org/10.1103/PhysRevB.72.165301.
[14] K.N. Pichugin, A.F. Sadreev, Phys. Rev. B 56 (1997) 9662.
[15] R.A. Webb, S. Washburn, C.P. Umbach, R.B. Laibowitz, Phys. Rev. Lett. 54 (1985) 2696, http://dx.doi.org/10.1103/PhysRevLett.54.2696.
[16] J. Nitta, T. Bergsten, New J. Phys. 9 (2007) 341, URL: ⟨http://stacks.iop.org/1367-2630/9/i=9/a=341⟩.
[17] Y.A. Bychkov, E.I. Rashba, J. Phys. C: Solid State Phys. 17 (1984) 6039, URL: ⟨http://stacks.iop.org/0022-3719/17/i=33/a=015⟩.
[18] G. Dresselhaus, Phys. Rev. 100 (1955) 580, http://dx.doi.org/10.1103/PhysRev.100.580.
[19] D. Frustaglia, K. Richter, Phys. Rev. B 69 (2004) 235310, http://dx.doi.org/10.1103/PhysRevB.69.235310.
[20] G. Ying-Fang, Z. Yong-Ping, L. Jiu-Qing, Chin. Phys. Lett. 21 (2004) 2093, URL: ⟨http://stacks.iop.org/0256-307X/21/i=11/a=006⟩.
[21] A.G. Aronov, Y.B. Lyanda-Geller, Phys. Rev. Lett. 70 (1993) 343, http://dx.doi.org/10.1103/PhysRevLett.70.343.
[22] Y.-S. Yi, T.-Z. Qian, Z.-B. Su, Phys. Rev. B 55 (1997) 10631, http://dx.doi.org/10.1103/PhysRevB.55.10631.
[23] X.F. Wang, P. Vasilopoulos, Phys. Rev. B 72 (2005) 165336, http://dx.doi.org/10.1103/PhysRevB.72.165336.
[24] H.-F. Cheung, Y. Gefen, E.K. Riedel, W.-H. Shih, Phys. Rev. B 37 (1988) 6050, http://dx.doi.org/10.1103/PhysRevB.37.6050.
[25] W.-C. Tan, J.C. Inkson, Phys. Rev. B 60 (1999) 5626.
[26] A.V. Balatsky, B.L. Altshuler, Phys. Rev. Lett. 70 (1993) 1678, http://dx.doi.org/10.1103/PhysRevLett.70.1678.
[27] S. Oh, C.-M. Ryu, Phys. Rev. B 51 (1995) 13441, http://dx.doi.org/10.1103/PhysRevB.51.13441.
[28] Z.-G. Zhu, J. Berakdar, J. Phys.: Condens. Matter 21 (2009) 145801, URL: ⟨http://stacks.iop.org/0953-8984/21/i=14/a=145801⟩.
[29] M. Nita, D.C. Marinescu, A. Manolescu, V. Gudmundsson, Phys. Rev. B 83 (2011) 155427, http://dx.doi.org/10.1103/PhysRevB.83.155427.
[30] Q.-f. Sun, X.C. Xie, J. Wang, Phys. Rev. B 77 (2008) 035327, http://dx.doi.org/10.1103/PhysRevB.77.035327.
[31] E.B. Sonin, Phys. Rev. Lett. 99 (2007) 266602, http://dx.doi.org/10.1103/PhysRevLett.99.266602.
[32] H. Walther, B.T.H. Varcoe, B.-G. Englert, T. Becker, Rep. Progr. Phys. 69 (2006) 1325, URL: ⟨http://stacks.iop.org/0034-4885/69/i=5/a=R02⟩.
[33] R. Miller, T.E. Northup, K.M. Birnbaum, A. Boca, A.D. Boozer, H.J. Kimble, J. Phys. B: Atom. Mol. Opt. Phys. 38 (2005) S551, URL: ⟨http://stacks.iop.org/0953-4075/38/i=9/a=007⟩.
[34] A.M. Khasraghi, S. Shojaei, A.S. Vala, M. Kalafi, Physica E 47 (2013) 17.
[35] O. Jonasson, C.-S. Tang, H.-S. Goan, A. Manolescu, V. Gudmundsson, New J. Phys. 14 (2012) 013036, URL: ⟨http://stacks.iop.org/1367-2630/14/i=1/a=013036⟩.
[36] E. Jaynes, F.W. Cummings, Proc. IEEE 51 (1963) 89, http://dx.doi.org/10.1109/PROC.1963.1664.
[37] Y. Wu, X. Yang, Phys. Rev. Lett. 98 (2007) 013601, http://dx.doi.org/10.1103/PhysRevLett.98.013601.
[38] A.T. Sornborger, A.N. Cleland, M.R. Geller, Phys. Rev. A 70 (2004) 052315, http://dx.doi.org/10.1103/PhysRevA.70.052315.
[39] C.S. Tang, C.S. Chu, Phys. Rev. B 60 (1999) 1830, http://dx.doi.org/10.1103/PhysRevB.60.1830.
[40] G. Zhou, Y. Li, J. Phys.: Condens. Matter 17 (2005) 6663.
[41] J.-W. Jung, K. Na, L.E. Reichl, Phys. Rev. A 85 (2012) 023420.
[42] C.S. Tang, C.S. Chu, Physica B 292 (2000) 127.
[43] G. Zhou, M. Yang, X. Xiao, Y. Li, Phys. Rev. B 68 (2003) 155309.
[44] H. Spohn, Rev. Mod. Phys. 52 (1980) 569.
[45] S.A. Gurvitz, Y.S. Prager, Phys. Rev. B 53 (1996) 15932.
[46] N.G. vanKampen, Stochastic Processes in Physics and Chemistry, 2nd ed., North-Holland, Amsterdam, 2001.
[47] U. Harbola, M. Esposito, S. Mukamel, Phys. Rev. B 74 (2006) 235309, URL: ⟨http://link.aps.org/abstract/PRB/v74/e235309⟩.
[48] C. Bruder, H. Schoeller, Phys. Rev. Lett. 72 (1994) 1076, http://dx.doi.org/10.1103/PhysRevLett.72.1076.
[49] A. Braggio, J. König, R. Fazio, Phys. Rev. Lett. 96 (2006) 026805.
[50] V. Moldoveanu, A. Manolescu, V. Gudmundsson, New J. Phys. 11 (2009) 073019, URL: ⟨http://stacks.iop.org/1367-2630/11/073019⟩.
[51] H.-P. Breuer, B. Kappler, F. Petruccione, Phys. Rev. A 59 (1999) 1633, http://dx.doi.org/10.1103/PhysRevA.59.1633.

[52] T. Arnold, C.-S. Tang, A. Manolescu, V. Gudmundsson, Phys. Rev. B 87 (2013) 035314, http://dx.doi.org/10.1103/PhysRevB.87.035314.

[53] T. Arnold, C.-S. Tang, A. Manolescu, V. Gudmundsson, Geometry and linearly polarized cavity photon effects on the charge and spin currents of spin–orbit interacting electrons in a quantum ring, Unpublished results. arXiv:1310.5870.

[54] M. Kaniber, A. Laucht, A. Neumann, M. Bichler, M.-C. Amann, J.J. Finley, J. Phys.: Condens. Matter 20 (2008) 454209, URL: ⟨http://stacks.iop.org/0953-8984/20/i=45/a=454209⟩.

[55] R.S. Whitney, J. Phys. A: Math. Theor. 41 (2008) 175304, http://dx.doi.org/10.1088/1751-8113/41/17/175304.

[56] V. Gudmundsson, O. Jonasson, C.-S. Tang, H.-S. Goan, A. Manolescu, Phys. Rev. B 85 (2012) 075306.

[57] V. Gudmundsson, C. Gainar, C.-S. Tang, V. Moldoveanu, A. Manolescu, New J. Phys. 11 (2009) 113007, URL: ⟨http://stacks.iop.org/1367-2630/11/i=11/a=113007⟩.

[58] E.I. Rashba, Phys. Rev. B 68 (2003) 241315, http://dx.doi.org/10.1103/PhysRevB.68.241315.

[59] E.B. Sonin, Phys. Rev. B 76 (2007) 033306, http://dx.doi.org/10.1103/PhysRevB.76.033306.

[60] J.B. Ko, H.C. Koo, H. Yi, J. Chang, S.H. Han, Electron. Mater. Lett. 2 (2006) 49.

THE EUROPEAN
PHYSICAL JOURNAL B

Effects of geometry and linearly polarized cavity photons on charge and spin currents in a quantum ring with spin-orbit interactions[⋆]

Thorsten Arnold[1,a], Chi-Shung Tang[2], Andrei Manolescu[3], and Vidar Gudmundsson[1]

[1] Science Institute, University of Iceland, Dunhaga 3, 107 Reykjavik, Iceland
[2] Department of Mechanical Engineering, National United University, 1, Lienda, 36003 Miaoli, Taiwan
[3] School of Science and Engineering, Reykjavik University, Menntavegur 1, 101 Reykjavik, Iceland

Abstract. We calculate the persistent charge and spin polarization current inside a finite-width quantum ring of realistic geometry as a function of the strength of the Rashba or Dresselhaus spin-orbit interaction. The time evolution in the transient regime of the two-dimensional (2D) quantum ring connected to electrically biased semi-infinite leads is governed by a time-convolutionless non-Markovian generalized master equation. The electrons are correlated via Coulomb interaction. In addition, the ring is embedded in a photon cavity with a single mode of linearly polarized photon field, which is polarized either perpendicular or parallel to the charge transport direction. To analyze carefully the physical effects, we compare to the analytical results of the toy model of a one-dimensional (1D) ring of non-interacting electrons with spin-orbit coupling. We find a pronounced charge current dip associated with many-electron level crossings at the Aharonov-Casher phase $\Delta\Phi = \pi$, which can be disguised by linearly polarized light. Qualitative agreement is found for the spin polarization currents of the 1D and 2D ring. Quantitatively, however, the spin polarization currents are weaker in the more realistic 2D ring, especially for weak spin-orbit interaction, but can be considerably enhanced with the aid of a linearly polarized electromagnetic field. Specific spin polarization current symmetries relating the Dresselhaus spin-orbit interaction case to the Rashba one are found to hold for the 2D ring, which is embedded in the photon cavity.

1 Introduction

Geometrical phases have captured much interest in the field of quantum transport. Electrons in a non-trivially connected region like a quantum ring can show a variety of geometrical phases. An Aharonov-Bohm (AB) phase [1] is acquired by a charged particle moving around a magnetic flux. An Aharonov-Casher (AC) phase [2] is acquired by a particle with magnetic moment encircling, for example, a charged line. The Aharonov-Anandan (AA) phase [3] is the remaining phase of the AC phase when subtracting the so-called dynamical phase. When the system is propagated adiabatically, the dynamical phase describes the whole time-dependence leaving an AA phase, which is static. This can be seen by introducing time-dependent parameters of the Hamiltonian [4]. In the non-adiabatic case, if the AA phase is defined similarly to the AA phase of the adiabatic system (for an alternative definition see Ref. [5]), a dependence of the AA phase on time-dependent

fields can in general not totally be avoided. The dynamical phase captures then only part of the dynamics of the global phase. Filipp [6] showed that the splitting of the global phase into the AA phase and the remaining dynamical phase can be achieved also in the non-adiabatic case. The Berry phase [7] is the adiabatic approximation of the AA phase. Transport properties of magnetic-flux threaded rings [8–11] have been investigated and the influence of a cavity photon mode on the AB oscillations explored [12]. Furthermore, the magnetic field leads to persistent charge currents [13]. Both, the persistent current [14] and the conductance through the ring show characteristic oscillations with period $\Phi_0 = hc/e$, the latter were first measured in 1985 [15].

The AC effect can be observed in the case of a more general electric field than the one produced by a charged line, i.e. including the radial component and a component in the z-direction [16]. Experimentally, it is relatively simple to realize an electric field in the z-direction, i.e. which is directed perpendicular to the two-dimensional (2D) plane containing the quantum ring structure. By changing the strength of the electric field, the spin-orbit interaction strength of the Rashba effect [17] can be

tuned. The AC effect appears also for a Dresselhaus spin-orbit interaction [18], which is typically stronger in GaAs. Persistent equilibrium spin currents due to geometrical phases were addressed for the Zeeman interaction with an inhomogeneous, static magnetic field [19]. Later, Balatsky and Altshuler [20] studied persistent spin currents related to the AC phase. Several authors addressed the persistent spin current oscillations as the strength of the spin-orbit interaction [16,21,22] (or magnetic flux through the ring [23]) is increased. As opposed to the AB oscillations with the magnetic flux, the AC oscillations are not periodic with the spin-orbit interaction strength. Optical control of the spin current can be achieved by a nonadiabatic, two-component laser pulse [24]. Suggestions to measure persistent spin currents by the induced mechanical torque [25] or the induced electric field [26] have been proposed. An analytical state-dependent expression for a specific spin polarization of the spin current has been stated in reference [27].

Charge persistent currents in quantum rings can be produced by two time-delayed light pulses with perpendicularly oriented, linear polarization [28] and phase-locked laser pulses based on the circular photon polarization influencing the many-electron (ME) angular momentum [29]. Moreover, energy splitting of degenerate states in interaction with a monochromatic circularly polarized electromagnetic mode and its vacuum fluctuations can lead to charge persistent currents [30,31]. Furthermore, the nonequilibrium dynamical response of the dipole moment and spin polarization of a quantum ring with spin-orbit interaction and magnetic field under two linearly polarized electromagnetic pulses has been studied [32]. Quantum systems embedded in an electromagnetic cavity have become one of the most promising devices for quantum information processing applications. We are considering here the influence of the cavity photons on the transient charge and spin transport inside the ring. We treat the electron-photon interaction by using exact numerical diagonalization including many levels [33], i.e. beyond a two-level Jaynes-Cummings model or the rotating wave approximation and higher order corrections of it [34–36].

Concentrating on the *electronic* transport through a quantum ring connected to leads, which is embedded in a magnetic field, several studies exist for only Rashba spin-orbit interaction [37–39], only Dresselhaus spin-orbit interaction [40] or both [41]. When the light-matter interaction is combined with the strong coupling of the quantum ring to leads, further interesting phenomena arise (especially when the leads have a bias, which breaks additional transport symmetries). The electronic transport through a quantum system in a strong system-lead coupling regime was studied for longitudinally polarized fields [42–44], or transversely polarized fields [45,46] – though without taking into consideration spin-orbit effects. For a weak coupling between the system and the leads, the Markovian approximation, which neglects memory effects in the system, can be used [47–50]. To describe a stronger transient system-lead coupling, we use a non-Markovian generalized master equation [51–53] involving energy-dependent cou-

pling elements. The dynamics of the open system under non-equilibrium conditions and realistic device geometries can be described with the time-convolutionless generalized master equation (TCL-GME) [12,54], which is suitable for higher system-lead coupling and allows for a controlled perturbative expansion in the system-lead coupling strength.

The time-dependent transport of spin-orbit and Coulomb interacting electrons through a topologically nontrivial broad ring geometry, embedded in an electromagnetic cavity with a quantized photon mode, and connected to leads has not yet been explored beyond the Markovian approximation. One of the objectives of the present work is to present and explain the similarities and differences of the charge and spin polarization current between one-dimensional (1D) and 2D rings [37,55]. To discern effects from the realistic 2D structure with Coulomb interaction between the electrons and transient coupling to electrically biased leads, we compare our results for the persistent spin polarization current in the 2D ring to the analytical results in the 1D ring with only Rashba or Dresselhaus spin-orbit interaction. For the 2D ring, we performed numerical calculations as analytical solutions are known only for rings without spin-orbit interaction [56]. Furthermore, we embed the 2D ring in a photon cavity with x- or y-polarized photon field to explore the influences of the photon field and its linear polarization on the current. The comparisons are performed in the range of the Rashba or Dresselhaus interaction strength almost up to an AC phase difference $\Delta\Phi \approx 3\pi$.

The paper is organized as follows. In Section 2, we provide a general description of the central ring system and its charge and spin polarization currents, which applies to both the 1D and 2D ring. Section 3 describes our dynamical model for the correlated electrons in the opened up 2D ring embedded in a photon cavity. Section 4 shows the numerical transient results for the 2D ring and sets them in comparison with the analytical 1D results (as described in the Appendices) as a function of the Rashba spin-orbit interaction strength. The influence of the linearly polarized electromagnetic cavity field on the spin polarization currents is studied for different photon field polarization. Furthermore, the differences between the Rashba and Dresselhaus interaction in a ring system are addressed. Our results lead to numerous interesting conclusions (Sect. 5), which we believe will be of practical use in experiments. The time- and space-dependence of the spin photocurrents are provided as supplementary material.

2 General description of the central ring system

In this section, we give the most general Hamiltonian that we consider for the central ring system including a homogeneous magnetic field in the z-direction, Zeeman interaction, Rashba and Dresselhaus spin-orbit interaction, Coulomb repulsion between the electrons and a single cavity photon mode interacting with the electronic system.

Furthermore, we use this general Hamiltonian to derive in two independent ways operators for the charge and spin polarization density, charge and spin polarization current density and spin polarization source terms. The spin polarization source terms result from the fact that the spin transport is not satisfying a continuity equation due to the spin-orbit coupling.

2.1 Central system Hamiltonian

The time-evolution operator of the closed system with respect to $t = 0$,

$$\hat{U}_S(t) = \exp\left(-\frac{i}{\hbar}\hat{H}_S t\right), \tag{1}$$

is defined by a many-body (MB) system Hamiltonian

$$\hat{H}_S = \int d^2r \, \hat{\boldsymbol{\Psi}}^\dagger(\mathbf{r})\left[\left(\frac{\hat{\mathbf{P}}^2}{2m^*} + V_S(\mathbf{r})\right) + H_Z \right. \\ \left. + \hat{H}_R(\mathbf{r}) + \hat{H}_D(\mathbf{r})\right]\hat{\boldsymbol{\Psi}}(\mathbf{r}) + \hat{H}_{ee} + \hbar\omega\hat{a}^\dagger\hat{a}, \tag{2}$$

with the two-component vector of field operators

$$\hat{\boldsymbol{\Psi}}(\mathbf{r}) = \begin{pmatrix} \hat{\psi}(\uparrow, \mathbf{r}) \\ \hat{\psi}(\downarrow, \mathbf{r}) \end{pmatrix}, \tag{3}$$

and

$$\hat{\boldsymbol{\Psi}}^\dagger(\mathbf{r}) = \left(\hat{\psi}^\dagger(\uparrow, \mathbf{r}), \hat{\psi}^\dagger(\downarrow, \mathbf{r})\right), \tag{4}$$

where

$$\hat{\psi}(x) = \sum_a \psi_a^S(x)\hat{C}_a \tag{5}$$

is the field operator with $x \equiv (\mathbf{r}, \sigma)$, $\sigma \in \{\uparrow, \downarrow\}$ and the annihilation operator, $\hat{C}_a$, for the single-electron state (SES) $\psi_a^S(x)$ in the central system. The SES $\psi_a^S(x)$ is defined as the eigenstate labeled by a of the Hamiltonian of equation (2), but without photons and Coulomb interaction ($\hat{H}_S - \hat{H}_{ee} - \hbar\omega\hat{a}^\dagger\hat{a}$ for $\hat{\mathbf{A}}^{\mathrm{ph}}(\mathbf{r}) = 0$, see Eq. (6)). The momentum operator is

$$\hat{\mathbf{p}}(\mathbf{r}) = \begin{pmatrix} \hat{p}_x(\mathbf{r}) \\ \hat{p}_y(\mathbf{r}) \end{pmatrix} = \frac{\hbar}{i}\nabla + \frac{e}{c}\left[\mathbf{A}(\mathbf{r}) + \hat{\mathbf{A}}^{\mathrm{ph}}(\mathbf{r})\right]. \tag{6}$$

The Hamiltonian in equation (2) includes a kinetic part, a constant magnetic field $\mathbf{B} = B\hat{\mathbf{z}}$, in Landau gauge being represented by $\mathbf{A}(\mathbf{r}) = -By\mathbf{e}_x$ and a photon field. Furthermore, in equation (2),

$$H_Z = \frac{\mu_B g_S B}{2}\sigma_z \tag{7}$$

describes the Zeeman interaction between the spin and the magnetic field, where g_S is the electron spin g-factor and $\mu_B = e\hbar/(2m_e c)$ is the Bohr magneton. The interaction between the spin and the orbital motion is described by the Rashba part

$$\hat{H}_R(\mathbf{r}) = \frac{\alpha}{\hbar}\left(\sigma_x\hat{p}_y(\mathbf{r}) - \sigma_y\hat{p}_x(\mathbf{r})\right) \tag{8}$$

with the Rashba coefficient α and the Dresselhaus part, which here is restricted to the first-order term in the momentum,

$$\hat{H}_D(\mathbf{r}) = \frac{\beta}{\hbar}\left(\sigma_x\hat{p}_x(\mathbf{r}) - \sigma_y\hat{p}_y(\mathbf{r})\right) \tag{9}$$

with the Dresselhaus coefficient β. In equations (7)–(9), σ_x, σ_y and σ_z represent the spin Pauli matrices. Equation (2) includes the exactly treated electron-electron interaction

$$\hat{H}_{ee} = \frac{e^2}{2\kappa}\int dx' \int dx \frac{\hat{\psi}^\dagger(x)\hat{\psi}^\dagger(x')\hat{\psi}(x')\hat{\psi}(x)}{\sqrt{|\mathbf{r} - \mathbf{r}'|^2 + \eta^2}} \tag{10}$$

with $e > 0$ being the magnitude of the electron charge and the integral over x being composed of a continuous 2D space integral and a sum over the spin. Only for numerical reasons, we include a small regularization parameter $\eta = 0.2387$ nm in equation (10). The last term in equation (2) indicates the quantized photon field, where $\hat{a}$ and $\hat{a}^\dagger$ are the photon annihilation and creation operators, respectively, and $\hbar\omega$ is the photon excitation energy. The photon field interacts with the electron system via the vector potential

$$\hat{\mathbf{A}}^{\mathrm{ph}} = A\left(\mathbf{e}\hat{a} + \mathbf{e}^*\hat{a}^\dagger\right) \tag{11}$$

with

$$\mathbf{e} = \begin{cases} \mathbf{e}_x, & \mathrm{TE}_{011} \\ \mathbf{e}_y, & \mathrm{TE}_{101} \end{cases} \tag{12}$$

for longitudinally-polarized (x-polarized) photon field (TE_{011}) and transversely-polarized (y-polarized) photon field (TE_{101}). The electron-photon coupling constant $g^{EM} = eAa_w\Omega_w/c$ scales with the amplitude A of the electromagnetic field. It is interesting to note that the photon field couples directly to the spin via equations (6), (8) and (9).

2.2 Charge and spin operators

The charge density satisfies the continuity equation

$$\frac{\partial}{\partial t}n^c(\mathbf{r}, t) + \nabla\mathbf{j}^c(\mathbf{r}, t) = 0 \tag{13}$$

while the continuity equation for the spin polarization density includes in general source terms

$$\frac{\partial}{\partial t}n^i(\mathbf{r}, t) + \nabla\mathbf{j}^i(\mathbf{r}, t) = s^i(\mathbf{r}, t) \tag{14}$$

for all spin polarizations $i = x, y, z$. Some controversy has been raised about spin currents and their conservation and several conserved spin currents proposed [57,58]. Today, it is accepted that a redefinition of the Rashba expression [59] is not necessary [26,60] as conservation laws cannot be restored in general [26,61]. We derived the expressions for all the corresponding operators from equations (13) and (14) by two independent ways, and come to

the same conclusion, which is: *though other definitions of the spin current are possible by a related compensation of the source, it is not possible to eliminate a spin polarization source term for our Hamiltonian.* First, we calculated the electron group velocity operator

$$\hat{\mathbf{v}} = \frac{1}{m^* i} \left(\hbar\nabla - \frac{e}{ic}\hat{\mathbf{A}}(\mathbf{r}) \right) + \frac{\alpha}{\hbar} \begin{pmatrix} -\sigma_y \\ \sigma_x \end{pmatrix} + \frac{\beta}{\hbar} \begin{pmatrix} \sigma_x \\ -\sigma_y \end{pmatrix} \quad (15)$$

with the space-dependent vector potential

$$\hat{\mathbf{A}}(\mathbf{r}) = \mathbf{A}(\mathbf{r}) + \hat{\mathbf{A}}^{\mathrm{ph}}(\mathbf{r}) \quad (16)$$

in first quantization for the standard expression, equation (6) in reference [59]. Second, we use the commutation relations for the field operators to derive expressions for the density, current density and source operators in second quantization in the Heisenberg picture with the equation of motion,

$$i\hbar\frac{\partial}{\partial t}\hat{\Psi}(x,t) = \left[\hat{\Psi}(x,t), \hat{H}_S \right], \quad (17)$$

starting from the continuity equation,

$$\frac{\partial}{\partial t}\left(\hat{\mathbf{\Psi}}^\dagger(\mathbf{r},t)\tilde{\sigma}_\gamma\hat{\mathbf{\Psi}}(\mathbf{r},t) \right) = \frac{1}{i\hbar}\left[\hat{\mathbf{\Psi}}^\dagger(\mathbf{r},t)\tilde{\sigma}_\gamma\hat{\mathbf{\Psi}}(\mathbf{r},t)\hat{H}_S \right.$$
$$\left. - \hat{H}_S\hat{\mathbf{\Psi}}^\dagger(\mathbf{r},t)\tilde{\sigma}_\gamma\hat{\mathbf{\Psi}}(\mathbf{r},t) \right] \quad (18)$$

with $\tilde{\sigma}_\gamma$ being proportional to the unity matrix if $\gamma = c$ (describes the charge), $\tilde{\sigma}_c = e\mathbb{1}_2$, or Pauli spin matrix coefficients if $\gamma = i = x, y, z$ (describes the spin polarization), $\tilde{\sigma}_i = \frac{\hbar}{2}\sigma_i$.

In equation (18), the system Hamiltonian $\hat{H}_S$ from equation (2) has to be written with Heisenberg operators instead of the Schrödinger operators. We attribute every contribution, which can be written in the form, $\nabla\mathbf{j}(\mathbf{r},t)$, to the current density operator, thus aiming towards the simplest possible expression for the source operator. Finally, we transform the operators into the Schrödinger picture. The expressions for the charge and spin polarization density operators, charge and spin polarization current density operators and spin polarization source operators are given in Appendix A. We note that our result agrees with the definition of the Rashba current when we limit ourselves to the case without magnetic and photon field and without Dresselhaus spin-orbit interaction [59,62].

3 Theoretical model for a 2D ring coupled to external leads

In this section, we describe the open finite-width quantum ring, which can only be treated numerically. The general expressions of the last section are elaborated for a realistic system. We define the central system potential V_S for the broad quantum ring and its connection to the leads. The electronic ring system is embedded in an electromagnetic cavity by coupling a many-level electron system with
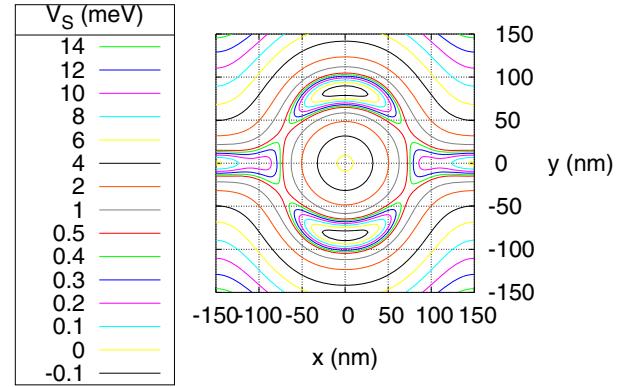
Fig. 1. Equipotential lines in the central ring system connected to the left and right leads. Note that the isolines are refined close to the bottom of the ring structure.

photons using the full photon energy spectrum of a single cavity mode. The central ring system is described by a MB system Hamiltonian $\hat{H}_S$ with a uniform perpendicular magnetic field, in which the electron-electron interaction and the electron-photon coupling to the x- or y-polarized photon field is explicitly taken into account. We employ the TCL-GME approach to explore the non-equilibrium electronic transport when the system is coupled to leads by a transient switching potential.

3.1 Quantum ring potential

The quantum ring is embedded in the central system of length $L_x = 300$ nm situated between two contact areas that will be coupled to the external leads, as is depicted in Figure 1. The system potential is described by

$$V_S(\mathbf{r}) = \sum_{i=1}^{6} V_i \exp\left[-(\beta_{xi}(x - x_{0i}))^2 - (\beta_{yi}y)^2 \right]$$
$$+ \frac{1}{2}m^*\Omega_0^2 y^2, \quad (19)$$

with the parameters from Table 1, which are selected such that the potential is a bit higher at the contact regions (the place where electrons tend otherwise to accumulate) than at the ring arms to guarantee a uniform density distribution along the ring. $x_{03} = \epsilon$ is a small numerical symmetry breaking parameter and $|\epsilon| = 10^{-5}$ nm is enough for numerical stability. In equation (19), $\hbar\Omega_0 = 1.0$ meV is the characteristic energy of the confinement and $m^* = 0.067m_e$ is the effective mass of an electron in GaAs-based material. The ring radius $a \approx 80$ nm, which is important to know for the relation between α and the Rashba parameter, x_R, see equation (B.3) in Appendix B, yielding $\alpha \approx x_R \times 7.1$ meV nm. The definition of the Rashba parameter is convenient to reduce the dependency of the AC phase on the ring size.

Table 1. Parameters of the central region ring potential.

i	V_i in meV	β_{xi} in $\frac{1}{\mathrm{nm}}$	x_{0i} in nm	β_{yi} in $\frac{1}{\mathrm{nm}}$
1	10	0.013	150	0
2	10	0.013	−150	0
3	11.1	0.0165	ϵ	0.0165
4	−4.7	0.02	149	0.02
5	−4.7	0.02	−149	0.02
6	−5.33	0	0	0

3.2 Lead Hamiltonian

The Hamiltonian for the semi-infinite lead $l \in \{L, R\}$ (left or right lead),

$$
\hat{H}_l = \int d^2r \int d^2r' \, \hat{\boldsymbol{\Psi}}_l^\dagger(\mathbf{r}')\delta(\mathbf{r}' - \mathbf{r})
$$
$$
\times \left[\left(\frac{\hat{\mathbf{p}}_l^2}{2m^*} + V_l(\mathbf{r}) \right) + H_Z + \hat{H}_R(\mathbf{r}) + \hat{H}_D(\mathbf{r}) \right] \hat{\boldsymbol{\Psi}}_l(\mathbf{r}),
\tag{20}
$$

with the momentum operator containing only the kinetic momentum and the vector potential coming from the magnetic field (i.e. no photon field)

$$
\hat{\mathbf{p}}_l(\mathbf{r}) = \frac{\hbar}{i}\nabla + \frac{e}{c}\mathbf{A}(\mathbf{r}).
\tag{21}
$$

We remind the reader that the Rashba part, $\hat{H}_R(\mathbf{r})$, (Eq. (8)) and Dresselhaus part, $\hat{H}_D(\mathbf{r})$, (Eq. (9)) of the spin-orbit interaction are momentum dependent and it is the momentum from equation (21), which is used for these terms in equation (20). Equation (20) contains the lead field operator

$$
\hat{\Psi}_l(x) = \sum_q \psi_{ql}(x)\hat{C}_{ql}
\tag{22}
$$

in the two-component vector

$$
\hat{\boldsymbol{\Psi}}_l(\mathbf{r}) = \begin{pmatrix} \hat{\Psi}_l(\uparrow, \mathbf{r}) \\ \hat{\Psi}_l(\downarrow, \mathbf{r}) \end{pmatrix}
\tag{23}
$$

and a corresponding definition of the Hermitian conjugate to equation (4). In equation (22), $\psi_{ql}(x)$ is a SES in the lead l (eigenstate with quantum number q of Hamiltonian Eq. (20)) and $\hat{C}_{ql}$ is the associated electron annihilation operator. The lead potential

$$
V_l(\mathbf{r}) = \frac{1}{2}m^*\Omega_l^2 y^2
\tag{24}
$$

confines the electrons parabolically in the y-direction. We use a relatively strong confinement, $\hbar\Omega_l = 2.0$ meV, to reduce the number of subbands in the leads and thereby the computational effort for our total time-dependent quantum system.

3.3 Time-convolutionless generalized master equation approach

We use the TCL-GME [54], which is a non-Markovian master equation that is local in time. This master equation satisfies the positivity conditions [63] for the MB state occupation probabilities in the reduced density operator (RDO) usually to a higher system-lead coupling strength [12]. We assume, the initial total statistical density matrix can be written as a product of the system and leads density matrices, before switching on the coupling to the leads,

$$
\hat{W}(0) = \hat{\rho}_L \otimes \hat{\rho}_R \otimes \hat{\rho}_S(0),
\tag{25}
$$

with ρ_l, $l \in \{L, R\}$, being the normalized density matrices of the leads. The coupling Hamiltonian between the central system and the leads reads

$$
\hat{H}_T(t) = \sum_{l=L,R} \int dq \, \chi^l(t) \left[\hat{\mathfrak{T}}^l(q)\hat{C}_{ql} + \hat{C}_{ql}^\dagger \hat{\mathfrak{T}}^{l\dagger}(q) \right].
\tag{26}
$$

The coupling is switched on at $t = 0$ via the switching function

$$
\chi^l(t) = 1 - \frac{2}{e^{\alpha^l t} + 1}
\tag{27}
$$

with switching parameter α^l and

$$
\hat{\mathfrak{T}}^l(q) = \sum_{\alpha\beta} |\alpha)(\beta| \sum_a T_{qa}^l (\alpha|\hat{C}_a^\dagger|\beta).
\tag{28}
$$

Equation (28) is written in the system Hamiltonian MB eigenbasis $\{|\alpha)\}$. The coupling tensor [64]

$$
T_{qa}^l = \sum_\sigma \sum_{\sigma'} \int_{\Omega^l} d^2r \int_{\Omega_S^l} d^2r' \, \psi_{ql}^*(\mathbf{r}, \sigma)
$$
$$
\times g_{aq}^l(\mathbf{r}, \mathbf{r}', \sigma, \sigma')\, \psi_a^S(\mathbf{r}', \sigma')
\tag{29}
$$

couples the lead SES $\{\psi_{ql}(\mathbf{r}, \sigma)\}$ with energy spectrum $\{\epsilon^l(q)\}$ to the system SES $\{\psi_a^S(\mathbf{r}, \sigma)\}$ with energy spectrum $\{E_a\}$ that reach into the contact regions [65], Ω_S^l and Ω_l, of system and lead l, respectively, and

$$
g_{aq}^l(\mathbf{r}, \mathbf{r}', \sigma, \sigma') = g_0^l \delta_{\sigma,\sigma'} \exp\left[-\delta_x^l(x - x')^2 - \delta_y^l(y - y')^2 \right]
$$
$$
\times \exp\left(-\frac{|E_a - \epsilon^l(q)|}{\Delta_E^l} \right)
\tag{30}
$$

includes the same-spin coupling condition. Note that the meaning of x in equation (30) is $\mathbf{r} = (x, y)$ and not $x = (\mathbf{r}, \sigma)$. In equation (30), g_0^l is the lead coupling strength. In addition, δ_x^l and δ_y^l are the contact region parameters for the lead l in the x- and the y-direction, respectively. Moreover, Δ_E^l denotes the affinity constant between the central system SES energy levels $\{E_a\}$ and the lead energy levels $\{\epsilon^l(q)\}$.

The time evolution of the RDO of the system,

$$
\hat{\rho}_S(t) = \mathrm{Tr}_L \mathrm{Tr}_R \left[\hat{W}(t) \right],
\tag{31}
$$

is governed by the TCL-GME of reference [12]. It is written in the Schrödinger picture and its kernel is second order in the lead coupling strength.

4 Results

We investigate the non-equilibrium electron transport properties through a quantum ring system, which is situated in a photon cavity and weakly coupled to leads. We assume GaAs-based material with electron effective mass $m^* = 0.067m_e$ and background relative dielectric constant $\kappa = 12.4$. We consider a single cavity mode with fixed photon excitation energy $\hbar\omega = 0.4$ meV. The electron-photon coupling constant in the central system is $g^{EM} = 0.1$ meV. Before switching on the coupling, we assume the central system to be in the pure initial state with electron occupation number $N_{e,\text{init}} = 0$ and photon occupation number $N_{ph,\text{init}} = 1$ of the electromagnetic field.

A small external perpendicular uniform magnetic field $B = 10^{-5}$ T is applied through the central ring system and the lead reservoirs to lift the spin degeneracy. The area of the central ring system is $A = \pi a^2 \approx 2 \times 10^4$ nm^2 leading to the magnetic field $B_0 = \Phi_0/A \approx 0.2$ T corresponding to one flux quantum $\Phi_0 = hc/e$. The applied magnetic field $B \ll B_0$ is therefore order of magnitudes outside the AB regime. The temperature of the reservoirs is assumed to be $T = 0.5$ K. The chemical potentials in the leads are $\mu_L = 1.55$ meV and $\mu_R = 0.7$ meV leading to a source-drain bias window $\Delta\mu = 0.85$ meV. We let the affinity constant $\Delta_E^l = 0.25$ meV to be close to the characteristic electronic excitation energy in the x-direction. In addition, we let the contact region parameters for lead $l \in \{L, R\}$ in the x- and y-direction be $\delta_x^l = \delta_y^l = 4.39 \times 10^{-4}$ nm^{-2}. The system-lead coupling strength $g_0^l = 1.371 \times 10^{-3}$ meV/nm$^{3/2}$.

There are several relevant length and time scales that should be mentioned. The 2D magnetic length is $l = [c\hbar/(eB)]^{1/2} = 8.12$ μm. The ring system is parabolically confined in the y-direction with characteristic energy $\hbar\Omega_0 = 1.0$ meV leading to a much shorter magnetic length scale

$$a_w = \left(\frac{\hbar}{m^*\Omega_0}\right)^{1/2} \frac{1}{\sqrt[4]{1 + [eB/(m^*c\Omega_0)]^2}}$$
$$= 33.74 \text{ nm.} \qquad (32)$$

The time-scale for the switching on of the system-lead coupling is $(\alpha^l)^{-1} = 3.291$ ps, the one-electron state (1ES) charging time-scale $\tau_{1ES} \approx 30$ ps, and the two-electron state (2ES) charging time-scale $\tau_{2ES} \gg 200$ ps described in the sequential tunneling regime. We study the transport properties for $0 \le t < \tau_{2ES}$, when the system has not yet reached a steady state.

To get more insight into the local current flow in the ring system, we define the top local charge ($\gamma = c$) and spin ($\gamma = x, y, z$) current through the upper arm ($y > 0$) of the ring

$$I_{\text{top}}^\gamma(t) = \int_0^\infty dy \, j_x^\gamma(x=0, y, t) \qquad (33)$$

and the bottom local charge and spin polarization current through the lower arm ($y < 0$) of the ring

$$I_{\text{bottom}}^\gamma(t) = \int_{-\infty}^0 dy \, j_x^\gamma(x=0, y, t). \qquad (34)$$

Here, the charge and spin polarization current density,

$$\mathbf{j}^\gamma(\mathbf{r}, t) = \begin{pmatrix} j_x^\gamma(\mathbf{r}, t) \\ j_y^\gamma(\mathbf{r}, t) \end{pmatrix} = \text{Tr}\left[\hat{\rho}_S(t)\hat{\mathbf{j}}^\gamma(\mathbf{r})\right], \qquad (35)$$

is given by the expectation value of the charge and spin polarization current density operator (Eqs. (A.3)–(A.6)). Furthermore, to distinguish better the type and driving schemes of the dynamical transport features, we define the total local (TL) charge or spin polarization current

$$I_{\text{tl}}^\gamma(t) = I_{\text{top}}^\gamma(t) + I_{\text{bottom}}^\gamma(t) \qquad (36)$$

and circular local (CL) charge or spin polarization current

$$I_{\text{cl}}^\gamma(t) = \frac{1}{2}\left[I_{\text{bottom}}^\gamma(t) - I_{\text{top}}^\gamma(t)\right], \qquad (37)$$

which is positive if the electrons move counter-clockwise in the ring. The TL charge current is usually bias driven while the CL charge current could be driven by a magnetic field or circularly polarized photon field. The TL spin polarization current is usually related to non-vanishing sources while a CL spin polarization current can exist without sources. In the Supplementary material* (j_ph^x,x.mpg, j_ph^y,x.mpg, j_ph^z,x.mpg, j_ph^x,y.mpg, j_ph^y,y.mpg, j_ph^z,y.mpg), we present the spin photocurrent densities

$$\mathbf{j}_{\text{ph}}^{\gamma,p}(\mathbf{r}, t) = \mathbf{j}^{\gamma,p}(\mathbf{r}, t) - \mathbf{j}^{\gamma,0}(\mathbf{r}, t), \qquad (38)$$

which are given by the difference of the associated local spin polarization current densities with ($\mathbf{j}^{\gamma,p}(\mathbf{r}, t)$) and without ($\mathbf{j}^{\gamma,0}(\mathbf{r}, t)$) photons, where $p = x, y$ denotes the polarization of the photon field (x: x-polarization, y: y-polarization) and $\gamma \in \{x, y, z\}$. Below, we shall explore the influence of the Rashba and Dresselhaus parameter and the photon field polarization on the non-equilibrium quantum transport in terms of the above time-dependent currents in the broad quantum ring system connected to leads.

4.1 Local charge current in Rashba ring

Here, we will describe the charge currents for the finite-width ring with only Rashba spin-orbit interaction and relate them to the ME spectrum. Figure 2 shows the local charge currents as a function of the Rashba coefficient. The CL charge current is close to zero as the linearly polarized photon field and negligible magnetic field promote no circular charge motion. This is in agreement with the exact result of the 1D closed (i.e. not connected to electron reservoirs) Rashba ring, where the charge current vanishes (see Appendix B). The non-vanishing TL charge current is therefore solely induced by the bias between the leads. Around the critical Rashba coefficient $\alpha^c \approx 13$ meV nm (blue arrow), the TL charge current has a pronounced minimum (dip) coming from the AC destructive phase interference at the critical Rashba parameter, $x_R^c = x_0^o = \sqrt{3} \approx 1.73$ (see Appendix B), which
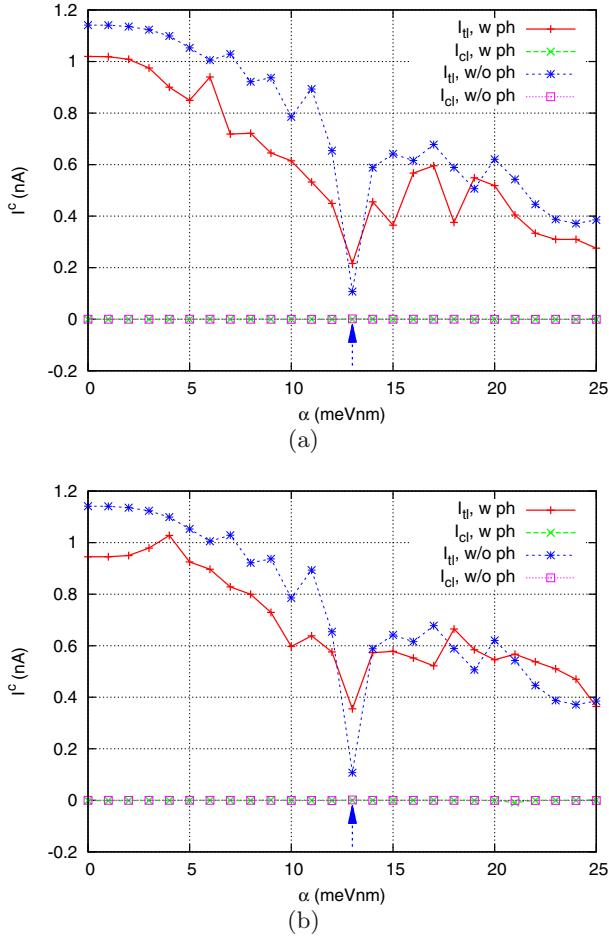
(a)

(b)

Fig. 2. TL current (I_{tl}^c) and CL current (I_{cl}^c) versus the Rashba coefficient and averaged over the time interval [180, 220] ps to give a more representative picture in the transient regime with (w) (a) x-polarized photon field and (b) y-polarized photon field or without (w/o) photon cavity. The Dresselhaus coefficient $\beta = 0$. The blue arrow denotes the position of the first destructive AC phase.

Fig. 3. ME energy spectrum of the system Hamiltonian equation (2) versus the Rashba coefficient α without photon cavity. The states are differentiated according to their electron content N_e: zero-electron state ($N_e = 0$, 0ES, green dot), one-electron states ($N_e = 1$, 1ES, red dots) and two-electron states ($N_e = 2$, 2ES, blue crosses). The Dresselhaus coefficient $\beta = 0$. The bias window $[\mu_R, \mu_L]$ is depicted by solid black lines. The orange parallelogram indicates the location of 1ES crossings.

corresponds to $\alpha^c \approx x_R^c \times 7.1$ meV nm $= 12.3$ meV nm. This confirms that the predicted AC phase manifests itself in the behavior of a measurable quantity (the charge current). The dip is very sharp, i.e. it is in a very narrow range of the the Rashba coefficient α around α^c. The linearly polarized photons tend in general to suppress the local charge current as the increasing number of possible MB states tends to constrict them to smaller energy differences in the MB spectrum. However, especially for the y-polarized photon field (Fig. 2b), the AC minimum appears weaker, and for large values $\alpha \geq 18$ meV nm, the TL current is sometimes enhanced.

To investigate the charge current minimum (blue arrow in Fig. 2) further, we have a look at the ME spectrum as a function of the Rashba coefficient (Fig. 3), where the zero-electron state (0ES) is marked in green color, the 1ES in red color and the 2ES in blue color. Around $\alpha \approx 13$ meV nm, we observe crossings of the 1ESs (inside the orange parallelogram in Fig. 3), which correspond to
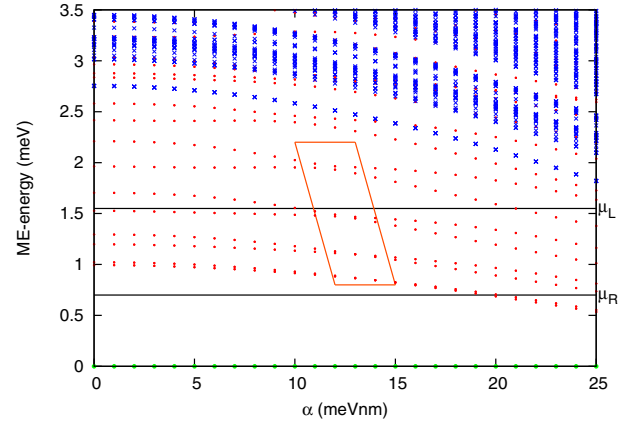
the AC destructive phase interference at x_R^c (similar to the situation in Fig. B.1). We see clearly that the phase relation and the TL charge current behavior are linked due to the appearance of a current-suppressing ME degeneracy [12]. It is also interesting to notice that the critical Rashba coeffient describing the location of the crossing point is the smaller the higher a selected 1ES lies in energy. As the spin-orbit wavefunctions of the higher-in-energy 1ESs are more extended the associated effective 1D ring radius a increases. Now, since $\alpha_0^o = \frac{\hbar^2 x_0^o}{2m^* a}$ obtained from equation (B.3), the first crossing point value α_0^o is located at smaller α-values for the 1ESs, which are higher in energy.

4.2 Local spin polarization current in Rashba ring

Here, we will describe our numerical results for the local spin polarization currents for the finite-width ring with only Rashba spin-orbit interaction and compare them to the corresponding exact analytical expressions for a 1D ring. The latter are described in detail in Appendix B. Our aim with the comparison to the analytical results is to clarify the role of the different parts of the central Hamiltonian (Eq. (2)).

In Figure 4, we compare the 2D local Rashba spin polarization currents $I_{tl/cl,2D,R}^i$ without photon field with the analogously defined 1D TL Rashba spin polarization current

$$I_{tl,1D,R}^{i,e/o} = -j_R^{i,e/o}\left(\frac{\pi}{2}\right) + j_R^{i,e/o}\left(-\frac{\pi}{2}\right) \tag{39}$$

and 1D CL Rashba spin polarization current

$$I_{cl,1D,R}^{i,e/o} = \frac{1}{2}\left(j_R^{i,e/o}\left(\frac{\pi}{2}\right) + j_R^{i,e/o}\left(-\frac{\pi}{2}\right)\right). \tag{40}$$
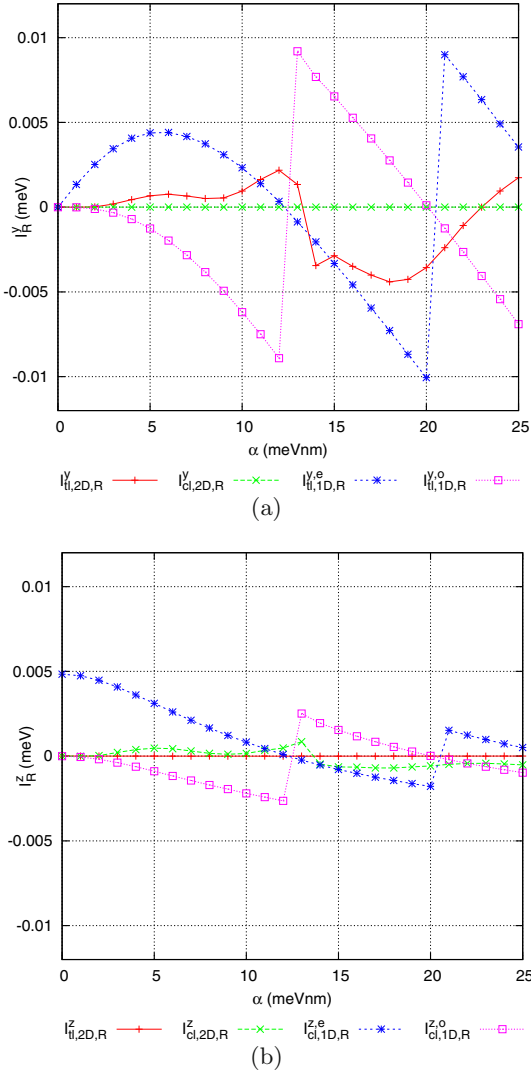
(a)

(b)

Fig. 4. 2D TL Rashba spin polarization current I_{tl}^i or 2D CL Rashba spin polarization current I_{cl}^i averaged over the time interval $[180, 220]$ ps without photon cavity in comparison with the 1D TL Rashba spin polarization current $I_{\mathrm{tl},1D,R}^{i,e/o}$ or 1D CL Rashba spin polarization current $I_{\mathrm{cl},1D,R}^{i,e/o}$ for even or odd cardinalities and with the electron number N_e taken from the 2D case. The Rashba spin polarization currents are shown for (a) S_y spin polarization and (b) S_z spin polarization versus the Rashba coefficient α. The Dresselhaus coefficient $\beta = 0$ and the ring radius $a = 80$ nm. The 1D TL and CL spin polarization currents, which are equal to zero, $I_{\mathrm{cl},1D,R}^{y,e/o} = I_{\mathrm{tl},1D,R}^{z,e/o} = 0$, are not shown.

For the electron number N_e, which $j_{1D,R}^{i,e/o}$ depends on, we have chosen the corresponding value of the 2D Rashba ring without photon cavity averaged over the time interval $[180, 220]$ ps. We need to compare the 2D local Rashba spin polarization currents to both the case of even and odd cardinalities (numbers of occupied states) for the 1D Rashba spin polarization current $j_{1D,R}^{i,e/o}$ (see Appendix B). This is because, first, $N_e/2$ is not an integer number in general and, second, the state occupancies in the central

system are not following a sharp Fermi distribution due to electron correlations and the geometry- and energy-dependent coupling to the biased leads. For S_x spin polarization, in a plot of the same scale as Figure 4, the 2D TL and CL Rashba spin polarization currents, I_{tl}^x and I_{cl}^x, cannot be distinguished from a zero line.

We are now analyzing the similarities and differences between the 2D and 1D Rashba spin polarization currents in detail. First, there is strong agreement in the spin polarization currents, which are zero: $I_{\mathrm{tl},2D,R}^x$, $I_{\mathrm{cl},2D,R}^x$, $I_{\mathrm{cl},2D,R}^y$ and $I_{\mathrm{tl},2D,R}^z$ are almost vanishing. In agreement with this, the corresponding 1D TL and CL Rashba spin polarization currents are vanishing: $I_{\mathrm{tl},1D,R}^{x,e/o} = I_{\mathrm{cl},1D,R}^{x,e/o} = I_{\mathrm{cl},1D,R}^{y,e/o} = I_{\mathrm{tl},1D,R}^{z,e/o} = 0$. Second, some similarities can be found regarding the position in α of the zero transitions when the even cardinality case is taken as a reference. Regarding the differences, Figure 4 reveals that the 2D spin polarization currents are in general smaller than the 1D spin polarization currents (often in between the 1D Rashba spin polarization currents for even and odd cardinality, $I_{1D,R}^{i,e}$ and $I_{1D,R}^{i,o}$, respectively). This is because many fractionally occupied ME states are contributing to the 2D currents. In addition the "peaks" of the 1D currents at α-values close to the constructive or destructive AC phase, $\Delta\Phi = n\pi$, $n = 0, 1, \ldots$, are smoothened in α (and thereby reduced) due to the 2D structure.

Figure 5 shows how the x- or y-polarized photon field influences the Rashba local spin polarization currents, which are far from zero (the photon field has no influence on the set of vanishing currents). For reasons of comparison also the currents without photon field are shown. For $\alpha \leq 8$ meV nm the photon cavity field enhances the spin polarization currents for both polarizations as opposed to the local charge current. In general, the modifications of the y-polarized photon field are a bit stronger due to the closer agreement of the characteristic electronic excitation energy in the y-direction with the photon mode energy $\hbar\omega = 0.4$ meV.

To continue our discussion about the similarities between the 2D and 1D Rashba spin polarization currents, we also would like to present the spatial distribution of the 2D currents. Figure 6 shows the spin polarization current densities $\mathbf{j}^x(x, y)$ (top panels), $\mathbf{j}^y(x, y)$ (middle panels) and $\mathbf{j}^z(x, y)$ (bottom panels). The photon field is switched off (left panels) or it is x-polarized (right panels). The spin polarization current densities are depicted for a Rashba coefficient $\alpha = 5$ meV nm below the first destructive AC interference (we note that the spin polarization current densities show increasingly vortex structures for larger α). The results without photon cavity (left panels) have the following similarities to the 1D ring: first, the S_x spin polarization current density is maximal at $\varphi = 0, \pi$ (Fig. 6a) and the S_y spin polarization current density is maximal at $\varphi = -\pi/2, \pi/2$ (Fig. 6b), which is in agreement with Figure B.2. Second, the S_z spin polarization current density is almost homogeneous in φ (Fig. 6c), which is also in agreement with Figure B.2. Third, the relative directions of the spin flow are in agreement between the 2D and 1D
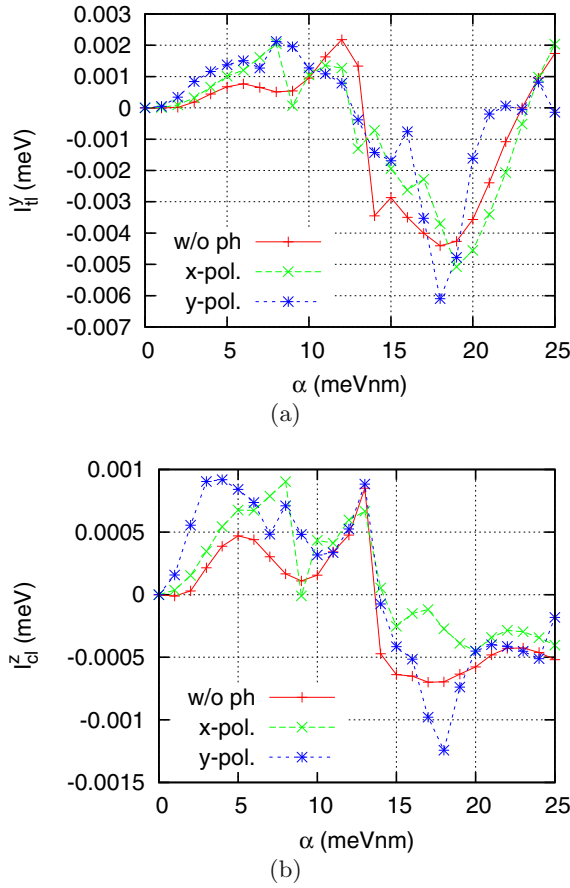
Fig. 5. (a) TL Rashba spin polarization current I_{tl}^y for S_y spin polarization and (b) CL Rashba spin polarization current I_{cl}^z for S_z spin polarization averaged over the time interval $[180, 220]$ ps without (w/o) photon cavity, x-polarized photon field and y-polarized photon field versus the Rashba coefficient α for the ring of finite width. The Dresselhaus coefficient $\beta = 0$.

case, when the flow directions for the different spin polarizations are related. Fourth, the spin flow is also in the 2D case along the φ-direction, except the vortices around charge density maxima at the contact regions of the 2D ring for S_z spin polarization.

Next, we want to study the influence of the linearly polarized photons on the spin polarization current density distributions (right versus left panels in Fig. 6). All spin polarization current densities are a bit larger for x-polarized photons except the vortices at the contact regions due to a redistribution of the charge density (i.e. the density of potential spin carriers) from the contact regions to the ring arms. For the time regime shown in Figure 6, the time dependence of the spin polarization current densities is still considerable, in particular with photon field. The time dependence of the spin polarization current densities without photon cavity in the non-equilibrium situation is shown in the supplementary material* (jˆx.mpg, jˆy.mpg, jˆz.mpg). The time dependence of the spin photocurrent densities is shown in the files (j_phˆx,x.mpg, j_phˆy,x.mpg, j_phˆz,x.mpg, j_phˆx,y.mpg, j_phˆy,y.mpg,

j_phˆz,y.mpg). In all files, the Rashba coefficient is chosen to be $\alpha = 5$ meV nm and the Dresselhaus coefficient $\beta = 0$.

4.3 Local spin polarization current in Dresselhaus ring

Here, we will present the results for the Dresselhaus ring and compare them to the results for the Rashba ring. The exact analytical expressions for a 1D Dresselhaus ring are described in Appendix D. The 2D charge currents from Figure 2 remain the same in the Dresselhaus case. How the 2D spin polarization currents shown in Figures 4 and 5 look like in the Dresselhaus case can be deduced from Figure 7, which shows the TL and CL 2D spin polarization currents with and without x-polarized photon field. The left panels correspond to the situation of only Rashba spin-orbit interaction, the right panels to the situation of only Dresselhaus spin-orbit interaction. It becomes clear from these figures that the symmetries between the Rashba and Dresselhaus ring (Eq. (D.7)), apply to the non-equilibrium situation of a 2D ring of interacting electrons, which is connected to leads. This is because neither the Coulomb interaction nor the 2D ring potential depend on the spin. The leads include spin-orbit interaction and the contact regions allow for tunneling of electron between same-spin states of the central system and leads (Eq. (30)). This is why the symmetries (Eq. (D.7)), are conserved (to support this, we note in passing that also the spin polarization currents from the left lead into the ring and from the ring into the right lead, satisfy Eq. (D.7)). Furthermore, the ring may be embedded in a photon cavity with linearly polarized photons without breaking the symmetry relations (Eq. (D.7)) (the symmetries are conserved also for y-polarization, not shown in Fig. 7). It can be easily understood that the photon field does not break this symmetry as the photonic part of the vector potential operator $\hat{A}^{\text{ph}}(\mathbf{r})$ enters the Rashba Hamiltonian (Eq. (8)) and Dresselhaus Hamiltonian (Eq. (9)) in the same way as the momentum operator.

Figure 8 shows the spin polarization current densities $\mathbf{j}^x(x, y)$ (top panels), $\mathbf{j}^y(x, y)$ (middle panels) and $\mathbf{j}^z(x, y)$ (bottom panels) for the 2D Rashba (left panels) and 2D Dresselhaus ring (right panels) in comparison. It confirms that equations (D.7) are valid at any location in the central system. Finally, we note that the Zeeman term equation (7) breaks the symmetry relations. The intricate effect from the magnetic field can be recognized for $B \geq 0.1$ T.

5 Conclusions

The transport of electrons can be controlled by various interference phenomena and geometric phases. In this work, we turned our focus to physical effects connected to the AC phase, which can be influenced by the strength of the spin-orbit coupling, ring radius, device geometry and cavity photons. For our open non-Markovian quantum system, it appears most convenient to us to consider directly the AC phase without separating the dynamical
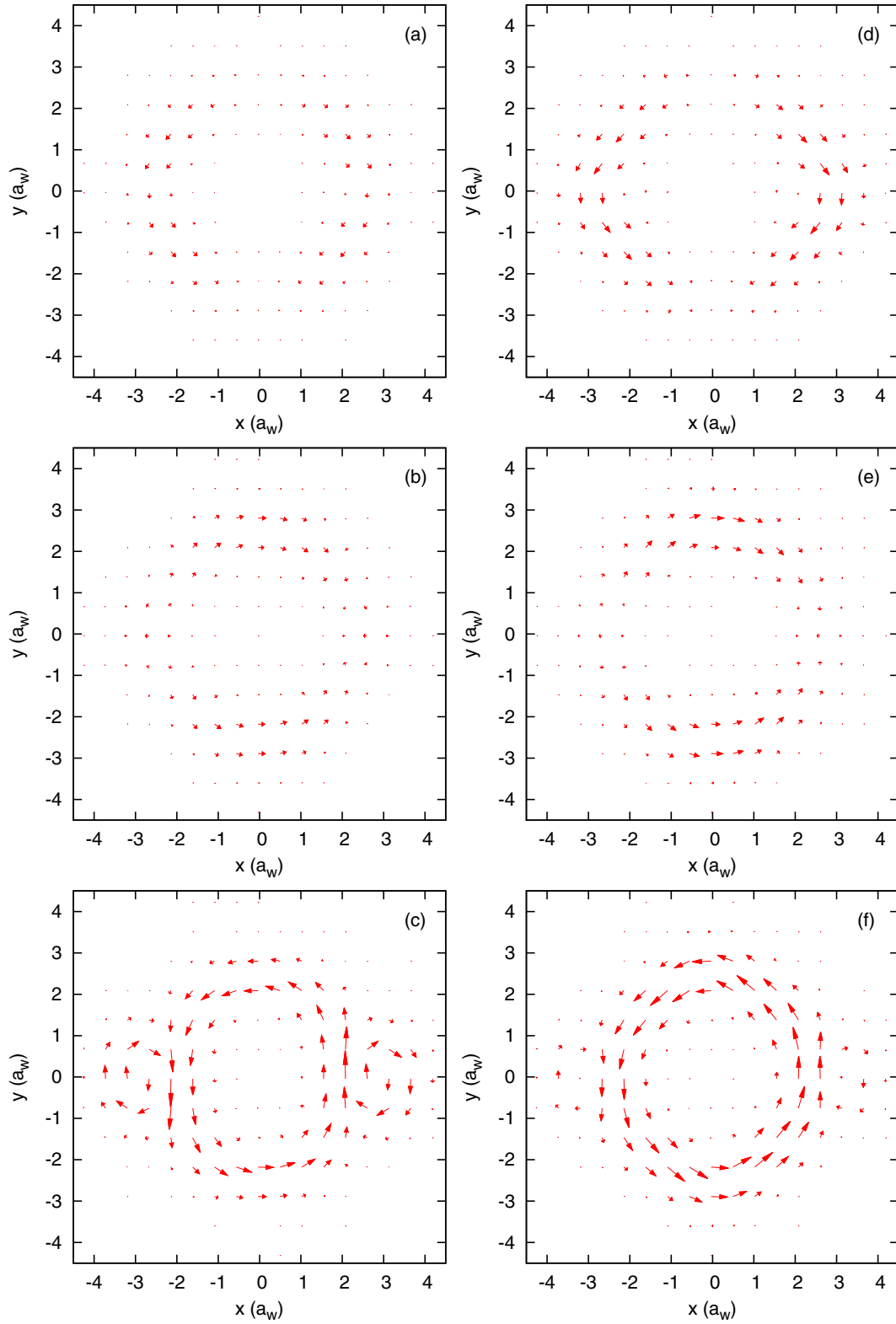
Fig. 6. Spin polarization current densities $\mathbf{j}^i(x,y)$, $i = x, y, z$ at $t = 200$ ps (a)–(c) without photon field or (d)–(e) with x-polarized photon field for (a) and (d) S_x spin polarization, (b) and (e) S_y spin polarization or (e) and (f) S_z spin polarization. The Rashba coefficient $\alpha = 5$ meV nm and the Dresselhaus coefficient $\beta = 0$. A spin polarization current density vector of length a_w corresponds to 1.25×10^{-3} meV/a_w.
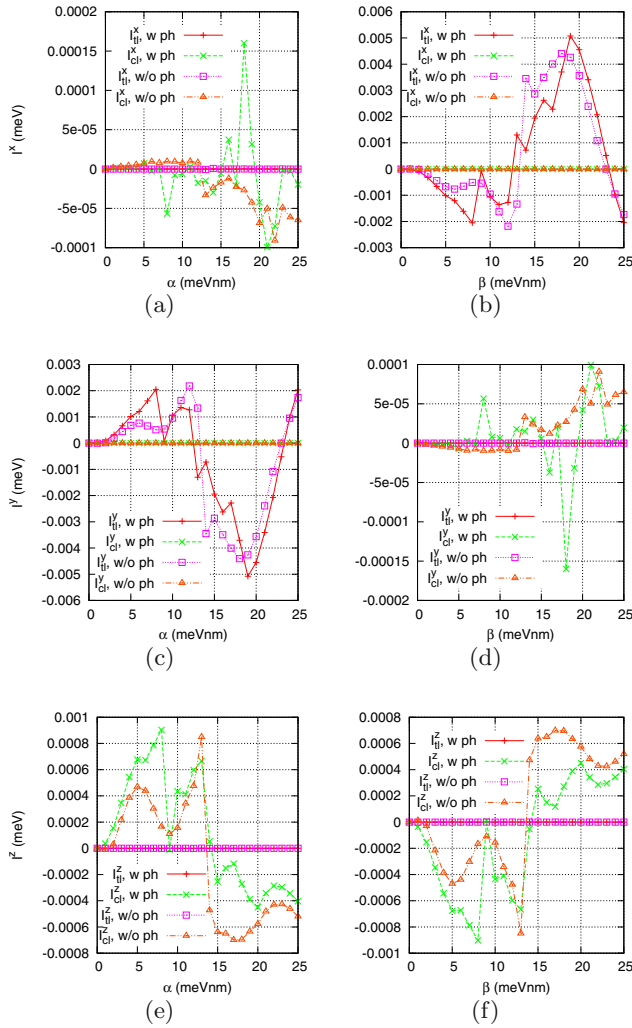
Fig. 7. TL and CL 2D spin polarization current, I_{tl}^i and I_{cl}^i, respectively, averaged over the time interval $[180, 220]$ ps with (w) x-polarized photon field or without (w/o) photon cavity for (a) S_x spin polarization and Rashba interaction ($\beta = 0$), (b) S_x spin polarization and Dresselhaus interaction ($\alpha = 0$), (c) S_y spin polarization and Rashba interaction ($\beta = 0$), (d) S_y spin polarization and Dresselhaus interaction ($\alpha = 0$), (e) S_z spin polarization and Rashba interaction ($\beta = 0$) and (f) S_z spin polarization and Dresselhaus interaction ($\alpha = 0$). Note that the scale for the ordinate may differ dramatically between the subfigures.

part. In an open system the adiabatic approximation is not valid [66] (especially when thinking about a non-Markovian formalism) and therefore the AA phase could not be reduced to the Berry phase. Furthermore, for a mixed state, the definition of a geometric phase would have to be revisited [67]. We have presented the charge and spin polarization currents inside a quantum ring, in which the spin of the electrons interacts with their orbital motion via the Rashba or Dresselhaus interaction. We presented analytical results for the currents in a simple 1D ring in Appendices B and D. For zero temperature and

divisibility of the electron number by 4, we predict a finite spin current of non-interacting electrons in the limit of the electric field causing the Rashba effect approaching zero. The current for the S_z spin polarization is flowing homogeneously around the ring, but the currents for the other spin polarizations, flows from a local source to a local sink. For a finite-width ring connected to leads, where the electrons are correlated by Coulomb interaction, we calculated numerically the transient currents before the equilibrium situation is reached using a TCL-GME formalism. We included spin-orbit coupling, but excluded Coulomb interaction in the electrically biased leads. In addition, we allow the system electrons to interact with a single cavity photon mode of x- or y-polarized photons. The broad ring geometry together with the spin degree of freedom required a substantial computational effort on state of the art machines.

A pronounced AC charge current dip can be recognized in the TL current flowing from the higher-biased lead through the ring to the lower-biased lead at the predicted position of the Rashba coefficient derived from the 1D model. The critical Rashba coefficient is related to two experimentally adjustable parameters, the ring radius and the gate voltage leading to the average electric field causing the Rashba effect. The dip structure is linked to crossings in the ME spectrum and can be removed partly by embedding the ring system in a photon cavity of preferably y-polarized photons. The spin polarization currents of the 1D and 2D rings agree qualitatively in their kind (TL or CL) and spin polarization (S_x, S_y or S_z), the position of sign changes with respect to the Rashba parameter and the geometric shape of the current flow distribution. Quantitatively, we can conclude that it is preferable to choose a narrow ring of weakly correlated electrons to obtain a strong spin polarization current. The linearly polarized photon field interacting with the electrons suppresses in general the charge current but enhances the spin polarization current in the small Rashba coefficient regime. Therefore, the linearly polarized photon field might be used to restore to some extent the strong spin polarization current for S_z spin polarization in the small Rashba coefficient regime, which is suppressed for the broad ring with electron correlations and coupling to the leads. This information could be very useful for experiments with spin polarization currents (for suggestions to measure it, see Refs. [25,26]) since the number of materials with a strong spin current could be considerably enhanced (without the requirement of a gate). The local spin polarization current and spin photocurrent inside the quantum ring are subjected to stronger changes in time than non-local quantities as the total charge in the system (which change due to the transport between the leads and ring). This shows that the non-equilibrium local transport promises to be a particularly interesting subject to study further. We established symmetry relations of the spin polarization currents between the Rashba and Dresselhaus ring. We have shown that they remain valid for a finite-width ring of correlated electrons connected to electrically biased leads via a spin-conserving coupling tensor. Furthermore, switching
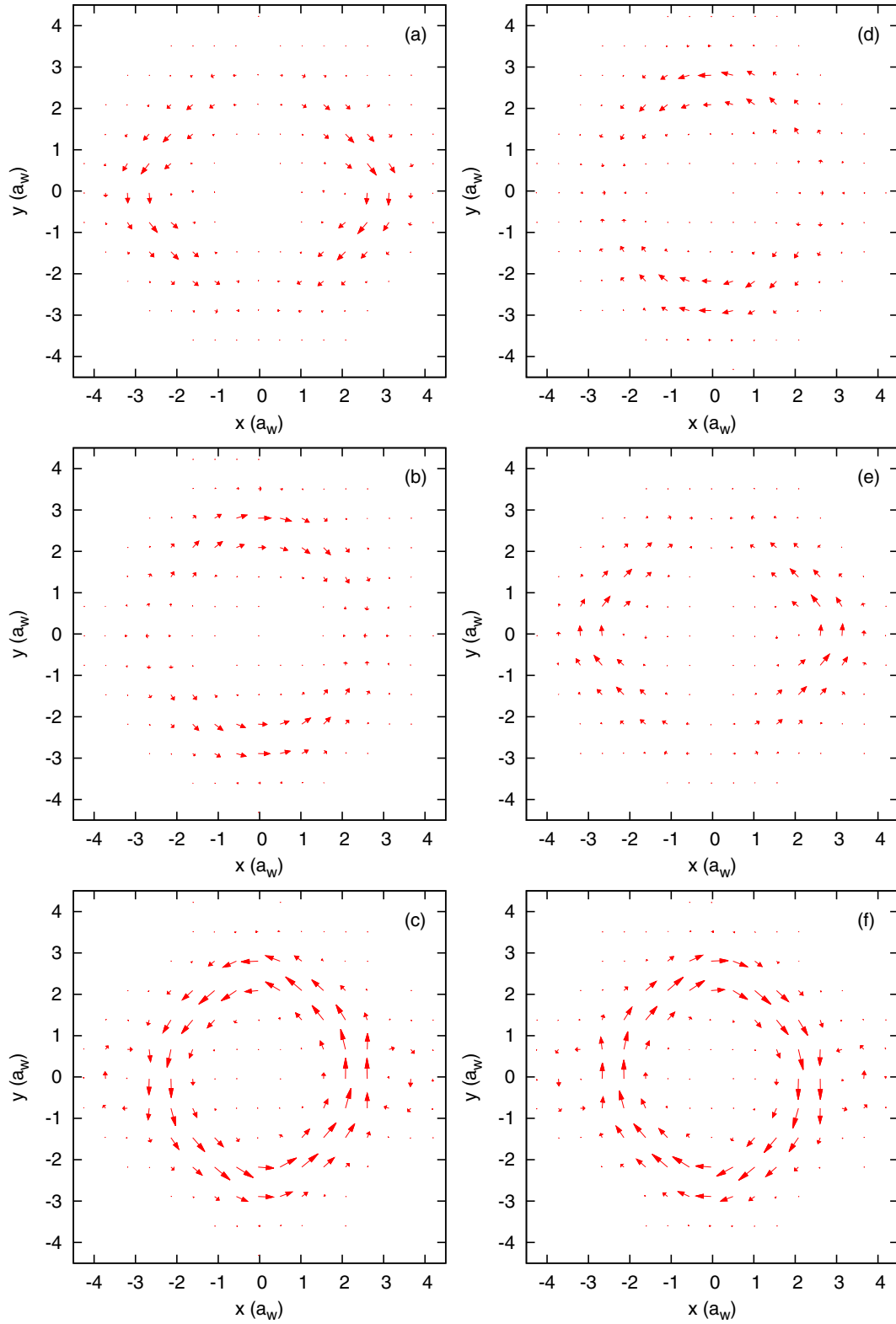
Fig. 8. Spin polarization current densities $\mathbf{j}^i(x, y)$, $i = x, y, z$ at $t = 200$ ps for (a)–(c) only Rashba spin-orbit interaction ($\alpha = 5$ meV nm and $\beta = 0$) or (d)–(f) only Dresselhaus spin-orbit interaction ($\alpha = 0$ and $\beta = 5$ meV nm) and for (a) and (d) S_x spin polarization, (b) and (e) S_y spin polarization or (e) and (f) S_z spin polarization. The photon field is x-polarized. A spin polarization current density vector of length a_w corresponds to 1.25×10^{-3} meV/a_w.

on the cavity photon field does not destroy the symmetry relations. The sign of the spin polarization current for S_z spin polarization could be used to distinguish the Rashba and Dresselhaus spin-orbit interactions provided that they are not too strong ($x < x_R^c$). In this case, the bias difference between the leads should be reduced, to constrict the magnetic field induced by the charge current.

The conceived quantum ring system in a photon cavity with adjustable spin-orbit interaction and photon field polarization could be helpful in the development of spin-optoelectronic quantum devices for quantum information processing. For example, our system suggested here could be directly considered as a spintronic device, which blocks an electrical circuit when the gate potential is very close to a specific value (see Fig. 2). This critical gate potential, which could be tuned with the ring radius (compare with Eq. (B.3)), corresponds to the critical magnitude of an electric field in the z-direction, which causes the AC phase in the ring interferometer to be precisely destructive. Thus, our device could be used as a quantum switch, which is extremely sensitive to the gate voltage.

Appendix A: Charge and spin polarization (current) density and spin polarization source operators

Here, we give the expressions for several operators: the charge density operator

$$\hat{n}^c(\mathbf{r}) = e\hat{\boldsymbol{\Psi}}^\dagger(\mathbf{r})\hat{\boldsymbol{\Psi}}(\mathbf{r}) \tag{A.1}$$

and the spin polarization density operator for spin polarization S_i

$$\hat{n}^i(\mathbf{r}) = \frac{\hbar}{2}\hat{\boldsymbol{\Psi}}^\dagger(\mathbf{r})\sigma_i\hat{\boldsymbol{\Psi}}(\mathbf{r}). \tag{A.2}$$

The component labeled with $j \in \{x, y\}$ of the charge current density operator is given by

$$\hat{j}_j^c(\mathbf{r}) = \frac{e\hbar}{2m^*i}\left[\hat{\boldsymbol{\Psi}}^\dagger(\mathbf{r})\nabla_j\hat{\boldsymbol{\Psi}}(\mathbf{r}) - \left(\nabla_j\hat{\boldsymbol{\Psi}}^\dagger(\mathbf{r})\right)\hat{\boldsymbol{\Psi}}(\mathbf{r})\right]$$
$$+ \frac{e^2}{m^*c}\hat{A}_j(\mathbf{r})\hat{\boldsymbol{\Psi}}^\dagger(\mathbf{r})\hat{\boldsymbol{\Psi}}(\mathbf{r})$$
$$+ \frac{e}{\hbar}\hat{\boldsymbol{\Psi}}^\dagger(\mathbf{r})(\beta\sigma_x - \alpha\sigma_y)\hat{\boldsymbol{\Psi}}(\mathbf{r})\delta_{x,j}$$
$$+ \frac{e}{\hbar}\hat{\boldsymbol{\Psi}}^\dagger(\mathbf{r})(\alpha\sigma_x - \beta\sigma_y)\hat{\boldsymbol{\Psi}}(\mathbf{r})\delta_{y,j}. \tag{A.3}$$

The current density operator for the j-component and S_x spin polarization

$$\hat{j}_j^x(\mathbf{r}) = \frac{\hbar^2}{4m^*i}\left[\hat{\boldsymbol{\Psi}}^\dagger(\mathbf{r})\sigma_x\nabla_j\hat{\boldsymbol{\Psi}}(\mathbf{r}) - \left(\nabla_j\hat{\boldsymbol{\Psi}}^\dagger(\mathbf{r})\right)\sigma_x\hat{\boldsymbol{\Psi}}(\mathbf{r})\right]$$
$$+ \frac{e\hbar}{2m^*c}\hat{A}_j(\mathbf{r})\hat{\boldsymbol{\Psi}}^\dagger(\mathbf{r})\sigma_x\hat{\boldsymbol{\Psi}}(\mathbf{r})$$
$$+ \frac{\beta\delta_{x,j} + \alpha\delta_{y,j}}{2}\hat{\boldsymbol{\Psi}}^\dagger(\mathbf{r})\hat{\boldsymbol{\Psi}}(\mathbf{r}). \tag{A.4}$$

The current density operator for S_y spin polarization

$$\hat{j}_j^y(\mathbf{r}) = \frac{\hbar^2}{4m^*i}\left[\hat{\boldsymbol{\Psi}}^\dagger(\mathbf{r})\sigma_y\nabla_j\hat{\boldsymbol{\Psi}}(\mathbf{r}) - \left(\nabla_j\hat{\boldsymbol{\Psi}}^\dagger(\mathbf{r})\right)\sigma_y\hat{\boldsymbol{\Psi}}(\mathbf{r})\right]$$
$$+ \frac{e\hbar}{2m^*c}\hat{A}_j(\mathbf{r})\hat{\boldsymbol{\Psi}}^\dagger(\mathbf{r})\sigma_y\hat{\boldsymbol{\Psi}}(\mathbf{r})$$
$$- \frac{\alpha\delta_{x,j} + \beta\delta_{y,j}}{2}\hat{\boldsymbol{\Psi}}^\dagger(\mathbf{r})\hat{\boldsymbol{\Psi}}(\mathbf{r}), \tag{A.5}$$

and S_z spin polarization

$$\hat{j}_j^z(\mathbf{r}) = \frac{\hbar^2}{4m^*i}\left[\hat{\boldsymbol{\Psi}}^\dagger(\mathbf{r})\sigma_z\nabla_j\hat{\boldsymbol{\Psi}}(\mathbf{r}) - \left(\nabla_j\hat{\boldsymbol{\Psi}}^\dagger(\mathbf{r})\right)\sigma_z\hat{\boldsymbol{\Psi}}(\mathbf{r})\right]$$
$$+ \frac{e\hbar}{2m^*c}\hat{A}_j(\mathbf{r})\hat{\boldsymbol{\Psi}}^\dagger(\mathbf{r})\sigma_z\hat{\boldsymbol{\Psi}}(\mathbf{r}). \tag{A.6}$$

The spin polarization source operator for S_x spin polarization

$$\hat{s}^x(\mathbf{r}) = -\frac{\mu_B g_S B}{2}\hat{\boldsymbol{\Psi}}^\dagger(\mathbf{r})\sigma_y\hat{\boldsymbol{\Psi}}(\mathbf{r})$$
$$- \frac{i\alpha}{2}\left[\frac{\partial}{\partial x}\left(\hat{\boldsymbol{\Psi}}^\dagger(\mathbf{r})\right)\sigma_z\hat{\boldsymbol{\Psi}}(\mathbf{r}) - \hat{\boldsymbol{\Psi}}^\dagger(\mathbf{r})\sigma_z\frac{\partial}{\partial x}\hat{\boldsymbol{\Psi}}(\mathbf{r})\right]$$
$$- \frac{i\beta}{2}\left[\frac{\partial}{\partial y}\left(\hat{\boldsymbol{\Psi}}^\dagger(\mathbf{r})\right)\sigma_z\hat{\boldsymbol{\Psi}}(\mathbf{r}) - \hat{\boldsymbol{\Psi}}^\dagger(\mathbf{r})\sigma_z\frac{\partial}{\partial y}\hat{\boldsymbol{\Psi}}(\mathbf{r})\right]$$
$$- \frac{e\alpha}{c\hbar}\hat{A}_x(\mathbf{r})\hat{\boldsymbol{\Psi}}^\dagger(\mathbf{r})\sigma_z\hat{\boldsymbol{\Psi}}(\mathbf{r})$$
$$- \frac{e\beta}{c\hbar}\hat{A}_y(\mathbf{r})\hat{\boldsymbol{\Psi}}^\dagger(\mathbf{r})\sigma_z\hat{\boldsymbol{\Psi}}(\mathbf{r}), \tag{A.7}$$

S_y spin polarization

$$\hat{s}^y(\mathbf{r}) = \frac{\mu_B g_S B}{2}\hat{\boldsymbol{\Psi}}^\dagger(\mathbf{r})\sigma_x\hat{\boldsymbol{\Psi}}(\mathbf{r})$$
$$- \frac{i\beta}{2}\left[\frac{\partial}{\partial x}\left(\hat{\boldsymbol{\Psi}}^\dagger(\mathbf{r})\right)\sigma_z\hat{\boldsymbol{\Psi}}(\mathbf{r}) - \hat{\boldsymbol{\Psi}}^\dagger(\mathbf{r})\sigma_z\frac{\partial}{\partial x}\hat{\boldsymbol{\Psi}}(\mathbf{r})\right]$$
$$- \frac{i\alpha}{2}\left[\frac{\partial}{\partial y}\left(\hat{\boldsymbol{\Psi}}^\dagger(\mathbf{r})\right)\sigma_z\hat{\boldsymbol{\Psi}}(\mathbf{r}) - \hat{\boldsymbol{\Psi}}^\dagger(\mathbf{r})\sigma_z\frac{\partial}{\partial y}\hat{\boldsymbol{\Psi}}(\mathbf{r})\right]$$
$$- \frac{e\beta}{c\hbar}\hat{A}_x(\mathbf{r})\hat{\boldsymbol{\Psi}}^\dagger(\mathbf{r})\sigma_z\hat{\boldsymbol{\Psi}}(\mathbf{r})$$
$$- \frac{e\alpha}{c\hbar}\hat{A}_y(\mathbf{r})\hat{\boldsymbol{\Psi}}^\dagger(\mathbf{r})\sigma_z\hat{\boldsymbol{\Psi}}(\mathbf{r}) \tag{A.8}$$

and S_z spin polarization

$$
\hat{s}^z(\mathbf{r}) = \frac{1}{2}\left[\frac{\partial}{\partial x}\left(\hat{\mathbf{\Psi}}^\dagger(\mathbf{r})\right)(i\alpha\sigma_x + i\beta\sigma_y)\,\hat{\mathbf{\Psi}}(\mathbf{r})\right.
$$
$$
\left. - \hat{\mathbf{\Psi}}^\dagger(\mathbf{r})(i\alpha\sigma_x + i\beta\sigma_y)\frac{\partial}{\partial x}\hat{\mathbf{\Psi}}(\mathbf{r})\right]
$$
$$
+ \frac{1}{2}\left[\frac{\partial}{\partial y}\left(\hat{\mathbf{\Psi}}^\dagger(\mathbf{r})\right)(i\beta\sigma_x + i\alpha\sigma_y)\,\hat{\mathbf{\Psi}}(\mathbf{r})\right.
$$
$$
\left. - \hat{\mathbf{\Psi}}^\dagger(\mathbf{r})(i\beta\sigma_x + i\alpha\sigma_y)\frac{\partial}{\partial y}\hat{\mathbf{\Psi}}(\mathbf{r})\right]
$$
$$
+ \frac{e}{ic\hbar}\hat{A}_x(\mathbf{r})\hat{\mathbf{\Psi}}^\dagger(\mathbf{r})(i\alpha\sigma_x + i\beta\sigma_y)\,\hat{\mathbf{\Psi}}(\mathbf{r})
$$
$$
+ \frac{e}{ic\hbar}\hat{A}_y(\mathbf{r})\hat{\mathbf{\Psi}}^\dagger(\mathbf{r})(i\beta\sigma_x + i\alpha\sigma_y)\,\hat{\mathbf{\Psi}}(\mathbf{r}). \quad \text{(A.9)}
$$

Appendix B: 1D Rashba ring

In this Appendix, we derive and describe analytical results for an ideal 1D ring, i.e. with infinitely narrow confinement, and with only Rashba spin-orbit interaction. We will neglect the magnetic field, electron-electron interaction and the photons. According to these assumptions, we use the general expressions of Section 2 for the Hamiltonian, equation (2), and the charge and spin operators (Eqs. (A.1)–(A.9)), in a simplified form for our derivations here.

Our Hamiltonian containing the kinetic and the Rashba term

$$
\hat{H} = -\frac{\hbar^2}{2m^*}\nabla^2 + \frac{\alpha}{i}\left[\sigma_x\frac{\partial}{\partial y} - \sigma_y\frac{\partial}{\partial x}\right], \quad \text{(B.1)}
$$

where α is the Rashba coefficient and σ_x and σ_y are the spin Pauli matrices, has the 1D ring limit [68,69]:

$$
\hat{H}^{1D} = -\hbar\Omega\frac{\partial^2}{\partial\varphi^2} - i\hbar\omega_R\left(\cos(\varphi)\sigma_x + \sin(\varphi)\sigma_y\right)\frac{\partial}{\partial\varphi}
$$
$$
- i\frac{\hbar\omega_R}{2}\left(\cos(\varphi)\sigma_y - \sin(\varphi)\sigma_x\right). \quad \text{(B.2)}
$$

It is convenient to introduce the dimensionless Rashba parameter, x_R, which scales linearly with the Rashba coefficient α, given by

$$
x_R := \frac{\omega_R}{\Omega} \quad \text{(B.3)}
$$

with the Rashba frequency $\omega_R := \alpha/(\hbar a)$ and kinetic frequency $\Omega := \hbar/(2m^*a^2)$. The advantage of the Rashba parameter x_R over the Rashba coefficient α is that the eigenvalues and eigenfunctions (except for a normalization constant) and physical properties based on them become independent of the ring radius a. In this sense, equation (B.3) is in agreement with the radius dependence of the AC oscillations found in reference [70] indicating that the oscillation length is smaller in the Rashba coefficient α when the radius is larger. The eigenvalues of the Hamiltonian in equation (B.2) are [71]:

$$
E_{\nu n} = \hbar\Omega\left[\left(n - \frac{\Phi^\nu}{2\pi}\right)^2 - \frac{x^2}{4}\right] \quad \text{(B.4)}
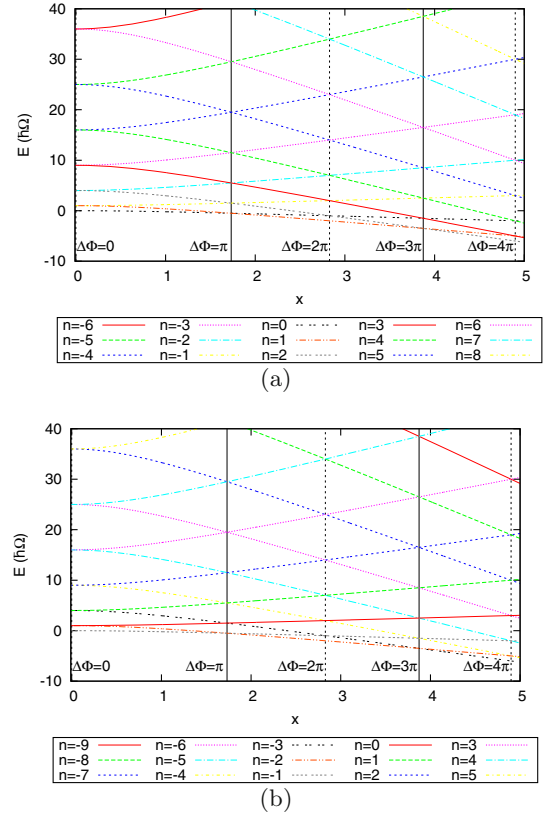$$

Fig. B.1. Spectrum from equation (B.4) as a function of $x = x_R$ or $x = x_D$ for (a) $\nu = -1$ and (b) $\nu = 1$. The vertical black lines indicate the positions of the constructive (short-dashed line, $\Delta\Phi = 2n\pi$, $n = 0, 1, \dots$) and destructive (solid line, $\Delta\Phi = (2n+1)\pi$, $n = 0, 1, \dots$) AC phase.

with the AC phase

$$
\Phi^\nu = -\pi\left[1 + \nu\sqrt{1 + x^2}\right], \quad \text{(B.5)}
$$

where we call n the total angular momentum quantum number, $\nu = \pm 1$ the spin quantum number and $x = x_R$ in the Rashba ring case. The spectrum is shown in Figure B.1. For zero temperature, $T = 0$, the lowest $N_e/2$ states are occupied both for $\nu = -1$ and $\nu = 1$. This leads to occupation changes at every other level crossing point.

The eigenfunctions are

$$
\Psi_{\nu n}^R(\varphi) = \begin{pmatrix} \Psi_{\nu n}^R(\varphi, \uparrow) \\ \Psi_{\nu n}^R(\varphi, \downarrow) \end{pmatrix}
$$
$$
= \frac{\exp(in\varphi)}{\sqrt{2\pi a}}\begin{pmatrix} A_{\nu,1}^R \\ A_{\nu,2}^R \exp(i\varphi) \end{pmatrix} \quad \text{(B.6)}
$$

with the 2×2 coefficient matrix

$$
A^R = \begin{pmatrix} A_{\nu,1}^R & A_{\nu,2}^R \end{pmatrix} = \begin{pmatrix} \cos\left(\frac{\theta_R}{2}\right) & \sin\left(\frac{\theta_R}{2}\right) \\ \sin\left(\frac{\theta_R}{2}\right) & -\cos\left(\frac{\theta_R}{2}\right) \end{pmatrix} \quad \text{(B.7)}
$$

and

$$
\tan\left(\frac{\theta_R}{2}\right) = \frac{1 - \sqrt{1 + x_R^2}}{x_R}. \quad \text{(B.8)}
$$

In our derivation of the exact analytical expressions for the spin polarization currents given in Appendix C, we assume that the number of electrons, N_e, is even, as this results in the same amount of states (distinguished by n) with $\nu = -1$ or $\nu = 1$ to be occupied provided that $T = 0$ (except possibly at the crossing points of the spectrum). Mathematically, we could phrase it that the cardinality (number of elements) of the two sets of occupied states $N_\pm$ for $\nu = \pm 1$ is equal meaning that $|N_-| = |N_+| = N_e/2$. The charge density is given by

$$n_R^c = \frac{e N_e}{2\pi a} \tag{B.9}$$

and the charge current $j_R^c = 0$. The spin polarization densities are all vanishing:

$$n_R^x = n_R^y = n_R^z = 0. \tag{B.10}$$

The reason behind this is the Kramers degeneracy for the time-reversal symmetric Hamiltonian (Eq. (B.1)). The spin polarization currents are given by

$$
\begin{aligned}
j_R^x(\varphi) =& \frac{\hbar j_\Phi \cos(\varphi) \left(x_R - x_R\sqrt{1+x_R^2}\right)}{N_e\left(2 + 2x_R^2 - 2\sqrt{1+x_R^2}\right)} \\
&\times \left[\sum_{n \in N_-}(2n+1) - \sum_{n \in N_+}(2n+1) \right] \\
&+ \frac{x_R \hbar j_\Phi \cos(\varphi)}{2},
\end{aligned}
\tag{B.11}
$$

$$j_R^y(\varphi) = \frac{\sin(\varphi)}{\cos(\varphi)} j_R^x(\varphi) \tag{B.12}$$

and

$$
\begin{aligned}
j_R^z =& \frac{\hbar j_\Phi}{N_e\left(2 + 2x_R^2 - 2\sqrt{1+x_R^2}\right)} \left\{ \left(2 + x_R^2 - 2\sqrt{1+x_R^2}\right) \right. \\
&\times \left[\sum_{n \in N_+} n - \sum_{n \in N_-}(n+1) \right] \\
&\left. + x_R^2 \left[\sum_{n \in N_-} n - \sum_{n \in N_+}(n+1) \right] \right\},
\end{aligned}
\tag{B.13}
$$

where $j_\Phi = N_e\hbar/(4\pi m^* a^2)$ is the maximum absolute value of the persistent charge current in units of the electron charge e as a function of the magnetic flux Φ for

$\alpha = \beta = 0$. Finally, the spin polarization source terms

$$
\begin{aligned}
s_R^x(\varphi) =& -\frac{\hbar \sin(\varphi) j_\Phi}{N_e a\left(2 + 2x_R^2 - 2\sqrt{1+x_R^2}\right)} \\
&\times \left\{ \left(2x_R + x_R^3 - 2x_R\sqrt{1+x_R^2}\right) \right. \\
&\times \left[\sum_{n \in N_-}(n+1) - \sum_{n \in N_+} n \right] \\
&\left. + x_R^3 \left[\sum_{n \in N_+}(n+1) - \sum_{n \in N_-} n \right] \right\},
\end{aligned}
\tag{B.14}
$$

$$s_R^y(\varphi) = -\frac{\cos(\varphi)}{\sin(\varphi)} s_R^x(\varphi) \tag{B.15}$$

and s_R^z is vanishing as expected since j_R^z depends not on φ.

To account properly for the rearrangements of the sets of occupied states N_- and N_+, we have to distinguish the case with the cardinalities, $|N_-|$ and $|N_+| = |N_-|$, to be even and state rearrangements at $x_n^{\mathrm{e}} = \sqrt{(2n+1)^2 - 1}$, $n = 0, 1, \ldots$ and the case with odd cardinalities and state rearrangements at $x_n^{\mathrm{o}} = \sqrt{(2n+2)^2 - 1}$, $n = 0, 1, \ldots$ In the even cardinality case, we define a multi-step function $\chi^{\mathrm{e}} = n$ for $x_n^{\mathrm{e}} < x < x_{n+1}^{\mathrm{e}}$, $n = 0, 1, \ldots$ In the odd cardinality case, $\chi^{\mathrm{o}} = 0$ for $x < x_0^{\mathrm{o}}$ and $\chi^{\mathrm{o}} = n+1$ for $x_n^{\mathrm{o}} < x < x_{n+1}^{\mathrm{o}}$, $n = 0, 1, \ldots$ Here, x is the Rashba parameter x_R or Dresselhaus parameter x_D to be defined later. Then, in the case of a given even cardinality, we have the sets of occupied states

$$
\begin{aligned}
N_-^{\mathrm{e}} = \{ & -|N_-^{\mathrm{e}}|/2 + \chi^{\mathrm{e}} + 1, \\
& -|N_-^{\mathrm{e}}|/2 + \chi^{\mathrm{e}} + 2, \ldots, |N_-^{\mathrm{e}}|/2 + \chi^{\mathrm{e}} \}
\end{aligned}
\tag{B.16}
$$

and

$$
\begin{aligned}
N_+^{\mathrm{e}} = \{ & -|N_+^{\mathrm{e}}|/2 - \chi^{\mathrm{e}} - 1, \\
& -|N_+^{\mathrm{e}}|/2 - \chi^{\mathrm{e}}, \ldots, |N_+^{\mathrm{e}}|/2 - \chi^{\mathrm{e}} - 2 \}
\end{aligned}
\tag{B.17}
$$

while in the case of a given odd cardinality, we have the sets

$$
\begin{aligned}
N_-^{\mathrm{o}} = \{ & -(|N_-^{\mathrm{o}}| - 1)/2 + \chi^{\mathrm{o}}, \\
& -(|N_-^{\mathrm{o}}| - 1)/2 + \chi^{\mathrm{o}} + 1, \ldots, (|N_-^{\mathrm{o}}| - 1)/2 + \chi^{\mathrm{o}} \}
\end{aligned}
\tag{B.18}
$$

and

$$
\begin{aligned}
N_+^{\mathrm{o}} = \{ & -(|N_+^{\mathrm{o}}| - 1)/2 - \chi^{\mathrm{o}} - 1, \\
& -(|N_+^{\mathrm{o}}| - 1)/2 - \chi^{\mathrm{o}}, \ldots, (|N_+^{\mathrm{o}}| - 1)/2 - \chi^{\mathrm{o}} - 1 \}.
\end{aligned}
\tag{B.19}
$$

The spin polarization currents are

$$j_R^{x,\mathrm{e/o}}(\varphi) = \frac{\hbar j_\Phi}{2} \cos(\varphi) f^{\mathrm{e/o}}(x_R), \tag{B.20}$$

$$j_R^{y,\mathrm{e/o}}(\varphi) = \frac{\hbar j_\Phi}{2} \sin(\varphi) f^{\mathrm{e/o}}(x_R) \tag{B.21}$$

and

$$j_R^{z,\mathrm{e/o}} = \frac{\hbar j_\Phi}{2} g^{\mathrm{e/o}}(x_R). \tag{B.22}$$

The non-vanishing source terms are

$$s_R^{x,\mathrm{e/o}}(\varphi) = -\frac{\hbar j_\Phi}{2a} f^{\mathrm{e/o}}(x_R) \sin(\varphi) \tag{B.23}$$

and

$$s_R^{y,\mathrm{e/o}}(\varphi) = \frac{\hbar j_\Phi}{2a} f^{\mathrm{e/o}}(x_R) \cos(\varphi). \tag{B.24}$$

The functions $f^{\mathrm{e/o}}(x)$ and $g^{\mathrm{e/o}}(x)$ describing the dependency on the Rashba parameter $x = x_R$ or Dresselhaus parameter $x = x_D$ have to be distinguished according to their cardinality.

For even cardinality, we have

$$f^{\mathrm{e}}(x) = \frac{2x - 2x\sqrt{1+x^2}}{2 + 2x^2 - 2\sqrt{1+x^2}} [2 + 2\chi^{\mathrm{e}}] + x \tag{B.25}$$

and

$$g^{\mathrm{e}}(x) = \frac{2}{2 + 2x^2 - 2\sqrt{1+x^2}} \left[x^2 \left[\chi^{\mathrm{e}} + \frac{1}{2} \right] \right. \\ \left. - \left(2 + x^2 - 2\sqrt{1+x^2} \right) \left[\frac{3}{2} + \chi^{\mathrm{e}} \right] \right]. \tag{B.26}$$

For odd cardinality, they are

$$f^{\mathrm{o}}(x) = \frac{2x - 2x\sqrt{1+x^2}}{2 + 2x^2 - 2\sqrt{1+x^2}} [1 + 2\chi^{\mathrm{o}}] + x \tag{B.27}$$

and

$$g^{\mathrm{o}}(x) = \frac{2}{2 + 2x^2 - 2\sqrt{1+x^2}} \left[x^2 \chi^{\mathrm{o}} \right. \\ \left. - \left(2 + x^2 - 2\sqrt{1+x^2} \right) [1 + \chi^{\mathrm{o}}] \right]. \tag{B.28}$$

Equations (B.20)–(B.28) represent the main result of this section. In the following, the properties of these Rashba spin polarization currents and spin polarization source terms will be described.

Figure B.2 shows the geometrical arrangement of the sources and spin polarization currents. For the x- and y-component of the spin (Figs. B.2a and B.2b), respectively, source and sink term are largest on opposite sites of the ring. Correspondingly, a non-homogeneous spin polarization current is flowing from the source to the sink with maxima at the intermediate positions, where the source term is zero. The only difference between the spin components S_x and S_y is a rotation by $\pi/2$. The source can interchange its position with the sink if we allow for variations in the Rashba parameter x_R. The ranges of x_R, where the case of Figure B.2 applies is dependent on the cardinality and can be alternatively summarized by either the condition $f^{\mathrm{e/o}}(x_R)) \leq 0$ or $g^{\mathrm{e/o}}(x_R) \geq 0$. The current for S_z spin polarization in Figure B.2c is equally large everywhere and circulating around the ring similar to the persistent current invoked by a magnetic flux [72,73].
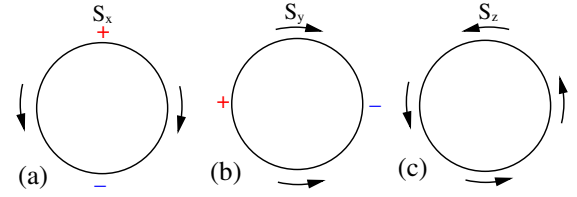

Fig. B.2. Geometrical arrangement of (a) the source term $s_R^{x,\mathrm{e/o}}(\varphi)$ and spin polarization current $j_R^{x,\mathrm{e/o}}(\varphi)$ of the x-component of the spin, (b) $s_R^{y,\mathrm{e/o}}(\varphi)$ and $j_R^{y,\mathrm{e/o}}(\varphi)$ of the y-component and (c) $j_R^{z,\mathrm{e/o}}$ for the z-component in the case that $B = \beta = 0$. The spin polarization current for the z-component of the spin is homogeneous in space due to the absence of the source term $s_R^{z,\mathrm{e/o}}(\varphi)$. The "+"-sign and "–"-sign indicate source and sink, respectively, in the case that x_R is such that $f^{\mathrm{e/o}}(x_R)) \leq 0$ or $g^{\mathrm{e/o}}(x_R) \geq 0$ and the arrows indicate the corresponding spin polarization current direction and are shown (a) and (b) at the positions of maximum current magnitude and (c) at arbitrary positions for $j_R^{z,\mathrm{e/o}}$, which is homogeneous in space.

The z-component of the spin is therefore source-free. This might be understood in the following way: similarly to the magnetic field acting on the spin via the Zeeman term, one can define an effective magnetic field for the Rashba spin-orbit interaction, $\hat{\mathbf{B}}_R = -\hat{\mathbf{p}} \times \mathbf{E}/(m^*c)$, due to the electronic motion inside the electric field $\mathbf{E} = E\mathbf{e}_z$ causing the Rashba interaction. The effective magnetic field is perpendicular to the electric field in the z-direction and the effective momentum of the electrons in the direction of $\mathbf{e}_\varphi$. Consequently, the effective magnetic field is always perpendicular to the S_z spin polarization suggesting that $\frac{\partial}{\partial t} n^z(\mathbf{r}, t) = 0$. In a local interpretation of the spin continuity equation (14), this corresponds to the case that the driving mechanism, i.e. the source term $s_R^{z,\mathrm{e/o}}(\varphi) = 0$. We note that the geometrical aspects of the spin polarization current flow could be summarized by stating that the spin polarization current for spin polarization S_i flows freely in the plane perpendicular to the unit vector $\mathbf{e}_i$. In our case, the spin polarization current is confined to a 1D system along $\mathbf{e}_\varphi$. The spin polarization current magnitude along the ring is then given by the projection $\mathbf{e}_\varphi$ onto the plane perpendicular to $\mathbf{e}_i$. For S_z spin polarization, $\mathbf{e}_\varphi$ is inside this plane and therefore the spin polarization current is space independent. As the spin polarization currents are not dependent on time, we will call them persistent spin polarization currents, not distinguishing whether they are homogeneous in space or not.

Figure B.3 shows the spin polarization currents as a function of the Rashba parameter x_R. As opposed to the magnetic flux dependency of the charge current, the Rashba parameter dependency of the spin polarization currents is not exactly periodic, in particular for small x_R. At the zero points of all the even cardinality spin polarization currents, the odd cardinality spin polarization currents are largest, changing discontinuously by sign due to sudden reoccupations among states of the same spin quantum number ν. Likewise, at the discontinuities of the even cardinality spin polarization currents, the odd cardinality
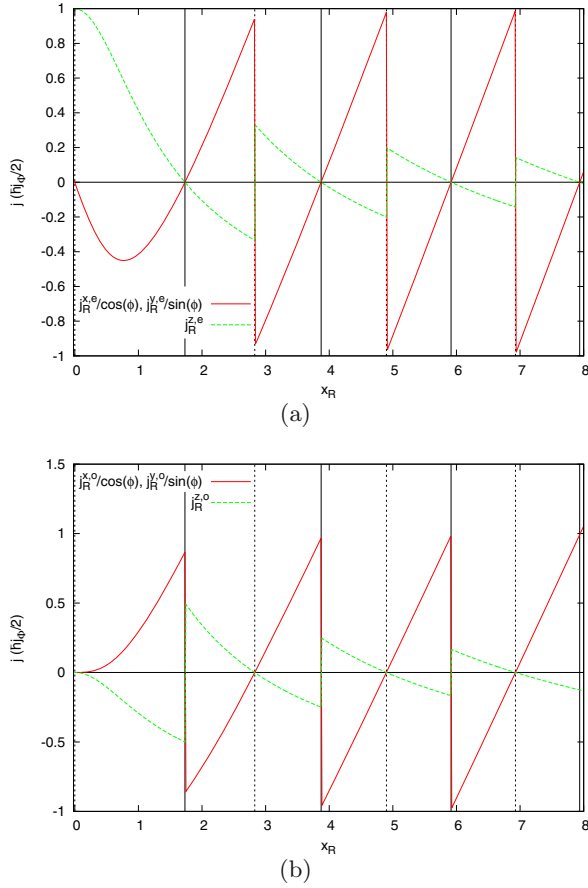
Fig. B.3. Rashba parameter dependency of $j_R^{x,\mathrm{e/o}}(x_R)/\cos(\varphi)$, $j_R^{y,\mathrm{e/o}}(x_R)/\sin(\varphi)$ and $j_R^{z,\mathrm{e/o}}(x_R)$ for $B = \beta = 0$ and (a) $N_e/2$ even, and (b) $N_e/2$ odd. The vertical black lines indicate the positions of the constructive (short-dashed line, $\Delta\Phi = 2n\pi$, $n = 0, 1, \dots$) and destructive (solid line, $\Delta\Phi = (2n+1)\pi$, $n = 0, 1, \dots$) AC phase.

spin polarization currents are zero. It is interesting to note that the z-component of the spin polarization current is commonly larger for small x_R and, in particular, that an infinitesimal small Rashba coefficient should lead to the relatively large spin polarization current $j_R^{z,\mathrm{e}} = \frac{\hbar j_\Phi}{2}$ provided that the total electron number N_e is divisible by 4. This way, an infinitesimal small effective electric field is enough to generate a considerable persistent AC current provided the system can be cooled down and ME interactions neglected. We note that for x_R exactly equal to zero, all spin polarization currents are correctly vanishing as $j_R^{z,\mathrm{e}}$ changes discontinuously at $x_R = 0$.

Appendix C: Derivation of equation (B.11)

Here, we show only the derivation of equation (B.11) in detail. All other Rashba or Dresselhaus charge or spin polarization densities, currents or source terms (Eqs. (B.9)–(B.15) and, in the Dresselhaus case, Eqs. (D.3) and (D.6) and the corresponding expressions, which can be inferred from Eq. (D.7) can be derived in analogy). For a 1D

ring geometry without magnetic and photon field, equation (A.4) can be simplified and the φ-component of the current density along the ring is given in first quantization with $\sum_{\nu=\pm1} N_\nu = N_e$:

$$
\begin{aligned}
j^x(\varphi) = {}& \frac{\hbar^2}{4im^*a} \sum_{\nu=\pm1} \sum_{n\in N_\nu} \left[\Psi_{\nu n}^*(\varphi,\uparrow) \frac{\partial}{\partial\varphi} \Psi_{\nu n}(\varphi,\downarrow) \right. \\
& - \Psi_{\nu n}(\varphi,\downarrow) \frac{\partial}{\partial\varphi} \Psi_{\nu n}^*(\varphi,\uparrow) + \Psi_{\nu n}^*(\varphi,\downarrow) \frac{\partial}{\partial\varphi} \Psi_{\nu n}(\varphi,\uparrow) \\
& \left. - \Psi_{\nu n}(\varphi,\uparrow) \frac{\partial}{\partial\varphi} \Psi_{\nu n}^*(\varphi,\downarrow) \right] \\
& + \frac{\alpha\cos(\varphi)}{2} \sum_{\nu=\pm1} \sum_{n\in N_\nu} \left[\Psi_{\nu n}^*(\varphi,\uparrow)\Psi_{\nu n}(\varphi,\uparrow) \right. \\
& \left. + \Psi_{\nu n}^*(\varphi,\downarrow)\Psi_{\nu n}(\varphi,\downarrow) \right].
\end{aligned}
\tag{C.1}
$$

Now, we introduce the eigenfunctions, equation (B.6), into equation (C.1) making already use of the fact that the coefficients $A_{\nu,\sigma}^R$ from equation (B.7) are real:

$$
\begin{aligned}
j_R^x(\varphi) = {}& \frac{\hbar^2}{8\pi m^*a^2} \left[A_{1,1}^R A_{1,2}^R \exp(i\varphi) \right. \\
& \times \sum_{n\in N_-} (n+1) + A_{2,1}^R A_{2,2}^R \exp(i\varphi) \\
& \times \sum_{n\in N_+} (n+1) + A_{1,1}^R A_{1,2}^R \exp(i\varphi) \\
& \times \sum_{n\in N_-} n + A_{2,1}^R A_{2,2}^R \exp(i\varphi) \\
& \times \sum_{n\in N_+} n + A_{1,1}^R A_{1,2}^R \exp(-i\varphi) \\
& \times \sum_{n\in N_-} n + A_{2,1}^R A_{2,2}^R \exp(-i\varphi) \\
& \times \sum_{n\in N_+} n + A_{1,1}^R A_{1,2}^R \exp(-i\varphi) \\
& \times \sum_{n\in N_-} (n+1) + A_{2,1}^R A_{2,2}^R \exp(-i\varphi) \\
& \left. \times \sum_{n\in N_+} (n_2+1) \right] \\
& + \frac{\alpha\cos(\varphi)}{4\pi a} \left[\left(A_{1,1}^R\right)^2 |N_-| + \left(A_{2,1}^R\right)^2 |N_+| \right. \\
& \left. + \left(A_{1,2}^R\right)^2 |N_-| + \left(A_{2,2}^R\right)^2 |N_+| \right].
\end{aligned}
\tag{C.2}
$$

This can be further simplified and the coefficients from equation (B.7) introduced yielding for even electron number N_e:

$$
\begin{aligned}
j_R^x(\varphi) = {}& \frac{\hbar j_\Phi \cos(\varphi) \cos(\frac{\theta_R}{2}) \sin(\frac{\theta_R}{2})}{N_e} \\
& \times \left[\sum_{n\in N_-} (n+1) - \sum_{n\in N_+} (n+1) + \sum_{n\in N_-} n - \sum_{n\in N_+} n \right] \\
& + \frac{\alpha\cos(\varphi)N_e}{4\pi a}.
\end{aligned}
\tag{C.3}
$$

With the aid of equation (B.8), a relation

$$\cos\left(\frac{\theta_R}{2}\right)\sin\left(\frac{\theta_R}{2}\right) = \frac{x_R - x_R\sqrt{1+x_R^2}}{2 + 2x_R^2 - 2\sqrt{1+x_R^2}} \qquad \text{(C.4)}$$

can be established and introduced in equation (C.3) together with the definition of the Rashba parameter (Eq. (B.3)), to get equation (B.11).

Appendix D: 1D Dresselhaus ring

In this Appendix, we derive and describe analytical results for an ideal 1D ring with only Dresselhaus spin-orbit interaction. We will neglect the magnetic field, electron-electron interaction and the photons. According to these assumptions, we use the general expressions of Section 2 for the Hamiltonian (Eq. (2)), and the charge and spin operators (Eqs. (A.1)–(A.9)), in a simplified form for our derivations here.

The Hamiltonian containing the kinetic and the Dresselhaus term,

$$\hat{H} = -\frac{\hbar^2}{2m^*}\nabla^2 + \frac{\beta}{i}\left[\hat{\sigma}_x\frac{\partial}{\partial x} - \hat{\sigma}_y\frac{\partial}{\partial y}\right], \qquad \text{(D.1)}$$

where β is the Dresselhaus coefficient. In analogy to the Rashba parameter x_R, it is convenient to introduce the dimensionless Dresselhaus parameter, x_D, which scales linearly with the Dresselhaus coefficient β, given by

$$x_D := \frac{\omega_D}{\Omega} \qquad \text{(D.2)}$$

with the Dresselhaus frequency $\omega_D := \beta/(\hbar a)$. The advantage of the Dresselhaus parameter x_D over the Dresselhaus coefficient β is that the eigenvalues and eigenfunctions (except for a normalization constant) become independent of the ring radius a. The Dresselhaus eigenvalues and coefficient matrix are derived in Appendix E. The Dresselhaus and Rashba spectrum are identical and shown in Figure B.1. The charge density is constant as in the Rashba case,

$$n_D^c = \frac{eN_e}{2\pi a}, \qquad \text{(D.3)}$$

and the charge current $j_D^c = 0$.

Thus, the spectrum, charge density and charge current are the same for the Rashba and Dresselhaus ring. More interestingly, we have calculated also the spin polarization densities, spin polarization currents and spin polarization source terms in analogy to the Rashba case. For the Dresselhaus ring, we will present the results by a comparison to the Rashba case and give an explanation of our findings by a comparison of the two Hamiltonians. The Dresselhaus Hamiltonian (Eq. (D.1)) is invariant to the Rashba Hamiltonian (Eq. (B.1)), if the replacement

$$\begin{pmatrix}\hat{\sigma}_x\\\hat{\sigma}_y\\\beta\end{pmatrix} \rightarrow \begin{pmatrix}-\hat{\sigma}_y\\-\hat{\sigma}_x\\\alpha\end{pmatrix}. \qquad \text{(D.4)}$$
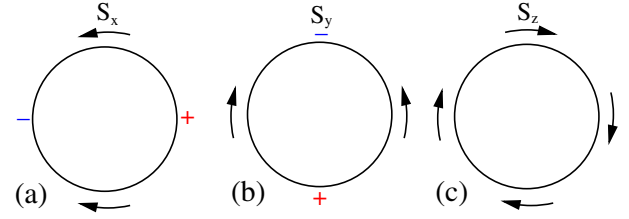

Fig. D.1. Same as Figure B.2, but for the Dresselhaus ring (the case $B = \alpha = 0$).

is performed. Moreover, using the commutation relation $\hat{\sigma}_z = [\hat{\sigma}_x, \hat{\sigma}_y]/(2i)$, the z-spin Pauli matrix transforms according to $\hat{\sigma}_z \rightarrow -\hat{\sigma}_z$. This suggests the following relations for the Dresselhaus spin densities for $x_D = x_R$:

$$\begin{pmatrix}n_D^x\\n_D^y\\n_D^z\end{pmatrix} = \begin{pmatrix}-n_R^y\\-n_R^x\\-n_R^z\end{pmatrix}. \qquad \text{(D.5)}$$

As a consequence, also in the Dresselhaus case, all spin polarization densities are vanishing:

$$n_D^x(\varphi) = n_D^y(\varphi) = n_D^z(\varphi) = 0. \qquad \text{(D.6)}$$

Furthermore, the Dresselhaus spin polarization currents and spin polarization sources are related to the Rashba ones for $x_D = x_R$:

$$\begin{pmatrix}j_D^{x,\text{e/o}}\\j_D^{y,\text{e/o}}\\j_D^{z,\text{e/o}}\end{pmatrix} = \begin{pmatrix}-j_R^{y,\text{e/o}}\\-j_R^{x,\text{e/o}}\\-j_R^{z,\text{e/o}}\end{pmatrix}, \quad \begin{pmatrix}s_D^{x,\text{e/o}}\\s_D^{y,\text{e/o}}\\s_D^{z,\text{e/o}}\end{pmatrix} = \begin{pmatrix}-s_R^{y,\text{e/o}}\\-s_R^{x,\text{e/o}}\\-s_R^{z,\text{e/o}}\end{pmatrix}. \qquad \text{(D.7)}$$

Figure D.1 shows the geometrical arrangement of the sources and spin polarization currents. The differences to the Rashba ring can be stated as follows.

1. The transport pattern for the x-component of the spin is rotated by $-\pi/2$.
2. The transport pattern for the y-component of the spin is rotated by $\pi/2$.
3. The φ-independent current for the z-component of the spin flows in the opposite direction.

Appendix E: Dresselhaus eigenvalues and coefficient matrix

The Hamiltonian equation (D.1) has the 1D ring (strong confinement) limit [69] as can be derived in analogy to reference [68],

$$\hat{H}^{1D} = -\hbar\Omega\frac{\partial^2}{\partial\varphi^2} + i\hbar\omega_D(\cos(\varphi)\hat{\sigma}_y + \sin(\varphi)\hat{\sigma}_x)\frac{\partial}{\partial\varphi}$$

$$+ i\frac{\hbar\omega_D}{2}(\cos(\varphi)\hat{\sigma}_x - \sin(\varphi)\hat{\sigma}_y), \qquad \text{(E.1)}$$

which can be reformulated

$$\hat{H}^{1D}(\varphi) = \hbar\Omega \left[\left(-i\frac{\partial}{\partial\varphi} - \frac{x_D}{2}\hat{R}(\varphi) \right)^2 - \frac{x_D^2}{4} \right] \quad (E.2)$$

with

$$R(\varphi) = \begin{pmatrix} 0 & \exp(i(\varphi - \frac{\pi}{2})) \\ \exp(-i(\varphi - \frac{\pi}{2})) & 0 \end{pmatrix}. \quad (E.3)$$

Using the ansatz

$$\Psi_{\nu n}^D(\varphi) = \begin{pmatrix} \Psi_{\nu n}^D(\varphi, \uparrow) \\ \Psi_{\nu n}^D(\varphi, \downarrow) \end{pmatrix}$$

$$= \frac{\exp(in\varphi)}{\sqrt{2\pi a}} \begin{pmatrix} A_{\nu,1}^D \exp(i\varphi) \\ A_{\nu,2}^D \end{pmatrix} \quad (E.4)$$

leads to the eigenvalue problem

$$\begin{pmatrix} 1 & i\frac{x_D}{2} \\ -i\frac{x_D}{2} & 0 \end{pmatrix} \begin{pmatrix} A_{\nu,1}^D \\ A_{\nu,2}^D \end{pmatrix} = (\Lambda_{\nu n} - n) \begin{pmatrix} A_{\nu,1}^D \\ A_{\nu,2}^D \end{pmatrix}, \quad (E.5)$$

where $\Lambda_{\nu n}$ is related to the Dresselhaus eigenvalues $E_{\nu n}^D$ of Hamiltonian (Eq. (E.2)) by

$$E_{\nu n}^D = \hbar\Omega \left(\Lambda_{\nu n}^2 - \frac{x_D^2}{4} \right). \quad (E.6)$$

The resulting Dresselhaus eigenvalues are identical with the Rashba eigenvalues (Eq. (B.4)). The complex Dresselhaus coefficient matrix is given by

$$A^D = \begin{pmatrix} A_{\nu,1}^D & A_{\nu,2}^D \end{pmatrix} = \begin{pmatrix} -i\cos\left(\frac{\theta_D}{2}\right) & \sin\left(\frac{\theta_D}{2}\right) \\ -i\sin\left(\frac{\theta_D}{2}\right) & -\cos\left(\frac{\theta_D}{2}\right) \end{pmatrix} \quad (E.7)$$

and

$$\tan\left(\frac{\theta_D}{2}\right) = \frac{1 + \sqrt{1 + x_D^2}}{x_D}. \quad (E.8)$$

References

1. Y. Aharonov, D. Bohm, Phys. Rev. **115**, 485 (1959)
2. Y. Aharonov, A. Casher, Phys. Rev. Lett. **53**, 319 (1984)
3. Y. Aharonov, J. Anandan, Phys. Rev. Lett. **58**, 1593 (1987)
4. D.J. Griffiths, *Introduction to Quantum Mechanics* (Pearson Education, 2005)
5. F. Nagasawa, D. Frustaglia, H. Saarikoski, K. Richter, J. Nitta, Nat. Commun. **4**, 2526 (2013)
6. S. Filipp, Ph.D. thesis, Technischen Universität Wien (2006)
7. M.V. Berry, Proc. R. Soc. Lond. A **392**, 45 (1984)
8. B. Szafran, F.M. Peeters, Phys. Rev. B **72**, 165301 (2005)
9. S.S. Buchholz, S.F. Fischer, U. Kunze, M. Bell, D. Reuter, A.D. Wieck, Phys. Rev. B **82**, 045432 (2010)
10. M. Büttiker, Y. Imry, M.Y. Azbel, Phys. Rev. A **30**, 1982 (1984)
11. K.N. Pichugin, A.F. Sadreev, Phys. Rev. B **56**, 9662 (1997)
12. T. Arnold, C.S. Tang, A. Manolescu, V. Gudmundsson, Phys. Rev. B **87**, 035314 (2013)
13. H.F. Cheung, Y. Gefen, E.K. Riedel, W.H. Shih, Phys. Rev. B **37**, 6050 (1988)
14. W.C. Tan, J.C. Inkson, Phys. Rev. B **60**, 5626 (1999)
15. R.A. Webb, S. Washburn, C.P. Umbach, R.B. Laibowitz, Phys. Rev. Lett. **54**, 2696 (1985)
16. S. Oh, C.M. Ryu, Phys. Rev. B **51**, 13441 (1995)
17. Y.A. Bychkov, E.I. Rashba, J. Phys. C **17**, 6039 (1984)
18. G. Dresselhaus, Phys. Rev. **100**, 580 (1955)
19. D. Loss, P. Goldbart, A.V. Balatsky, Phys. Rev. Lett. **65**, 1655 (1990)
20. A.V. Balatsky, B.L. Altshuler, Phys. Rev. Lett. **70**, 1678 (1993)
21. A.A. Kovalev, M.F. Borunda, T. Jungwirth, L.W. Molenkamp, J. Sinova, Phys. Rev. B **76**, 125307 (2007)
22. S.K. Maiti, M. Dey, S. Sil, A. Chakrabarti, S.N. Karmakar, Europhys. Lett. **95**, 57008 (2011)
23. J. Splettstoesser, M. Governale, U. Zülicke, Phys. Rev. B **68**, 165341 (2003)
24. M. Nita, D.C. Marinescu, A. Manolescu, V. Gudmundsson, Phys. Rev. B **83**, 155427 (2011)
25. E.B. Sonin, Phys. Rev. Lett. **99**, 266602 (2007)
26. Q.F. Sun, X.C. Xie, J. Wang, Phys. Rev. B **77**, 035327 (2008)
27. J.S. Sheng, K. Chang, Phys. Rev. B **74**, 235315 (2006)
28. A. Matos-Abiague, J. Berakdar, Phys. Rev. Lett. **94**, 166801 (2005)
29. Y.V. Pershin, C. Piermarocchi, Phys. Rev. B **72**, 245331 (2005)
30. O.V. Kibis, Phys. Rev. Lett. **107**, 106802 (2011)
31. O.V. Kibis, O. Kyriienko, I.A. Shelykh, Phys. Rev. B **87**, 245437 (2013)
32. Z.G. Zhu, J. Berakdar, Phys. Rev. B **77**, 235438 (2008)
33. O. Jonasson, C.S. Tang, H.S. Goan, A. Manolescu, V. Gudmundsson, New J. Phys. **14**, 013036 (2012)
34. E. Jaynes, F.W. Cummings, Proc. IEEE **51**, 89 (1963)
35. Y. Wu, X. Yang, Phys. Rev. Lett. **98**, 013601 (2007)
36. A.T. Sornborger, A.N. Cleland, M.R. Geller, Phys. Rev. A **70**, 052315 (2004)
37. D. Frustaglia, K. Richter, Phys. Rev. B **69**, 235310 (2004)
38. G. Ying-Fang, Z. Yong-Ping, L. Jiu-Qing, Chinese Phys. Lett. **21**, 2093 (2004)
39. Y.S. Yi, T.Z. Qian, Z.B. Su, Phys. Rev. B **55**, 10631 (1997)
40. A.G. Aronov, Y.B. Lyanda-Geller, Phys. Rev. Lett. **70**, 343 (1993)
41. X.F. Wang, P. Vasilopoulos, Phys. Rev. B **72**, 165336 (2005)
42. C.S. Tang, C.S. Chu, Phys. Rev. B **60**, 1830 (1999)
43. G. Zhou, Y. Li, J. Phys.: Condens. Matter **17**, 6663 (2005)
44. J.W. Jung, K. Na, L.E. Reichl, Phys. Rev. A **85**, 023420 (2012)
45. C.S. Tang, C.S. Chu, Physica B **292**, 127 (2000)
46. G. Zhou, M. Yang, X. Xiao, Y. Li, Phys. Rev. B **68**, 155309 (2003)
47. H. Spohn, Rev. Mod. Phys. **52**, 569 (1980)
48. S.A. Gurvitz, Y.S. Prager, Phys. Rev. B **53**, 15932 (1996)
49. N.G. van Kampen, *Stochastic Processes in Physics and Chemistry*, 2nd edn. (North-Holland, Amsterdam, 2001)
50. U. Harbola, M. Esposito, S. Mukamel, Phys. Rev. B **74**, 235309 (2006)
51. C. Bruder, H. Schoeller, Phys. Rev. Lett. **72**, 1076 (1994)

52. A. Braggio, J. König, R. Fazio, Phys. Rev. Lett. **96**, 026805 (2006)

53. V. Moldoveanu, A. Manolescu, V. Gudmundsson, New J. Phys. **11**, 073019 (2009)

54. H.P. Breuer, B. Kappler, F. Petruccione, Phys. Rev. A **59**, 1633 (1999)

55. T. Arnold, M. Siegmund, O. Pankratov, J. Phys.: Condens. Matter **23**, 335601 (2011)

56. W.C. Tan, J.C. Inkson, Semicond. Sci. Technol. **11**, 1635 (1996)

57. J. Shi, P. Zhang, D. Xiao, Q. Niu, Phys. Rev. Lett. **96**, 076604 (2006)

58. N. Bray-Ali, Z. Nussinov, Phys. Rev. B **80**, 012401 (2009)

59. E.I. Rashba, Phys. Rev. B **68**, 241315 (2003)

60. H.J. Drouhin, G. Fishman, J.E. Wegrowe, Phys. Rev. B **83**, 113307 (2011)

61. F. Bottegoni, H.J. Drouhin, G. Fishman, J.E. Wegrowe, Phys. Rev. B **85**, 235313 (2012)

62. E.B. Sonin, Phys. Rev. B **76**, 033306 (2007)

63. R.S. Whitney, J. Phys. A **41**, 175304 (2008)

64. V. Gudmundsson, O. Jonasson, C.S. Tang, H.S. Goan, A. Manolescu, Phys. Rev. B **85**, 075306 (2012)

65. V. Gudmundsson, C. Gainar, C.S. Tang, V. Moldoveanu, A. Manolescu, New J. Phys. **11**, 113007 (2009)

66. M.S. Sarandy, D.A. Lidar, Phys. Rev. Lett. **95**, 250503 (2005)

67. A. Carollo, I. Fuentes-Guridi, M.F.M.C. Santos, V. Vedral, Phys. Rev. Lett. **90**, 160402 (2003)

68. F.E. Meijer, A.F. Morpurgo, T.M. Klapwijk, Phys. Rev. B **66**, 033107 (2002)

69. K. Shakouri, B. Szafran, M. Esmaeilzadeh, F.M. Peeters, Phys. Rev. B **85**, 165314 (2012)

70. F. Nagasawa, J. Takagi, Y. Kunihashi, M. Kohda, J. Nitta, Phys. Rev. Lett. **108**, 086801 (2012)

71. B. Molnár, F.M. Peeters, P. Vasilopoulos, Phys. Rev. B **69**, 155335 (2004)

72. N. Byers, C.N. Yang, Phys. Rev. Lett. **7**, 46 (1961)

73. S. Viefers, P. Koskinen, P.S. Deo, M. Manninen, Physica E **21**, 1 (2004)